

EFFECTS OF APEX ANGLE VARIATION ON FLOW DEVELOPMENT IN JETS  
ISSUING FROM DIFFERENT ISOSCELES TRIANGULAR ORIFICES

by

Mohammad Abul Kalam Azad

Submitted in partial fulfillment of the requirements  
for the degree of Master of Applied Science

at

Dalhousie University  
Halifax, Nova Scotia  
July 2011

© Copyright by Mohammad Abul Kalam Azad, 2011

DALHOUSIE UNIVERSITY  
DEPARTMENT OF MECHANICAL ENGINEERING

The undersigned hereby certify that they have read and recommend to the Faculty of Graduate Studies for acceptance of a thesis entitled “EFFECTS OF APEX ANGLE VARIATION ON FLOW DEVELOPMENT IN JETS ISSUING FROM DIFFERENT ISOSCELES TRIANGULAR ORIFICES” by Mohammad Abul Kalam Azad in partial fulfillment of the requirements for the degree of Master of Applied Science.

Dated: July 15, 2011

Supervisors:

\_\_\_\_\_  
\_\_\_\_\_

Readers:

\_\_\_\_\_  
\_\_\_\_\_

DALHOUSIE UNIVERSITY

DATE: July 15, 2011

AUTHOR: Mohammad Abul Kalam Azad

TITLE: EFFECTS OF APEX ANGLE VARIATION ON FLOW  
DEVELOPMENT IN JETS ISSUING FROM DIFFERENT  
ISOSCELES TRIANGULAR ORIFICES

DEPARTMENT: Department of Mechanical Engineering

DEGREE: MASC CONVOCATION: October YEAR: 2011

Permission is herewith granted to Dalhousie University to circulate and to have copied for non-commercial purposes, at its discretion, the above title upon the request of individuals or institutions. I understand that my thesis will be electronically available to the public.

The author reserves other publication rights, and neither the thesis nor extensive extracts from it may be printed or otherwise reproduced without the author's written permission.

The author attests that permission has been obtained for the use of any copyrighted material appearing in the thesis (other than the brief excerpts requiring only proper acknowledgement in scholarly writing), and that all such use is clearly acknowledged.

---

Signature of Author

To my parents

## TABLE OF CONTENTS

LIST OF TABLES.....	ix
LIST OF FIGURES.....	x
ABSTRACT.....	xv
LIST OF ABBREVIATIONS AND SYMBOLS USED.....	xvi
ACKNOWLEDGEMENTS.....	xix
CHAPTER 1: Introduction.....	1
1.1    Previous studies on triangular jets.....	1
1.2    Objectives.....	10
CHAPTER 2: Experimental set-up and equipment.....	12
2.1    Jet facility.....	12
2.2    Traverse system.....	14
2.3    Orifices used in the experiments.....	15
2.4    Pitot-static tube.....	19
2.4.1    Operating principle of the pitot-static tube.....	19
2.5    Hot-wire anemometer.....	22
2.5.1    Operating principle of the CTA.....	22
2.5.2    Heat loss from the wire.....	24
2.5.3    Anemometer type and the hot-wire probe.....	24
2.5.4    Velocity Measurement.....	25
2.5.5    Calibration of Hot Wire probes.....	28
2.5.6    Linearization and digitization of hot-wire signals.....	29
2.6    Number of samples used in calculations.....	30

CHAPTER 3: Results.....	31
3.1    Initial conditions.....	31
3.1.1    Exit mean streamwise velocity profiles.....	31
3.1.2    Exit streamwise turbulence intensities.....	33
3.1.3    Mean static pressure distribution.....	35
3.2    Mean streamwise centreline velocity decay.....	37
3.3    Development of the jet half-velocity widths.....	40
3.4    Geometric mean of the jet half-velocity widths.....	43
3.5    Mean streamwise velocity contour maps.....	45
3.6    Mass entrainment into the jets.....	63
3.7    Streamwise turbulence intensities on the jet centreline.....	64
3.8    Spanwise turbulence intensities on the jet centreline.....	67
3.9    One-dimensional energy spectra of the streamwise fluctuating velocity on the jet centreline.....	70
3.10    Distribution of autocorrelation coefficients of the streamwise fluctuating velocity on the jet centreline.....	84
CHAPTER 4: Discussion.....	97
4.1    Mean streamwise centreline velocity decay.....	97
4.2    Development of the jet half-velocity widths.....	105
4.3    Geometric mean of the jet half-velocity widths.....	108
4.4    Mean streamwise velocity contour maps.....	111
4.5    Mass entrainment into the jets.....	113
4.6    Streamwise turbulence intensities on the jet centreline.....	116
4.7    Spanwise turbulence intensities on the jet centreline.....	118

4.8	One-dimensional energy spectra of the streamwise fluctuating velocity on the jet centreline.....	119
4.9	Distribution of autocorrelation coefficients of the streamwise fluctuating velocity on the jet centreline.....	121
CHAPTER 5: Conclusions and recommendations for future work.....		123
5.1	Conclusions.....	123
5.2	Recommendations for future work.....	125
References.....		127
APPENDIX A: Hot wire calibration curves.....		131
A.1	Velocity calibration curve.....	131
A.2	Yaw calibration curve.....	133
APPENDIX B: Calculation of bulk velocity.....		134
APPENDIX C: Mean streamwise centreline velocity decay and potential core length data.....		137
C.1	Mean streamwise centreline velocity decay and potential core length data for the 10° jet.....	138
C.2	Mean streamwise centreline velocity decay and potential core length data for the 20° jet.....	139
C.3	Mean streamwise centreline velocity decay and potential core length data for the 30° jet.....	141
C.4	Mean streamwise centreline velocity decay and potential core length data for the 70° jet.....	143
C.5	Mean streamwise centreline velocity decay and potential core length data for the 160° jet.....	145
C.6	Mean streamwise centreline velocity decay and potential core length data for the sharp-edged orifice round jet.....	147
C.7	Mean streamwise centreline velocity decay and potential core length data for the contoured nozzle round jet.....	149

APPENDIX D: Curve fitting of the mean streamwise centreline velocity decay data.....	151
APPENDIX E: Curve fitting of the geometric mean of the half-velocity widths.....	158
APPENDIX F: Curve fitting of the mass entrainment ratio data.....	165
APPENDIX G: Derivation of the decay law of the mean streamwise centreline velocity in the developed flow region.....	172

## LIST OF TABLES

Table 2.1	Aspect ratio and perimeter of the orifices.....	19
Table 4.1	Mean streamwise centreline velocity decay rates and kinematic virtual origins.....	103
Table 4.2	Spreading rates and geometric virtual origins.....	108
Table 4.3	Rates of mass entrainment of the jets and values of $C_e$ .....	114

## LIST OF FIGURES

Figure 2.1	Plan view section of the flow facility.....	13
Figure 2.2	Components of the traverse system. (a) streamwise and spanwise components (b) lateral component.....	15
Figure 2.3	Isosceles sharp-edged triangular orifices with apex angles of (a) 10°, (b) 20°, (c) 30°, (d) 70°, (e) 160° and (f) sharp-edged round orifice.....	18
Figure 2.4	Pitot-static tube.....	21
Figure 2.5	Pressure transducer.....	22
Figure 2.6	Constant Temperature Anemometer with electronic testing sub circuit.....	23
Figure 2.7	Orientation of the wires of an x-array probe to the flow field.....	26
Figure 3.1	Exit mean streamwise velocity profiles.....	32
Figure 3.2	Exit mean streamwise velocity profiles (continued).....	33
Figure 3.3	Exit streamwise turbulence intensity profiles.....	34
Figure 3.4	Exit streamwise turbulence intensity profiles (continued).....	35
Figure 3.5	Static pressure distribution across the jet.....	36
Figure 3.6	Mean streamwise centreline velocity decay.....	38
Figure 3.7	Mean streamwise centreline velocity decay (log-log).....	39
Figure 3.8	Development of the jet half-velocity widths.....	42
Figure 3.9	Development of the jet half-velocity widths (continued).....	43
Figure 3.10	Geometric mean of the jet half-velocity widths.....	44
Figure 3.11	Geometric mean of the jet half-velocity widths in near field.....	45
Figure 3.12	Mean streamwise velocity contour maps for the 10° jet.....	49
Figure 3.13	Mean streamwise velocity contour maps for the 10° jet (continued).....	50
Figure 3.14	Mean streamwise velocity contour maps for the 20° jet.....	51

Figure 3.15	Mean streamwise velocity contour maps for the 20° jet (continued).....	52
Figure 3.16	Mean streamwise velocity contour maps for the 30° jet.....	53
Figure 3.17	Mean streamwise velocity contour maps for the 30° jet (continued).....	54
Figure 3.18	Mean streamwise velocity contour maps for the 70° jet.....	55
Figure 3.19	Mean streamwise velocity contour maps for the 70° jet (continued).....	56
Figure 3.20	Mean streamwise velocity contour maps for the 160° jet.....	57
Figure 3.21	Mean streamwise velocity contour maps for the 160° jet (continued).....	58
Figure 3.22	Mean streamwise velocity contour maps for the sharp-edged orifice round jet.....	59
Figure 3.23	Mean streamwise velocity contour maps for the sharp-edged orifice round jet (continued).....	60
Figure 3.24	Mean streamwise velocity contour maps for the contoured nozzle round jet.....	61
Figure 3.25	Mean streamwise velocity contour maps for the contoured nozzle round jet (continued).....	62
Figure 3.26	Mass entrainment into the jets.....	64
Figure 3.27	Streamwise turbulence intensities on the jet centreline.....	65
Figure 3.28	Streamwise turbulence intensities on the jet centreline (log-log).....	67
Figure 3.29	Spanwise turbulence intensities on the jet centreline.....	68
Figure 3.30	Spanwise turbulence intensities on the jet centreline (log-log).....	70
Figure 3.31	One-dimensional energy spectra of the streamwise fluctuating velocity on the centreline of the 10° jet.....	72
Figure 3.32	One-dimensional energy spectra of the streamwise fluctuating velocity on the centreline of the 10° jet (continued).....	73
Figure 3.33	One-dimensional energy spectra of the streamwise fluctuating velocity on the centreline of the 20° jet.....	74

Figure 3.34	One-dimensional energy spectra of the streamwise fluctuating velocity on the centreline of the 20° jet (continued).....	75
Figure 3.35	One-dimensional energy spectra of the streamwise fluctuating velocity on the centreline of the 30° jet.....	76
Figure 3.36	One-dimensional energy spectra of the streamwise fluctuating velocity on the centreline of the 30° jet (Continued).....	77
Figure 3.37	One-dimensional energy spectra of the streamwise fluctuating velocity on the centreline of the 70° jet.....	78
Figure 3.38	One-dimensional energy spectra of the streamwise fluctuating velocity on the centreline of the jet 70° jet (continued).....	79
Figure 3.39	One-dimensional energy spectra of the streamwise fluctuating velocity on the centreline of the 160° jet.....	80
Figure 3.40	One-dimensional energy spectra of the streamwise fluctuating velocity on the centreline of the 160° jet (continued).....	81
Figure 3.41	One-dimensional energy spectra of the streamwise fluctuating velocity on the centreline of the sharp-edged orifice round jet.....	82
Figure 3.42	One-dimensional energy spectra of the streamwise fluctuating velocity on the centreline of the sharp-edged orifice round jet (continued).....	83
Figure 3.43	Autocorrelation distribution of the streamwise fluctuating velocity on the centreline of the 10° jet.....	85
Figure 3.44	Autocorrelation distribution of the streamwise fluctuating velocity on the centreline of the 10° jet (continued).....	86
Figure 3.45	Autocorrelation distribution of the streamwise fluctuating velocity on the centreline of the 20° jet.....	87
Figure 3.46	Autocorrelation distribution of the streamwise fluctuating velocity on the centreline of the 20° jet (continued).....	88
Figure 3.47	Autocorrelation distribution of the streamwise fluctuating velocity on the centreline of the 30° jet.....	89
Figure 3.48	Autocorrelation distribution of the streamwise fluctuating velocity on the centreline of the 30° jet (continued).....	90

Figure 3.49	Autocorrelation distribution of the streamwise fluctuating velocity on the centreline of the 70° jet.....	91
Figure 3.50	Autocorrelation distribution of the streamwise fluctuating velocity on the centreline of the 70° jet (continued).....	92
Figure 3.51	Autocorrelation distribution of the streamwise fluctuating velocity on the centreline of the 160° jet.....	93
Figure 3.52	Autocorrelation distribution of the streamwise fluctuating velocity on the centreline of the 160° jet (continued).....	94
Figure 3.53	Autocorrelation distribution of the streamwise fluctuating velocity on the centreline of the sharp-edged orifice round jet.....	95
Figure 3.54	Autocorrelation distribution of the streamwise fluctuating velocity on the centreline of the sharp-edged orifice round jet (continued).....	96
Figure 4.1	Side shear layer development in the 70° and 20° triangular jets.....	99
Figure 4.2	Base shear layer development in the 70° and 20° triangular jets.....	100
Figure 4.3	Spreading of the 30° jets of the present study and of Quinn (2005a).....	110
Figure A.1	Typical linear least squares fit for the velocity calibration of the x-array probe used.....	131
Figure A.2	Typical velocity calibration curve for the x-array probe used.....	132
Figure A.3	Typical Yaw calibration curve of the x-array probe used.....	133
Figure B.1	A typical velocity profile close to the exit of an orifice jet.....	134
Figure D.1	Curve fitting of the mean streamwise centreline velocity decay data for the 10° jet.....	151
Figure D.2	Curve fitting of the mean streamwise centreline velocity decay data for the 20° jet.....	152
Figure D.3	Curve fitting of the mean streamwise centreline velocity decay data for the 30° jet.....	153
Figure D.4	Curve fitting of the mean streamwise centreline velocity decay data for the 70° jet.....	154

Figure D.5	Curve fitting of the mean streamwise centreline velocity decay data for the 160° jet.....	155
Figure D.6	Curve fitting of the mean streamwise centreline velocity decay data for the sharp-edged orifice round jet.....	156
Figure D.7	Curve fitting of the mean streamwise centreline velocity decay data for the contoured nozzle round jet.....	157
Figure E.1	Curve fitting of the geometric mean of half-velocity width data for the 10° jet.....	158
Figure E.2	Curve fitting of the geometric mean of half-velocity width data for the 20° jet.....	159
Figure E.3	Curve fitting of the geometric mean of half-velocity width data for the 30° jet.....	160
Figure E.4	Curve fitting of the geometric mean of half-velocity width data for the 70° jet.....	161
Figure E.5	Curve fitting of the geometric mean of half-velocity width data for the 160° jet.....	162
Figure E.6	Curve fitting of the geometric mean of half-velocity width data for the sharp-edged orifice round jet.....	163
Figure E.7	Curve fitting of the geometric mean of half-velocity width data for the contoured nozzle round jet.....	164
Figure F.1	Curve fitting of the mass entrainment ratio data for the 10° jet.....	165
Figure F.2	Curve fitting of the mass entrainment ratio data for the 20° jet.....	166
Figure F.3	Curve fitting of the mass entrainment ratio data for the 30° jet.....	167
Figure F.4	Curve fitting of the mass entrainment ratio data for the 70° jet.....	168
Figure F.5	Curve fitting of the mass entrainment ratio data for the 160° jet.....	169
Figure F.6	Curve fitting of the mass entrainment ratio data for the sharp-edged orifice round jet.....	170
Figure F.7	Curve fitting of the mass entrainment ratio data for the contoured nozzle round jet.....	171

## ABSTRACT

Isothermal, incompressible jets of air issuing from sharp-edged isosceles triangular orifices with apex angles of  $10^\circ$ ,  $20^\circ$ ,  $30^\circ$ ,  $70^\circ$  and  $160^\circ$  into still surrounding air, were used to study the effects of apex angle variation on flow development in the jets. Some measurements were made in two round jets issuing from a sharp-edged orifice and from a contoured nozzle. All the orifices and the nozzle had the same exit area. The Reynolds number, based on the equivalent diameter of the triangular orifices (the same as the diameter of the round orifice and nozzle), was approximately 193,000 in all the jets. The mean velocities and turbulence quantities were measured with an x-array type hot-wire probe. A pitot-static tube was also used to measure the mean streamwise velocity.

The mean streamwise centreline velocity decay, mass entrainment and spreading results show that the  $160^\circ$  jet, which originates from the orifice with the longest perimeter, has the highest mixing rate in the near flow field ( $X/D_e \leq 10$ ). The high near-field mixing rate of the  $160^\circ$  jet is supported by the following experimental results: first, the streamwise and spanwise turbulence intensities on the centreline grow at the fastest rate in this jet; second, the one-dimensional energy spectrum develops most rapidly in this jet, which has the highest preferred mode Strouhal number among all the jets. The near-field results also show that the mixing rate increases with increase in the orifice perimeter except in the region  $2 \leq X/D_e \leq 9$ . In this region, the  $70^\circ$  jet has a higher mixing rate than the  $20^\circ$  and  $30^\circ$  jets, although the  $70^\circ$  triangular orifice has a shorter perimeter than the  $20^\circ$  and  $30^\circ$  orifices.

The mean streamwise centreline velocity decay rate, spreading rate and mass entrainment rate results suggest that the  $10^\circ$  jet has the highest mixing rate in the far field ( $X/D_e \geq 10$ ) and that the mixing rate decreases as the perimeter of the orifice decreases, except for the  $160^\circ$  jet.

The results demonstrate that all the triangular jets have higher mixing rates than the round jets, throughout the flow region investigated. Although the sharp-edged orifice round jet has a higher mixing rate than the contoured nozzle round jet in the far field, it has a lower mixing rate in the near field.

## LIST OF ABBREVIATIONS AND SYMBOLS USED

### SYMBOLS

$A_1$	Constant for wire #1 in the hot-wire power law equation
$A_2$	Constant for wire #2 in the hot-wire power law equation
$B_1$	Constant for wire #1 in the hot-wire power law equation
$B_2$	Constant for wire #2 in the hot-wire power law equation
$B_{1/2}$	Geometric mean of jet half-velocity widths of the jets
$C_e$	Constant in the rate of mass entrainment equation
$C_s$	Geometric virtual origin
$C_u$	Kinematic virtual origin
$D_e$	Equivalent diameter of the triangular orifices and diameter of the contoured round orifice or nozzle
$E_0$	Hot-wire output voltage when the probe is not rotated during yaw calibration
$E_1$	Hot-wire output voltage for wire #1
$E_2$	Hot-wire output voltage for wire #2
$f$	Frequency
$K_e$	Rate of mass entrainment into the jets
$K_s$	Spreading rate of the jets
$K_u$	Mean streamwise centreline velocity decay rate
$n_1$	Exponent for wire #1 in the hot-wire power law equation
$n_2$	Exponent for wire #2 in the hot-wire power law equation
$P_s$	Mean static pressure
$P_{atm}$	Atmospheric pressure
$Q$	Mass flow rate at a streamwise location

$Q_0$	Mass flow rate close to the orifice or nozzle exit plane
$St_{D_e}$	Preferred mode Strouhal number based on $D_e$
$t$	Time
$U$	Streamwise component of the mean velocity vector
$U_{bulk}$	Area-averaged value of $U$ close to the exit
$U_{cl}$	Value of $U$ on the jet centreline
$U_{exit}$	Value of $U$ at the centre of the orifice or nozzle exit plane
$U_{max}$	Maximum value of $U$ on the jet centreline
$\overline{u'^2}$	Streamwise Reynolds normal stress
$\sqrt{\overline{u'^2}}$	Root-mean-square of the streamwise fluctuating velocity
$V_{eff_1}$	Effective hot-wire cooling velocity for wire #1
$V_{eff_2}$	Effective hot-wire cooling velocity for wire #2
$\overline{v'^2}$	Spanwise Reynolds normal stress
$\sqrt{\overline{v'^2}}$	Root-mean-square of the spanwise fluctuating velocity
$X$	Streamwise coordinate
$Y$	Spanwise coordinate
$Y_{1/2}$	Jet half-velocity width in the $Y$ -direction
$Z$	Lateral coordinate
$Z_{1/2}$	Jet half-velocity width in the $Z$ -direction

#### GREEK SYMBOLS

$\phi_u$	Power spectral density
----------	------------------------

$\rho$	Density of the jet fluid
$\rho_u(\tau)$	Autocorrelation coefficient
$\sigma$	Generic fluctuating velocity
$\theta_1$	Effective angle for wire #1
$\theta_2$	Effective angle for wire #2
$\theta_{eff}$	Effective angle of the hot-wire
$\tau$	Time delay

#### ABBREVIATIONS

CCA	Constant Current Anemometer
CTA	Constant Temperature Anemometer
HWA	Hot Wire Anemometer

## ACKNOWLEDGEMENTS

I must express my sincerest gratitude to my supervisor Prof. Willie R. Quinn for his guidance and support. I cannot thank him enough for his continuous help and inspiration as I carried out the research which led to this thesis. I am also very grateful to my other supervisor Dr. Dominic Groulx for his support and encouragement.

In addition to my supervisors, I am also thankful to Prof. Mysore Satish and Prof. Prabir Basu for agreeing to serve on my thesis committee.

I am grateful to Mr. Craig Seaboyer, electronics technologist at St. Francis Xavier University, for all his help in solving the problems I encountered with electronics and to Mr. Werner Schnepf and Mr. Steven MacDonald, machinists at St. Francis Xavier University, for their help with manufacturing the orifices used and solving mechanical problems I had in the laboratory.

There are many other individuals, including my family members and friends, who have helped me along the route to completing my master's thesis. I wish to extend my sincere thanks to all of them.

# CHAPTER 1

## Introduction

### 1.1 Previous studies on triangular jets

Turbulent jets are used in many engineering applications, such as in chemical reactors, combustion chambers of jet engines and boiler furnaces. Fast mixing is a requirement for good performance in most of the applications mentioned above. In combustion applications, the combination of bulk mixing and molecular mixing of the fuel and oxidizer is very advantageous. While circular orifices are widely used in engineering applications because of the ease with which they can be manufactured, noncircular jets with corners, such as rectangular, square, triangular, provide both bulk and molecular mixing.

A few studies have, thus far, been devoted entirely to triangular jets. Schadow et al. (1988) studied triangular jets as a means of enhancing small-scale mixing and reducing flow coherence. The test jets issued from pipes and orifices with two triangular shapes, namely, equilateral and isosceles with an apex angle of  $30^\circ$ . Some experiments were done in jets issuing from a round pipe and a round orifice. Two exit plane velocities: 50 m/s (high velocity) and 12 m/s (low velocity), were used. The Reynolds numbers, based on the equivalent diameters, in the high velocity tests were  $2.4 \times 10^5$  and  $1.6 \times 10^5$  in the pipe and orifice jets, respectively. In the low velocity experiments, the measurements were made only in the jets issuing from a round and from an equilateral

triangular orifice, which had the same equivalent diameter. The Reynolds number, based on the equivalent diameter, in the low-velocity jets was  $4 \times 10^4$ . The results of these tests showed that the initial turbulence intensity at a corner of the triangle was higher than that on the flat side. As the jet evolved downstream, the turbulence intensity on the flat side increased significantly while remaining almost the same at the corner. The results also showed that the spectra of the streamwise fluctuating velocity exhibited discernible peaks on the flat side and were broadband at the corner. The autocorrelation coefficient distribution in the forced isosceles triangular jet at the high velocity was periodic on the flat side and non-periodic at the vertex section. It was concluded that large-scale and small-scale structures were generated on the flat side and at the corner, respectively. The results also showed that forcing of the jet increased the spreading on the flat side but had no effect on the spreading at the corner.

Detailed mean flow and turbulence measurements were made, using hot-wire anemometry, in an incompressible, isothermal equilateral triangular jet at a Reynolds number, based on the equivalent diameter of the triangular orifice, of  $2.08 \times 10^5$  by Quinn (1990). The quantities measured were the three components of the mean velocity vector, the three Reynolds normal and the two primary shear stresses. It was found that the jet spreads faster on its base side than at its apex. These different spreading rates led to the inversion of the jet shape at about five equivalent diameters downstream of the orifice exit. The results for this jet were compared to those of a round jet issuing from a sharp-edged orifice and it was found that the mixing rate in the triangular jet was higher than that in the round jet.

Vandsburger and Ding (1995) used active control to study the evolution of an equilateral triangular jet, with fully sheared initial velocity profile and initial high level of turbulence, in the far field. The Reynolds number in this study, based on the equivalent diameter, was 8000. While previous researchers observed axis-switching in triangular jets, this phenomenon was absent in the unexcited jet of this study. The discrepancy was claimed to be due to the absence of a potential core in the jet. Iso-velocity contours were presented in the range of  $X/D_e=0.5$  to 30. It was found that the unexcited jet attained an axisymmetric shape at  $X/D_e=30$ . When the jet was forced in single helical mode (i.e.,  $m=1$ ) at small amplitude, there was no change in the shape of the jet cross-section in the far field but the area of the cross-section increased slightly. On the other hand, when the jet was forced at a non-integer counter-rotating mode (i.e.,  $m=\pm 0.5$ ), the cross-section of the jet changed from an axisymmetric to an elliptic shape in the far field and the area of the jet cross-section also increased significantly. The rate of entrainment of the forced jet was, therefore, much more than that of the unforced jet.

Quinn (2005a) studied the near field mean flow and turbulence characteristics of an air jet issuing from a sharp-edged isosceles triangular orifice, with an apex angle of  $30^\circ$ , using hot-wire anemometry and a pitot-static tube. Some measurements were made, for comparison, in an equilateral triangular jet and in a round jet. Both the equilateral triangular and round jets also issued from sharp-edged orifices. The Reynolds number, based on the equivalent diameter of the orifices, was  $1.84 \times 10^5$  in each of the jets. The measured quantities in these jets were the three components of the mean velocity vector, the Reynolds normal and primary shear stresses, the one-dimensional energy spectra of the streamwise fluctuating velocities and the mean static pressure. The mean streamwise

vorticity, the half-velocity widths, the turbulence kinetic energy and the local shear in the mean streamwise velocity were calculated from the measured quantities. The equilateral triangular jet showed faster mixing than the isosceles triangular jet and the round jet in the near flow field. It was found that in the isosceles triangular jet, the mean streamwise vorticity field was dominated by counter-rotating pairs of vortices, which influenced mixing and entrainment in the jet. The one-dimensional energy spectra showed that coherent structures were present in the near field of all of the three jets and the equilateral triangular jet was found to be more energetic than the isosceles triangular and the round jets.

Hot-wire time series data, acquired in the near field of an isosceles triangular jet, were phase-averaged, i.e., the fluctuating velocities at different phases were averaged to obtain the coherent component which was then deducted from the total fluctuating signal to get the random component by Quinn (2005b). The phase-averaging was done to find out the contribution of the coherent and random Reynolds primary shear stresses to momentum transfer. The Reynolds number was the same as in Quinn (2005a). Contour maps of the coherent and random spanwise primary shear stresses were presented. It was found that the contours of the coherent primary shear stresses were very similar to those of the spanwise Reynolds primary shear stress in Quinn (2005a) and that the random spanwise Reynolds primary shear stresses were scattered. The coherent spanwise primary shear stresses were larger than their random counterparts, anywhere in the region  $X/D_e \leq 10$ . The aforementioned observations suggest that the momentum transfer by the Reynolds primary shear stresses occurs mainly through the coherent primary shear

stresses in the isosceles triangular jet. This has also been observed in elliptic jets (Husain and Hussain 1991).

The work reported in Quinn (1990) was extended in a later study by Quinn (2005c). In this study, the Reynolds number, based on the equivalent diameter of the orifice, was  $1.84 \times 10^5$  and the three components of the mean velocity vector, the Reynolds normal and primary shear stresses, the distribution of the autocorrelation coefficients and the one-dimensional energy spectra of the fluctuating velocities, and the mean static pressure were measured. The quantities calculated from the measured data were the mean streamwise vorticity, the half-velocity widths, mass entrainment and the local shear in the mean streamwise velocity. Mixing in the equilateral triangular jet, measured by the entrainment of the ambient fluid by the jet fluid, the spread of the jet, the peak of the turbulence intensity on the jet centreline and the recovery of the mean static pressure on the jet centreline, was deduced to be faster than that in the round jet. The mean streamwise vorticity field was found to be dominated by counter-rotating pairs of vortices which, as mentioned before in connection with the isosceles triangular jet (Quinn 2005a), facilitated mixing and entrainment in the equilateral triangular jet. The one-dimensional energy spectra and the distribution of autocorrelation coefficients of the fluctuating velocities showed the presence of coherent structures in the near field of the equilateral triangular jet.

Some studies were done on triangular jets in conjunction with other noncircular and circular jets. Gutmark et al. (1989) studied the combustion dynamics of square and triangular burners using Planar Laser Induced Fluorescence (PLIF) imaging. Two triangular burners were used; one with an equilateral triangular and the other with an

isosceles triangular, with an apex angle of  $30^\circ$ , exit shape. The Reynolds number, based on the equivalent diameter, was 65,000. The air supply was forced at the preferred mode ( $St=0.4$ ) of the jet. It was found that the flame was periodic at the flat side and that small-scale structures were generated at the apex. When the air supply was forced at the first harmonic ( $St=0.8$ ), the same behaviour at the flat side and at the apex was observed. The flow behaviour observed in these reacting tests was also found in the cold tests. The jet was found to spread faster on the flat sides than at the apex. This difference in the spreading rates resulted in a change of the geometry of the jet cross-section.

Seif et al. (1994) investigated turbulent free jets issuing from sharp-edged equilateral triangular and square orifices of the same cross-sectional area, using hot-wire anemometry. Measurements were also made in a free jet issuing from a circular nozzle with the same cross-sectional area for comparison to the results of the triangular and square jets. The Reynolds number, based on the equivalent diameter, was  $6.35 \times 10^4$  in all of the jets. Mean streamwise velocities, turbulence intensities and spectral information were presented. It was found that the development of the jets was significantly different, although all of the jets became axisymmetric in the far field. It was stated that “The development of the asymmetric jets is slower than that of the round jet, with the triangular being the slowest”. However, the spectra showed an opposite scenario, namely, the development of the asymmetric jet was faster than the round jet and the triangular jet showed the fastest development. Large-scale structures dominated the flow along the flat sides of the asymmetric jets, in the near field flow, while small-scale turbulent structures were dominant at the vertices.

Miller et al. (1995) presented the results of direct numerical simulations of spatially developing three-dimensional jets issuing from different orifices with circular and noncircular shapes. The equivalent diameters of all the orifices were the same. The orifices were round, elliptic, square, rectangular, equilateral triangular and isosceles triangular in shape. The jets issued into coflowing surroundings at a Reynolds number, based on the orifice equivalent diameter, of 800. The results showed that coherent structures were formed in both the jets with corners and in those without. The characteristics of the triangular jets were clearly different from those of the other jets. The coherent structures in the triangular jets were rapidly covered by the small-scale structures generated at the corners of the orifices. The axis-switching phenomenon was observed in all of the non-unity aspect-ratio jets and also in the equilateral triangular jet. In the region  $X/D_e \leq 9$ , the triangular jets switched their axes twice, while the other jets switched axes only once. All of the non-circular jets had higher mixing rates than the circular jet. The isosceles triangular jet had the highest mixing rate among all the jets. It was also reported that the isosceles triangular jet and the rectangular jet had the shortest and longest potential core, respectively.

The mean streamwise centreline velocity decay and the streamwise turbulence intensity distribution on the jet centreline in jets issuing from a contoured circular nozzle and eight other differently shaped orifices, namely, circular, elliptical, equilateral triangular, isosceles triangular, square, rectangular, cross- and star-shape were studied by Mi et al (2000). The corners of the noncircular orifices were rounded to a small radius of 1.5 mm. The experiments were performed with hot-wire anemometry. The Reynolds number, based on the equivalent diameter of the orifices, was 15000. It was found that

the length of the potential core was shorter in the jets from the noncircular orifices than that in the jets from the circular orifice and contoured nozzle and that the jet issuing from the isosceles triangular orifice had the shortest potential core length. The mean streamwise centreline velocity decay rates, in the near flow field ( $X/D_e < 10$ ), were higher in the noncircular than in the circular jets. In the region  $X/D_e \geq 10$  the mean streamwise centreline velocity decay rates of the jets issuing from the orifices with square, cross- and star-shape were nearly the same as that of the circular orifice jet. The isosceles triangular jet had the highest mixing rate, as deduced from the mean streamwise centreline velocity decay rate, among all the jets.

Iyogun and Birouk (2009) studied the effects of nozzle geometry and quarl (a cylindrical sudden expansion) on jet entrainment and spreading in turbulent free jets issuing from five different nozzle geometries, namely, smooth pipe, contoured circular, rectangular, equilateral triangular, and square, using laser doppler velocimetry. The mean streamwise centreline velocity decay, jet half-velocity widths, turbulence intensities, and Reynolds primary shear stresses were reported. It was found that the jets issuing from the noncircular nozzles without quarl had higher entrainment and spreading rates compared to the jet issuing from the circular nozzle. The improved entrainment and spreading rates of the noncircular jets were related to the increased level of turbulence in the near field. Although not stated by the authors, it is assumed that the initial turbulence level was the same in all the test jets. It was also found that the triangular nozzle without quarl provided the highest rates of entrainment and spreading. The quarl affected the noncircular jets more than the circular jets and the rectangular nozzle with the quarl had the highest mixing rate.

The work reported in Mi et al. (2000) was extended by Mi and Nathan (2010). The nozzles used in this study were the same as those in the previous study. The Reynolds number was also the same. It was reported that changing the nozzle exit shape results in shifts in the location of the virtual origin and in the potential core length of the jet but that this does not affect the asymptotic mean streamwise centreline velocity decay rate. As in the previous study, the isosceles triangular jet was found to have the shortest potential core length and the highest near-field mean streamwise centreline velocity decay rate among all the jets. It was also found that the isosceles triangular jet had the broadest peak in the one-dimensional energy spectra of the streamwise fluctuating velocities and that this peak disappeared closest to the orifice exit, compared to the other jets tested.

The previous studies on triangular and other noncircular jets have shown that triangular jets have higher mixing rates than those of circular and other noncircular jets. In addition, triangular jets have been found to spread at different rates on the flat sides and at the vertex and that these jets provide a unique combination of large-scale structures, generated at the flat sides, and small-scale structures, generated at the vertices of the triangular orifices. This feature is important for combustion facilities where large-scale mixing is required to mix large amounts of fuel and oxidizer and small-scale mixing is used to enhance chemical reaction by increasing the molecular contact. Like other noncircular jets, triangular jets have also been found to exhibit axis-switching, a phenomenon which enhances mixing. In elliptic and rectangular jets, previous studies have found that the axis-switching is delayed as the aspect ratio of the orifice increases (Tsuchiya and Horikoshi 1986, Hussain and Husain 1989, Quinn 1992). Previous studies

on rectangular jets have also shown that these jets exhibit enhanced mixing when the orifice aspect ratio is large (Quinn 1992). In spite of the importance of triangular jets in combustion systems and the fact that isosceles triangular jets have been found to have the highest mixing rates among jets, no detailed studies have been done on the effects of apex angle variation, that is, the change in orifice aspect ratio on the development of these jets. The present work, therefore, seeks to investigate the effects of apex angle variation on the mixing in isosceles triangular jets.

## 1.2 Objectives

The principal objective of this thesis is to study the effects of apex angle variation on the development of isosceles triangular jets using orifices with apex angles of  $10^\circ$ ,  $20^\circ$ ,  $30^\circ$ ,  $70^\circ$ , and  $160^\circ$ . The results for these triangular jets will be compared to those for round jets issuing from a sharp-edged orifice and from a contoured nozzle. The minor objectives which will facilitate the achievement of the principal objective are:

- To measure the mean streamwise velocity along the centreline of the jets and to calculate the mean streamwise centreline velocity decay rates of the jets.
- To measure the mean streamwise velocities on the central  $X-Y$  (i.e., horizontal) and  $X-Z$  (i.e., vertical) planes, to compare the spreading on those planes and to calculate the overall spreading rates of the jets.
- To measure the mean streamwise velocity on entire  $Y-Z$  planes (i.e., parallel to the orifice exit plane) at different streamwise locations and thus to determine the change in shape of the mean streamwise velocity field with downstream distance and to calculate the entrainment rates of the jets.

- To measure the streamwise and spanwise turbulence intensities on the jet centreline in the test jets.
- To measure the one-dimensional energy spectra and autocorrelation coefficient distribution of the fluctuating streamwise velocity at different locations on the jet centreline in the near flow fields of the jets.

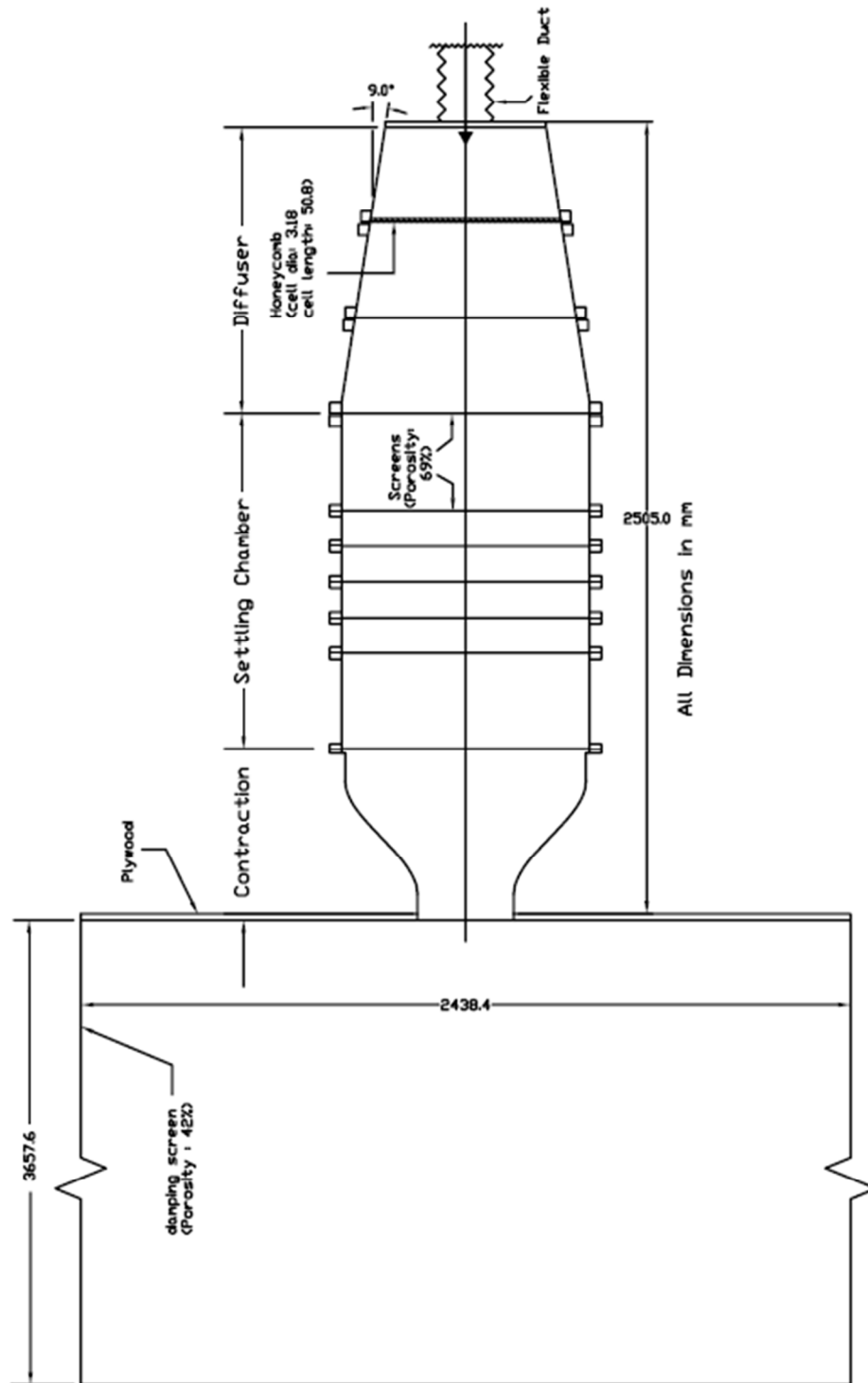
# CHAPTER 2

## Experimental set-up and equipment

### 2.1 Jet facility

The jet flow facility used for the experiments was of the blow down type, which is shown in Figure 2.1. It consists of a centrifugal fan, a diffuser, a settling chamber, a contraction, and a screen cage. The centrifugal fan, which is supported on anti-vibration neoprene pads, drew air from an air-conditioned room adjacent to the room where the experiments were conducted and delivered it, by means of a flexible duct, to the orifices through the diffuser, settling chamber and contraction. The diffuser is fitted with honeycomb and mesh-wire screens. The settling chamber, a plywood box with a cross section of  $0.762\text{ m} \times 0.762\text{ m}$  and a length of  $1.054\text{ m}$ , has seven mesh-wire screens of 69% porosity. The three-dimensional contraction has a contour based on a third-order polynomial with zero first order derivatives as the end conditions. The upstream end of the contraction is circular in cross-section, with a diameter of  $0.762\text{ m}$ , and the downstream end has a  $0.305\text{ m} \times 0.305\text{ m}$  square cross-section. The length of the contraction is  $0.523\text{ m}$  and the contraction ratio is 283. The different orifices capped the downstream end of the contraction. A plywood wall forms the upstream end of a screen cage which extends  $3.658\text{ m}$  downstream from the wall. The experiments were conducted in a  $7.70\text{ m} \times 7.01\text{ m} \times 2.87\text{ m}$  room. The spanwise ( $Y$ ) and lateral ( $Z$ )

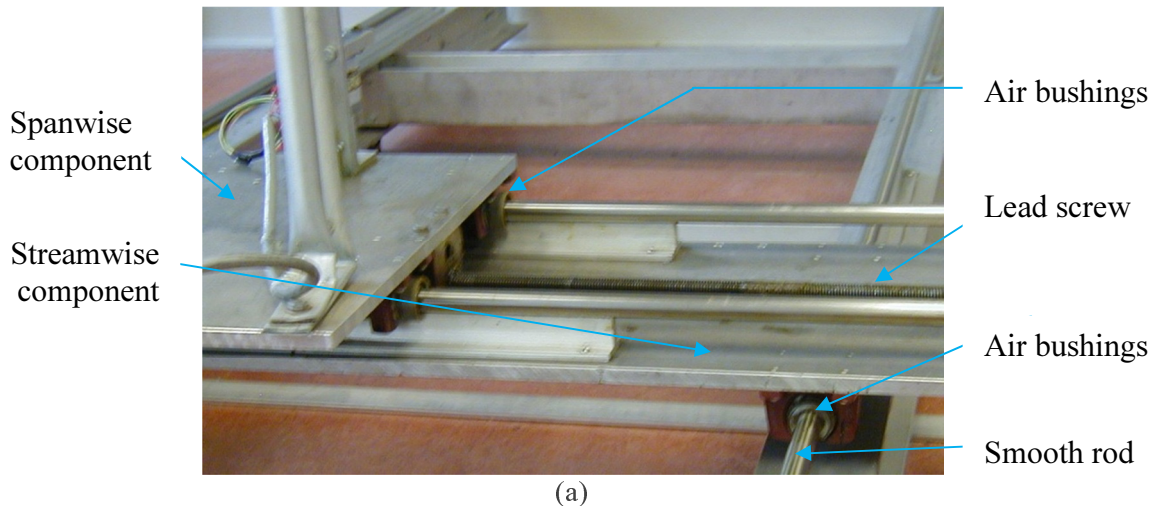
coordinates are shown in Figure 2.3. The streamwise ( $X$ ) coordinate is perpendicular to  $Y$  and  $Z$ .



**Figure 2.1** Plan view section of the flow facility.

## 2.2 Traverse system

A three-dimensional traversing system was used to move the sensing probes in the flow field. This system consists of a rack and pinion for traversing in the streamwise direction and lead screws for traversing in the spanwise and lateral directions. The base of the traversing system is supported on anti-vibration neoprene pads. The streamwise and spanwise components of the system are supported on smooth rods with air bushings (as shown in Figure 2.2a) and the lateral component has a T piece as the inner part of a flat-type slideway system (as shown in Figure 2.2b) which is driven by the rotation of a lead screw. Traversing in all three directions is done by microcomputer-controlled stepping motors. Positioning accuracy of the sensing probes is 0.3 mm in the streamwise direction and 0.01 mm in both the spanwise and lateral directions.



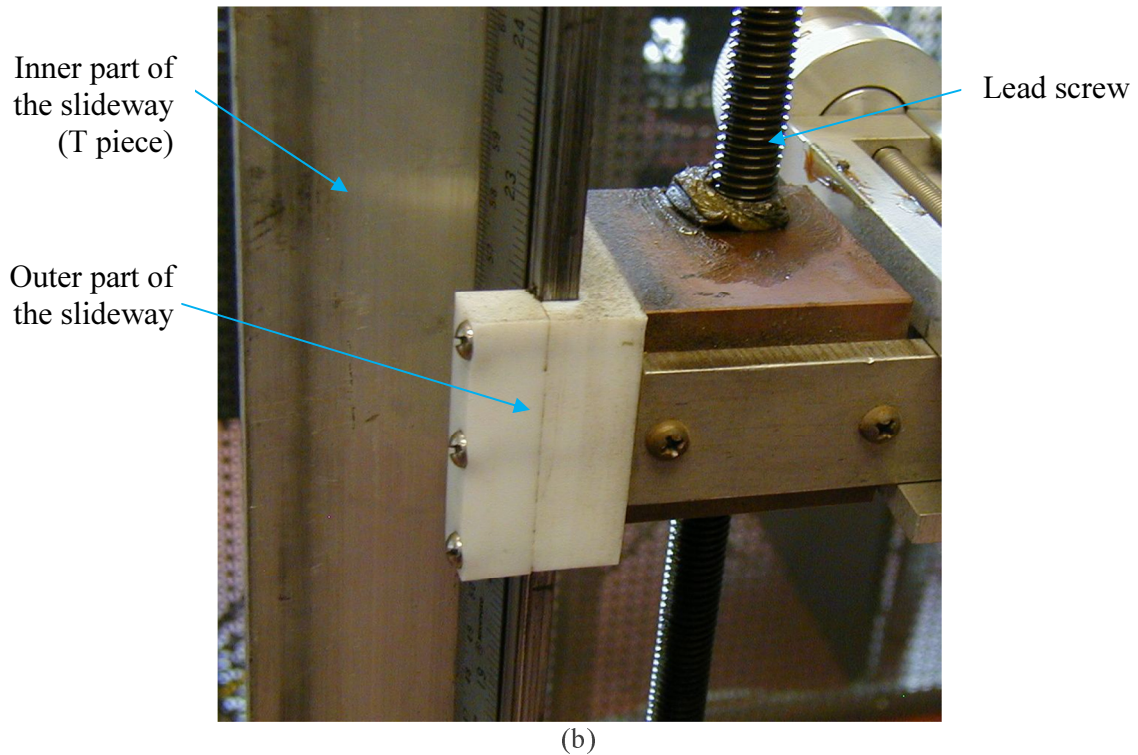
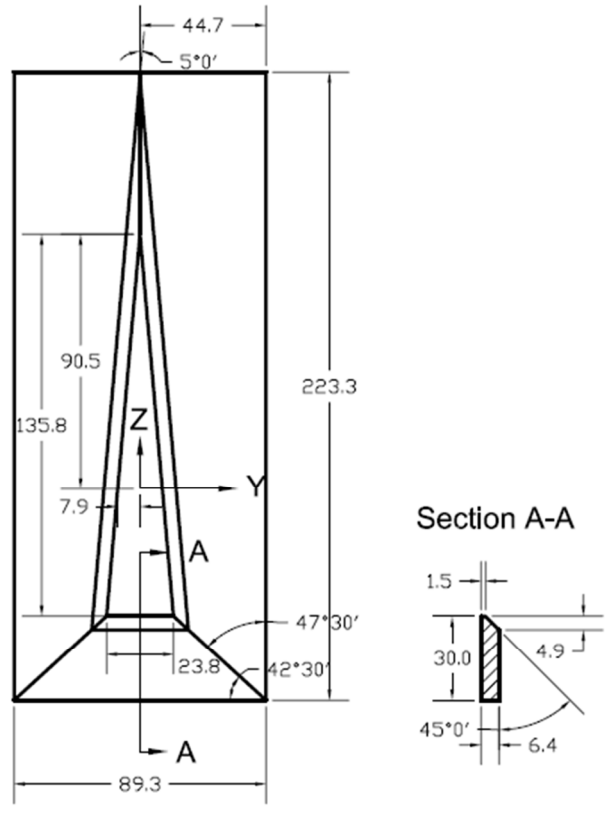


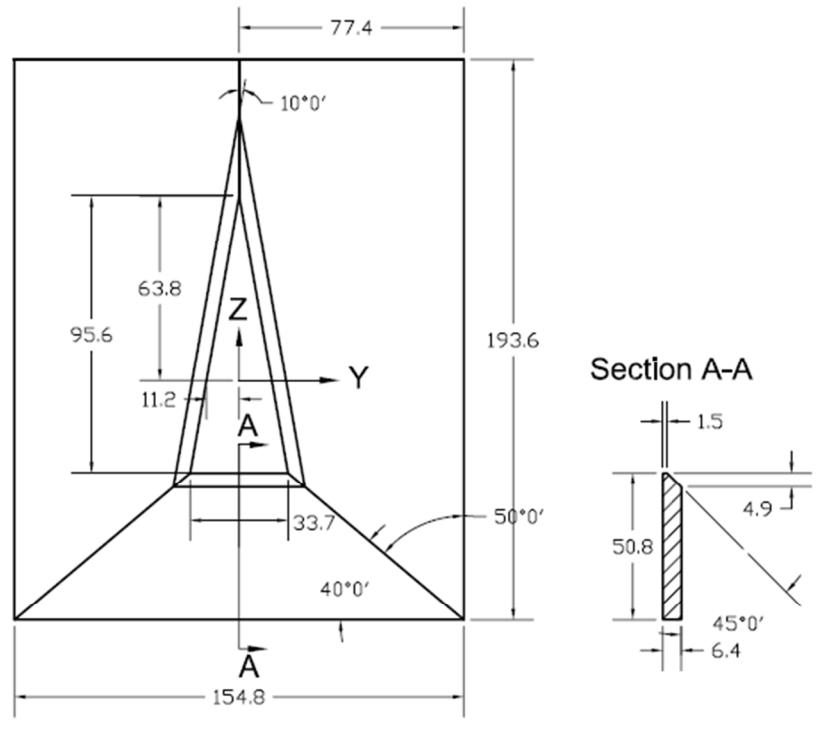
**Figure 2.2** Components of the traverse system. (a) streamwise and spanwise components (b) lateral component.

### 2.3 Orifices used in the experiments

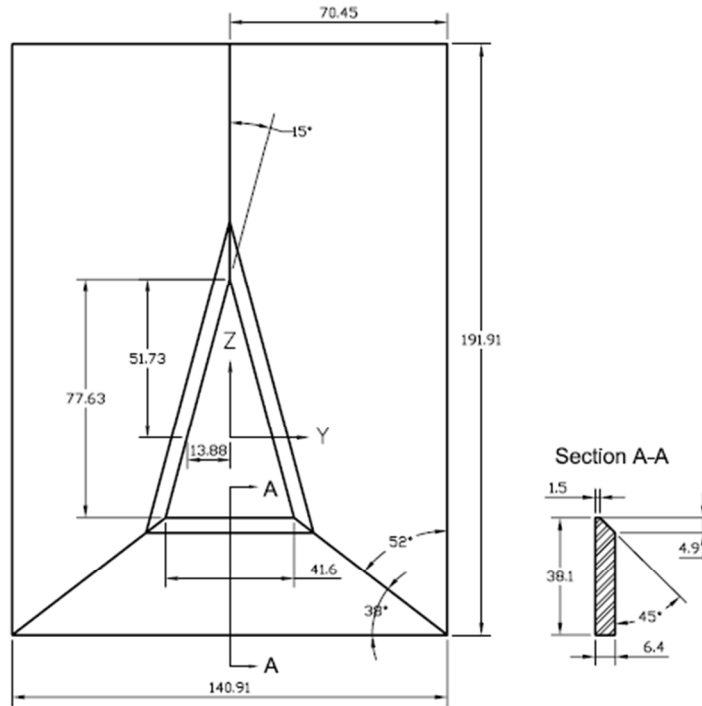
A total of six orifices were used in these experiments; five of these were sharp-edged isosceles triangular orifices with apex angles of  $10^\circ$ ,  $20^\circ$ ,  $30^\circ$ ,  $70^\circ$ , and  $160^\circ$  as shown in Figure 2.3(a), (b), (c), (d), and (e), respectively. The sharp-edged round orifice is shown in Figure 2.3(f). All dimensions in the figures are in mm. It should be noted that the \*'s in Figure 2.3(e) indicate that the dimensions are different from the corresponding ones of the other orifices. It was not possible, due to geometrical constraints in the flow facility, to keep these \* dimensions in the triangular orifice with apex angle  $160^\circ$  the same as those in the other orifices. The aspect ratios of the triangular orifices and perimeters, in mm, of all the orifices are shown in table 2.1.



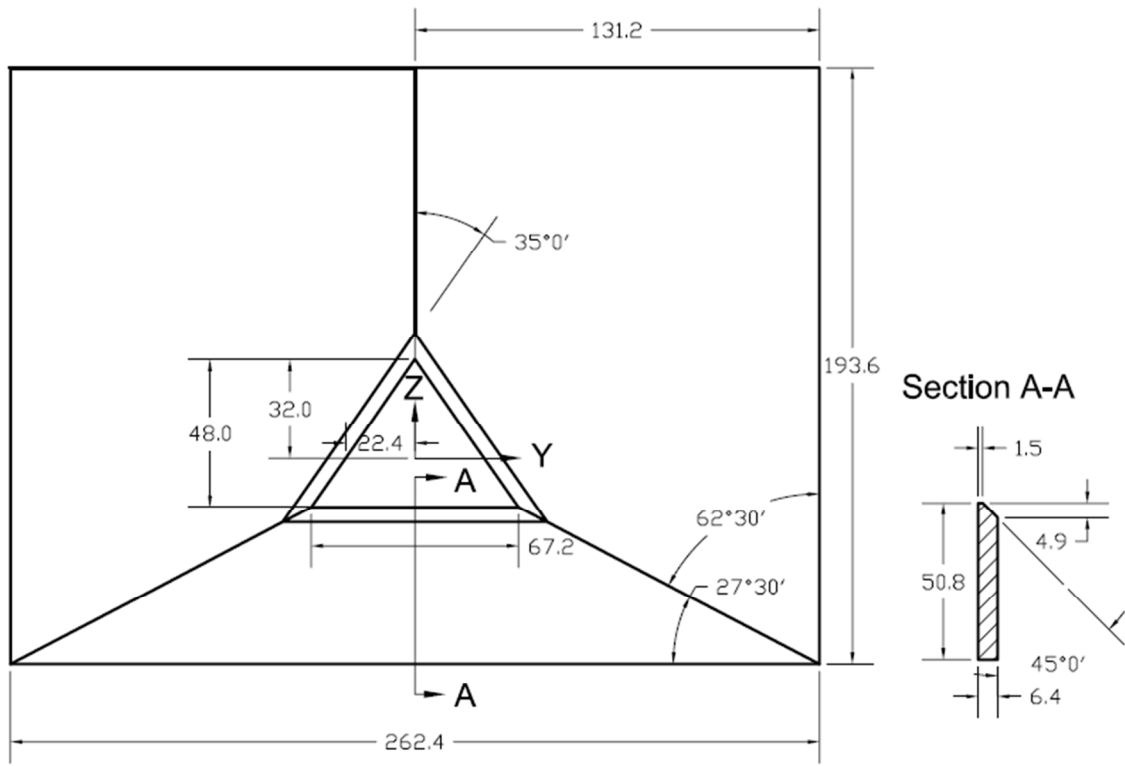
(a)



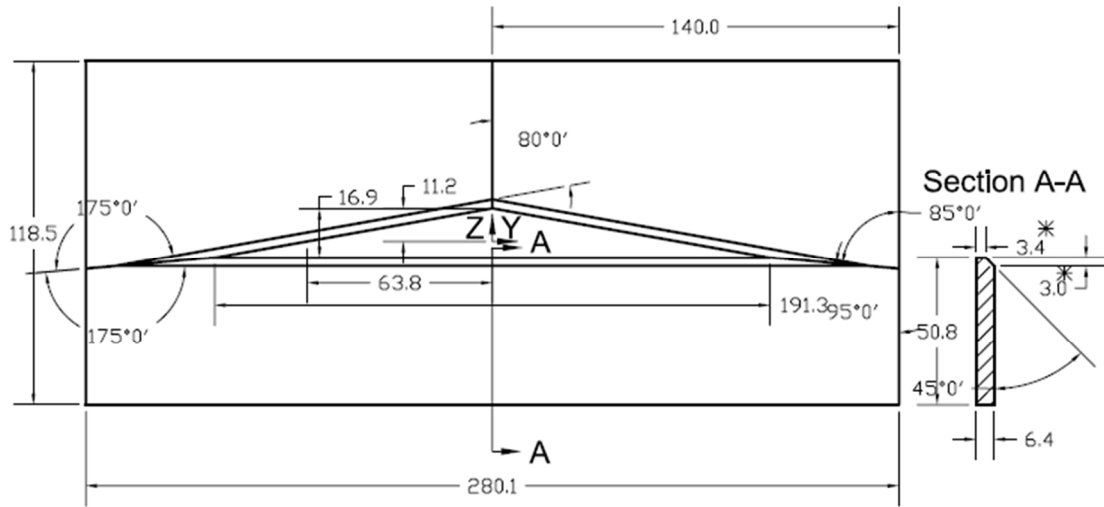
(b)



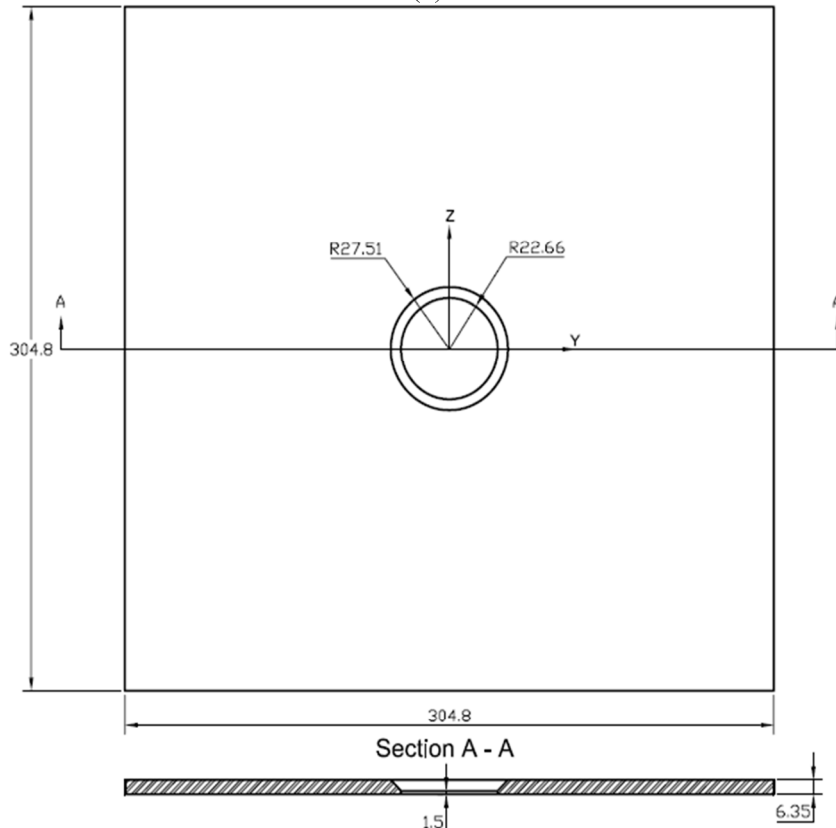
(c)



(d)



(e)



(f)

**Figure 2.3** Isosceles sharp-edged triangular orifices with apex angles of (a) 10°, (b) 20°, (c) 30° (Quinn 2005a), (d) 70°, (e) 160° and (f) sharp-edged round orifice (Quinn 2006). All dimensions in the figures are in mm.

**Table 2.1** Aspect ratio and perimeter of the orifices

Orifice type	Apex angle	Aspect ratio	Perimeter
Sharp-edged triangular	10°	0.18	296.4
	20°	0.35	228.0
	30°	0.54	202.2
	70°	1.40	184.4
	160°	11.32	385.5
Sharp-edged round	-	-	142.4

## 2.4 Pitot-static tube

The mean streamwise velocities and the static pressures in all of the jets were measured with a 2.3 mm diameter pitot-static tube which is made of stainless steel with an ellipsoidal head and four circumferentially located static-pressure holes. The tube was connected to a DATAMETRICS pressure transducer, which, in turn, was hooked up to an electronic manometer. The signals from the electronic manometer were digitized by a National Instruments AT-A2150 board. The electronic manometer signals (0 to 10 volts) were above the input range (to be given later) of the AT-A2150 board and so a voltage divider was used.

### 2.4.1 Operating principle of the pitot-static tube

The working principle of a pitot-static tube is based on Bernoulli's equation. For a steady, frictionless, incompressible flow along a streamline this equation can be written as:

$$P/\rho + V^2/2 + gZ = \text{constant} \quad (2.1)$$

where,  $P$ ,  $V$ ,  $\rho$ ,  $g$  and  $Z$  are the pressure, velocity, density of the fluid, the gravitational acceleration and elevation, respectively.

The first, second and third terms on the left side of (2.1) are the pressure energy, kinetic energy and potential energy per unit mass, respectively. The equation, therefore, states that the mechanical energy of a fluid in motion is conserved. At the same elevation, the potential energy is constant and (2.1) reduces to:

$$P/\rho + V^2/2 = \text{constant} \quad (2.2)$$

Therefore, at constant elevation, any decrease in the kinetic energy will cause the pressure energy to increase. A pitot-static tube has an inner tube and an outer shell, into which tiny holes, called static-pressure holes, are drilled circumferentially, as mentioned previously (see Figure 2.4). In a flow, the fluid is brought to rest at the leading edge of the tube where the kinetic energy is converted to pressure energy. This pressure is called the total or stagnation pressure. The static-pressure holes, located downstream of the leading edge of the tube, sense the pressure of the undisturbed flow, known as the static pressure. The difference between the total and static pressures is called the dynamic pressure, which is used to calculate the velocity of the flow. Use of the pitot-static tube in a flow requires that the tube be aligned with the predominant flow direction. The inner tube in Figure 2.4 is connected to one end (port 1 in Figure 2.5) and the shell is connected to the other end (port 2 in Figure 2.5) of the pressure transducer which measures the difference between the pressure applied to port 1 (total pressure) and that (static pressure) applied to port 2. For static pressure measurements, the shell of the pitot-static tube is

connected to port 1 and port 2 is open to the atmosphere and the pressure transducer measures the difference between the static pressure and the atmospheric pressure.

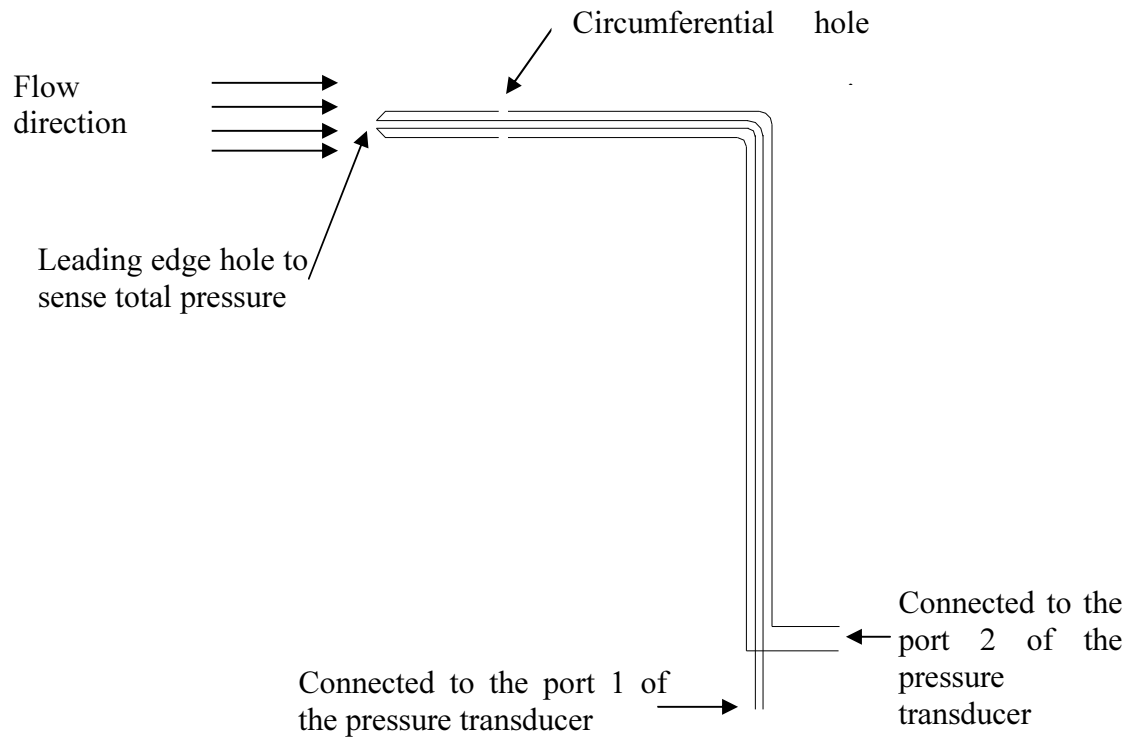


**Figure 2.4** Pitot-static tube. Note that the figure is not drawn to scale.



**Figure 2.5** Pressure transducer; 1- total pressure port, 2- static pressure port, 3- connected to the electronic manometer.

## 2.5 Hot-wire anemometer

Hot-wire anemometry is based on the principle of convective heat loss from a heated wire placed in a fluid flow. There are two types of hot-wire anemometers (HWA): Constant current anemometer (CCA) and Constant temperature anemometer (CTA). In the experiments reported here, the CTA was used to measure the mean velocities and turbulence quantities.

In the following subsections the operating principle of the CTA, the types of heat losses involved, the hot-wire probe used, the velocity measurement, the hot-wire calibration procedure, and the linearization and digitization of hot-wire signals will be briefly described.

### 2.5.1 Operating principle of the CTA

The CTA utilizes the principle that the resistance of the sensing wire is proportional to its temperature. The temperature of the hot-wire is kept constant

throughout the experiment by balancing the wheat-stone bridge, shown in Figure 2.6 in which  $R_w$  is the resistance of the wire. A certain value of the resistor and its lead can be set by using the adjustable resistor. The other two legs of the bridge have identical resistances. The servo amplifier (G) in the figure keeps the voltages  $e_1$  and  $e_2$  the same, and hence, holds the wire resistance and the adjustable resistance to the same value. When the probe is placed in the flow, the flowing fluid cools it. The bridge voltage has to be increased to compensate for this heat loss. The faster the flow, the higher the value of the heat loss and thus the higher the value of the voltage required to compensate for the heat loss. The velocity of the jet corresponding to this voltage is calculated using an empirical relationship between voltage and velocity.

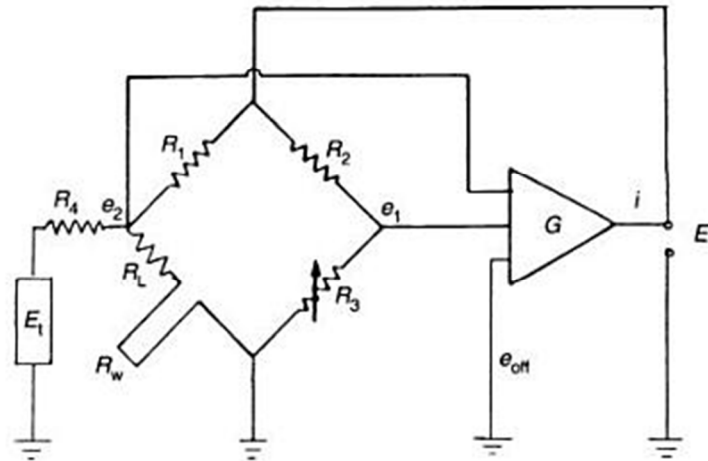


**Figure 2.6** Constant Temperature Anemometer with electronic testing sub circuit (Brunn 1995).

### **2.5.2 Heat loss from the wire**

The hot-wire is cooled in four ways, namely, radiative heat transfer, buoyant convection, conduction heat transfer along the wire to its end supports and forced convective heat transfer. The heat loss from typical hot-wires by radiation is about 0.1 percent of the electric heat input and, therefore, can be neglected. Buoyant convection plays an important role only when the flow velocity is very low. Heat loss by buoyant convection can be neglected when the Reynolds number is greater than twice the cube root of the Grashof number (see Bradshaw 1975). It should be noted that the Reynolds number is the ratio of the inertial force to the viscous force and that the Grashof number is the ratio of the buoyancy force to the viscous force in a flow. In the experiments reported here, the Reynolds number was much higher than the Grashof number and, therefore, the buoyancy effect can be neglected. The main contributions to the heat loss from the wire, then, are conduction heat transfer to the end supports and forced convection heat transfer. Typically, the end supports of the hot-wires are made so much thicker than the sensing wire to ensure that they are not heated considerably by the electric current and that they are strong. Since the end supports are made much thicker than the sensing wire, the temperature at the ends of the sensing wire remains very close to that of the flowing fluid (Bradshaw 1975). Therefore, the only significant amount of electric heat loss from the hot-wire is due to the forced convective heat transfer.

### **2.5.3 Anemometer type and the hot-wire probe**

In isothermal flows, CTA is commonly used to measure velocities because of the very good frequency response of the system (Bruun 1995). A DANTEC x-array probe,

consisting of two platinum-plated tungsten wires was used to acquire mean and fluctuating velocity data. The two wires of the probe are 5  $\mu\text{m}$  in diameter, 1.25 mm long and are 1 mm apart. The overheat or resistance ratio was 1.8.

#### 2.5.4 Velocity Measurement

The output voltages from an x-array probe can be expressed as:

$$E_1^2 = A_1 + B_1 V_{eff_1}^{n_1} \quad (2.3)$$

$$E_2^2 = A_2 + B_2 V_{eff_2}^{n_2} \quad (2.4)$$

where  $A_1$ ,  $B_1$ ,  $n_1$  and  $A_2$ ,  $B_2$ ,  $n_2$  are calibration constants and  $V_{eff_1}$  and  $V_{eff_2}$  are the effective cooling or normal velocities of wire # 1 and wire # 2, respectively.

The constants in (2.3) and (2.4) are determined by calibration which will be described later.

The values of  $V_{eff_1}$  and  $V_{eff_2}$ , using the calibration constants, are obtained from (2.5) and (2.6).

$$V_{eff_1} = \left( \frac{E_1^2 - A_1}{B_1} \right)^{1/n_1} \quad (2.5)$$

$$V_{eff_2} = \left( \frac{E_2^2 - A_2}{B_2} \right)^{1/n_2} \quad (2.6)$$

It is necessary to show the orientation of the wires to the flow field to illustrate how the instantaneous streamwise and spanwise velocities were calculated. The orientation of the two wires of an x-array probe to the flow field is shown in Figure 2.7.

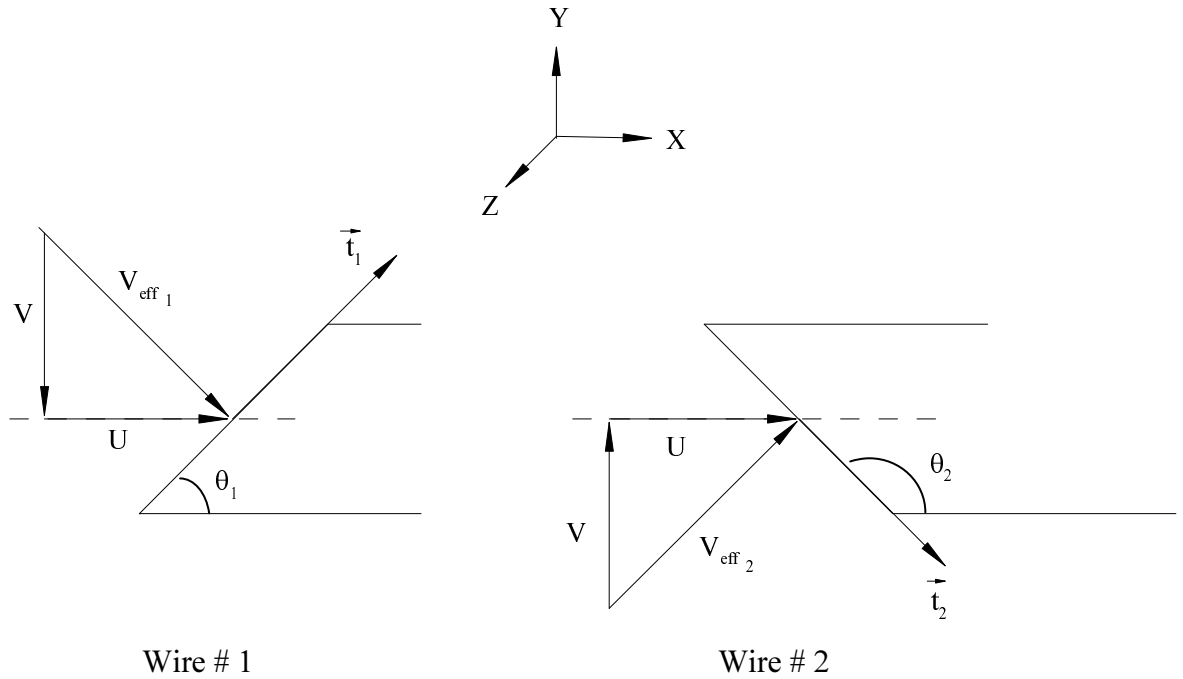


**Figure 2.7** Orientation of the wires of an x-array probe to the flow field.

In Figure 2.7,  $U$  and  $V$  are the instantaneous streamwise and spanwise velocities,  $\theta_1$  and  $\theta_2$  are the effective angles for wire # 1 and wire # 2, respectively,  $V_{eff_1}$  and  $V_{eff_2}$  are the effective or normal cooling velocities for wire # 1 and wire # 2, respectively and  $\vec{t}_1$  and  $\vec{t}_2$  are the unit tangent vectors along wire # 1 and wire # 2, respectively.

The equations of the effective cooling velocities can thus be written (from Figure 2.7) as:

$$V_{eff_1} = U \cos(90 - \theta_1) - V \cos \theta_1$$

$$\Rightarrow V_{eff_1} = U \sin \theta_1 - V \cos \theta_1 \quad (2.7)$$

$$V_{eff_2} = U \cos(\theta_2 - 90^\circ) + V \cos(180^\circ - \theta_2)$$

$$\Rightarrow V_{eff_2} = U \sin \theta_2 - V \cos \theta_2 \quad (2.8)$$

From (2.7) and (2.8), it follows that:

$$U = \frac{V_{eff_2} \cos \theta_1 - V_{eff_1} \cos \theta_2}{\cos \theta_1 \sin \theta_2 - \sin \theta_1 \cos \theta_2} \quad (2.9)$$

$$V = \frac{V_{eff_2} \sin \theta_1 - V_{eff_1} \sin \theta_2}{\cos \theta_1 \sin \theta_2 - \sin \theta_1 \cos \theta_2} \quad (2.10)$$

(2.9) and (2.10) give the instantaneous velocities, which can also be expressed as:

$$U = \bar{U} + u' \quad (2.11)$$

$$V = \bar{V} + v' \quad (2.12)$$

where the overbar and prime denote mean and fluctuating velocities, respectively. The mean velocities were calculated by taking the ensemble averages of the instantaneous velocities as shown in (2.13) and (2.14)

$$\bar{U} = \frac{1}{N} \sum_{N=1}^N U \quad (2.13)$$

$$\bar{V} = \frac{1}{N} \sum_{N=1}^N V \quad (2.14)$$

where  $N$  is the number of samples.

Once the mean velocities were known, the mean square values of the fluctuating velocities were calculated by applying Reynolds averaging.

Time averaging the squared values in (2.11) and (2.12) gives:

$$\overline{U^2} = \bar{U}^2 + \overline{u'^2}$$

$$\Rightarrow \overline{u'^2} = \overline{U^2} - \bar{U}^2 \quad (2.15)$$

$$\overline{V^2} = \bar{V}^2 + \overline{v'^2}$$

$$\Rightarrow \overline{v'^2} = \overline{V^2} - \bar{V}^2 \quad (2.16)$$

(2.15) and (2.16) enabled the calculation of mean squared values of the fluctuating components of the instantaneous velocities.

### 2.5.5 Calibration of Hot Wire probes

(2.5) and (2.6) contain several constants, such as  $A_1, B_1, n_1$  and  $A_2, B_2, n_2$ . These constants had to be determined by calibration to obtain the effective cooling velocities, as mentioned previously. The velocity calibration was carried out online in a known flow field close to the exit of the jet where the turbulence intensity was low. The mean streamwise velocity distribution at the calibration location was uniform on both the central  $X$ - $Y$  and the central  $X$ - $Z$  planes.

The plane of the wires was parallel to the  $X$ - $Y$  plane and the velocity along the  $Z$  direction was assumed to be negligible. The calibration adopted in these experiments was a two-step procedure. First, voltages of the hot-wires were acquired against the mean velocities obtained by a pitot-static tube in a velocity range of approximately 8.0 m/s to 65.0 m/s. The acquired data were then fitted to the exponent power law:

$$E^2 = A + BV_{eff}^n \quad (2.17)$$

for both wires and  $A$ ,  $B$ , and  $n$  were optimized with a linear least-squares goodness-of-fit procedure. Second, the effective angles for both wires were obtained from a yaw

calibration, following Bradshaw (1975). A “cosine law” response to yaw was assumed and voltages were acquired at fifteen different yaw angles in the range of  $-35^\circ \leq \theta \leq 35^\circ$ , in steps of  $5^\circ$  with respect to the main flow direction. The data were then fitted to:

$$\left[ \frac{E^2 - E_0^2}{(E^2 - E_0^2)_{\Delta\theta=0}} \right]^{1/n} - \cos\Delta\theta \equiv -\tan\theta_{eff} \sin\Delta\theta \quad (2.18)$$

where  $E$  and  $E_0$  are voltages at any  $\Delta\theta$  and  $\Delta\theta = 0$ , respectively. The slope of the straight lines then enabled the calculation of the effective angles of the wires (see Bradshaw 1975).

### 2.5.6 Linearization and digitization of hot-wire signals

Linearization of the hot-wire signals was done, according to (2.5) and (2.6), by the laboratory microcomputer and the signals were digitized, along with the signals from the thermocouple, with the National Instruments AT-A2150 dynamic signal acquisition board, which consists of four analog input channels, each of 16-bit resolution. Each of the analog input channels was preceded by a third-order Butterworth low-pass analog anti-aliasing filter with an 80 kHz cut off frequency. The filtered signal was sampled with a 1-bit delta-sigma modulating analog sampler at 64 times the chosen sampling rate. This reduced the quantization noise considerably. The output of the sampler was then fed to a digital anti-aliasing filter, which was built into the A/D converter chip, and the output of this filter re-sampled the signal to the data rate, namely, 16-bit digital samples. It should be noted that all four analog input channels can be sampled simultaneously and, therefore, no sample-and-hold units were needed here. The input range of the AT-A2150

board was  $\pm 2.828$  V (or 2 V rms) and so amplification was only needed for the thermocouple signal and not for the hot-wire signals.

## **2.6 Number of samples used in calculations**

For pitot-static tube measurements, the number of samples used to obtain stable values of the mean streamwise velocities was, depending on the measurement location, in the range of 100,000 to 500,000. For hot-wire measurements, 131,072 samples per channel were acquired at each location, at a rate of 4 KHz. This ensured that the measured data were stable. The acquired hot-wire data were used to calculate the mean velocities and turbulence quantities, such as the Reynolds normal and primary shearing stresses. The one-dimensional energy spectra and autocorrelation coefficients were calculated from the data acquired at a sampling rate of 25.6 KHz.

# CHAPTER 3

## Results

### 3.1 Initial conditions

#### 3.1.1 Exit mean streamwise velocity profiles

The mean streamwise velocity profiles ( $U/U_{cl}$  vs.  $Y/Y_{1/2}$ ) close to the orifice or nozzle exit plane, at  $X/D_e = 0.035$ , are shown in Figures 3.1 and 3.2 for all the test jets. The half-velocity width ( $Y_{1/2}$  or  $Z_{1/2}$ ) in the  $Y$ - or  $Z$ -direction of a jet is defined as the distance from the centreline to the point where  $U = 0.5U_{cl}$ . Among all the jets, the sharp-edged orifice round jet has the most pronounced off-centre peaks in the mean streamwise velocity profile. These peaks are generated by secondary flows of the Prandtl first kind. Such secondary flows are driven by the pressure difference arising from streamline curvature, due to the vena contracta effect. The  $10^\circ$  jet has the least pronounced and the  $70^\circ$  jet has the most pronounced off-centre peaks in the mean streamwise velocity profile among the triangular jets. As the apex angle of the triangular orifice increases, the off-centre peaks become more pronounced, except for the  $160^\circ$  jet. Whereas the effect of the vena contracta is observed in all the orifice jets, it is absent in the contoured nozzle round jet. The contoured nozzle round jet has a fairly uniform mean streamwise velocity profile.

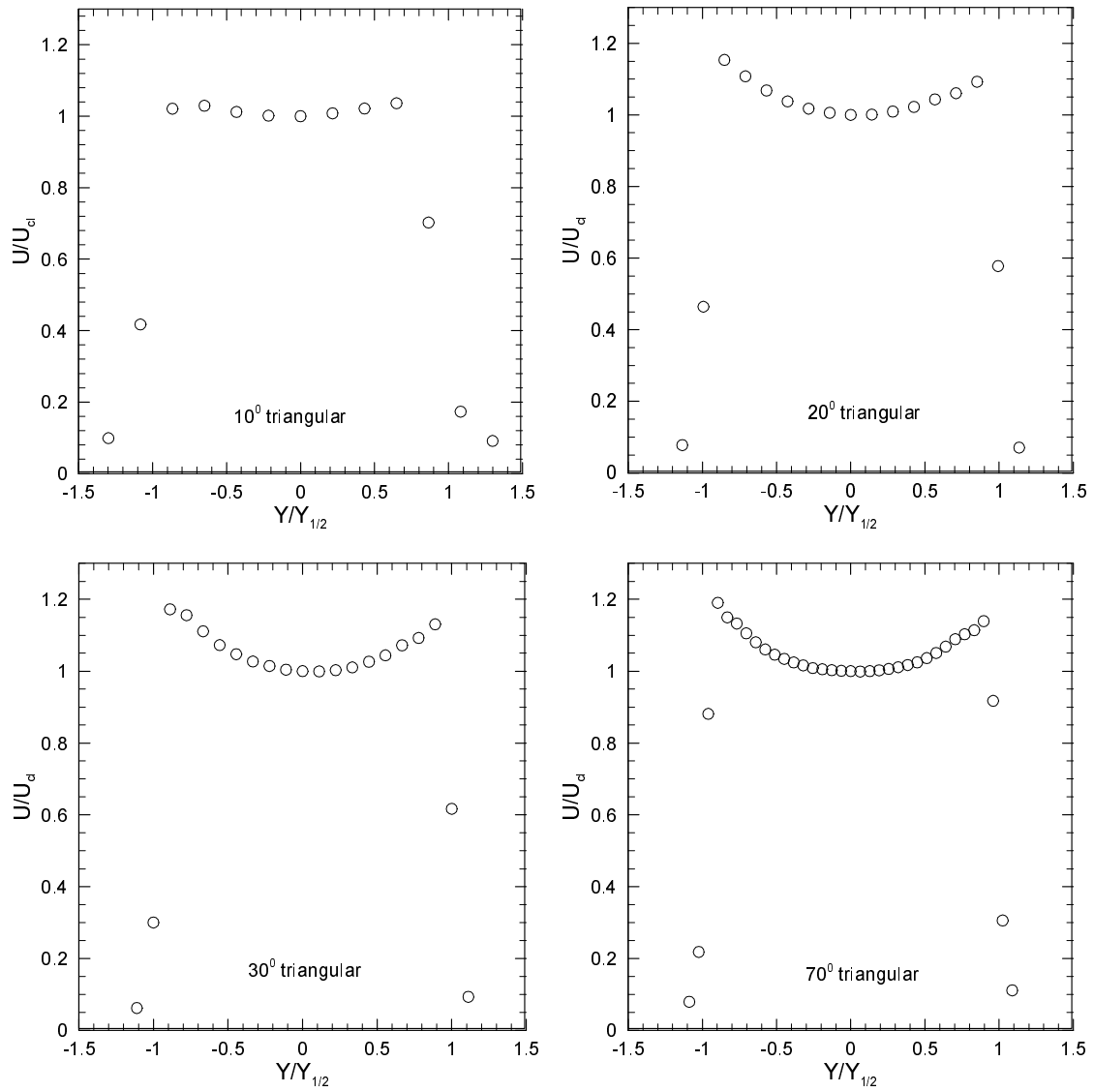


**Figure 3.1** Exit mean streamwise velocity profiles.

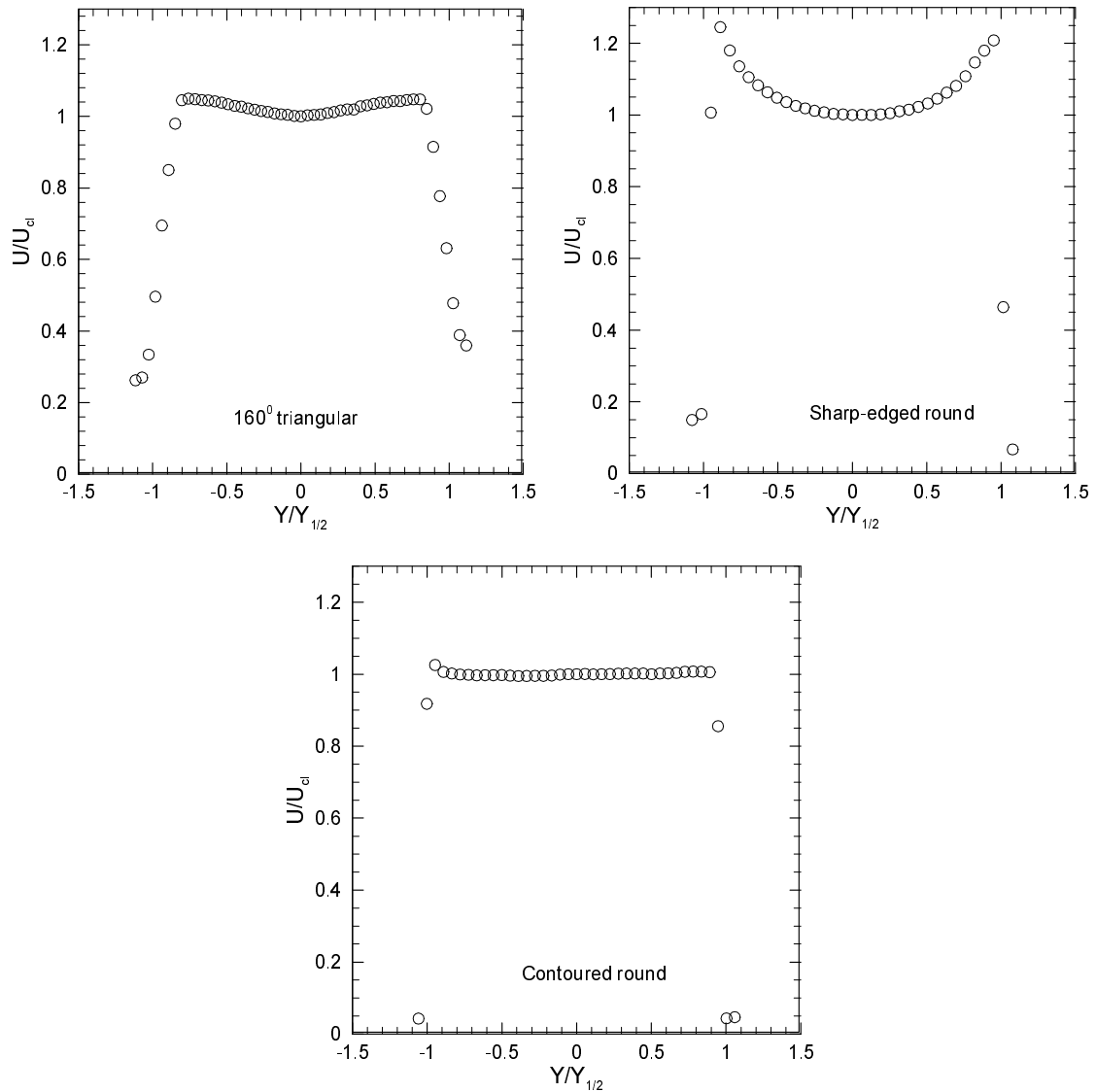


**Figure 3.2** Exit mean streamwise velocity profiles (continued).

### 3.1.2 Exit streamwise turbulence intensities

The  $Y$ -profiles of the streamwise turbulence intensities ( $\sqrt{u'^2}/U_{cl}$ ) at  $X/D_e = 0.035$  are shown in Figures 3.3 and 3.4 for all the test jets. The  $\sqrt{u'^2}/U_{cl}$  profile is flat in the central region where the  $U$  profile is nearly uniform, in all the jets. The value of  $\sqrt{u'^2}/U_{cl}$  is 0.33% at the centre of the  $20^\circ$ ,  $30^\circ$ ,  $70^\circ$  and sharp-edged orifice round jets

and 0.37% at the centre of the  $10^\circ$  and  $160^\circ$  jets. The contoured nozzle round jet has a value of 0.29% at the centre. In the outer region,  $\sqrt{\overline{u'^2}}/U_{cl}$  starts to increase reaching a maximum value of around 6% in the shear layers of all the jets.

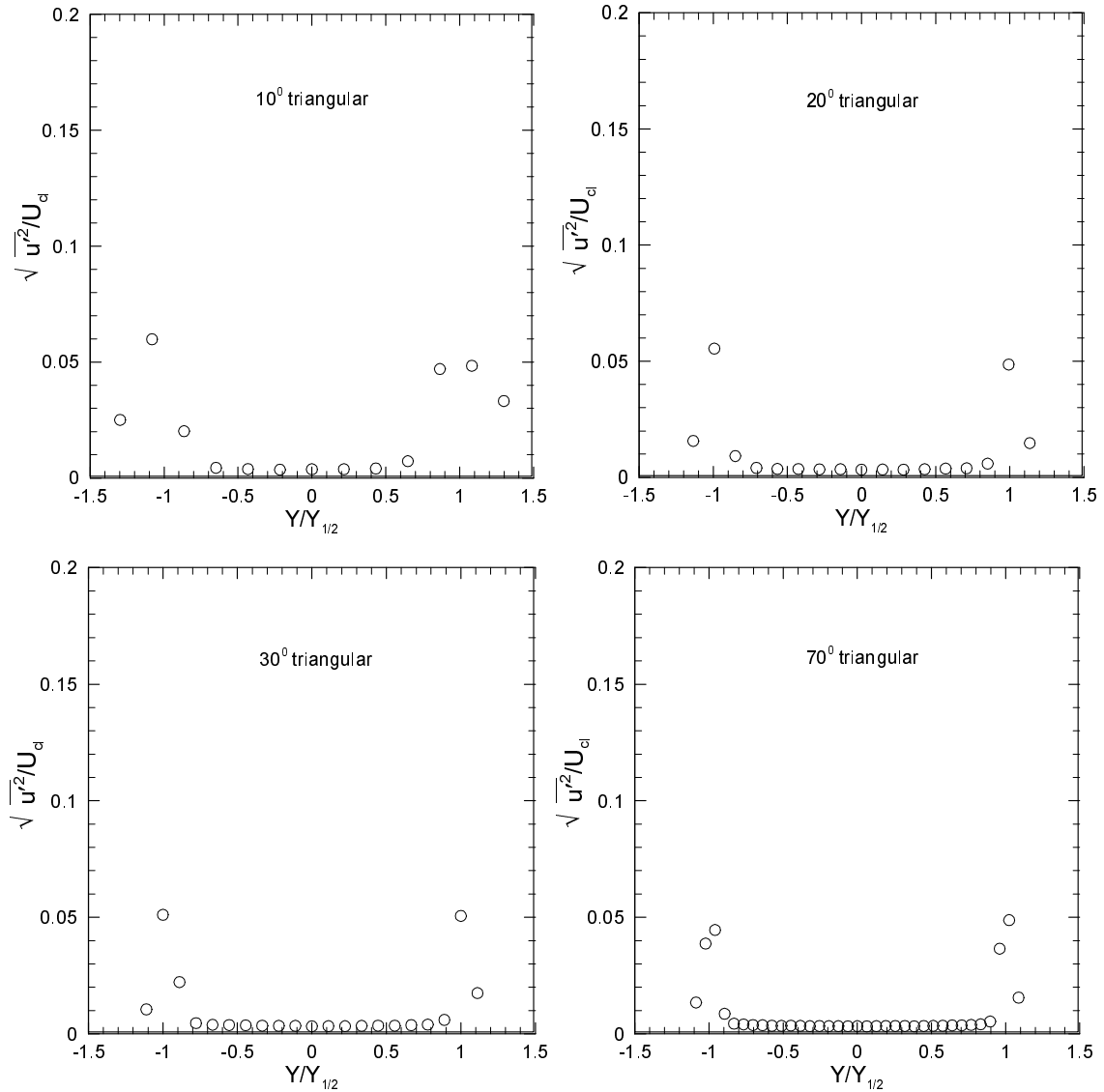


**Figure 3.3** Exit streamwise turbulence intensity profiles.

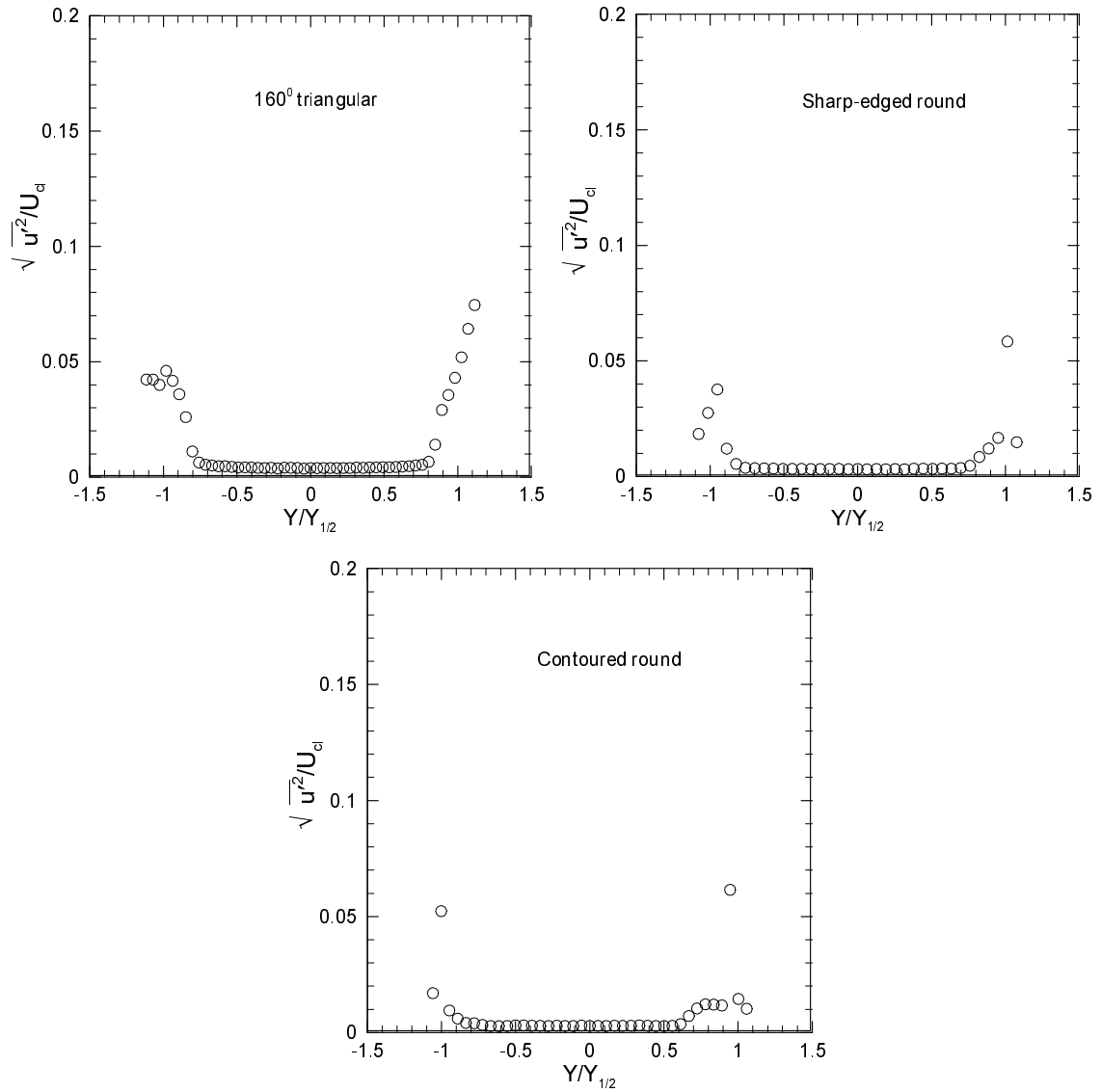


**Figure 3.4** Exit streamwise turbulence intensity profiles (continued).

### 3.1.3 Mean static pressure distribution

The distribution of mean static pressure  $(2(P_s - P_{atm})/\rho U_{cl}^2)$  along the  $Y$ -direction for the  $10^\circ$ ,  $20^\circ$ ,  $30^\circ$ ,  $70^\circ$ ,  $160^\circ$  and sharp-edged orifice round jets is shown in Figure 3.5. The mean static pressure at the centre of the sharp-edged orifice round jet, which has the most pronounced off-centre peaks in the mean streamwise velocity profile, is higher than that in any of the other jets. The  $10^\circ$  jet, in which the off-centre peaks have

their lowest value, has a centreline mean static pressure value close to atmospheric pressure. As the apex angle of the triangular orifice increases, the mean static pressure at the jet centre also increases and the off-centre peaks in the velocity profile take on higher values, except for the 160° jet, which has an approximately uniform mean streamwise velocity profile close to the exit plane (see Figure 3.2).

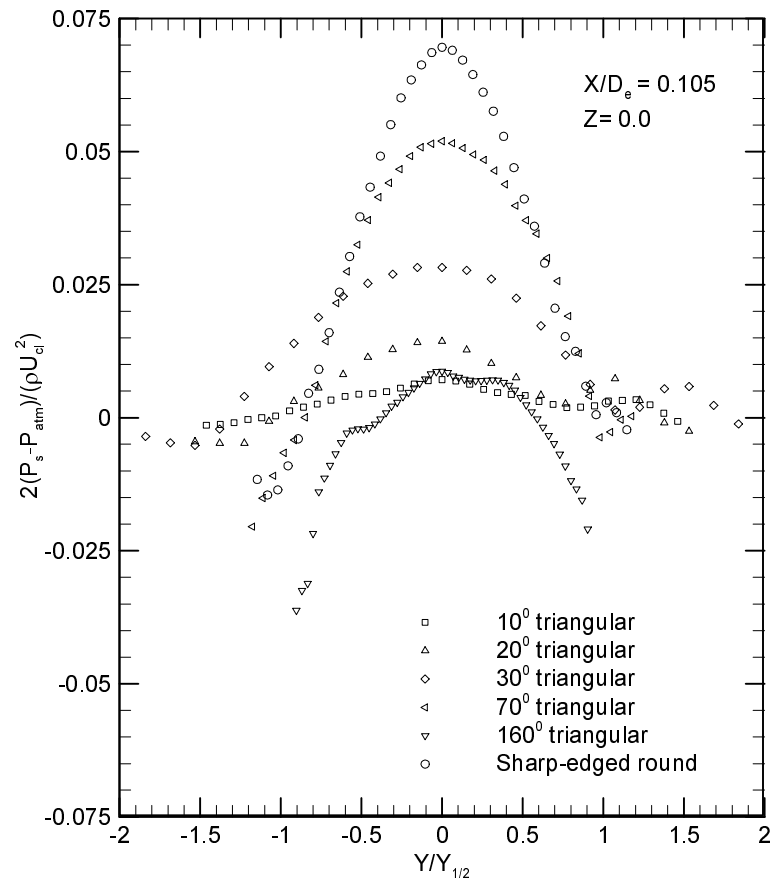


**Figure 3.5** Static pressure distribution across the jet.

Uncertainties in the results were calculated using the multiple-sample theorem method in Tavoularis (2005). The calculated uncertainties in the different quantities are as follows:

$$U = \pm 1.5\%$$

$$\overline{u'^2} = \pm 3.35\%$$

$$\overline{v'^2} = \pm 3.75\%$$

$$P_S = \pm 2.76\%$$

### 3.2 Mean streamwise centreline velocity decay

The results for the mean streamwise centreline velocity decay in all the test jets are shown in Figure 3.6.  $U_{bulk}/U_{cl}$  starts at a value slightly larger than one at the exit of the orifice and decreases slightly afterwards, due to the vena contracta effect, remains constant over varying values of  $X/D_e$ , and then increases monotonically in all the orifice jets.  $U_{bulk}/U_{cl}$  in the contoured nozzle round jet does not decrease downstream of the exit plane, unlike the behaviour observed for the other jets, but remains rather constant before increasing in the streamwise direction. In the far field, the  $10^\circ$  jet has the highest and the  $70^\circ$  jet has the lowest mean streamwise centreline velocity decay rate among all the triangular jets. It is noteworthy that both the round jets have lower mean streamwise centreline velocity decay rates than the triangular jets, regardless of the apex angle of the triangular orifice. Also, in this far-field region, the sharp-edged orifice round jet has a higher mean streamwise centreline velocity decay rate than the contoured nozzle round jet.

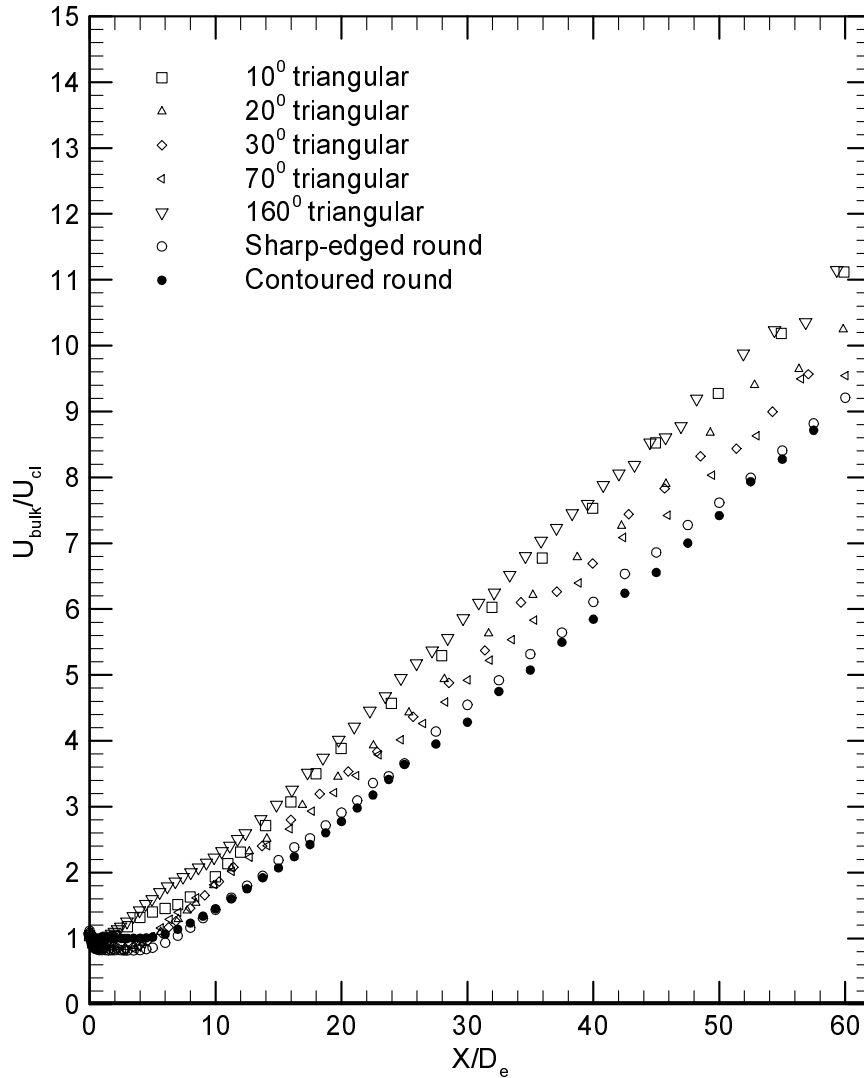


**Figure 3.6** Mean streamwise centreline velocity decay.

The results shown in Figure 3.6 are presented in log-log form in Figure 3.7 to emphasize the near field ( $X/D_e \leq 10$ ) behaviour of the mean streamwise centreline velocity decay in the jets. In this region, the  $160^\circ$  jet, issuing from the orifice with the longest perimeter, has the highest mean streamwise centreline velocity decay rate. Also, all the triangular jets have higher mean streamwise centreline velocity decay rates than both round jets, as was observed in the far field region. The sharp-edged orifice round jet has a lower mean streamwise centreline velocity decay rate than the contoured nozzle

round jet in near field, unlike the behaviour observed in the far field. In region  $5.5 \leq X/D_e \leq 9$ , i.e., in the near field, the  $70^\circ$  jet has higher values of  $U_{bulk}/U_{cl}$  than the other jets, except for the  $10^\circ$  and  $160^\circ$  jets.

The mean streamwise centreline velocity decay consists of three regions in all the jets, namely, a constant mean streamwise centreline velocity region, a short transition region followed by a linear mean streamwise centreline velocity decay region, except for the  $10^\circ$  and  $160^\circ$  jets. These jets have a nonlinear decay region between the constant velocity and linear decay regions.

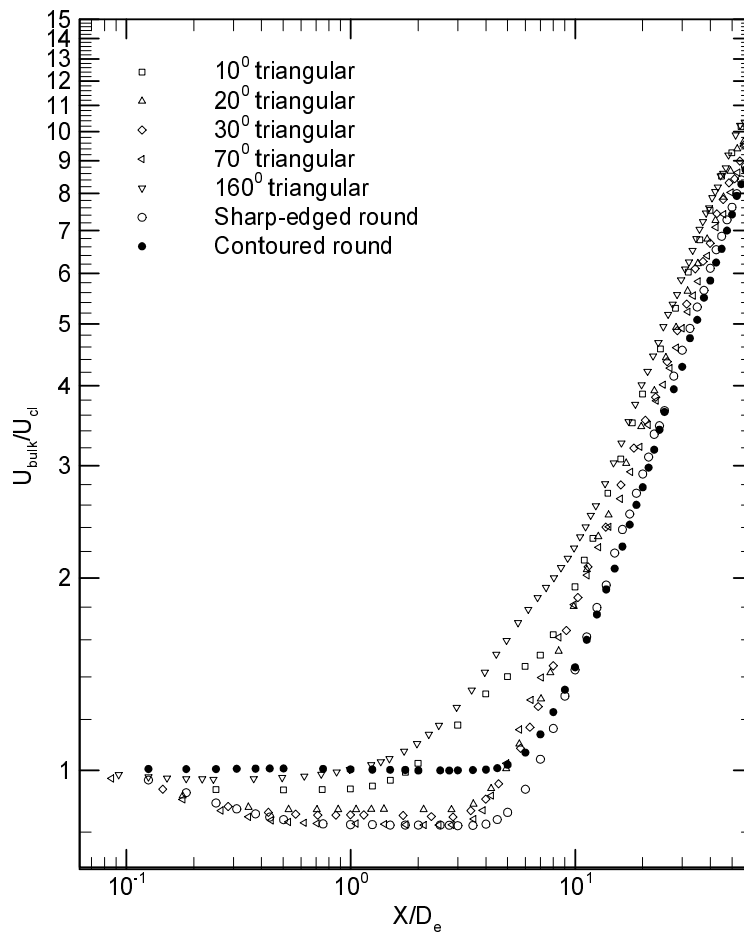


**Figure 3.7** Mean streamwise centreline velocity decay (log-log).

### 3.3 Development of the jet half-velocity widths

The development of the normalized jet half-velocity widths in the streamwise direction is shown in Figures 3.8 and 3.9 for all the test jets. In these figures,  $Y_{\frac{1}{2}}/D_e$  is the normalized half-velocity width in the central  $X$ - $Y$  plane and  $Z_{\frac{1}{2}}/D_e$  is the normalized half-velocity width in the central  $X$ - $Z$  plane. The half-velocity widths were calculated from the  $U$  data obtained using the pitot-static tube in the central  $X$ - $Y$  and  $X$ - $Z$  planes at different  $X/D_e$  locations. In both planes, an average of the half-velocity widths on either side of the centreline was used. There was no significant difference between  $Y_{\frac{1}{2}}/D_e$  and  $Z_{\frac{1}{2}}/D_e$  for both of the round jets and, therefore, only  $Y_{\frac{1}{2}}/D_e$  is presented for those jets.

$Y_{\frac{1}{2}}/D_e$  in all the triangular jets, except for the  $70^\circ$  and  $160^\circ$  jets, increases monotonically with downstream distance. In the  $70^\circ$  and  $160^\circ$  jets,  $Y_{\frac{1}{2}}/D_e$  increases slightly close to the orifice exit plane and then decreases up to some distance downstream before increasing in monotonic fashion in the streamwise direction. In both round jets,  $Y_{\frac{1}{2}}/D_e$  remains constant for some distance downstream before increasing linearly in the streamwise direction.  $Z_{\frac{1}{2}}/D_e$  in the  $70^\circ$  and  $160^\circ$  jets increases throughout the downstream distance considered here. In the other triangular jets,  $Z_{\frac{1}{2}}/D_e$  increases slightly close to the orifice exit plane and then decreases in some distance downstream before increasing monotonically in the streamwise direction. In both round jets, the development of  $Z_{\frac{1}{2}}/D_e$  is similar to that of  $Y_{\frac{1}{2}}/D_e$ , as has been mentioned earlier and is, therefore, not shown in the figures.

There are two cross-over locations in the  $Y_{\frac{1}{2}}/D_e$  and  $Z_{\frac{1}{2}}/D_e$  profiles in all the triangular jets, except for the  $160^\circ$  jet. The cross-over location is defined as the point where the half-velocity widths in both planes become equal (Hussain and Husain 1989). The location of the first cross-over is approximately  $X/D_e = 5.0$  and  $X/D_e = 3.0$ , respectively, in the  $10^\circ$  and  $20^\circ$  jets. In the  $30^\circ$  and  $70^\circ$  jets, the first cross-over takes place at  $X/D_e = 3.0$  and  $X/D_e = 2.0$ , respectively. Unlike the other triangular jets, only one cross-over, at  $X/D_e = 8.0$ , in the  $Y_{\frac{1}{2}}/D_e$  and  $Z_{\frac{1}{2}}/D_e$  profiles is observed in the  $160^\circ$  jet. The second cross-over in the  $Y_{\frac{1}{2}}/D_e$  and  $Z_{\frac{1}{2}}/D_e$  profiles takes place at  $X/D_e = 20$ ,  $X/D_e = 21$ ,  $X/D_e = 23$  and at  $X/D_e = 16$  in the  $10^\circ$ ,  $20^\circ$ ,  $30^\circ$  and  $70^\circ$  jets, respectively.

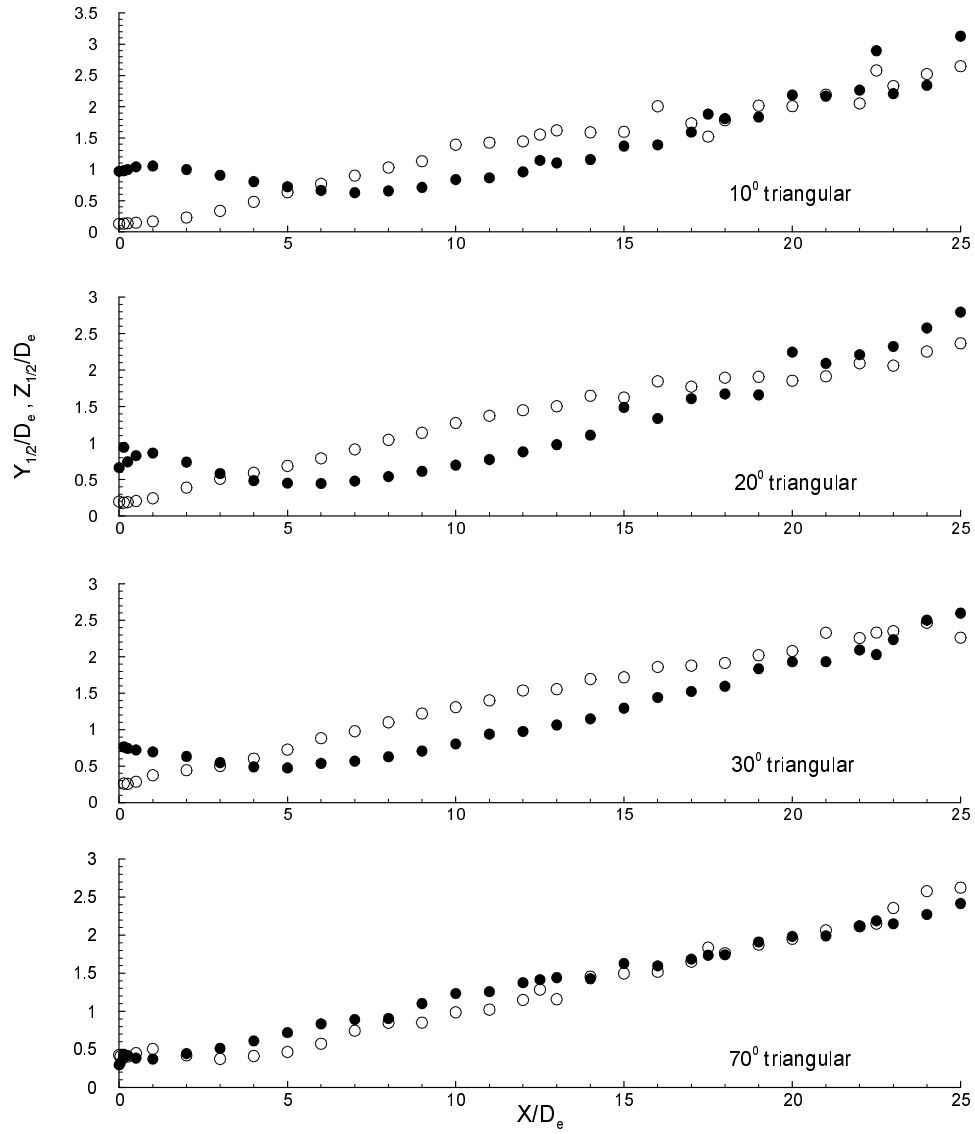


**Figure 3.8** Development of the jet half-velocity widths;  $Y_{1/2}/D_e$ : open symbols,  $Z_{1/2}/D_e$ : filled symbols.

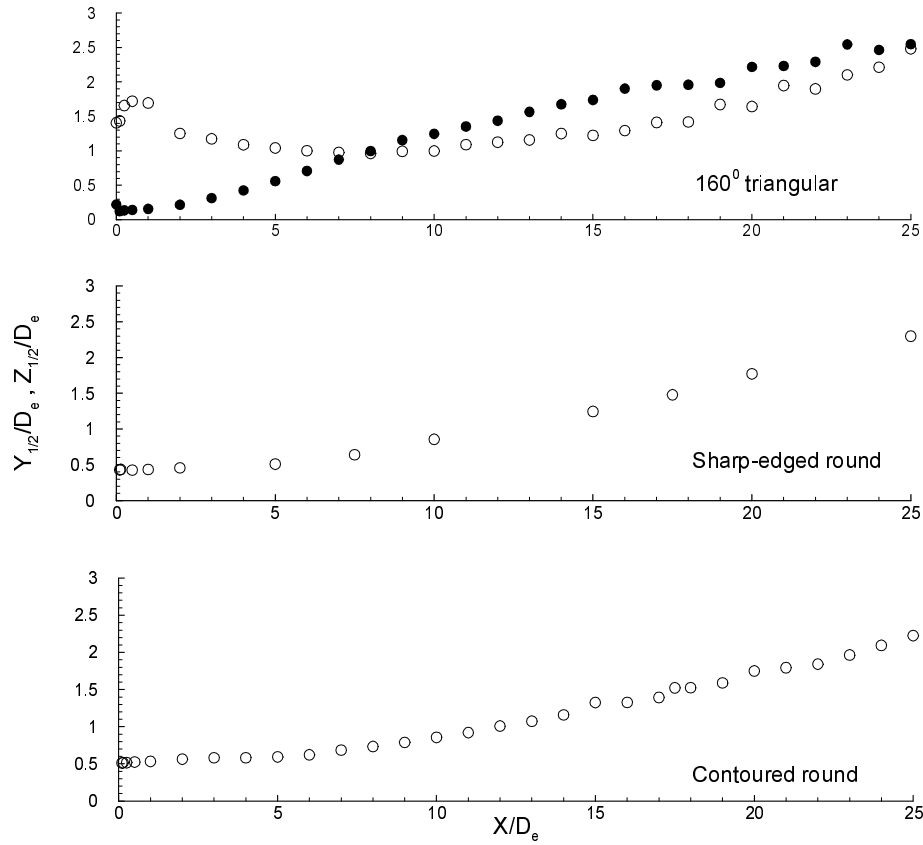


**Figure 3.9** Development of the jet half-velocity widths (continued);  $Y_{1/2}/D_e$ : open symbols,  $Z_{1/2}/D_e$ : filled symbols.

### 3.4 Geometric mean of the jet half-velocity widths

The variation of the geometric mean of the normalized jet half-velocity widths ( $B_{1/2}/D_e$ ) with streamwise distance is shown in Figure 3.10 for all the test jets.  $B_{1/2}/D_e$  of the normalized half-velocity widths was calculated from:

$$B_{1/2}/D_e = \sqrt{\left(Y_{1/2}/D_e\right) \cdot \left(Z_{1/2}/D_e\right)} \quad (3.1)$$

All the jets spread linearly in the far field (beyond  $X/D_e=10$ ). The triangular jets have higher values of  $B_{1/2}/D_e$  than those of the round jets, regardless of the apex angle

of the triangular orifice. In the far field, the  $10^\circ$  jet spreads faster and the  $160^\circ$  jet spreads slower than any of the other triangular jets. It should also be noted that the sharp-edged round orifice round jet spreads faster than the contoured nozzle round jet, in the far field.

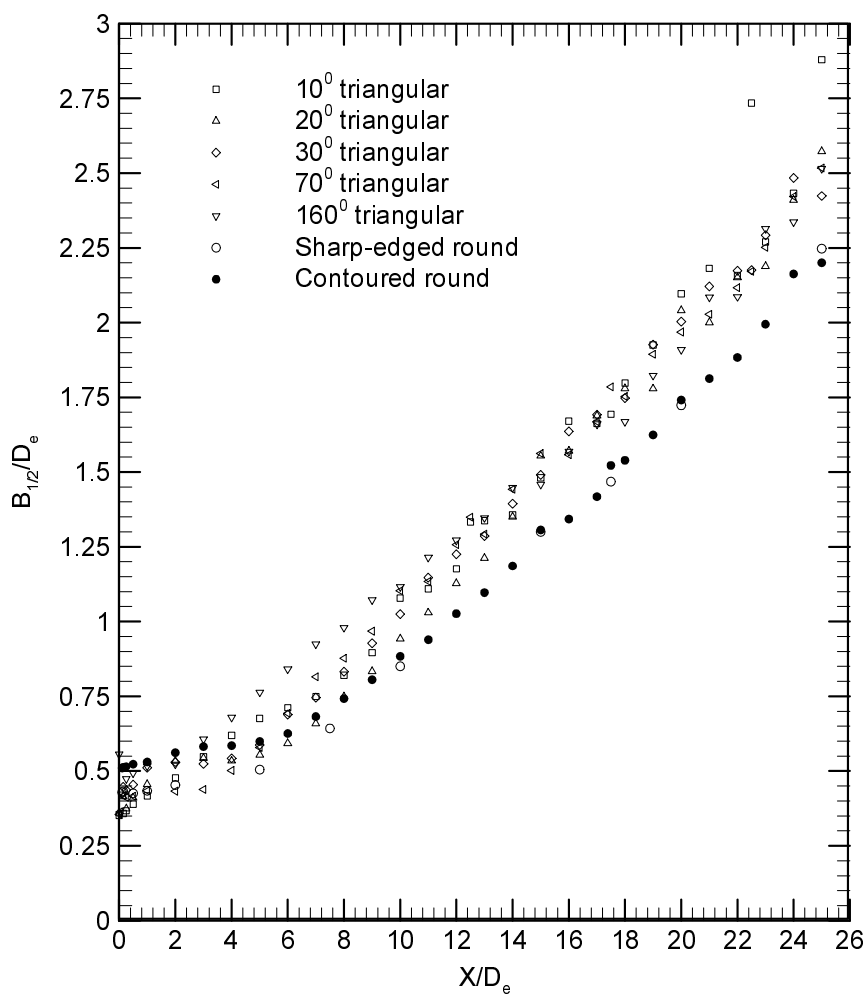


**Figure 3.10** Geometric mean of the jet half-velocity widths.

The near field (up to  $X/D_e=10$ ) spreading results are shown in Figure 3.11.  $B_{1/2}/D_e$  for the  $160^\circ$  jet has the highest values among all the jets up to  $X/D_e = 10$  (Figure 3.11) and the lowest values thereafter among all the triangular jets, at least up to  $X/D_e = 25.0$ .  $B_{1/2}/D_e$  of the  $10^\circ$  jet starts with the lowest value at the exit and increases

gradually; it has the highest values among all the jets after  $X/D_e=15$ . This jet has the second highest values of  $B_{1/2}/D_e$  in the region of  $4 \leq X/D_e \leq 6$ . The  $70^\circ$  jet has higher values of  $B_{1/2}/D_e$  than the other jets, except for the  $160^\circ$  jet, in the region  $5 \leq X/D_e \leq 10$ . The sharp-edged orifice round jet has lower values of  $B_{1/2}/D_e$  than the contoured nozzle round jet in this region.

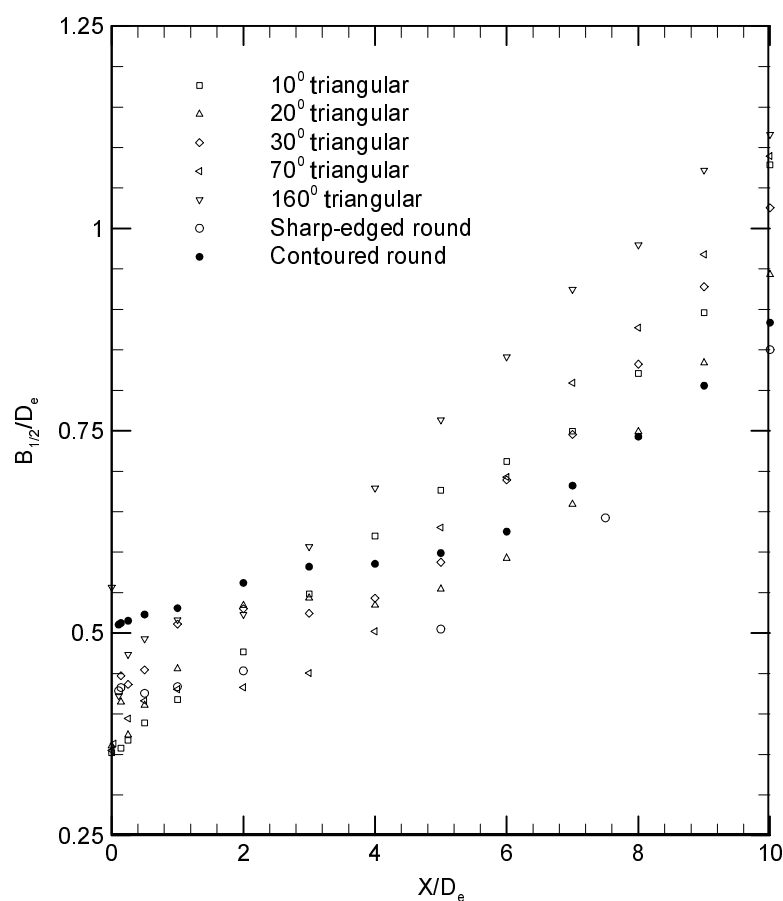


**Figure 3.11** Geometric mean of the jet half-velocity widths in near field.

### 3.5 Mean streamwise velocity contour maps

Contour maps of the normalized mean streamwise velocity ( $U/U_{cl}$ ) for all the test jets, at different streamwise locations, are shown in Figures 3.12-3.25. Very close to the

orifice or nozzle exit plane, at  $X/D_e = 0.14$  (at  $X/D_e = 0.07$  for the  $160^\circ$  jet), the contour levels of all the jets are very closely spaced with a large area of high velocity. The shapes of the  $U/U_{cl}$  contours are very similar to that of the corresponding orifice or nozzle.

At  $X/D_e = 0.25$ , the  $U/U_{cl}$  contours of the triangular jets are still isosceles triangular in shape and the space between the contour levels has increased slightly. The area of high velocity core of the  $U/U_{cl}$  contours is smaller at this location than it was initially in all the triangular jets. It should be noted that the contour levels at this location are spaced more widely in the  $10^\circ$  and  $160^\circ$  jets than in any of the other jets. The area of high velocity at this location is also smaller in the  $10^\circ$  and  $160^\circ$  jets than in any of the other jets. The  $U/U_{cl}$  contours in both round jets have the shape of the orifice or nozzle at  $X/D_e = 0.5$  but the contour levels are slightly more widely spaced here than at the upstream location. The area of high velocity is, as observed for the triangular jets, also smaller at this location than at the upstream location.

At  $X/D_e = 1.0$ , the shape of the  $U/U_{cl}$  contours becomes oval in the  $10^\circ$ ,  $20^\circ$  and  $30^\circ$  jets. The  $U/U_{cl}$  contours are close to a round shape in the  $70^\circ$  jet and are more or less rectangular in the  $160^\circ$  jet, at this location. While in the sharp-edged orifice round jet  $U/U_{cl}$  contours have a round shape at this location, the contoured nozzle round jet has a square shape. In all the jets, the contour levels are more widely spaced here than at the upstream locations and the high velocity area decreases further. It should also be noted, as observed previously, that the contour levels are spaced more widely in the  $10^\circ$  and  $160^\circ$  jets than in any of the other jets and that the  $160^\circ$  jet has the most widely spaced  $U/U_{cl}$  contours. The area of high velocity is also smaller in the  $10^\circ$  and  $160^\circ$  jets at this location than in any of the other jets and the  $160^\circ$  jet has the smallest high velocity area.

At  $X/D_e = 3.0$ , the shape of the  $U/U_{cl}$  contours is no longer triangular in the  $10^\circ$ ,  $20^\circ$  and  $160^\circ$  jets. The  $U/U_{cl}$  contours are close to an ellipse in shape in the  $10^\circ$  jet, have a deformed elliptic shape in the  $160^\circ$  jet and a rhomboidal shape in the  $20^\circ$  jet at this location. The  $U/U_{cl}$  contours have an inverted triangular shape in the  $30^\circ$  and  $70^\circ$  jets. The contour levels are spaced more widely here in all the jets, compared to the locations upstream, and they are most widely spaced in the  $160^\circ$  jet. At  $X/D_e = 2.0$ , the contour levels are more widely spaced in both round jets compared to the upstream locations. While the  $U/U_{cl}$  contours in the sharp-edged orifice round jet have the circular shape of the orifice, the  $U/U_{cl}$  contours in the contoured nozzle round jet have a square shape, as was the case at  $X/D_e = 1.0$ .

At  $X/D_e = 5.0$ , the memory of the orifice geometry is completely lost in the  $10^\circ$ ,  $20^\circ$  and  $160^\circ$  jets. The  $U/U_{cl}$  contours have a roundish shape in the  $10^\circ$  jet and almost a square shape in the  $20^\circ$  jet. The contours have an elliptic shape in the  $160^\circ$  jet. The triangular shape of the  $U/U_{cl}$  contours is still evident in the  $30^\circ$  and  $70^\circ$  jets at  $X/D_e = 5.0$ , albeit in inverted form. The shape of the  $U/U_{cl}$  contours is still round in the sharp-edged orifice round jet and is almost circular in the contoured nozzle round jet at this location.

The  $U/U_{cl}$  contours in  $10^\circ$ ,  $20^\circ$  and  $30^\circ$  jets are elliptic, with axes rotated through  $45^\circ$ , at  $X/D_e = 10.0$ . The triangular shape of these contours is still evident in the  $70^\circ$  jet at this location but they are almost circular in the  $160^\circ$  jet. The  $U/U_{cl}$  contours are circular in shape in both round jets. The contour levels are evenly and more widely spaced here than at the locations upstream in all the jets.

At  $X/D_e = 25.0$ , the  $U/U_{cl}$  contours are almost circular in shape in all the triangular jets, except for the  $160^\circ$  jet. The  $160^\circ$  jet has an elliptic shape with a rotation of the axes by approximately  $45^\circ$ . The  $U/U_{cl}$  contours in both round jets are circular at this location.

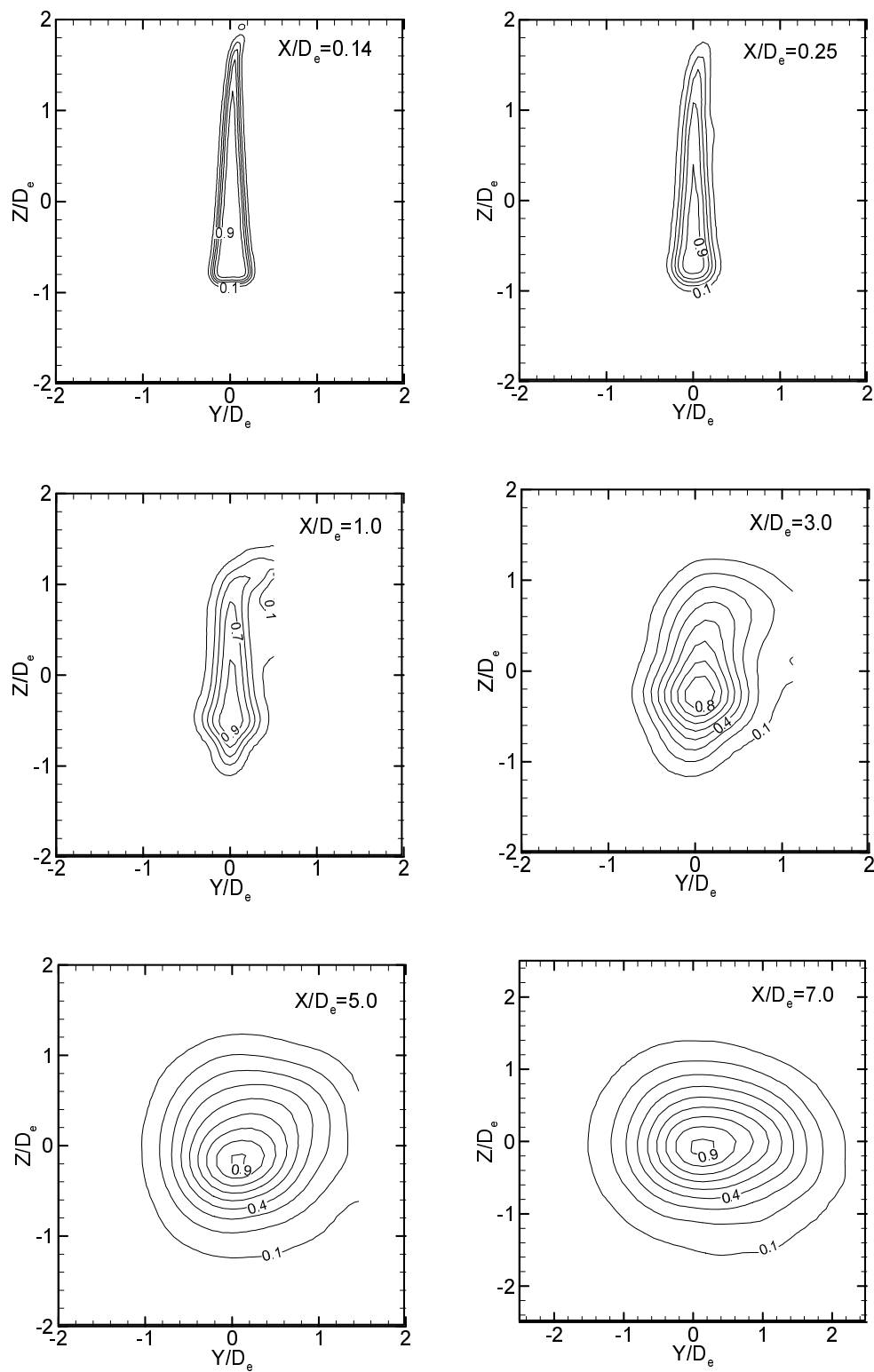


**Figure 3.12** Mean streamwise velocity contour maps for the  $10^\circ$  jet.

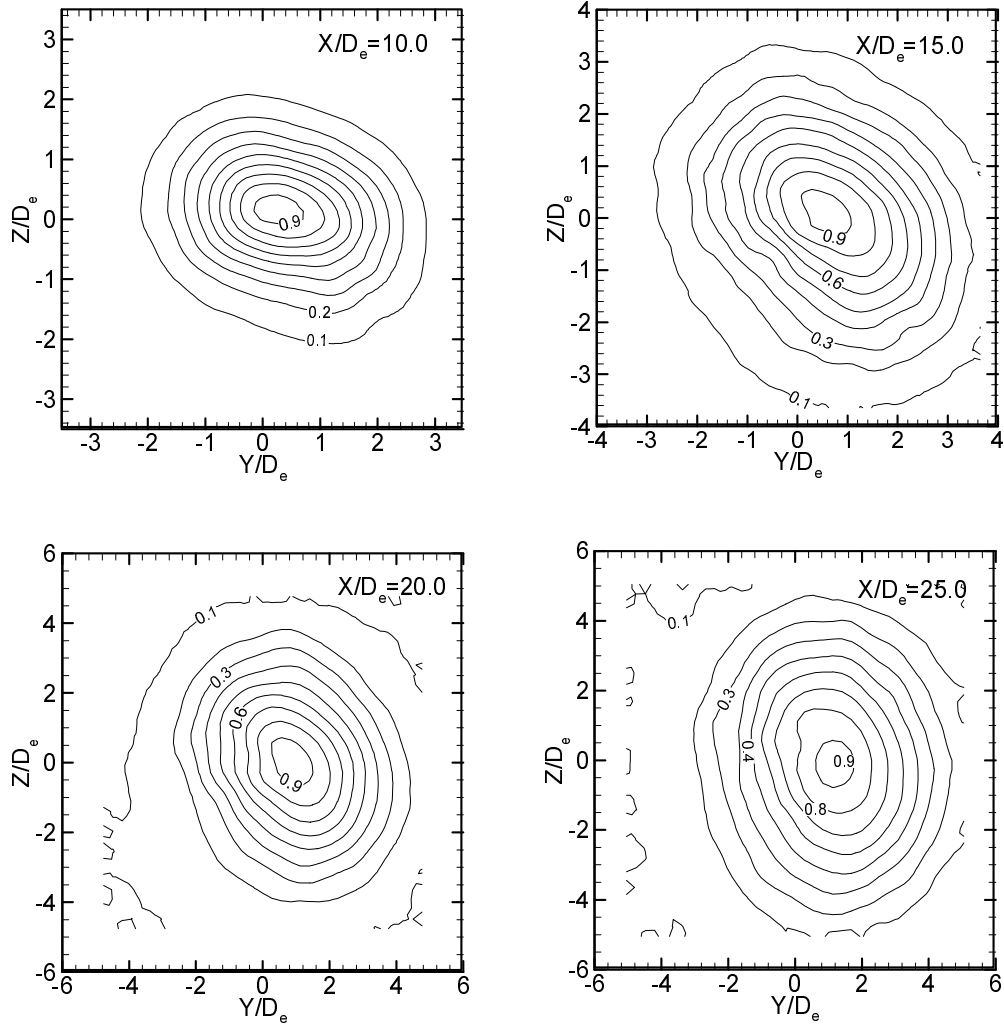


**Figure 3.13** Mean streamwise velocity contour maps for the  $10^\circ$  jet (continued).

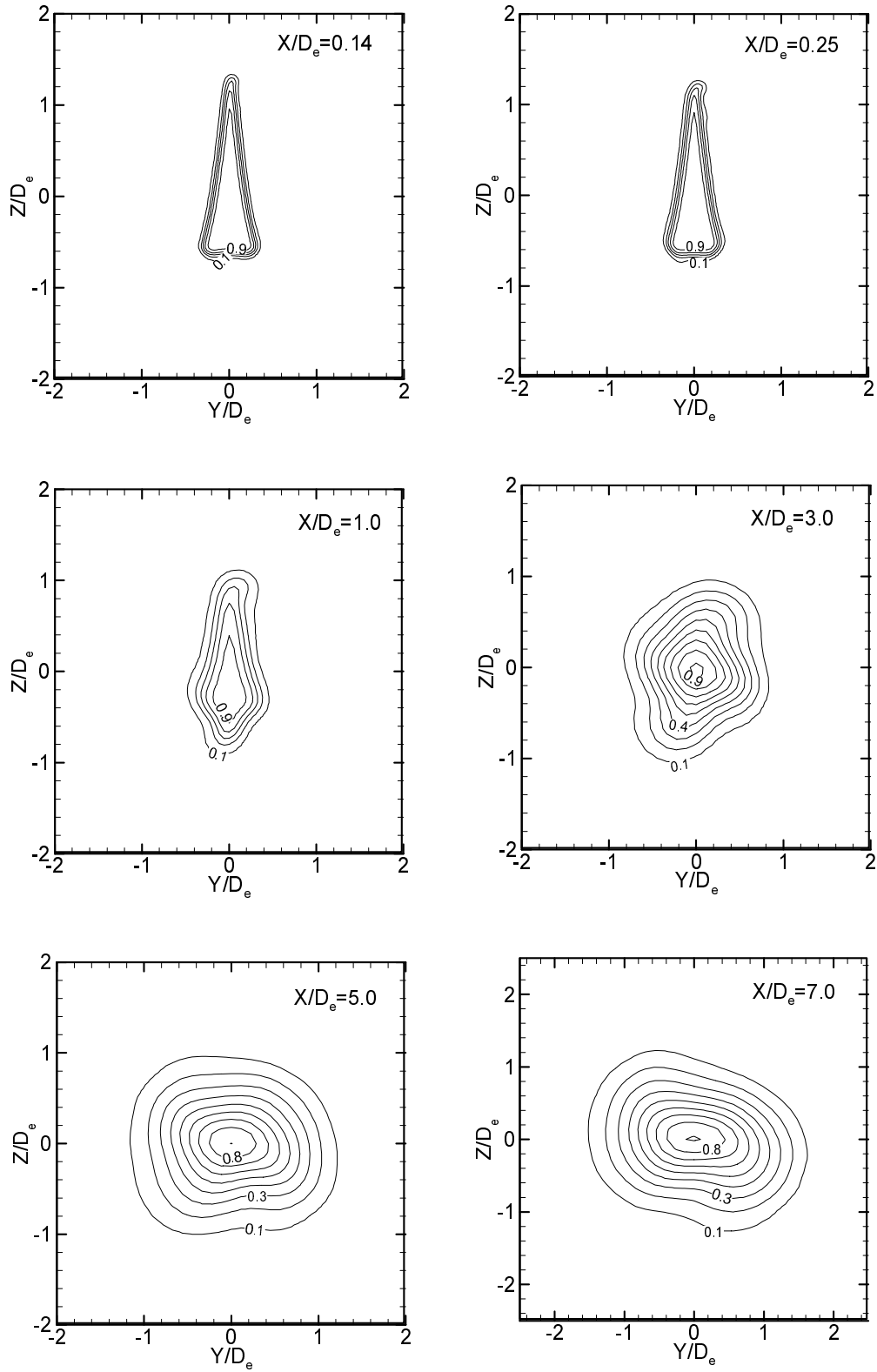


**Figure 3.14** Mean streamwise velocity contour maps for the  $20^\circ$  jet.

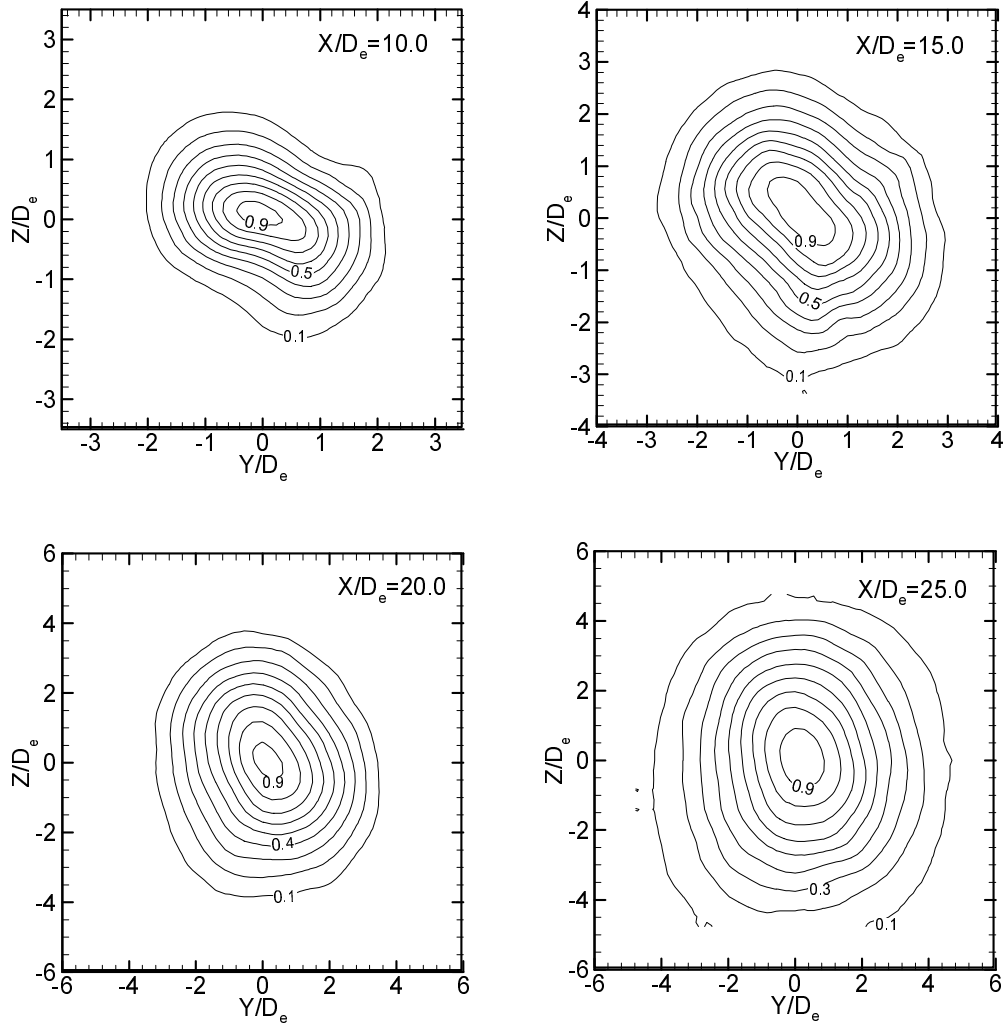


**Figure 3.15** Mean streamwise velocity contour maps for the 20° jet (continued).

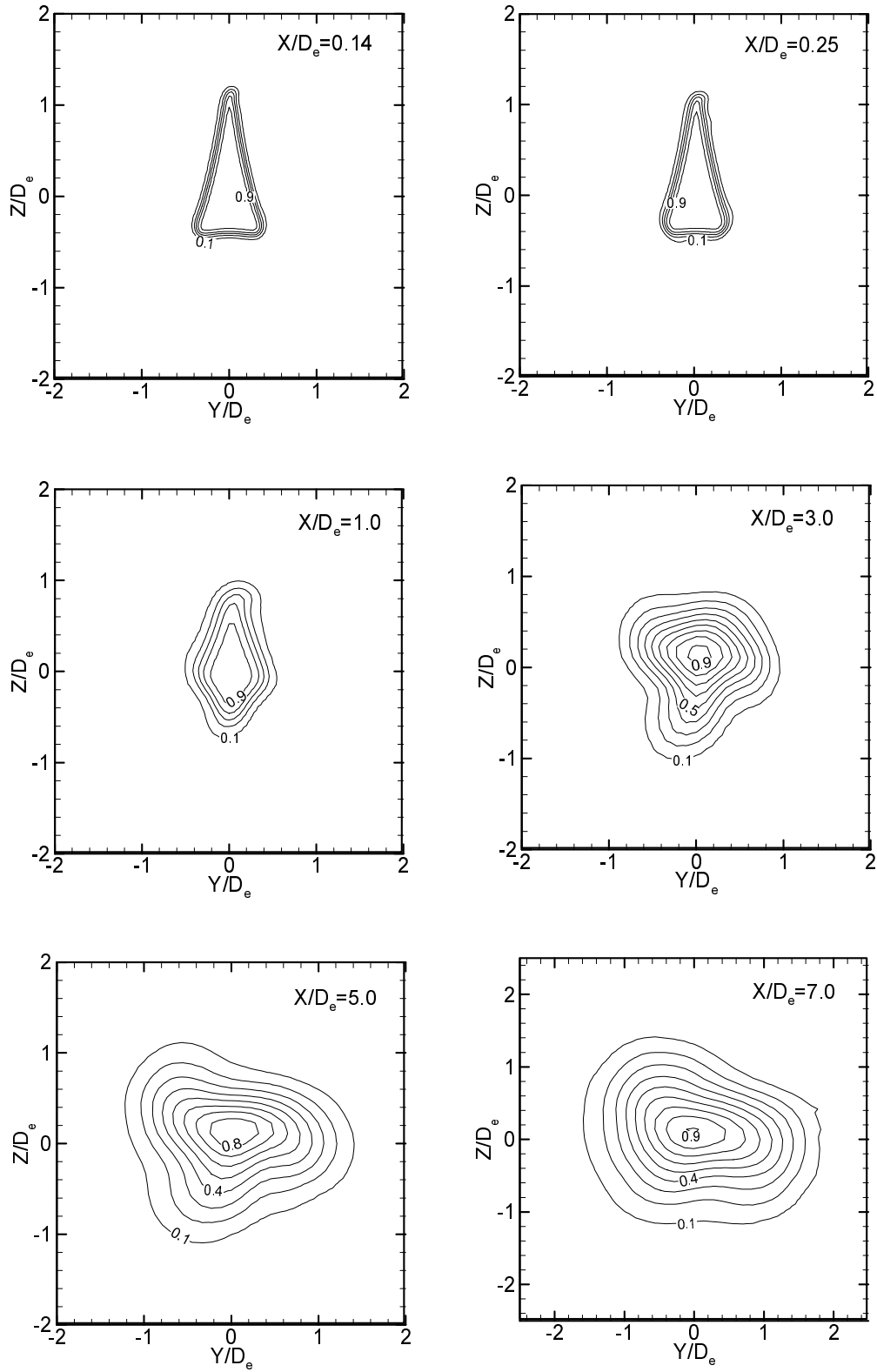


**Figure 3.16** Mean streamwise velocity contour maps for the 30° jet.

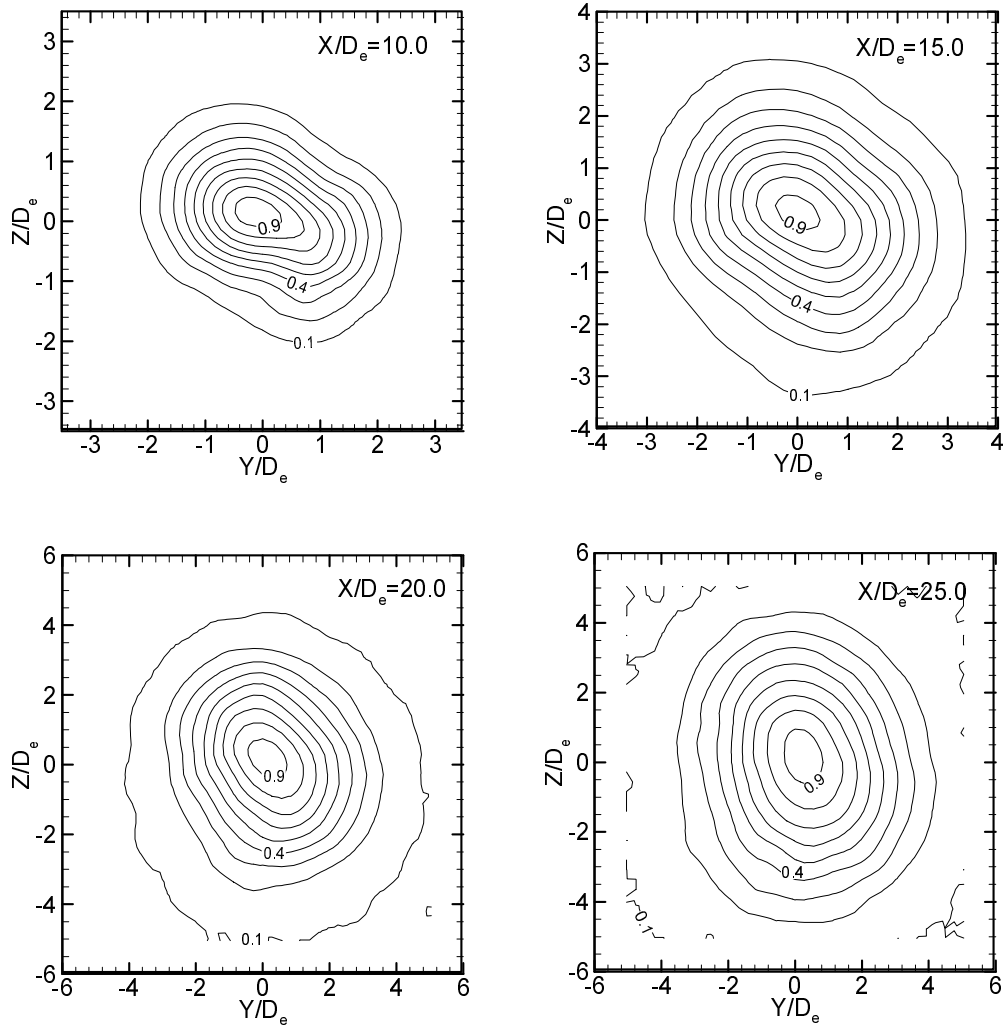


**Figure 3.17** Mean streamwise velocity contour maps for the 30° jet (continued).

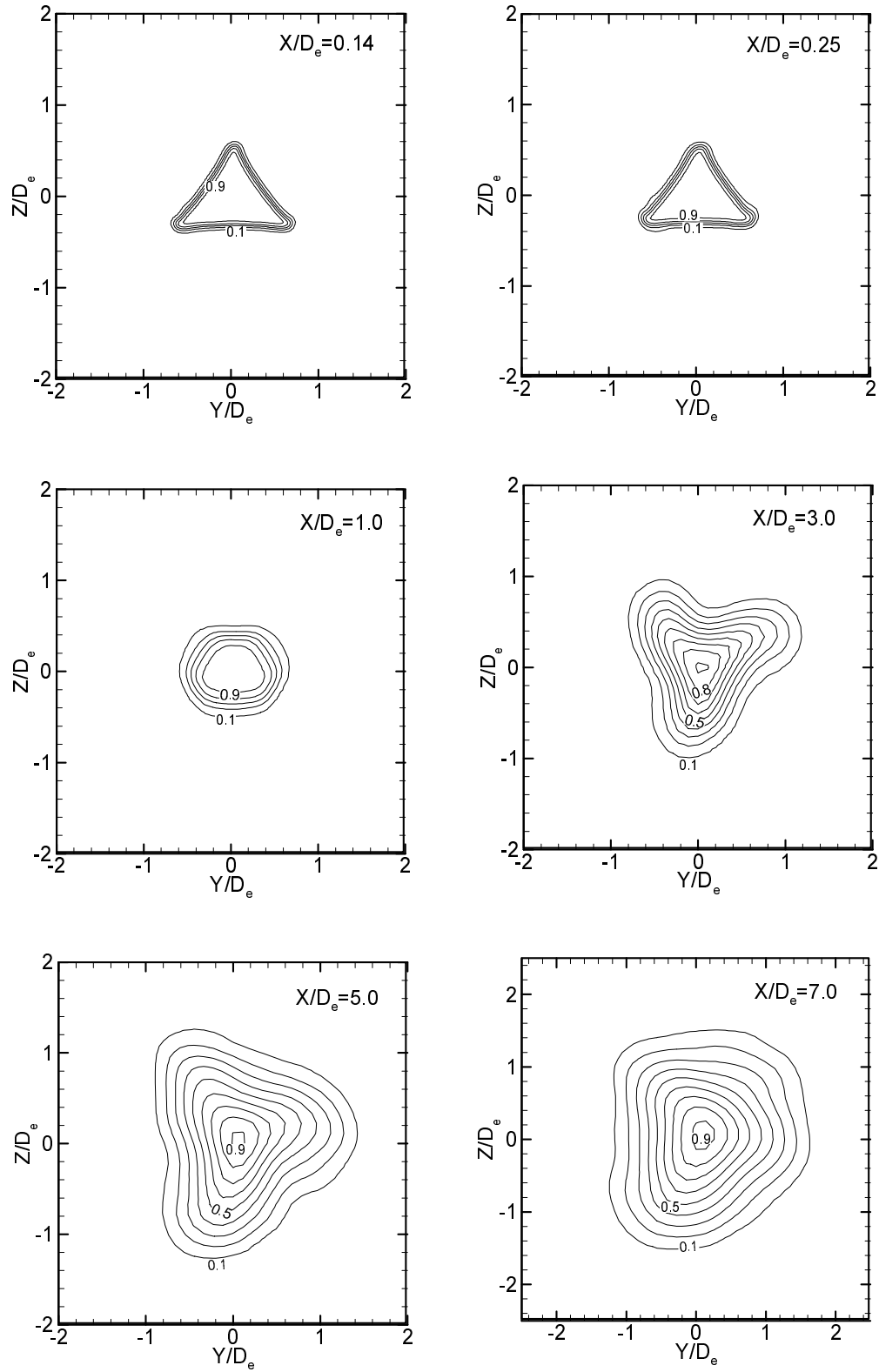


**Figure 3.18** Mean streamwise velocity contour maps for the 70° jet.

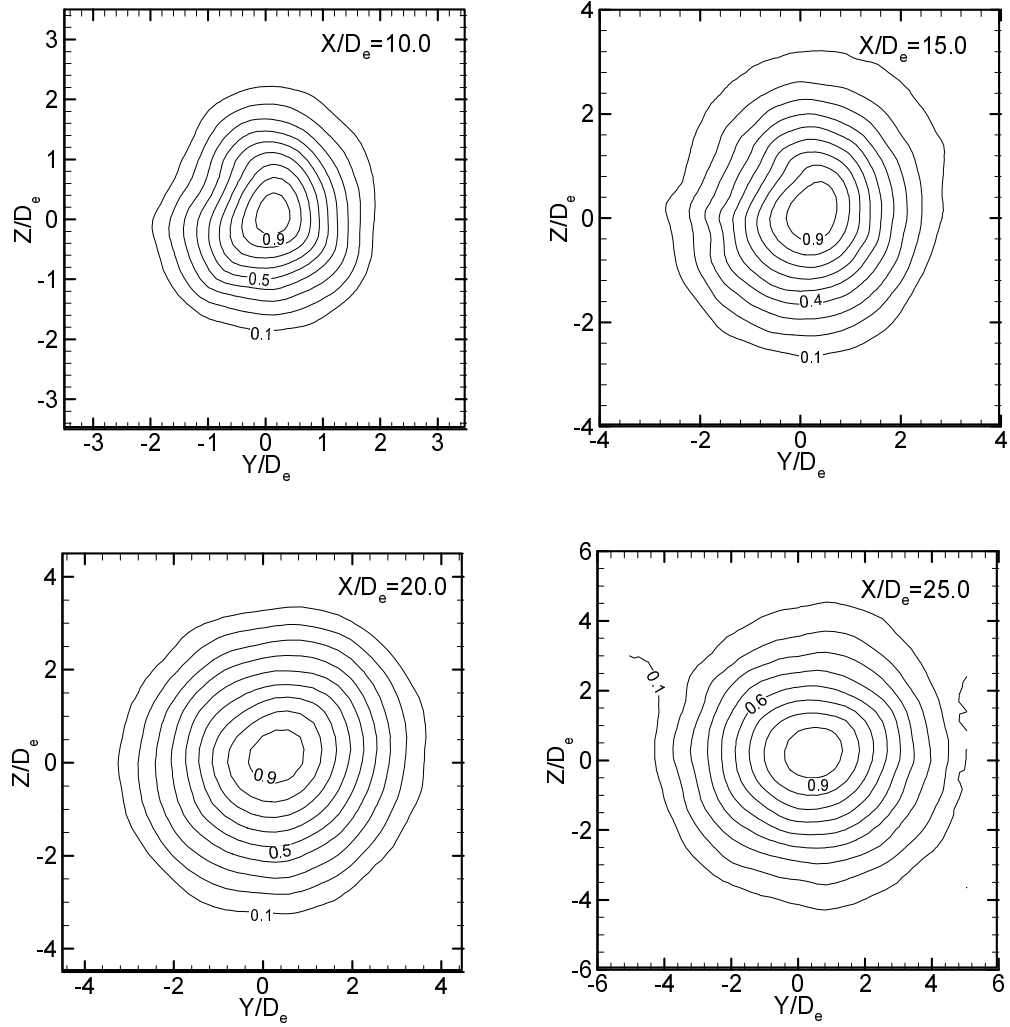


**Figure 3.19** Mean streamwise velocity contour maps for the 70° jet (continued).

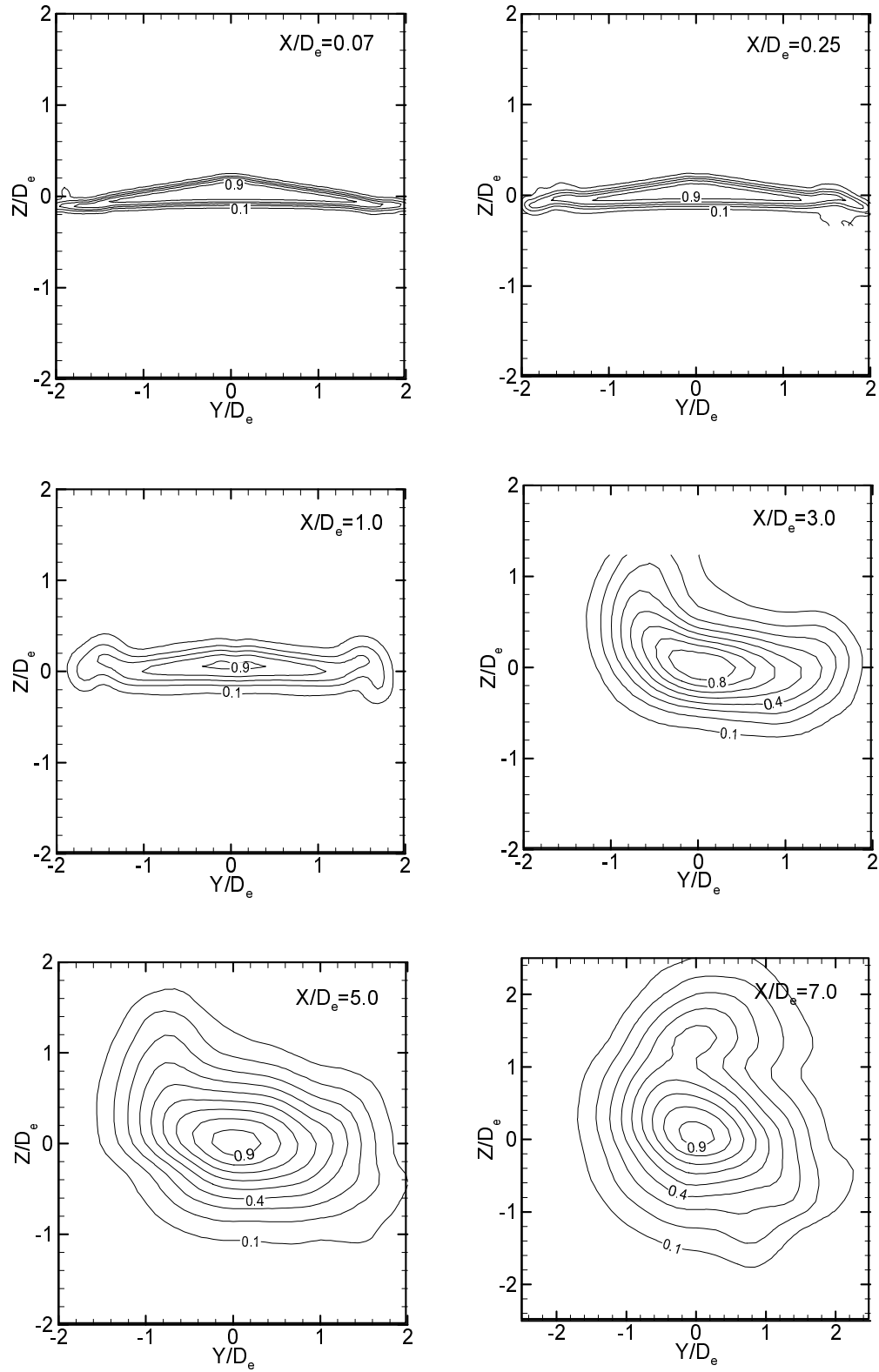


**Figure 3.20** Mean streamwise velocity contour maps for the  $160^\circ$  jet.

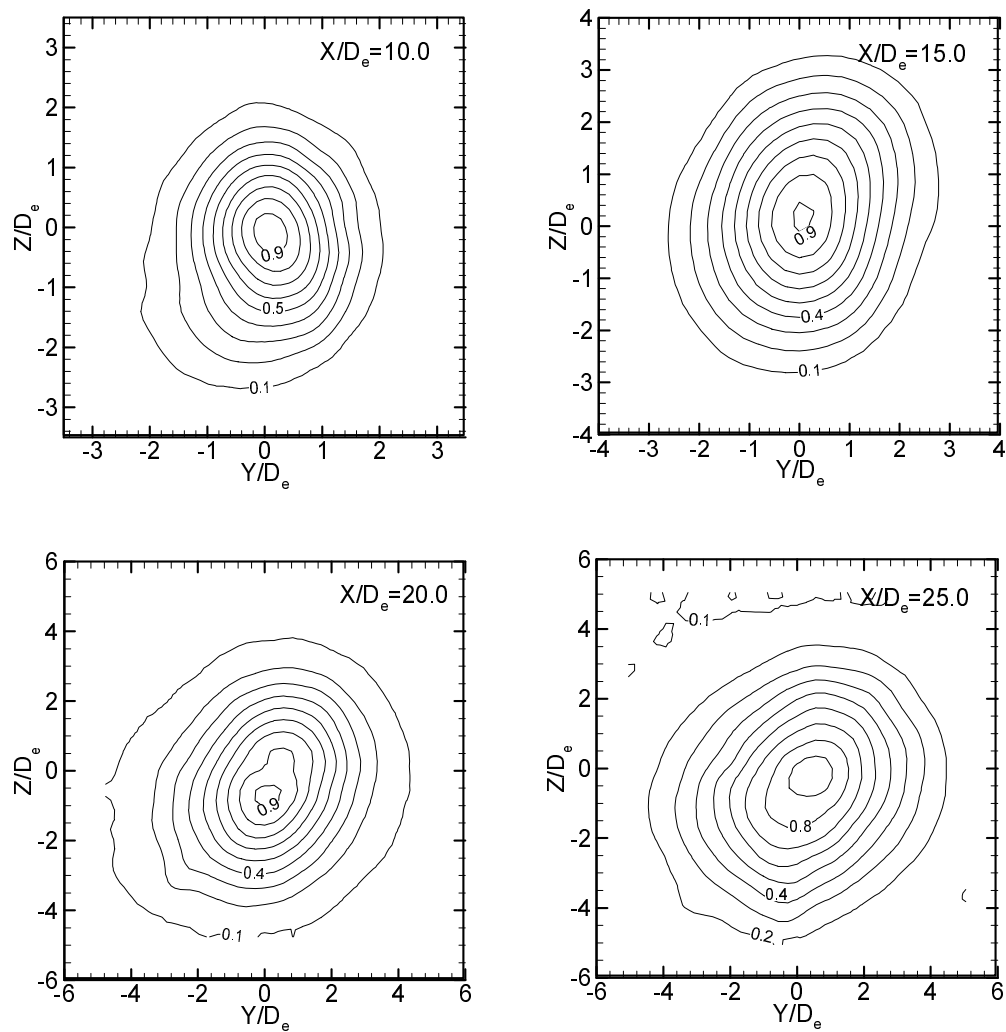


**Figure 3.21** Mean streamwise velocity contour maps for the 160° jet (continued).

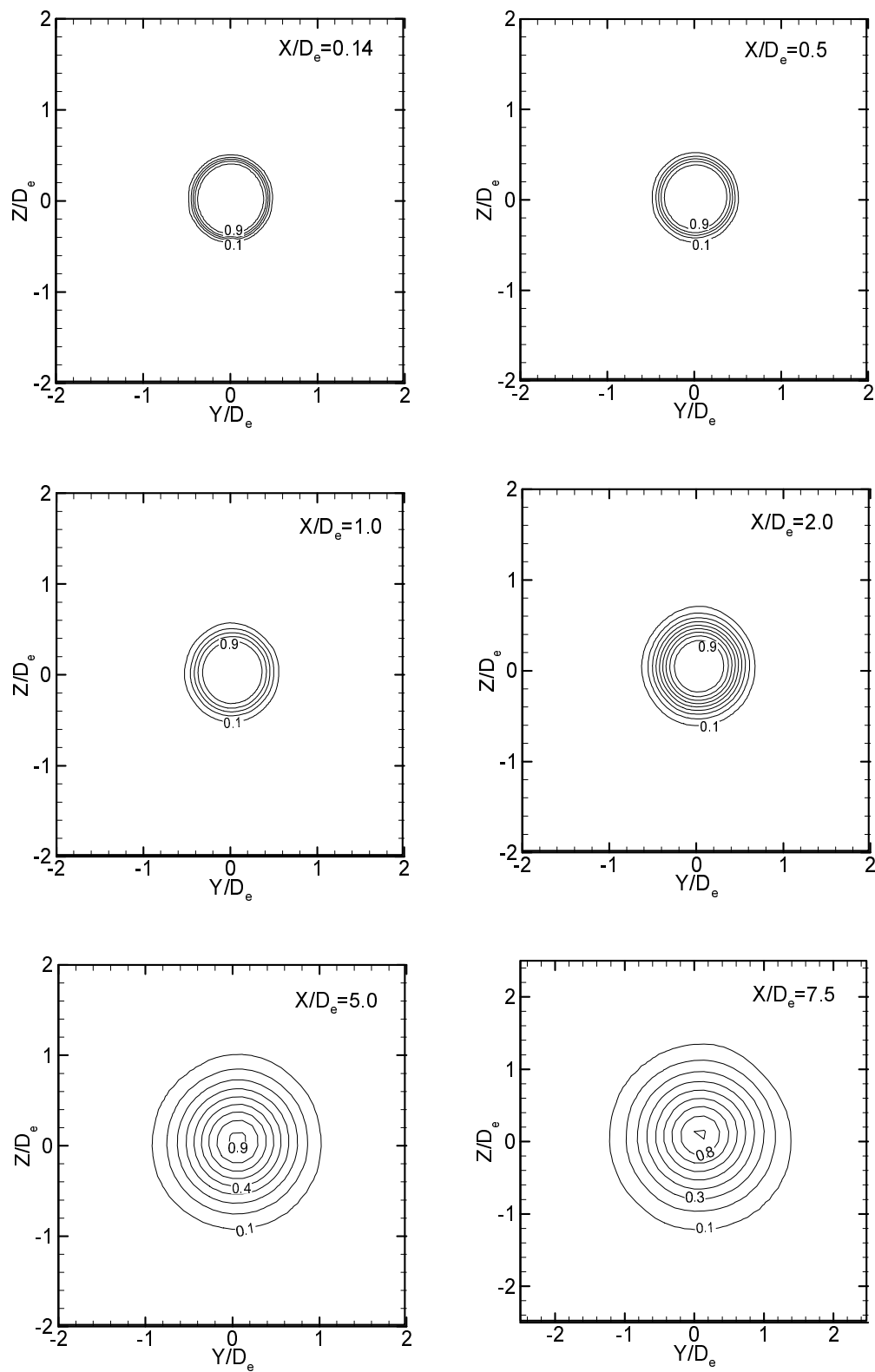


**Figure 3.22** Mean streamwise velocity contour maps for the sharp-edged orifice round jet.

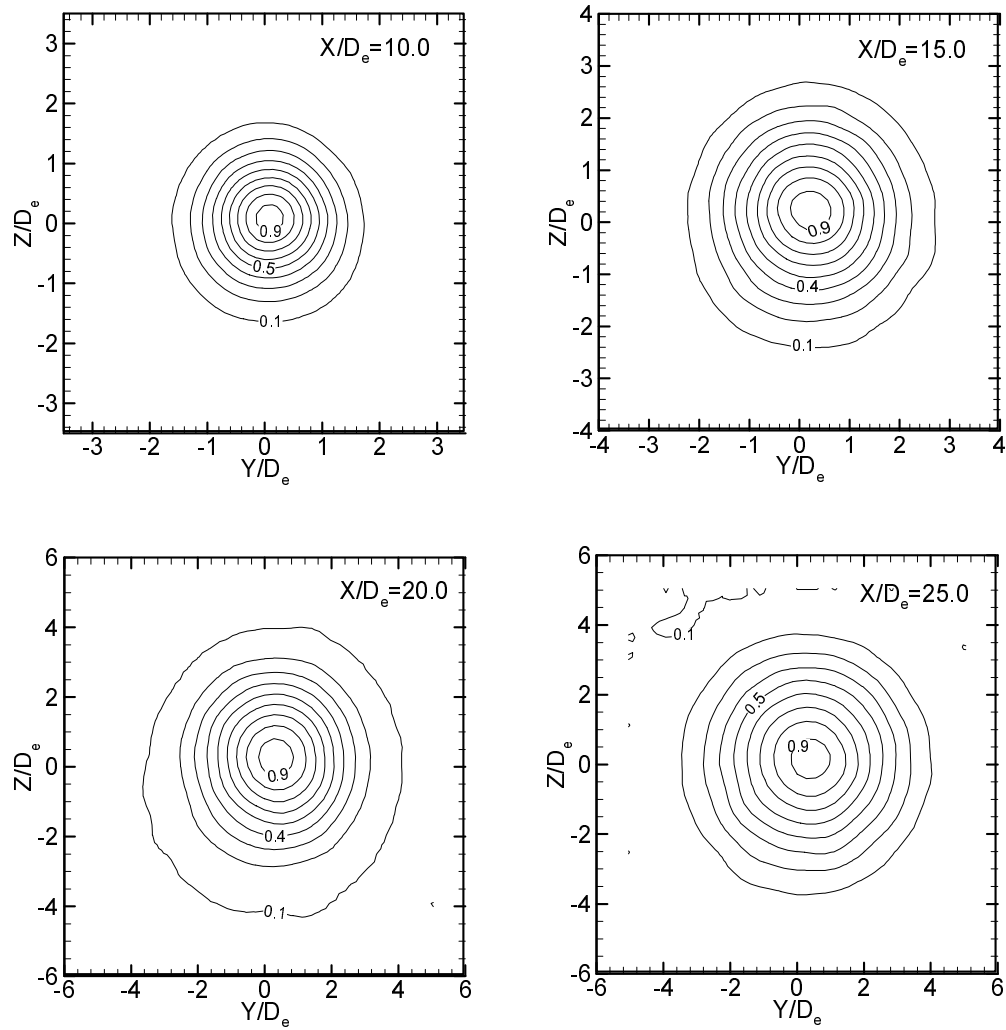


**Figure 3.23** Mean streamwise velocity contour maps for the sharp-edged orifice round jet (continued).

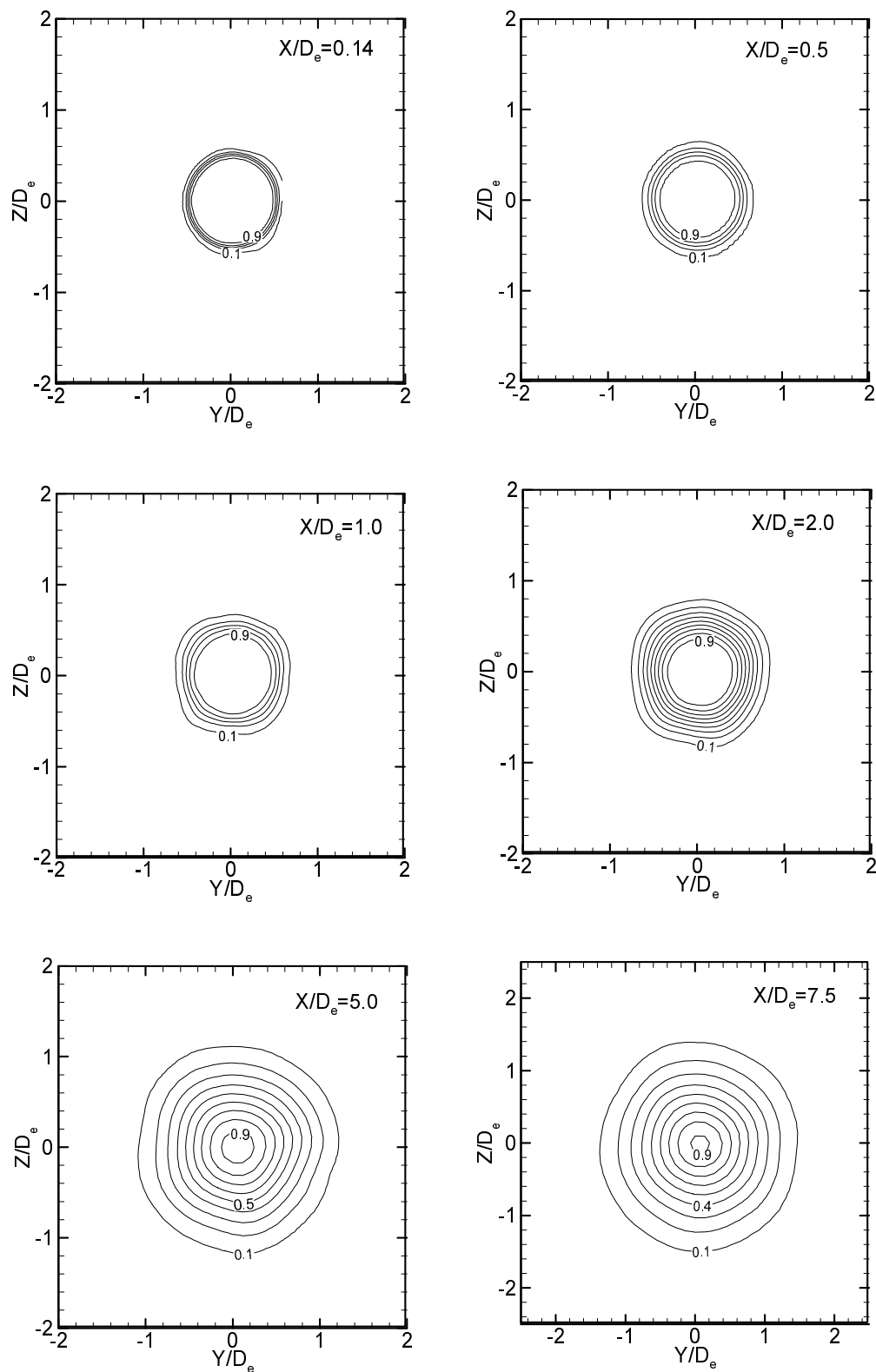


**Figure 3.24** Mean streamwise velocity contour maps for the contoured nozzle round jet.

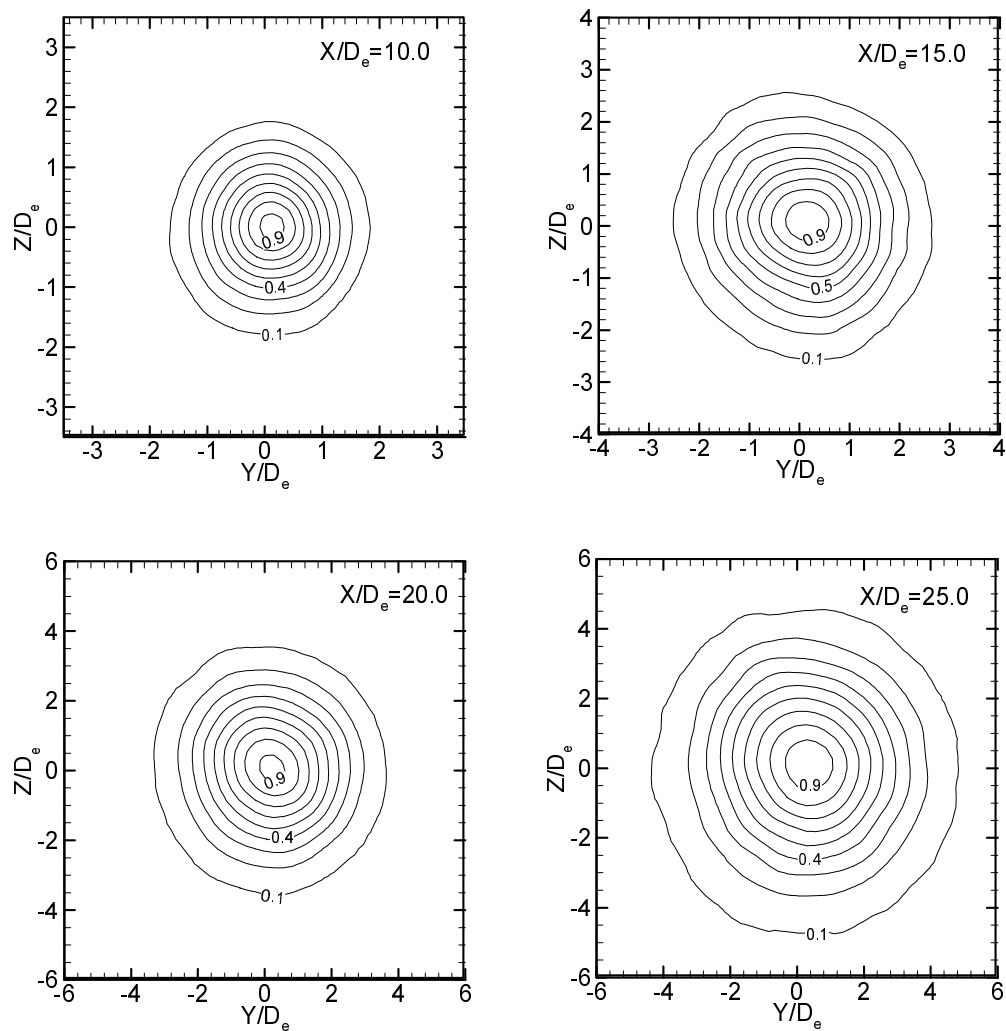


**Figure 3.25** Mean streamwise velocity contour maps for the contoured nozzle round jet (continued).

### 3.6 Mass entrainment into the jets

The mass entrainment ratio  $((Q - Q_0)/Q_0)$  variation with streamwise distance is shown in Figure 3.26 for all the test jets. The mass flow rate into the jets was calculated from the mean streamwise velocity data, obtained by the pitot-static tube on  $Y-Z$  planes at several  $X/D_e$  locations from:

$$Q = \int_A \rho U dA \quad (3.2)$$

using Simpson's 1/3 rule of numerical integration. Here,  $dA$  is an elemental area on a  $Y-Z$  plane. The density of air ( $\rho$ ) was set constant and the integration was carried out to the point where the mean streamwise velocity was 10% of its value on the jet centreline.

In the near field ( $X/D_e \leq 10$ ), all the triangular jets have higher mass entrainment ratios than both of the round jets and the  $160^\circ$  jet has the highest mass entrainment ratios. In this region, the contoured nozzle round jet has higher mass entrainment ratios than the sharp-edged orifice round jet. In the region  $2 \leq X/D_e \leq 10$ , the  $70^\circ$  jet has higher mass entrainment ratios than the other jets, except for the  $10^\circ$  and  $160^\circ$  jets.  $(Q - Q_0)/Q_0$  increases almost linearly in the far field of all the jets. The  $10^\circ$  jet has the highest and the contoured nozzle round jet has the lowest mass entrainment ratios in the far field. Among all the triangular jets tested, the  $160^\circ$  jet has the lowest mass entrainment ratios in the far field. It should also be mentioned here that the sharp-edged orifice round jet has higher mass entrainment ratios in the far field than the contoured nozzle round jet, unlike in the near field.

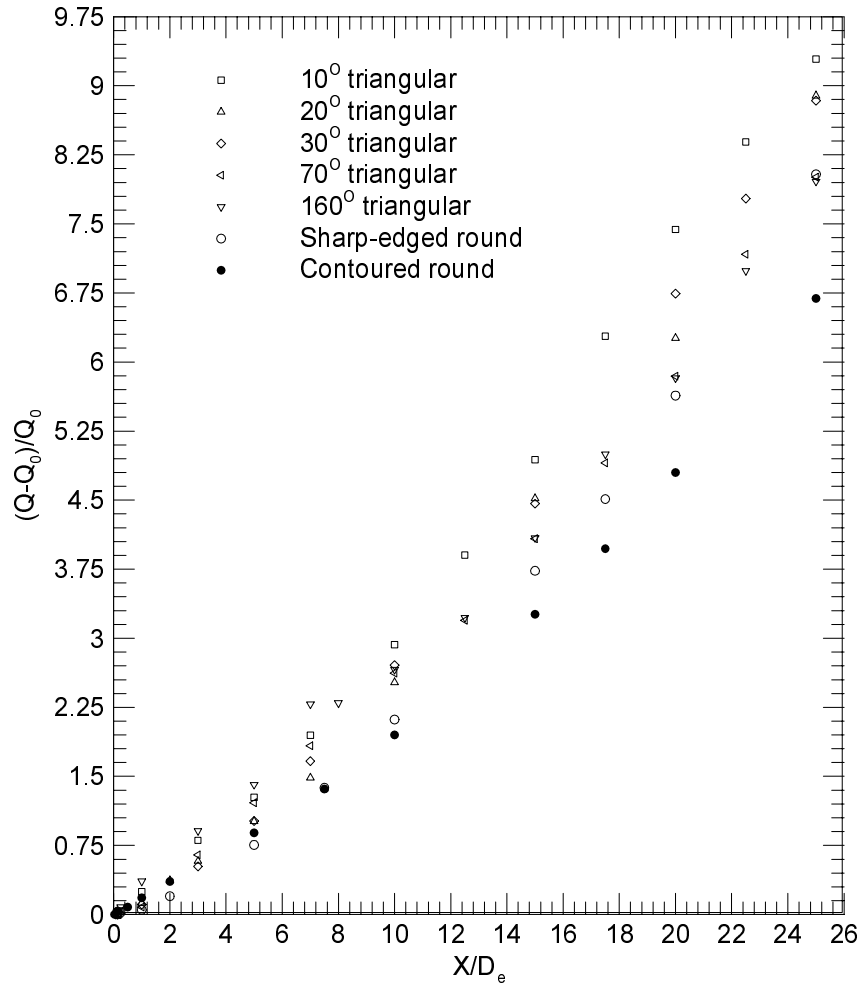
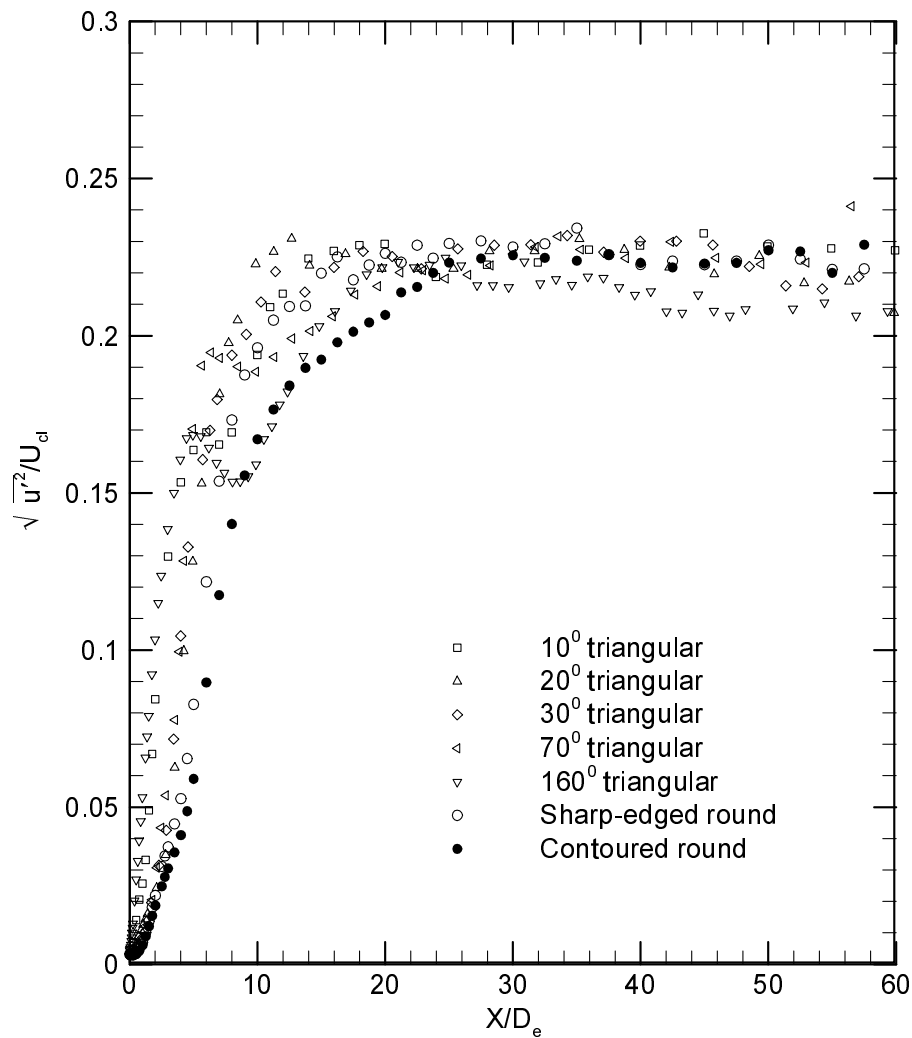


Figure 3.26 Mass entrainment into the jets.

### 3.7 Streamwise turbulence intensities on the jet centreline

The evolution of the streamwise turbulence intensities ( $\sqrt{u'^2}/U_{cl}$ ) along the jet centreline is shown in Figure 3.27 for all the test jets.  $\sqrt{u'^2}/U_{cl}$  increases rapidly in the near field of all the jets and becomes almost constant in the far field. The asymptotic value of  $\sqrt{u'^2}/U_{cl}$  in the different jets is in the range of 22% to 24%.

While there is no dip observed in the evolution of  $\sqrt{u'^2}/U_{cl}$  along the jet centreline in both round jets, such dips are observed in the triangular jets. The  $160^\circ$  jet has the deepest dip and, after the dip, there is a region of slower growth of  $\sqrt{u'^2}/U_{cl}$  in the  $10^\circ$ ,  $70^\circ$  and  $160^\circ$  jets, which is not present in the other jets.



**Figure 3.27** Streamwise turbulence intensities on the jet centreline.

The results shown in Figure 3.27 are presented using logarithmic scales for both axes in Figure 3.28 to highlight the near-field evolution of  $\sqrt{u'^2}/U_{cl}$  in the different jets.

$\sqrt{u'^2}/U_{cl}$  grows more rapidly in the near field of all the triangular jets than in the round

jets. The  $160^\circ$  jet, issuing from the orifice with the longest perimeter, has the highest growth rate of  $\sqrt{u'^2}/U_{cl}$  in the near field. In the very near field ( $X/D_e \leq 2$ ),  $\sqrt{u'^2}/U_{cl}$  increases with increase in orifice perimeter but in the region  $2 \leq X/D_e \leq 7$ , the  $70^\circ$  jet, which issues from the triangular orifice with the lowest perimeter, has higher values of  $\sqrt{u'^2}/U_{cl}$  than the  $20^\circ$  and  $30^\circ$  jets.  $\sqrt{u'^2}/U_{cl}$  grows more rapidly in the near field of the sharp-edged orifice round jet than in the contoured nozzle round jet.

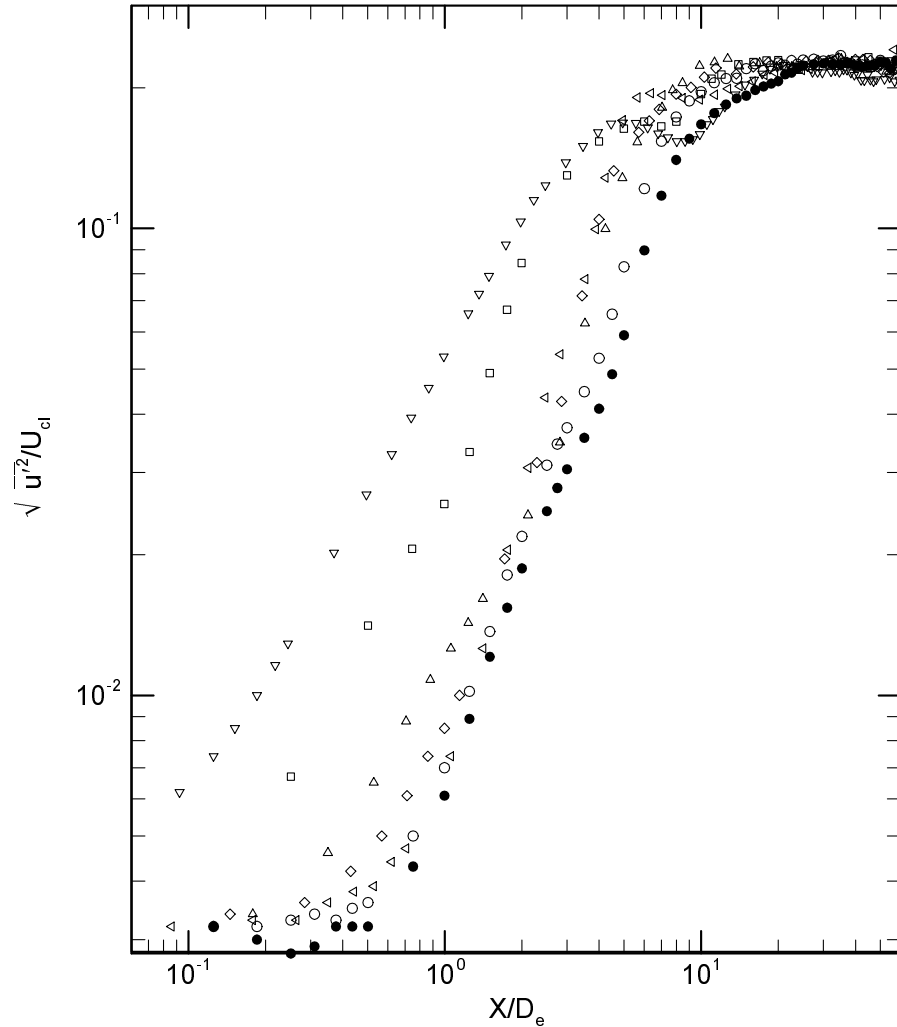


**Figure 3.28** Streamwise turbulence intensities on the jet centreline (log-log). The legends are as shown in Figure 3.27.

### 3.8 Spanwise turbulence intensities on the jet centreline

The evolution of the spanwise turbulence intensities ( $\sqrt{v'^2}/U_{cl}$ ) along the jet centreline is shown in Figure 3.29 for all the test jets.  $\sqrt{v'^2}/U_{cl}$  increases rapidly in the near field of all the jets and in the far field,  $\sqrt{v'^2}/U_{cl}$  becomes almost constant, as was observed for  $\sqrt{u'^2}/U_{cl}$ .  $\sqrt{v'^2}/U_{cl}$  reaches a maximum value of around 15%, which is

smaller than  $\sqrt{u'^2}/U_{cl}$ , in all the jets, except for the  $10^\circ$ ,  $160^\circ$  and contoured nozzle round jets. The  $10^\circ$ ,  $160^\circ$  and contoured nozzle round jets have an asymptotic value of  $\sqrt{v'^2}/U_{cl}$  of about 18%.

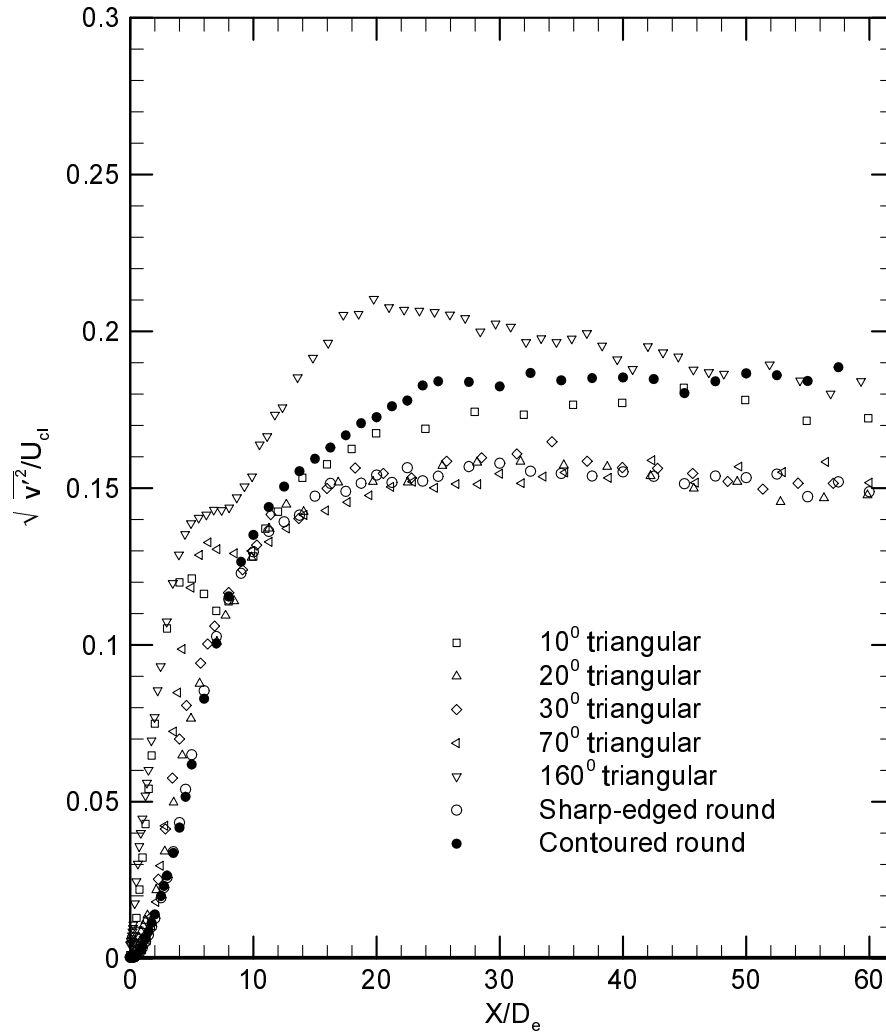


**Figure 3.29** Spanwise turbulence intensities on the jet centreline.

The results shown in Figure 3.29 are presented in Figure 3.30 using logarithmic scales for both axes to bring the near-field behaviour of  $\sqrt{v'^2}/U_{cl}$  in the different jets into focus.  $\sqrt{v'^2}/U_{cl}$  in the near field of the  $160^\circ$  jet grows most rapidly followed by that of

the  $10^\circ$  jet, like the centreline evolution of  $\sqrt{u'^2}/U_{cl}$ . The growth rate of  $\sqrt{v'^2}/U_{cl}$  in the round jets is slower than that of the triangular jets, as was the case in the evolution of  $\sqrt{u'^2}/U_{cl}$ , regardless of the apex angle of the triangular orifice. Overall, the evolution of  $\sqrt{v'^2}/U_{cl}$  is similar to that of  $\sqrt{u'^2}/U_{cl}$  but the values of  $\sqrt{v'^2}/U_{cl}$  are smaller.

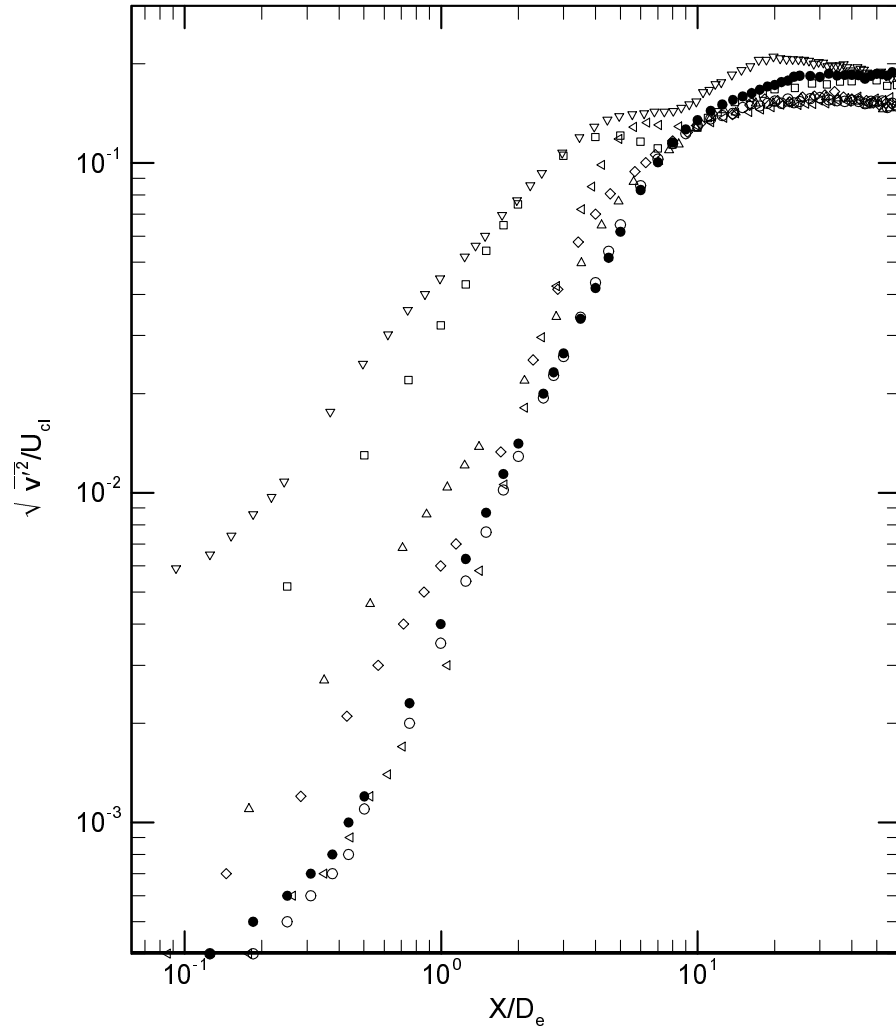


**Figure 3.30** Spanwise turbulence intensities on the jet centreline (log-log). The legends are as shown in Figure 3.29.

### 3.9 One-dimensional energy spectra of the streamwise fluctuating velocity on the jet centreline

The one-dimensional energy spectra of the streamwise fluctuating velocities at several streamwise locations on the jet centreline are shown in Figures 3.31, 3.32, 3.33, 3.34, 3.35, 3.36, 3.37, 3.38, 3.39 and 3.40 for all the triangular jets. Those for the sharp-edged orifice round jet are shown in Figures 3.41 and 3.42 for comparison. It should be noted that the scales of both the ordinate and abscissa in all the aforementioned figures

are logarithmic. These one-dimensional energy spectra have been obtained from Fast Fourier Transforms (FFT) of the digital hot-wire time series data. It can be shown that:

$$\overline{u'^2} = \int_0^{\infty} \phi_u(f) df \quad (3.3)$$

assuming that the data are statistically stationary. At each location, therefore, the one-dimensional energy spectra have been normalized by  $\overline{u'^2}$ . Discernible peaks in the one-dimensional energy spectra are observed in all the jets close to the orifice exit plane. The peak frequency in the one-dimensional energy spectra changes in the streamwise direction in all the jets. These peaks are not identifiable after  $X/D_e = 1.25, 3.52, 3.43, 3.53, 0.99$  in the triangular jets with apex angles of  $10^\circ, 20^\circ, 30^\circ, 70^\circ$  and  $160^\circ$ , respectively. In the sharp-edged orifice round jet, the peaks in the one-dimensional energy spectra are present up to  $X/D_e = 4.5$ . The inertial subrange is observed starting at the locations mentioned above throughout the downstream distance (not all of them are shown) in all the triangular jets. The inertial subrange is first observed at  $X/D_e = 6.0$  in the sharp-edged orifice round jet. In the inertial subrange the energy decreases following the  $-5/3$  law of Kolmogorov. The dashed lines in the figures refer to the lines with a slope of  $-5/3$ .

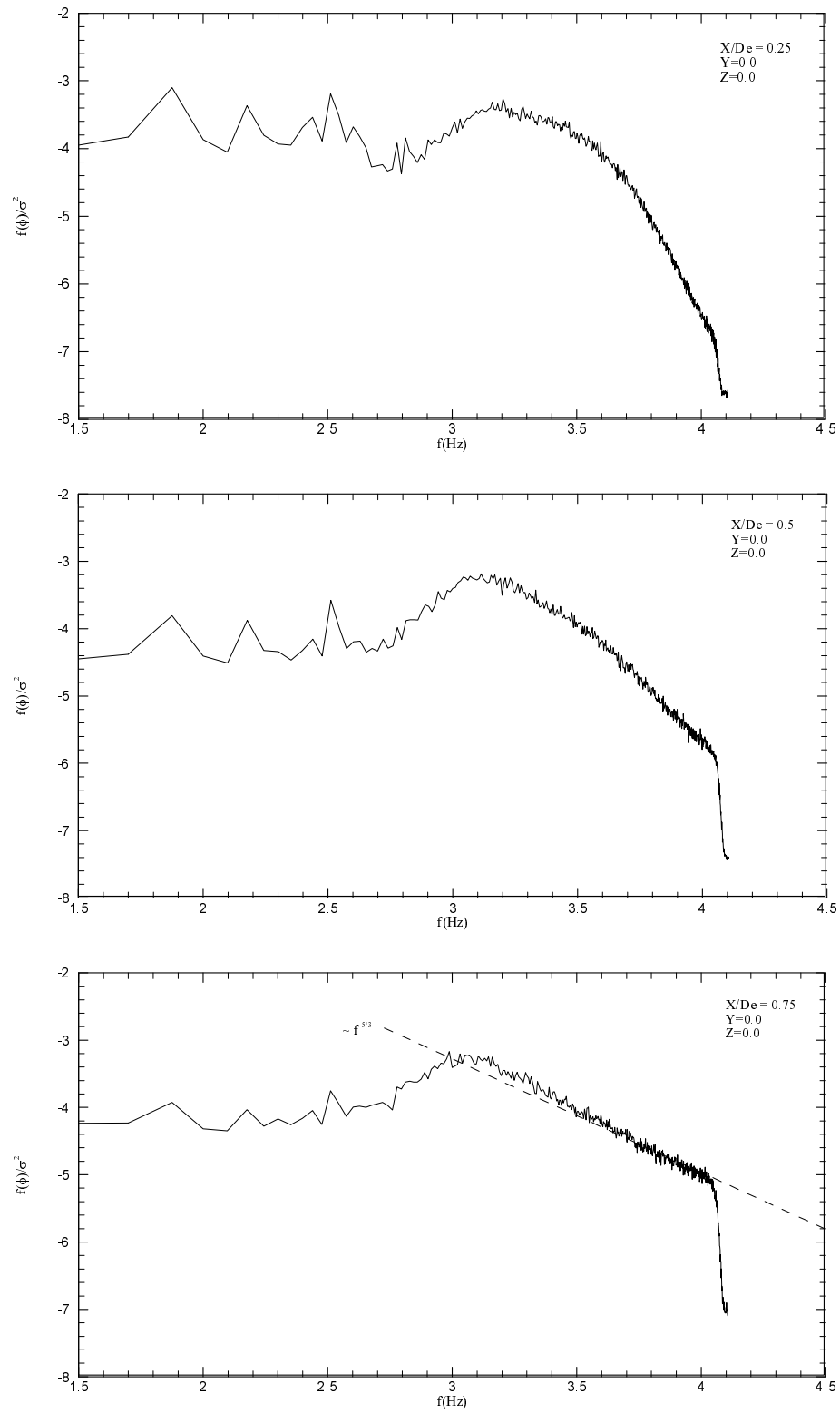


**Figure 3.31** One-dimensional energy spectra of the streamwise fluctuating velocity on the centerline of the  $10^\circ$  jet.

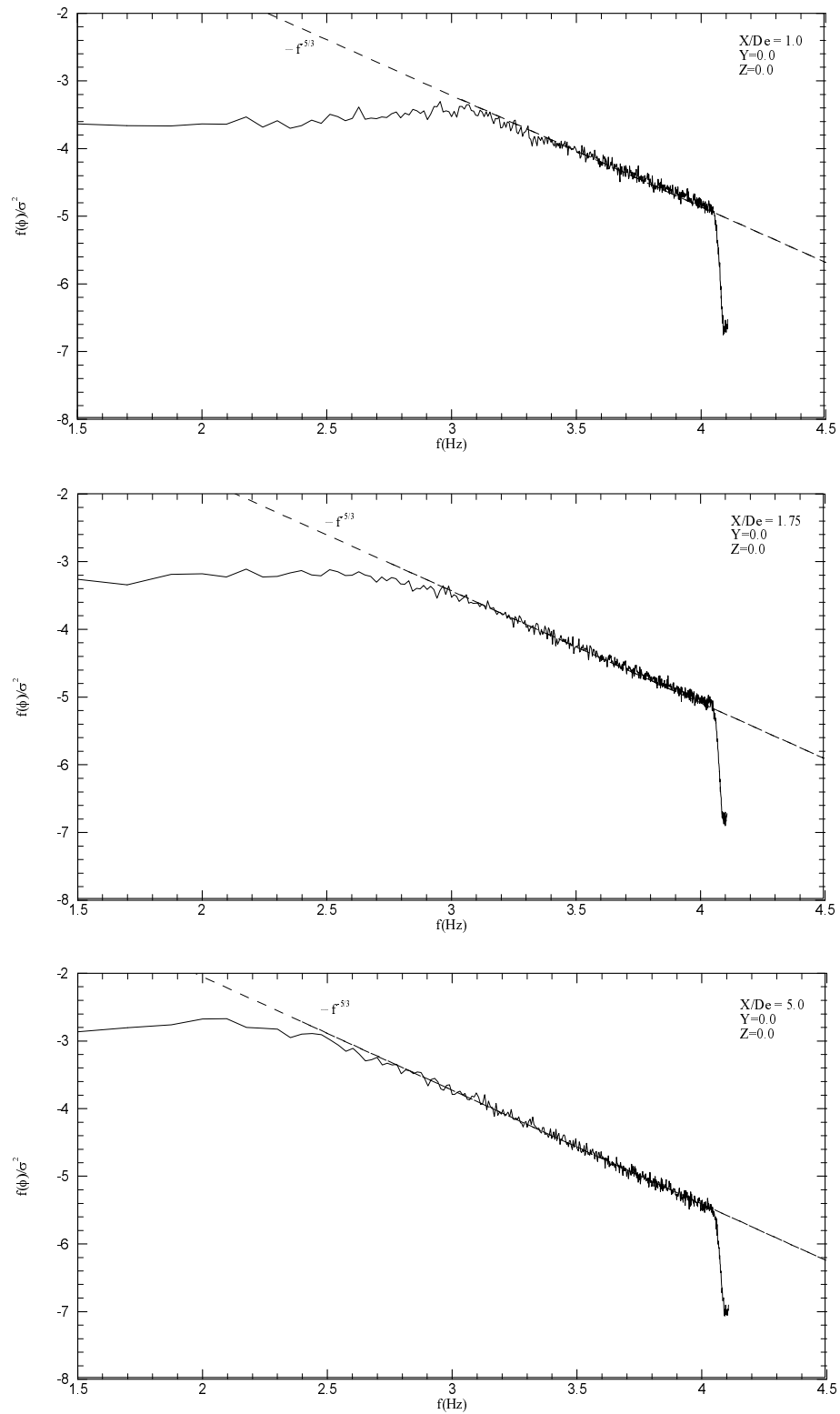


**Figure 3.32** One-dimensional energy spectra of the streamwise fluctuating velocity on the centreline of the  $10^\circ$  jet (continued).

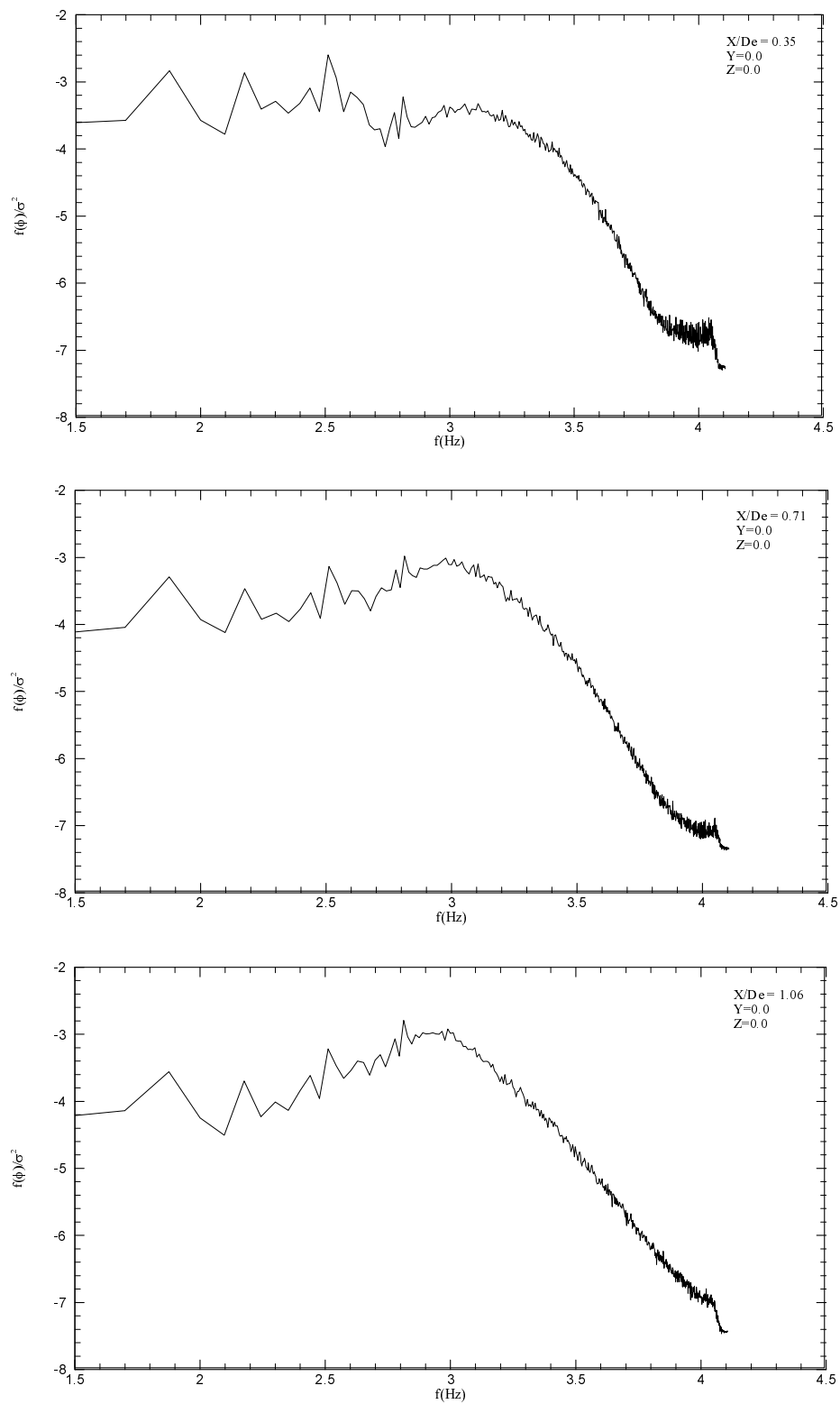


**Figure 3.33** One-dimensional energy spectra of the streamwise fluctuating velocity on the centreline of the  $20^\circ$  jet.

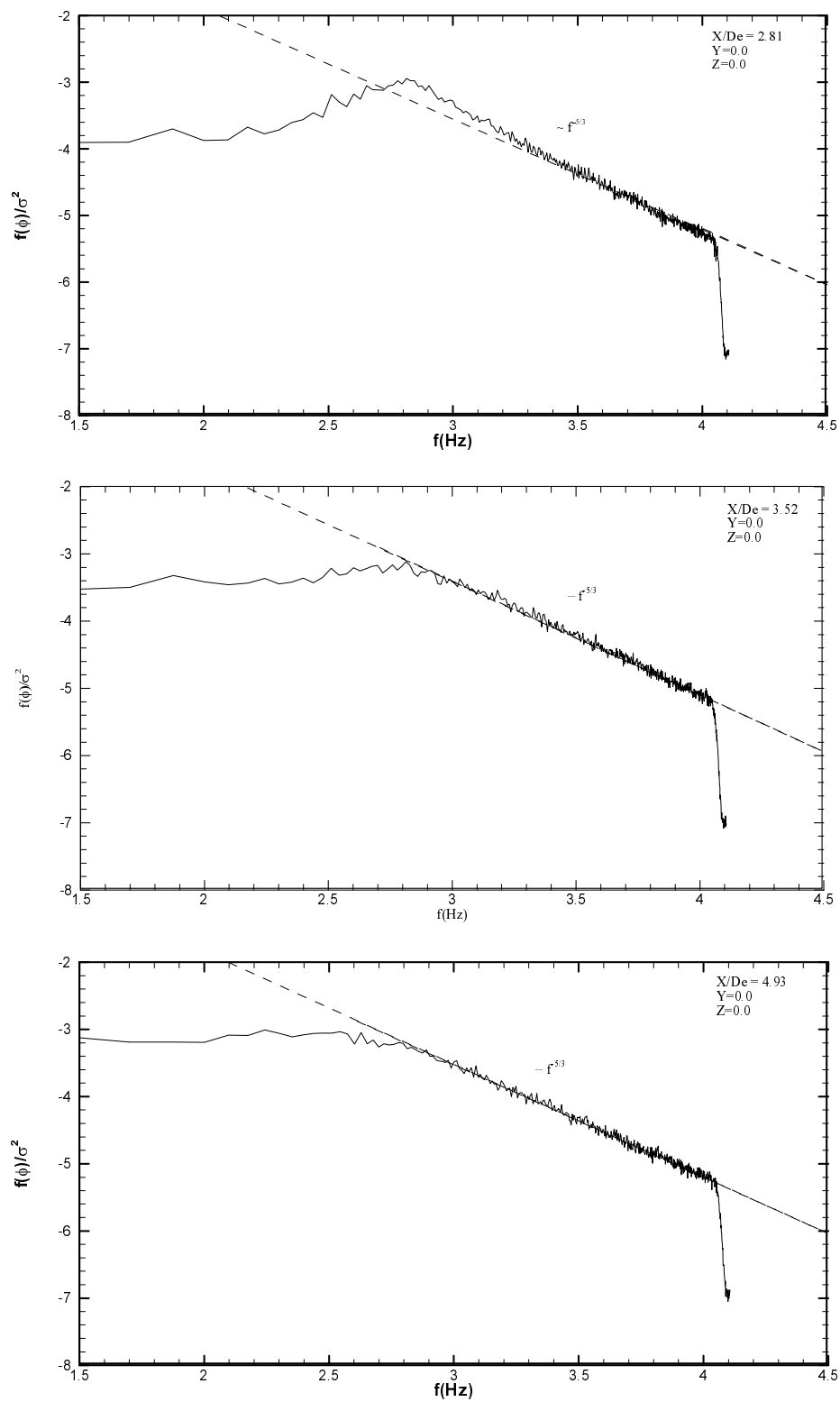


**Figure 3.34** One-dimensional energy spectra of the streamwise fluctuating velocity on the centreline of the  $20^\circ$  jet (continued).

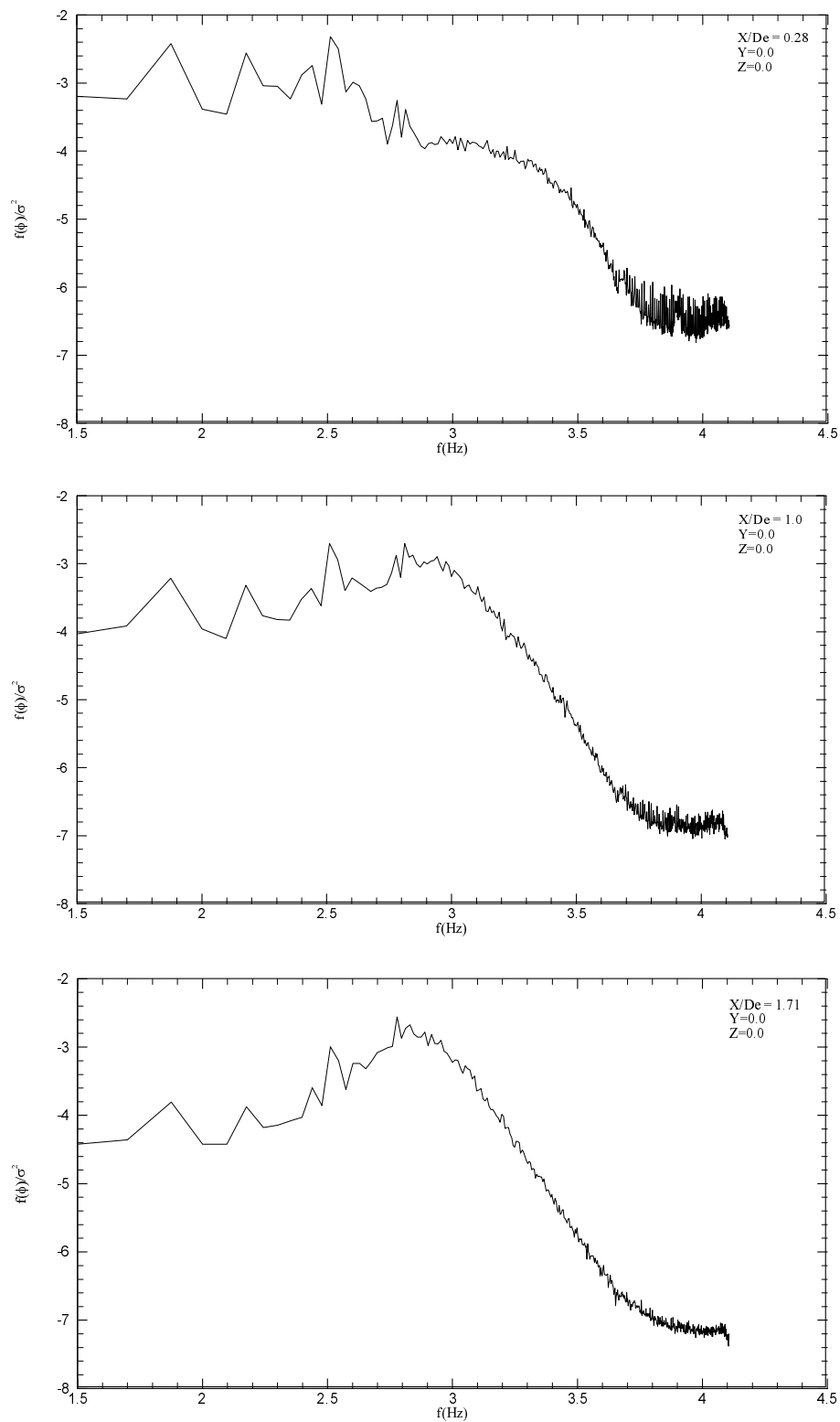


**Figure 3.35** One-dimensional energy spectra of the streamwise fluctuating velocity on the centreline of the 30° jet.

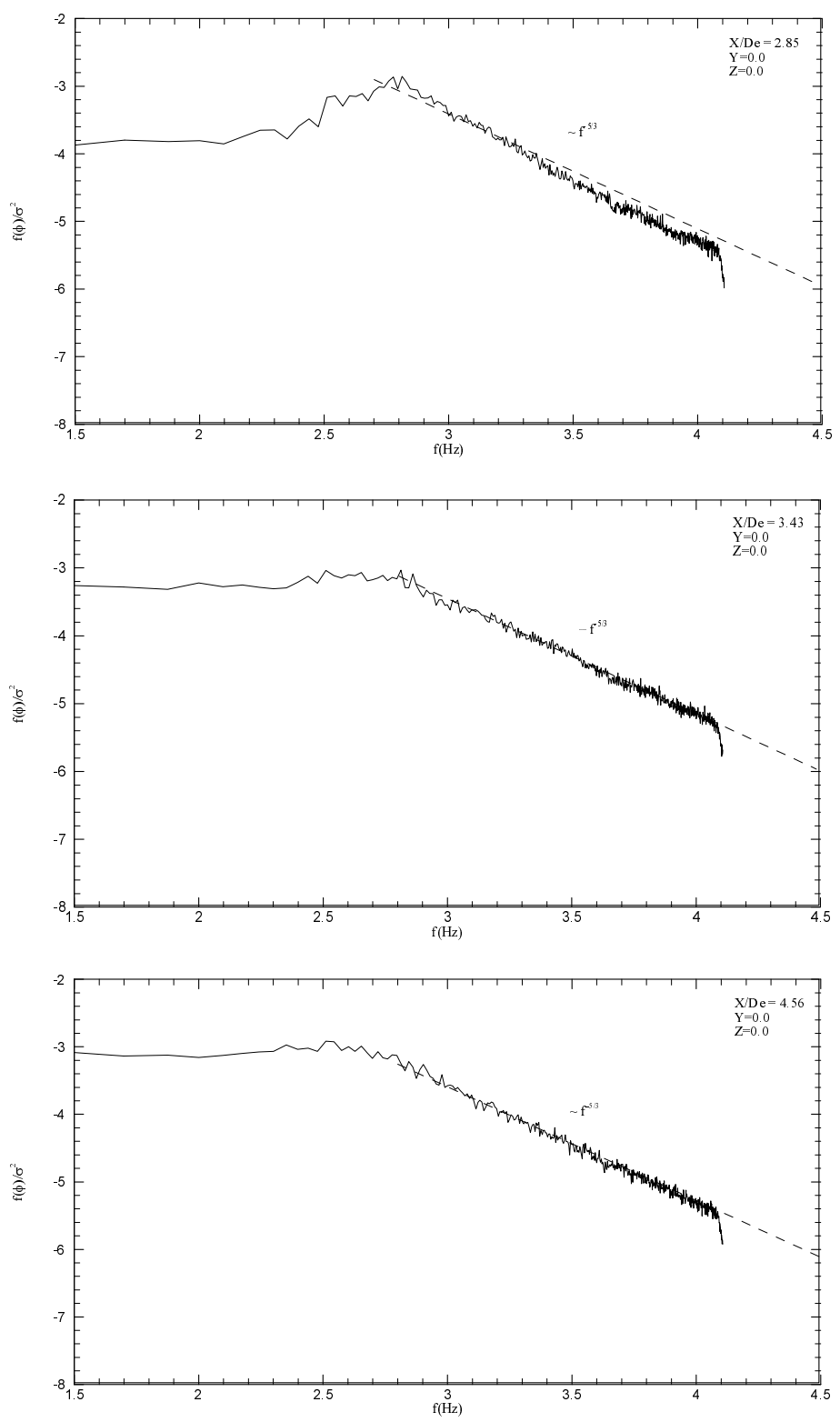


**Figure 3.36** One-dimensional energy spectra of the streamwise fluctuating velocity on the centreline of the 30° jet (Continued).

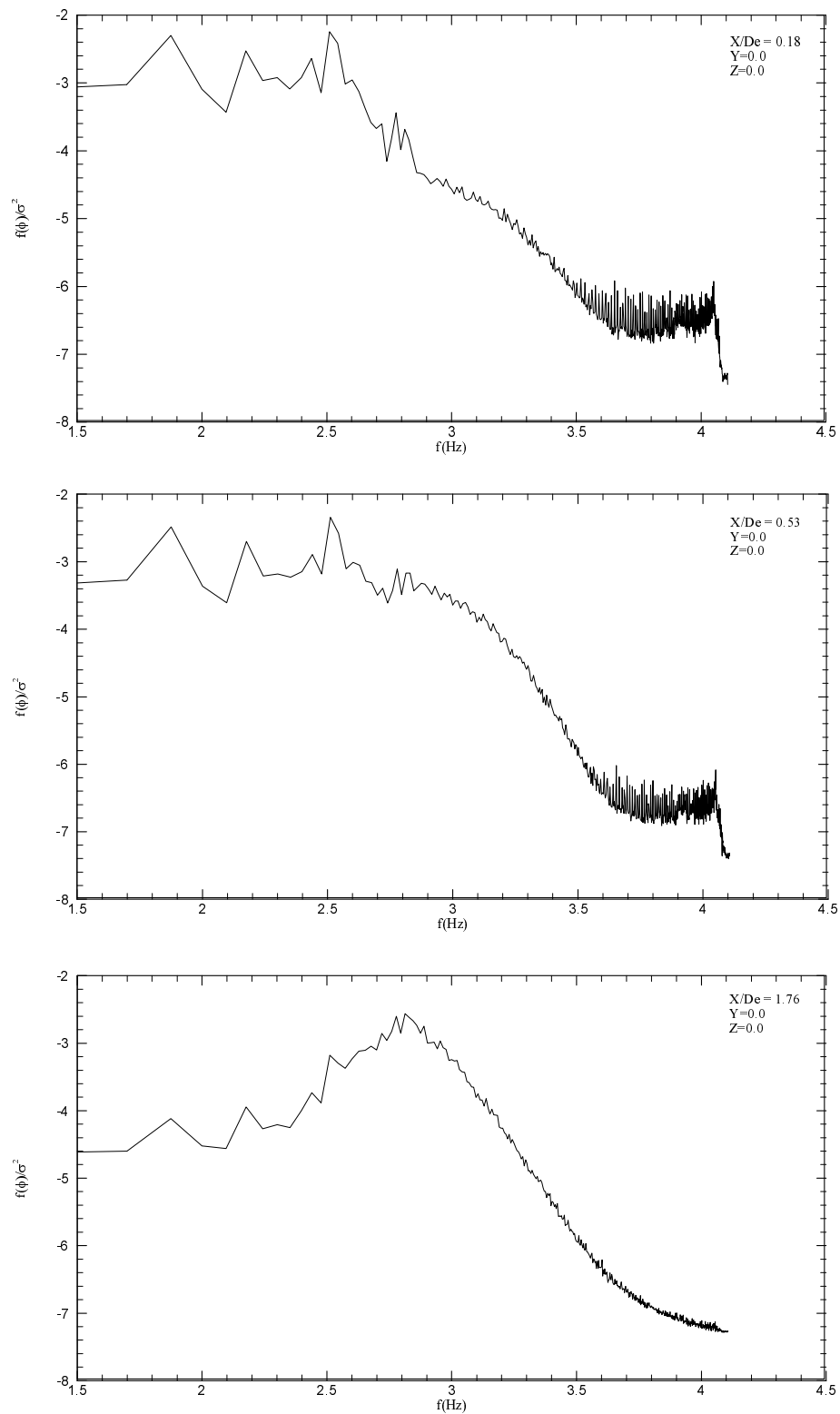


**Figure 3.37** One-dimensional energy spectra of the streamwise fluctuating velocity on the centreline of the 70° jet.

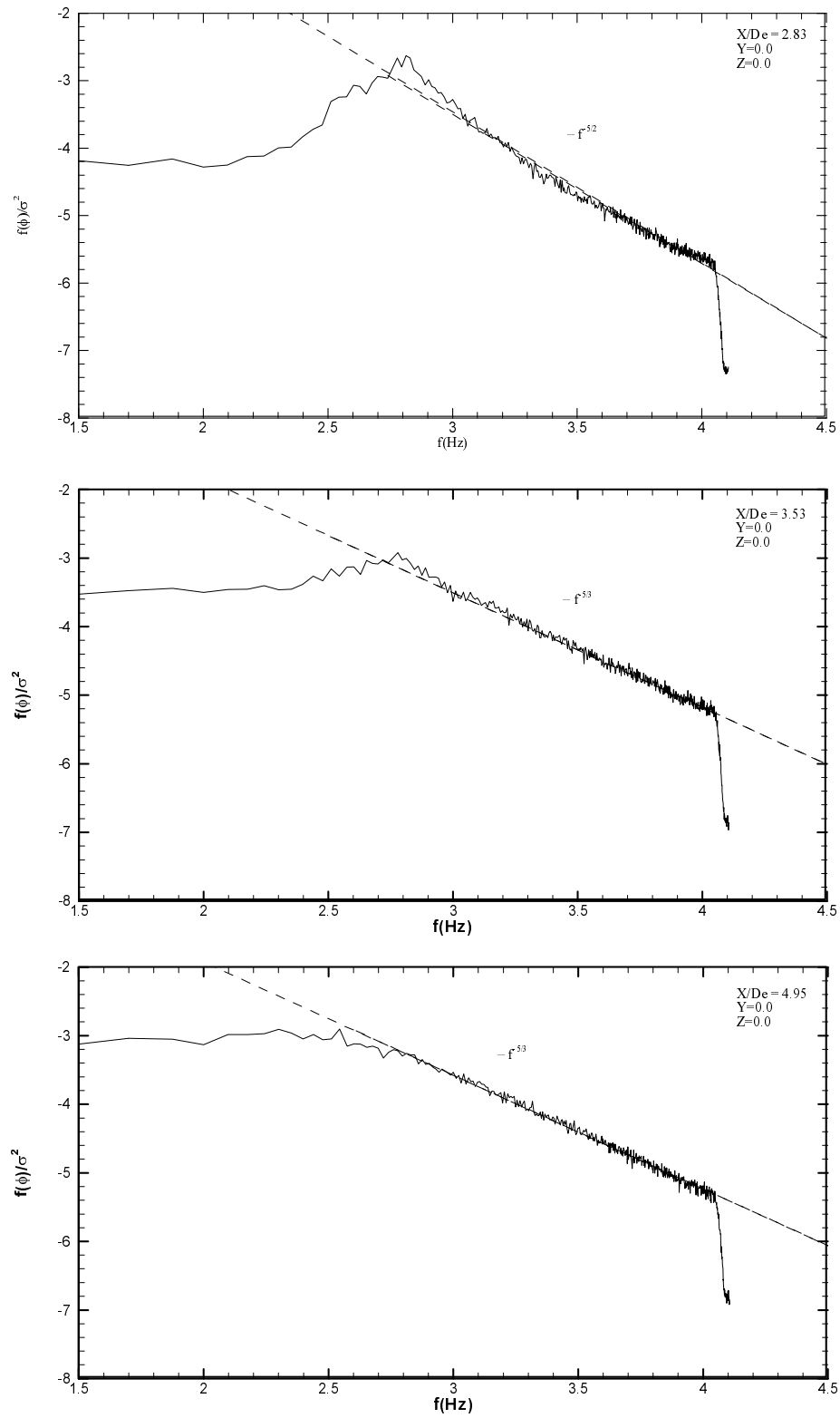


**Figure 3.38** One-dimensional energy spectra of the streamwise fluctuating velocity on the centreline of the jet  $70^\circ$  jet (continued).

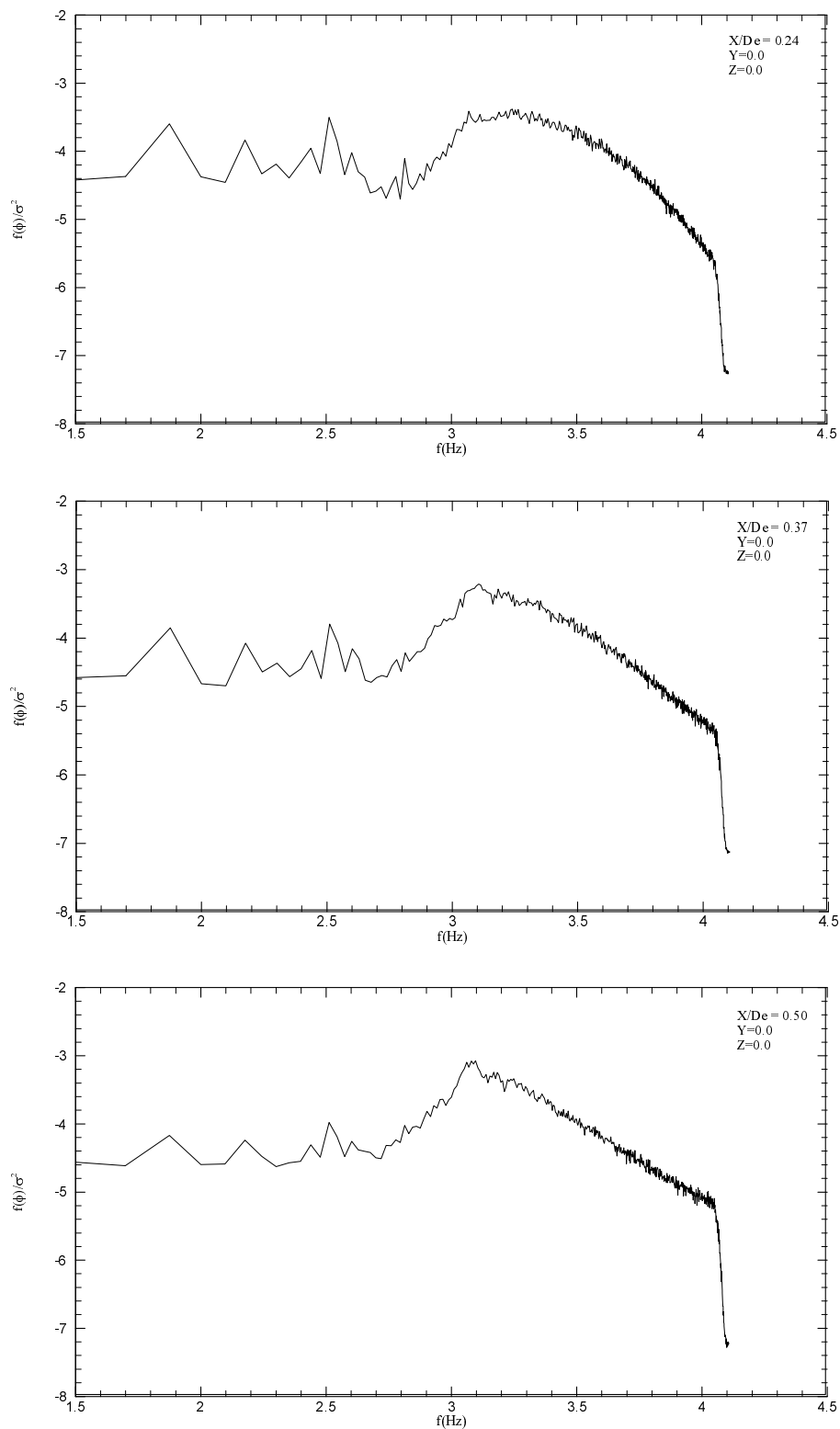


**Figure 3.39** One-dimensional energy spectra of the streamwise fluctuating velocity on the centreline of the  $160^\circ$  jet.

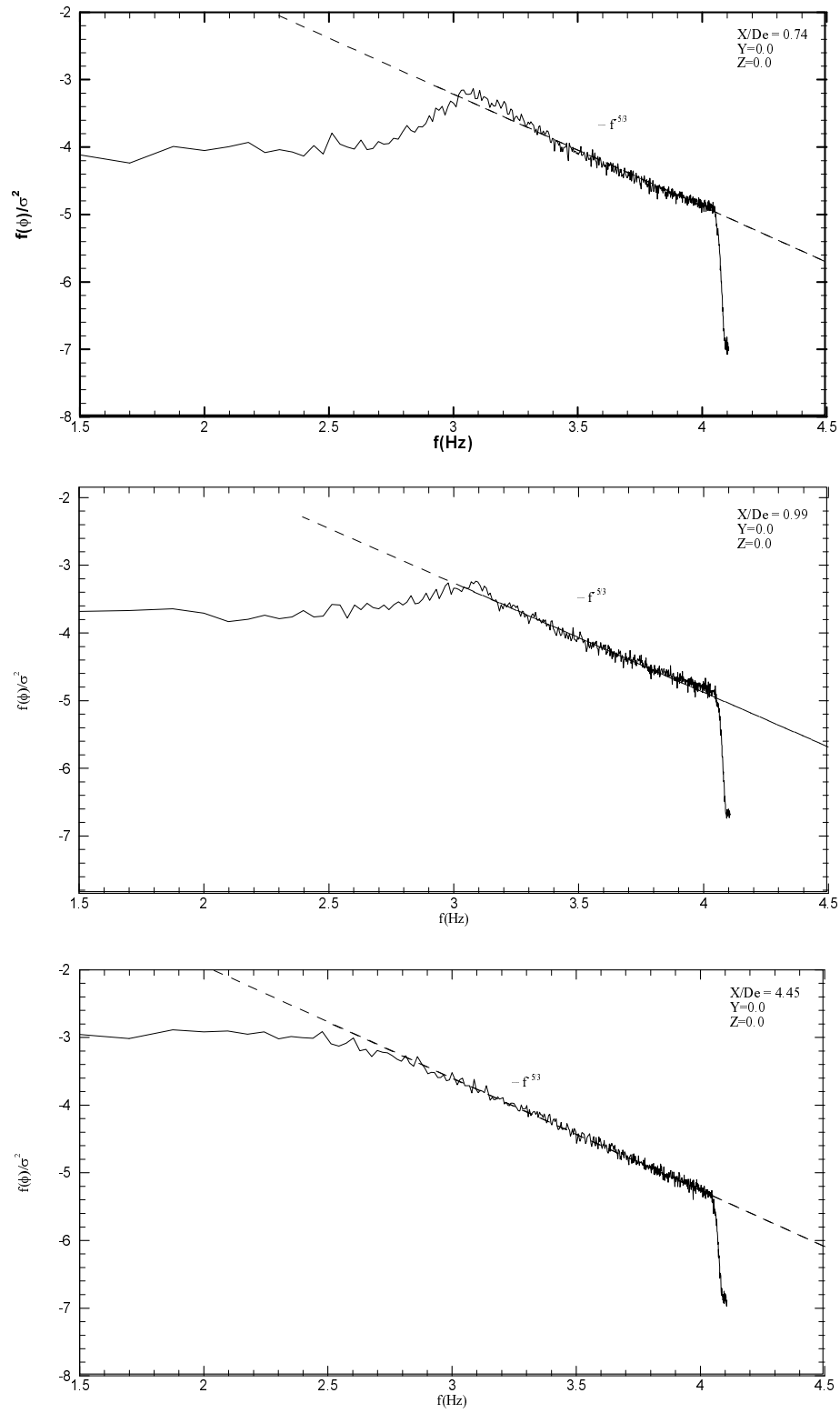


**Figure 3.40** One-dimensional energy spectra of the streamwise fluctuating velocity on the centreline of the  $160^\circ$  jet (continued).

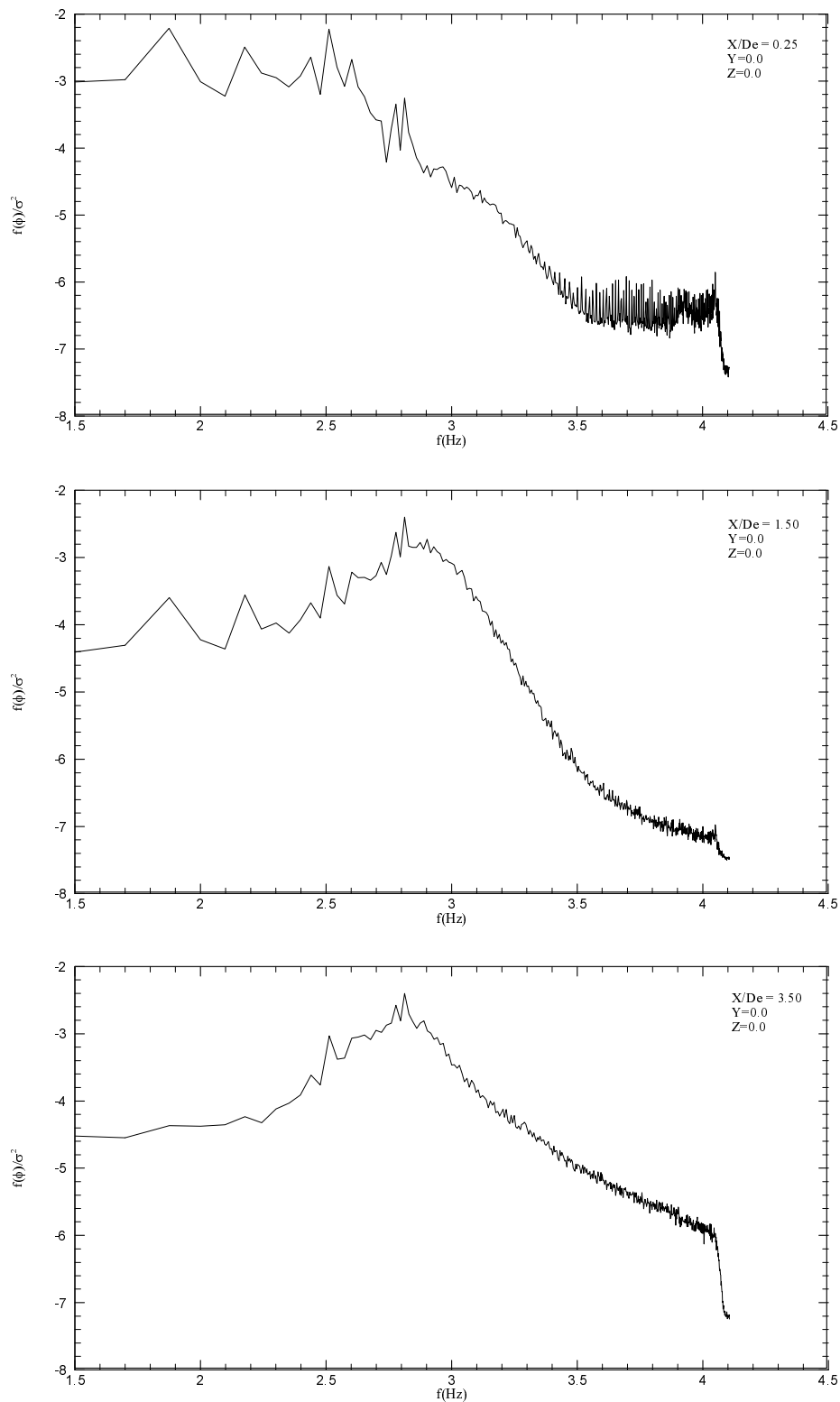


**Figure 3.41** One-dimensional energy spectra of the streamwise fluctuating velocity on the centreline of the sharp-edged orifice round jet.

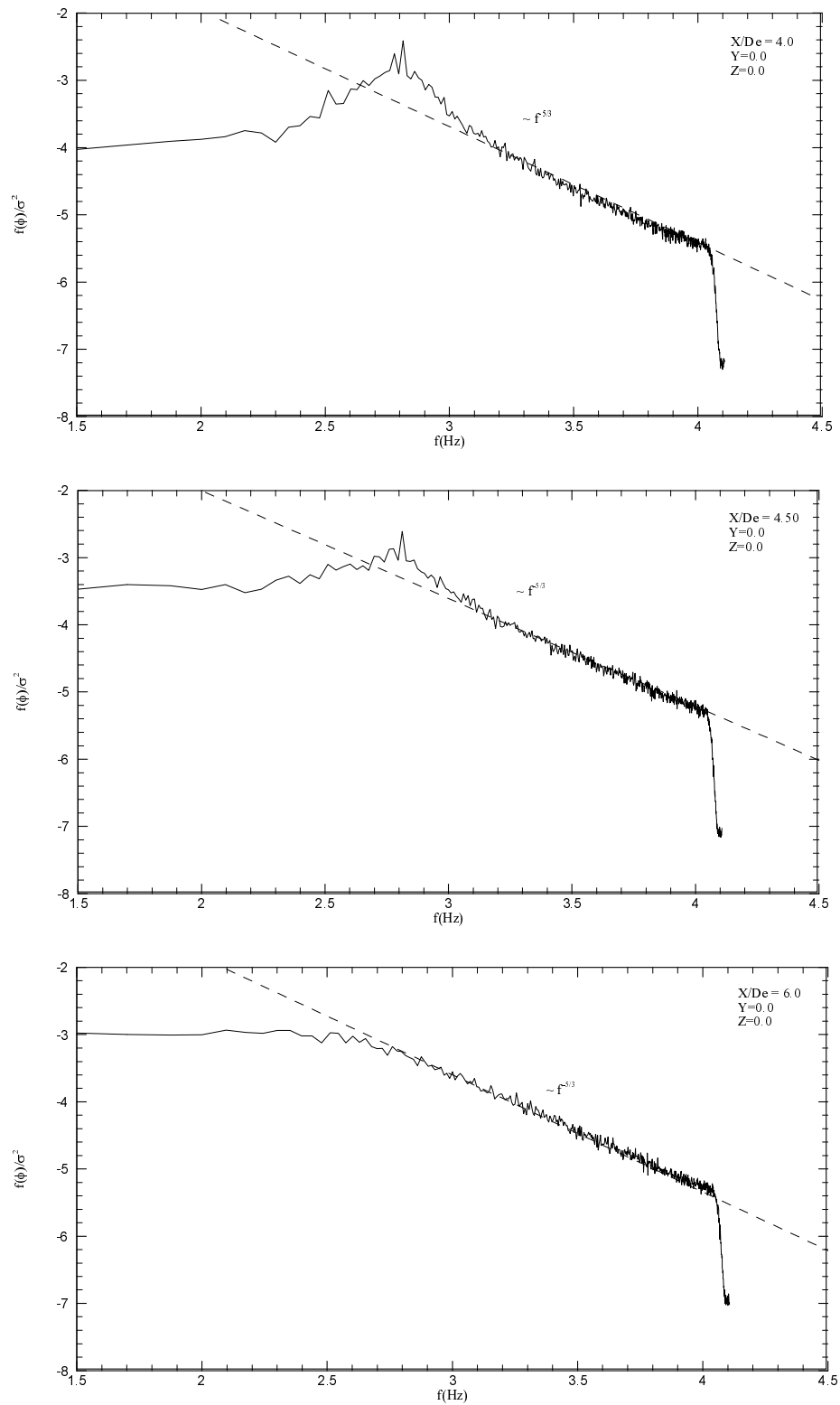


**Figure 3.42** One-dimensional energy spectra of the streamwise fluctuating velocity on the centerline of the sharp-edged orifice round jet (continued).

### 3.10 Distribution of autocorrelation coefficients of the streamwise fluctuating velocity on the jet centreline

The autocorrelation coefficient of the streamwise fluctuating velocity ( $u'$ ) is given by:

$$\rho_u(\tau) = \frac{\overline{u'(t)u'(t+\tau)}}{u'^2(t)} \quad (3.4)$$

The distribution of the autocorrelation coefficients of the streamwise fluctuating velocity at different streamwise locations on the centreline of the triangular jets is shown in Figures 3.43, 3.44, 3.45, 3.46, 3.47, 3.48, 3.49, 3.50, 3.51 and 3.52, and that in the sharp-edged orifice round jet is shown in Figures 3.53 and 3.54, for comparison. In all the jets, the distribution of the autocorrelation coefficients is periodic in the near field and becomes nonperiodic in the far field.

The distribution of the autocorrelation coefficients in the 10° and 160° jets, which have close to uniform exit mean streamwise velocity profiles (Figures 3.1 and 3.2), exhibits long tails and in the other jets, with less uniform initial velocity profiles, the distributions are more periodic.

As the jets evolve downstream, the periodicity in the distribution of the autocorrelation coefficients decreases and, at some point, the distribution becomes nonperiodic. The farthest downstream locations at which periodicity in the distribution of the autocorrelation coefficients is observed are  $X/D_e = 1.06, 1.71, 2.85$  and  $4.50$  in the 20°, 30°, 70° and sharp-edged orifice round jet, respectively.

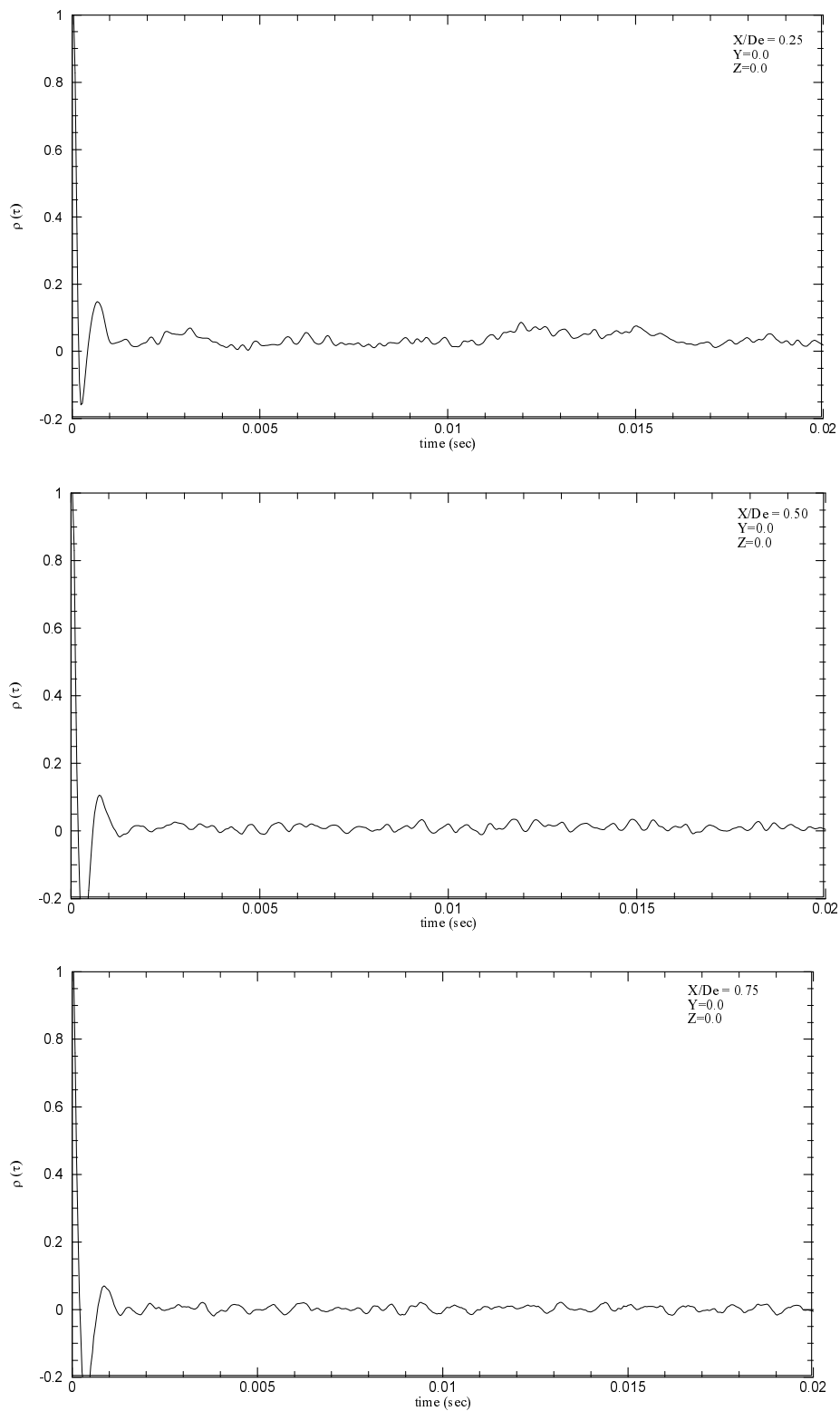


**Figure 3.43** Autocorrelation distribution of the streamwise fluctuating velocity on the centreline of the  $10^\circ$  jet.

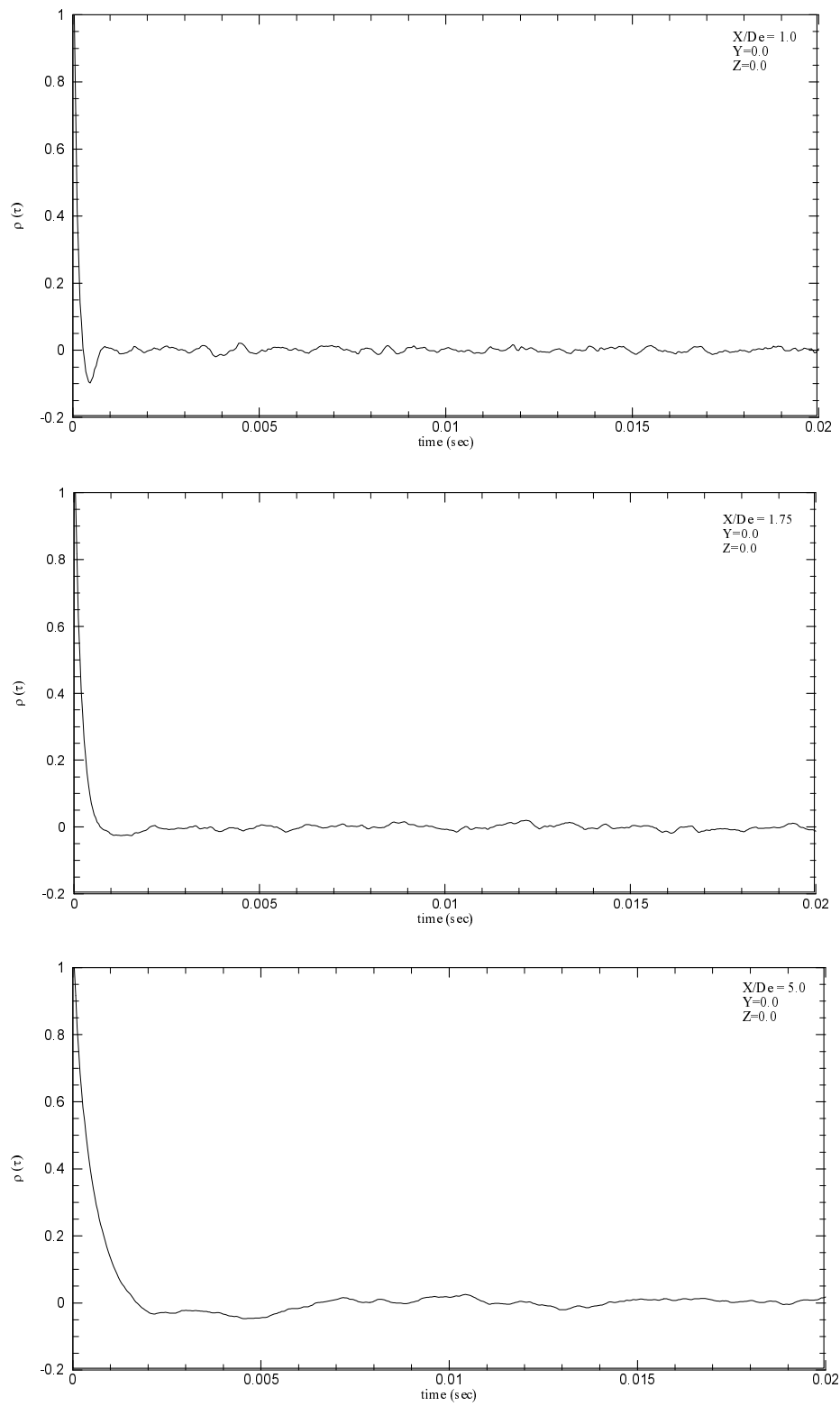


**Figure 3.44** Autocorrelation distribution of the streamwise fluctuating velocity on the centreline of the  $10^\circ$  jet (continued).

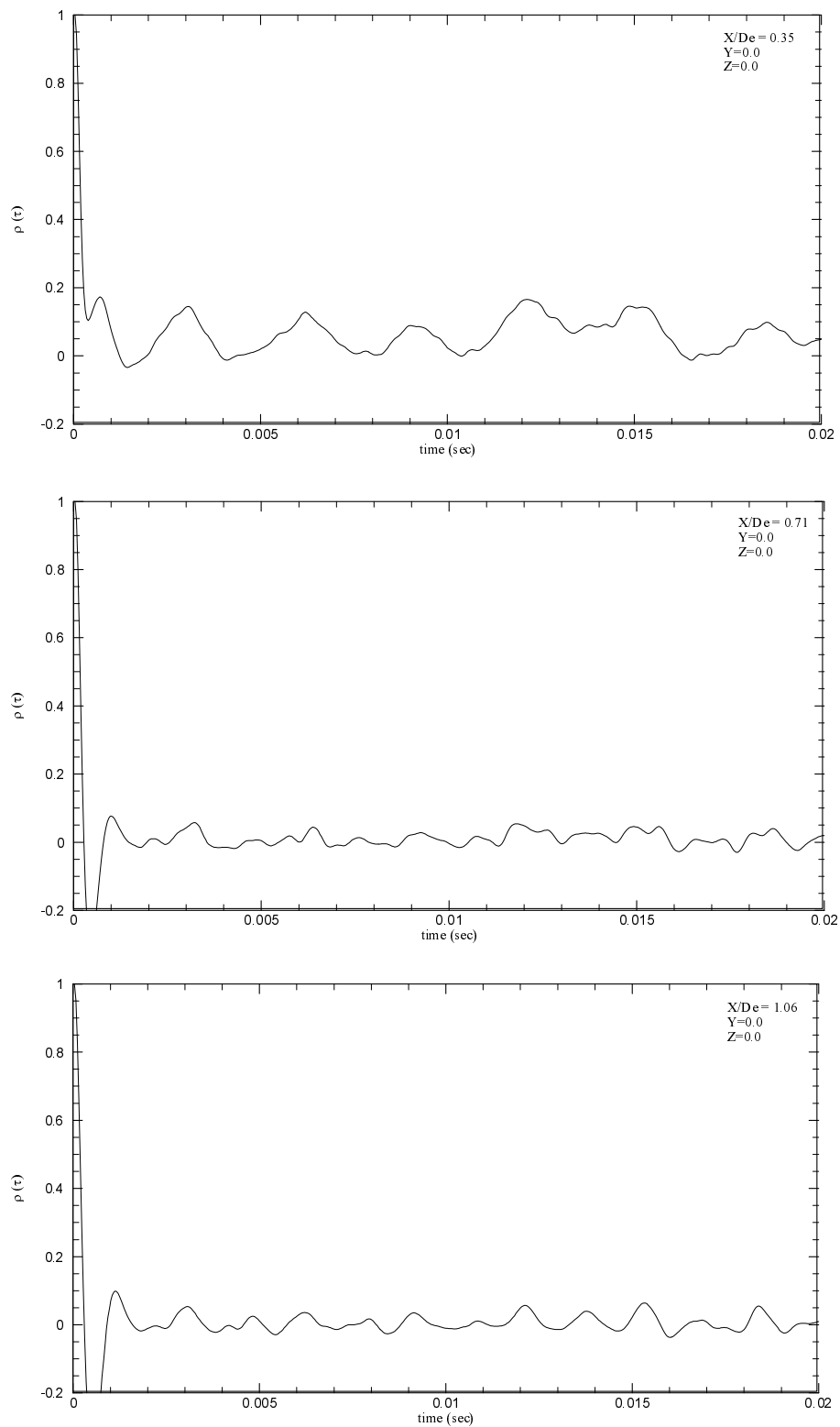


**Figure 3.45** Autocorrelation distribution of the streamwise fluctuating velocity on the centreline of the  $20^\circ$  jet.

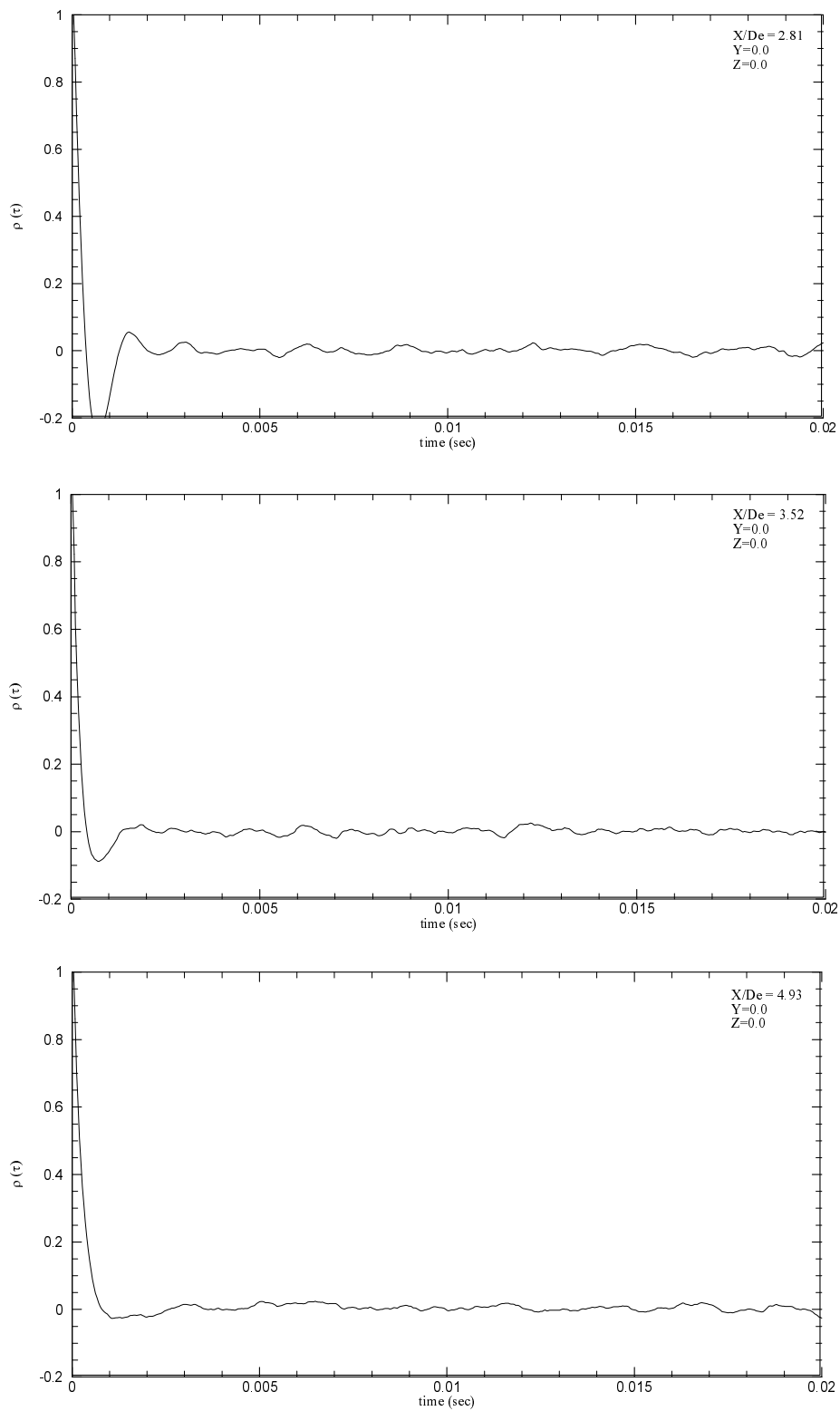


**Figure 3.46** Autocorrelation distribution of the streamwise fluctuating velocity on the centerline of the  $20^\circ$  jet (continued).

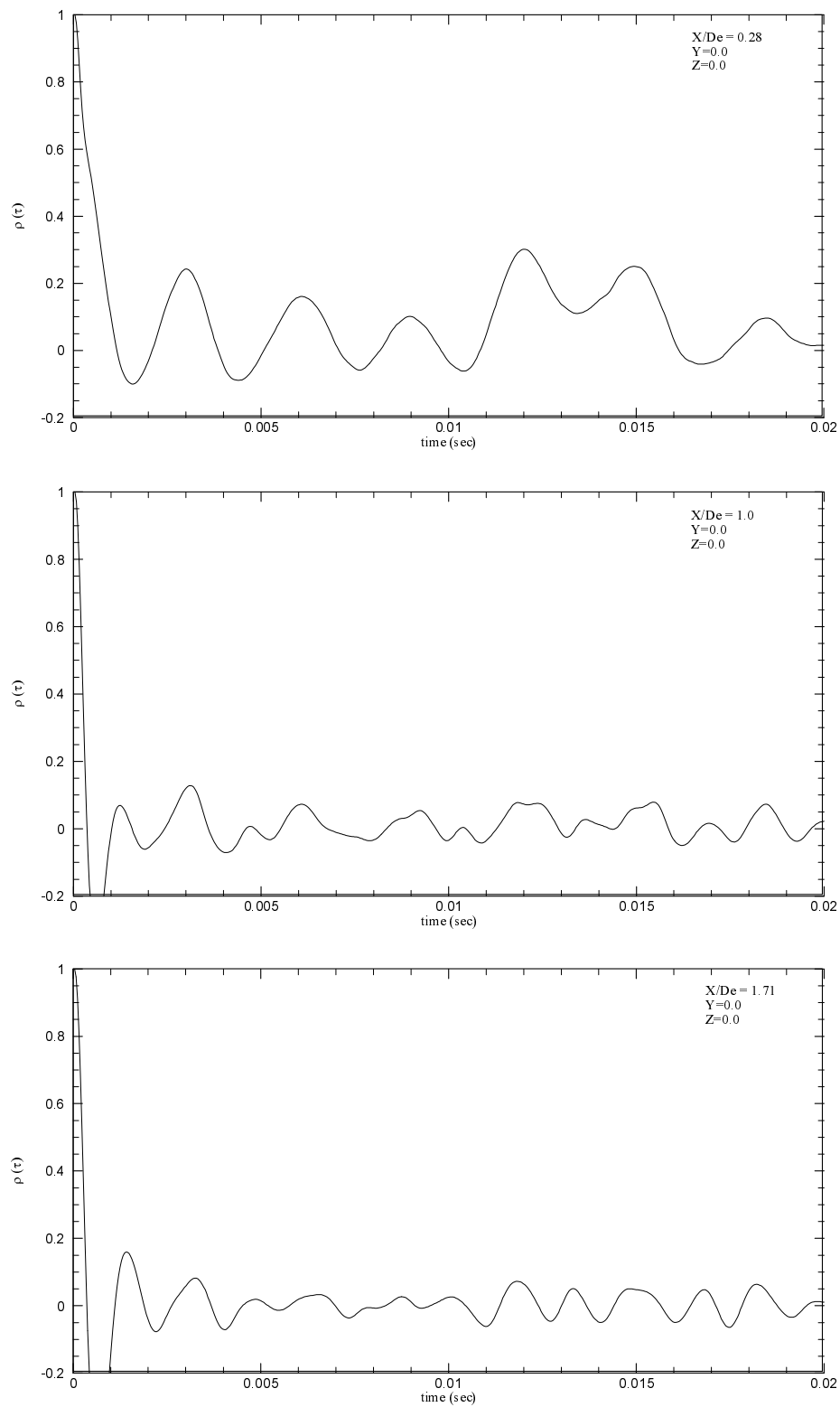


**Figure 3.47** Autocorrelation distribution of the streamwise fluctuating velocity on the centreline of the 30° jet.

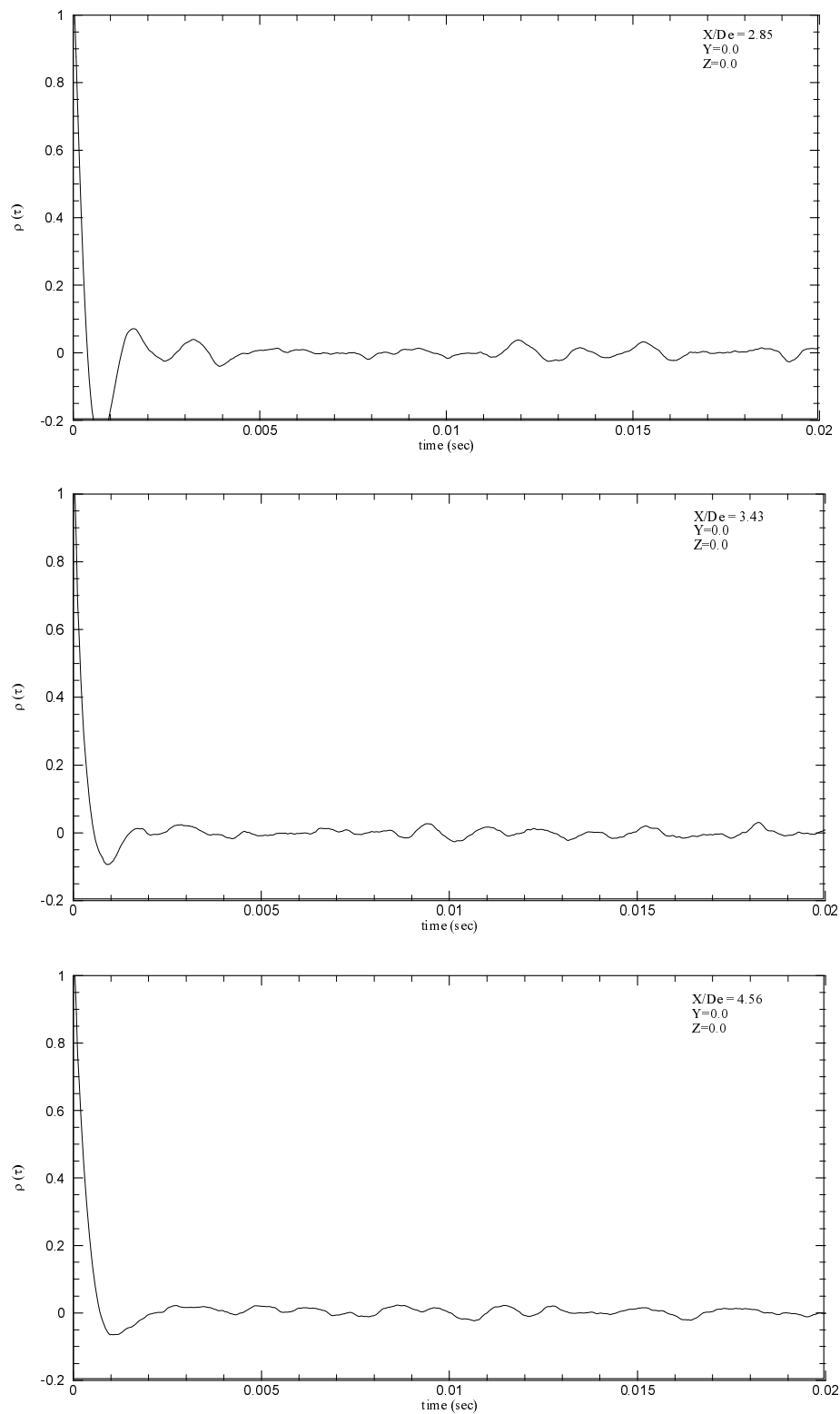


**Figure 3.48** Autocorrelation distribution of the streamwise fluctuating velocity on the centerline of the  $30^\circ$  jet (continued).

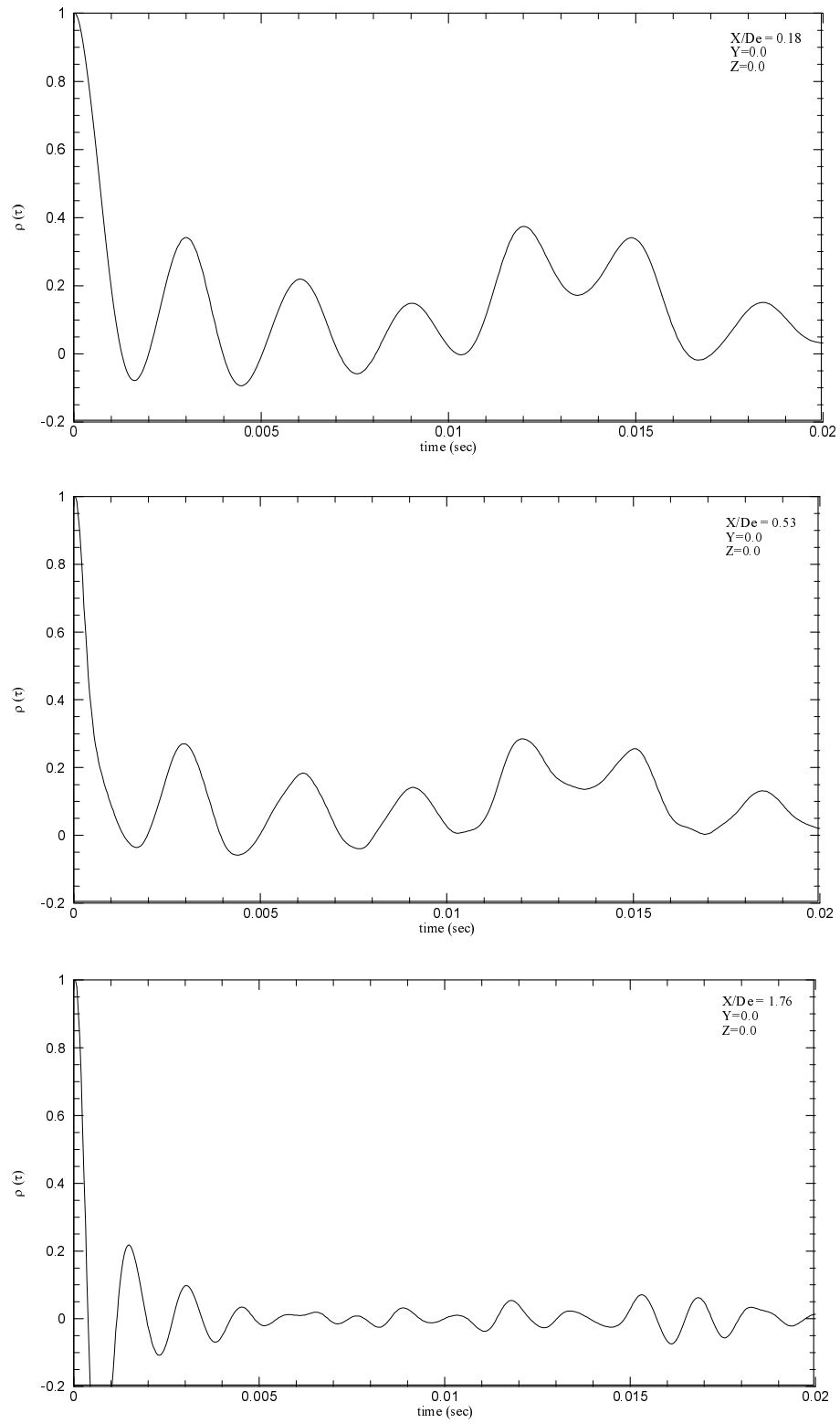


**Figure 3.49** Autocorrelation distribution of the streamwise fluctuating velocity on the centreline of the  $70^\circ$  jet.

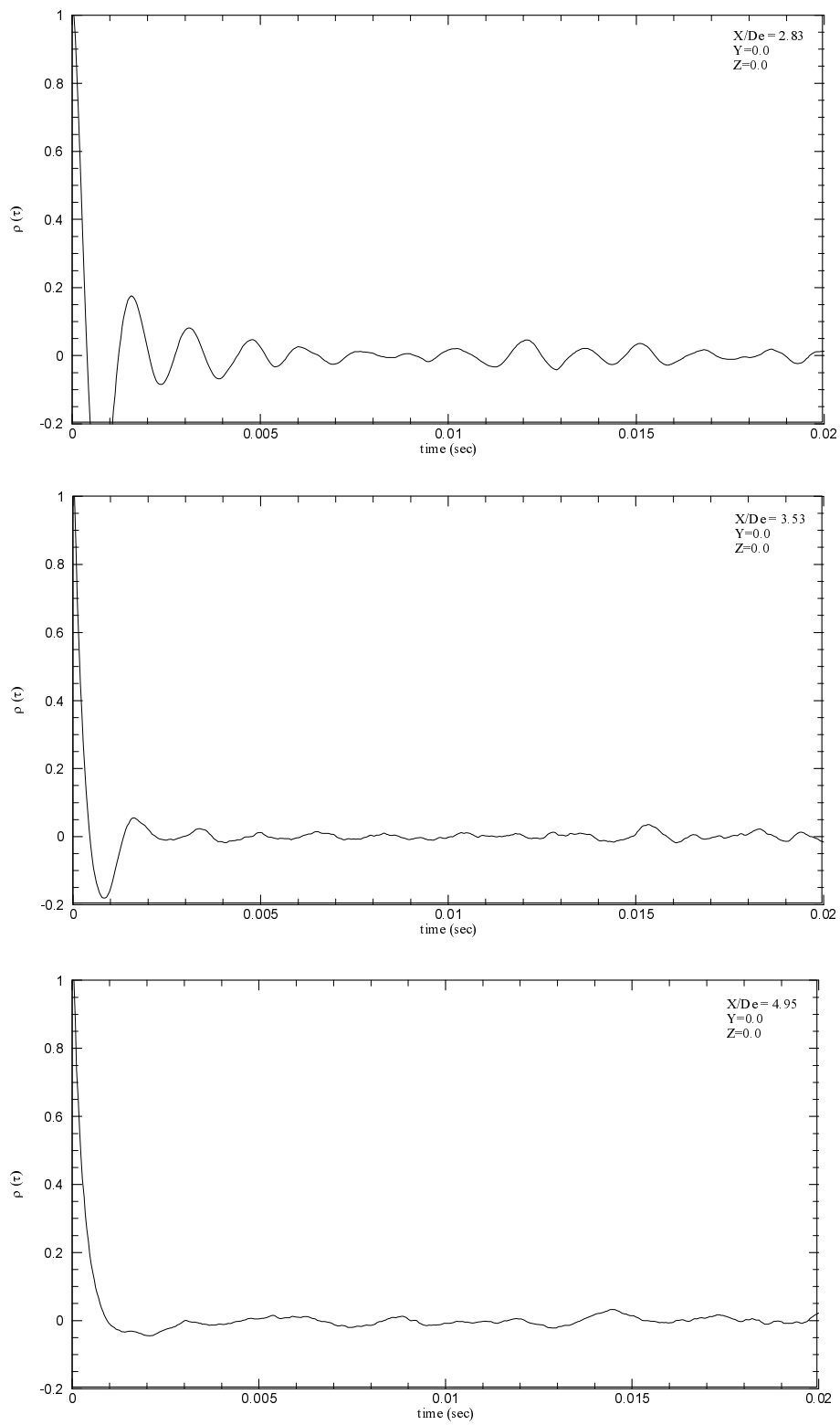


**Figure 3.50** Autocorrelation distribution of the streamwise fluctuating velocity on the centreline of the 70° jet (continued).

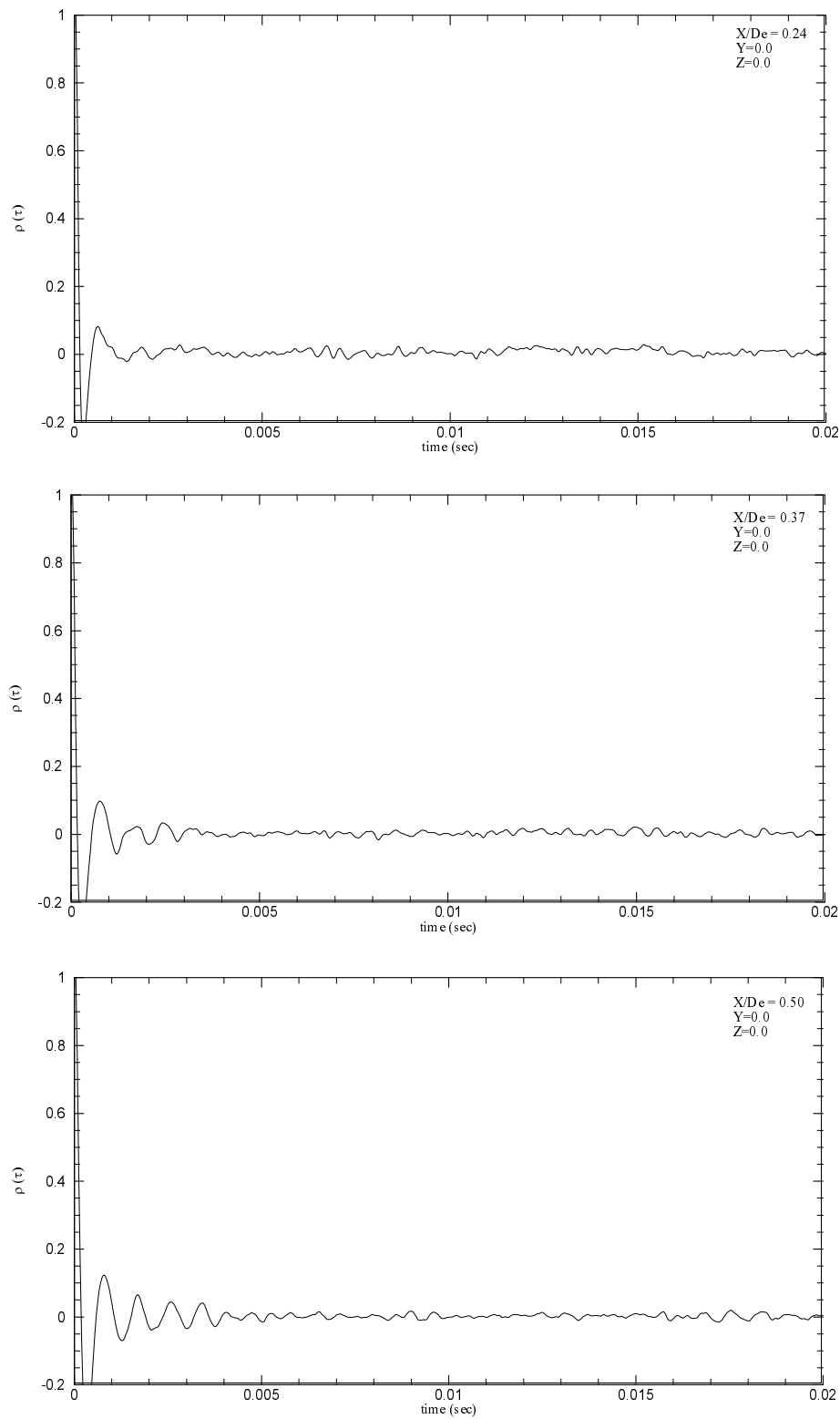


**Figure 3.51** Autocorrelation distribution of the streamwise fluctuating velocity on the centerline of the 160° jet.

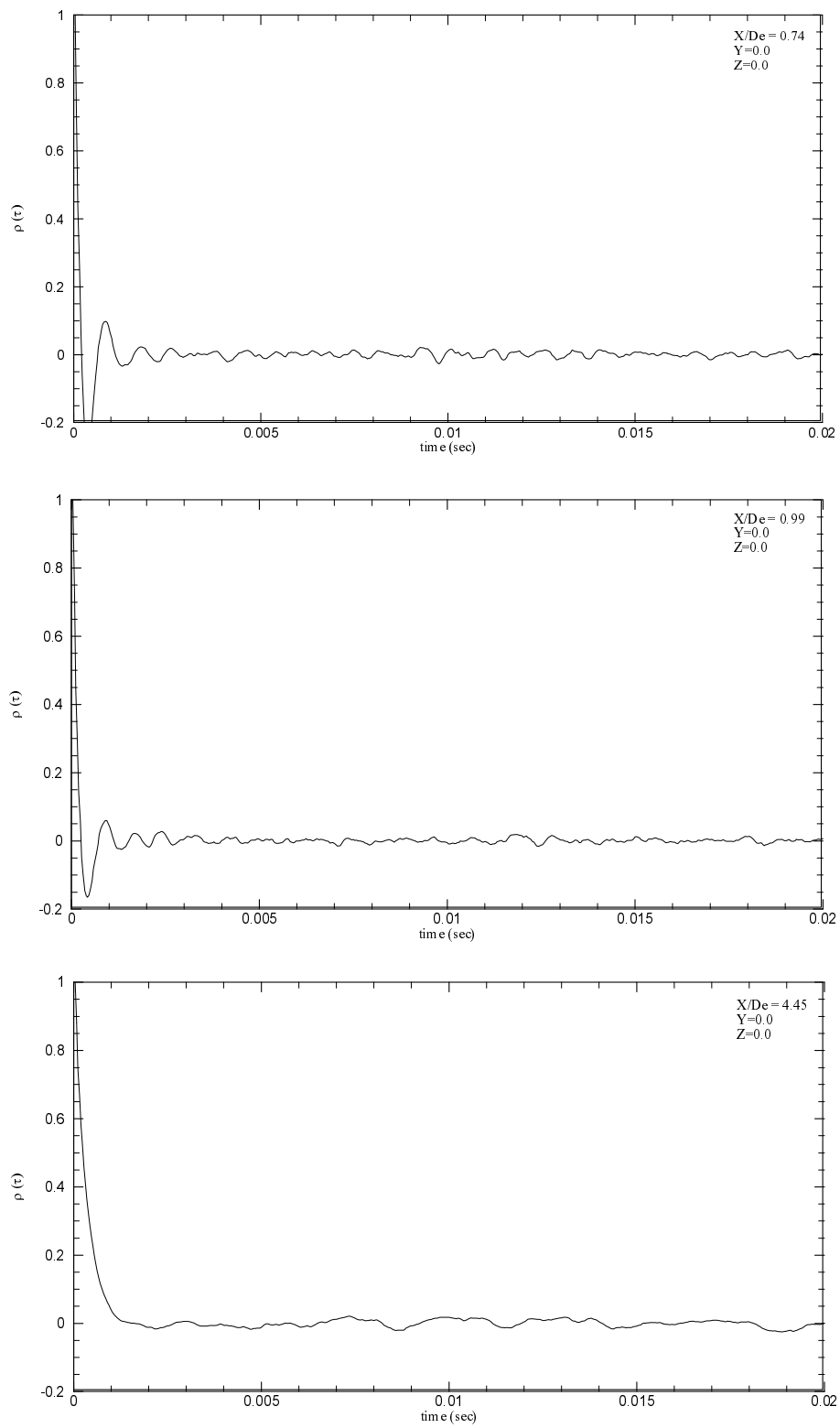


**Figure 3.52** Autocorrelation distribution of the streamwise fluctuating velocity on the centerline of the  $160^\circ$  jet (continued).

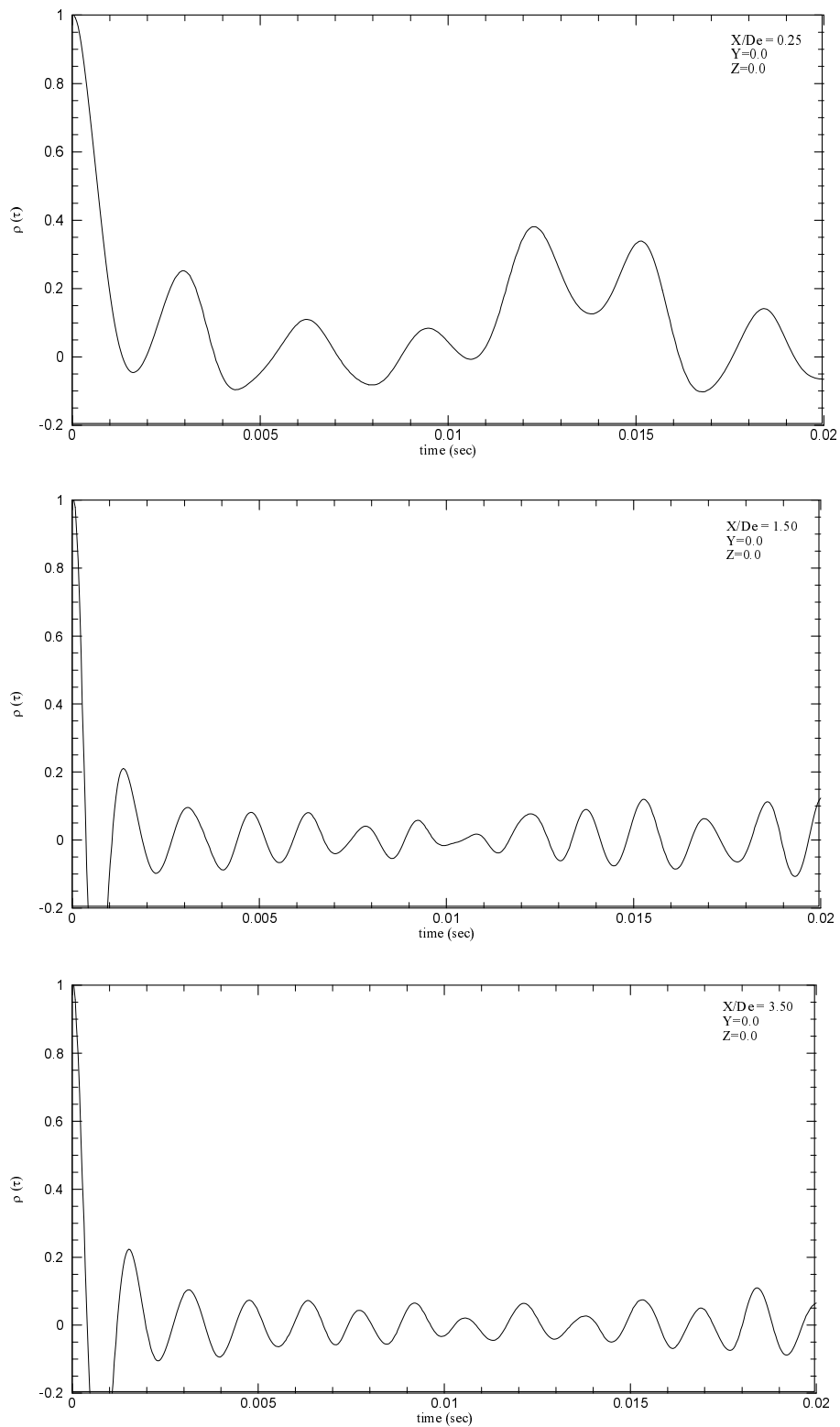


**Figure 3.53** Autocorrelation distribution of the streamwise fluctuating velocity on the centerline of the sharp-edged orifice round jet.

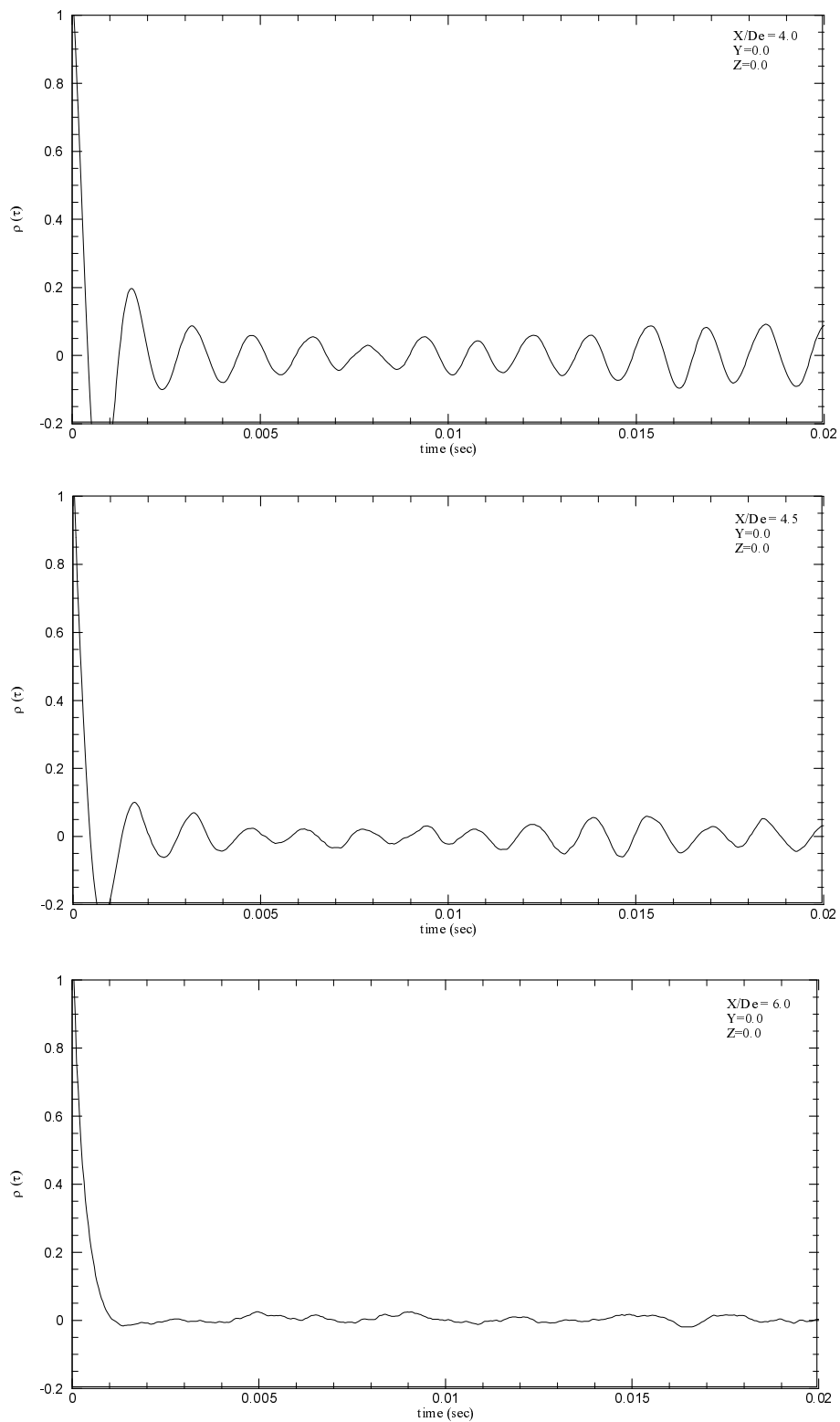


**Figure 3.54** Autocorrelation distribution of the streamwise fluctuating velocity on the centerline of the sharp-edged orifice round jet (continued).

# CHAPTER 4

## Discussion

### 4.1 Mean streamwise centreline velocity decay

Throughout the flow field investigated, except in the very near field ( $X/D_e \leq 5$ ), all the triangular jets have higher mean streamwise centreline velocity decay rates than both round jets, as has been mentioned in chapter 3. This finding is in agreement with those of other researchers (Quinn 2005a, Mi and Nathan 2010). In the near field, the  $160^\circ$  jet, which originates from the orifice with the longest perimeter, has the highest mean streamwise centreline velocity decay rate. Overall, the mean streamwise centreline velocity decay rate in the near field increases with the orifice perimeter. But, as mentioned in chapter 3, the  $70^\circ$  jet has a higher mean streamwise centreline velocity decay rate than the  $20^\circ$  and  $30^\circ$  jets in the region  $5.5 \leq X/D_e \leq 9$ . This is inconsistent with the general trend of increase in the mean streamwise centreline velocity decay rate with increase in the perimeter of the orifice, as mentioned previously. This discrepancy needs to be discussed. In non-circular jets with corners, such as rectangular and triangular jets, the shear layers emanating from the flat sides of the orifice do not reach the jet centreline at the same location. The first set of shear layers to reach the jet centreline does so at the end of the jet potential core and the second set of shear layers arrives on the jet centreline at the end of the developing flow region. For example, in rectangular jets, the shear layers from the longer flat sides, which are closer to the jet centreline, merge on the centreline at the end of the potential core and those from the shorter flat sides, which are

wider spaced, reach the jet centreline at the location where the flow becomes fully-developed. There are three shear layers (two from the inclined flat sides and one from the base flat side) in triangular jets.

The geometry of the shear layers in the  $70^\circ$  and  $20^\circ$  jets is shown in scaled drawings in Figures 4.1 and 4.2. The spreading rates obtained from linear fits of the far field data (see Table 4.2) have been used to calculate the merging locations on the jet centreline given in Figures 4.1 and 4.2. The potential core length of the  $20^\circ$  jet (and also for the  $30^\circ$  jet which is not shown in Figures 4.1 and 4.2) is shorter than that of the  $70^\circ$  jet. On the other hand, the flow development region of the  $70^\circ$  jet is shorter than that of the  $20^\circ$  jet and this difference in the length of the flow development region accounts for the observed higher mean streamwise centreline velocity decay rate of the  $70^\circ$  jet compared to the  $20^\circ$  and  $30^\circ$  jets in the region  $5.5 \leq X/D_e \leq 9$ .

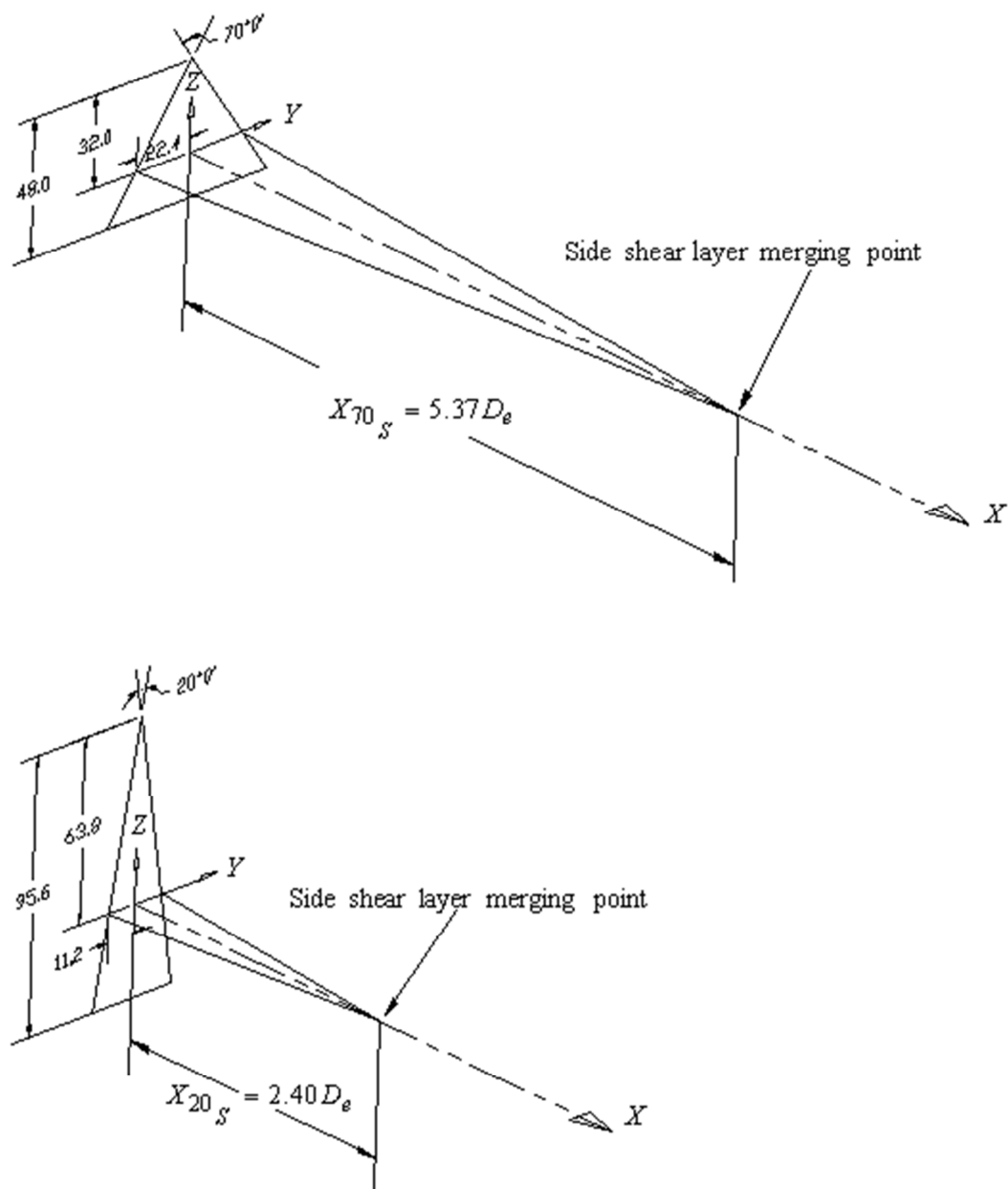


**Figure 4.1** Side shear layer development in the 70° and 20° triangular jets.

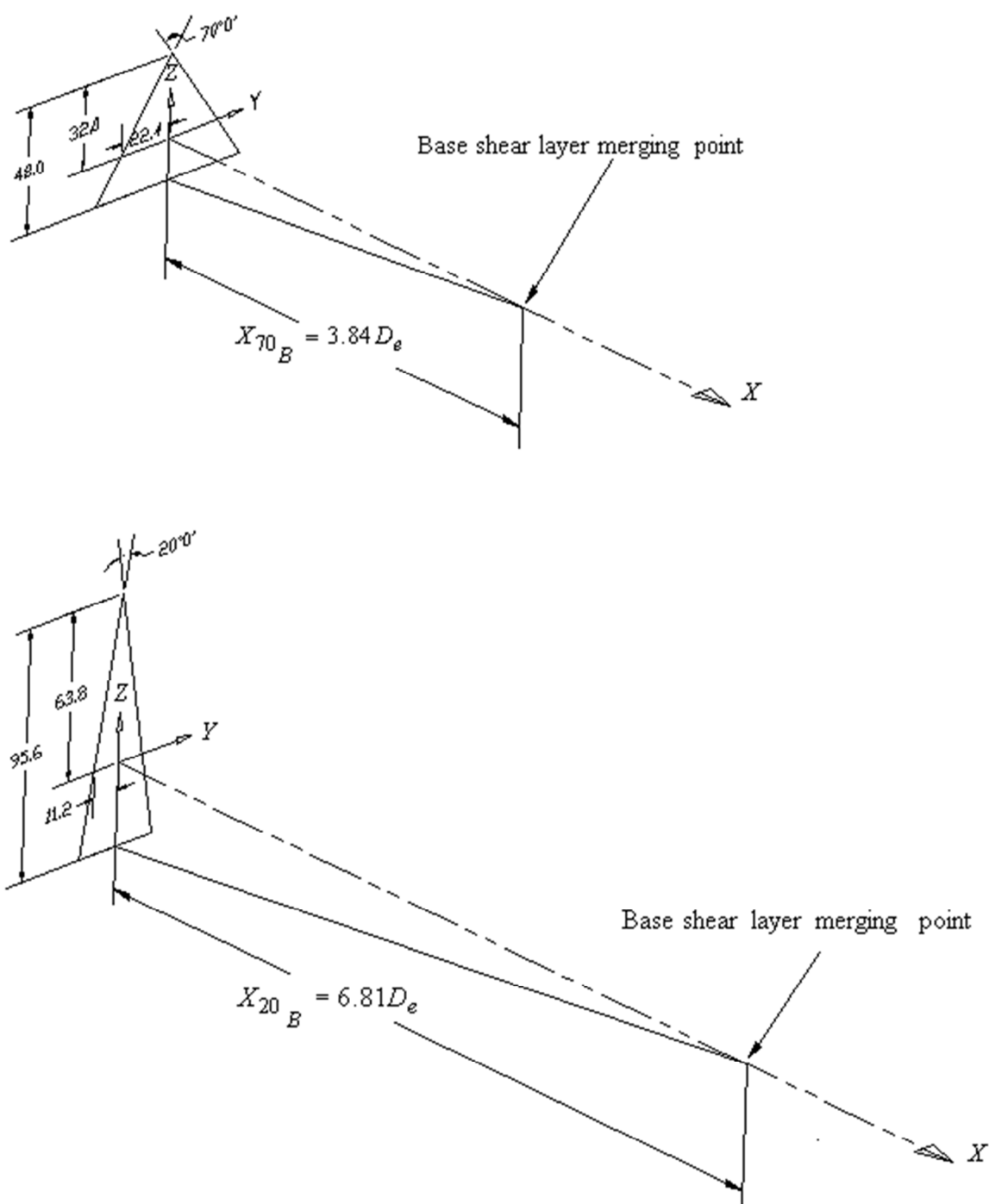


**Figure 4.2** Base shear layer development in the 70° and 20° triangular jets.

The sharp-edged orifice round jet has a lower mean streamwise centreline velocity decay rate than the contoured nozzle round jet in the near field.  $U_{cl}$  increases close to the orifice exit plane in all jets issuing from the sharp-edged orifices, due to the vena contracta effect. The increase in  $U_{cl}$  is highest in the sharp-edged orifice round jet. Close to the exit plane of the contoured nozzle round jet, however,  $U_{cl}$  remains constant.

The potential core lengths of the  $10^\circ$ ,  $20^\circ$ ,  $30^\circ$ ,  $70^\circ$  and  $160^\circ$  jets are  $1.14 D_e$ ,  $3.15 D_e$ ,  $3.11 D_e$ ,  $3.13 D_e$  and  $0.59 D_e$ , respectively. Those for the round jets issuing from the sharp-edged orifice and contoured nozzle are  $4.14 D_e$  and  $4.56 D_e$ , respectively (see appendix C for the potential core lengths and mean streamwise centreline velocity decay data). The potential core lengths of the  $70^\circ$  and  $20^\circ$  jets given here are different from those in Figures 4.1 and 4.2. This is not surprising since the latter values are obtained from purely geometrical considerations and by extrapolating the far field spreading rate to the orifice exit plane while the former values are obtained from velocity measurements. In the extant literature, there are a few results on the mean streamwise centreline velocity decay in isosceles triangular jets (Quinn 2005a, Mi and Nathan 2010). Quinn (2005a) reported the potential core length of his  $30^\circ$  isosceles triangular jet as  $3.14D_e$ , which is very close to that of the present  $30^\circ$  jet. Mi and Nathan (2010) reported the potential core length of their triangular jet issuing from an isosceles triangular orifice with apex angle of  $23^\circ$ , approximately, as  $1.1D_e$ , which is shorter compared to the present jets. This difference likely stems from the difference in the initial conditions, mainly in the flow Reynolds number ( $1.5 \times 10^4$  for Mi and Nathan (2010) and  $1.93 \times 10^5$  for the present jets) and the fact that the corners of the triangular orifices used in the present study were sharp and those in the triangular orifices used by Mi and Nathan (2010) had a

small radius. Compared to triangular jets, there are more results in the extant literature for round jets. The potential core length of the sharp-edged orifice round jet is in the range:  $3.50D_e$  to  $4.20D_e$  and that for the contoured nozzle round jet varies from  $4.26D_e$  to  $5.60D_e$  (Xu and Antonia 2002, Quinn 2006, Mi and Nathan 2010). The potential core lengths of both round jets of the present study fall within the aforementioned ranges. The data indicate that the  $160^\circ$  jet has the shortest potential core length, a finding which is consistent with the fact that this jet has the highest mean streamwise centreline velocity decay rate in the near field. It is also evident from the data that, as the orifice perimeter increases, the potential core length decreases (except for the  $20^\circ$  jet), a trend which is in agreement with the mean streamwise centreline velocity decay rates in the near field. The fact that the  $160^\circ$  jet has the shortest potential core length can be explained by referring to Figure 4.2 and recognizing that the base shear layer in this jet reaches the jet centreline faster than the shear layers in all the other triangular jets.

The data for the mean streamwise centreline velocity decay in the far field of all the test jets have been fitted (see appendix D) by linear regression to:

$$U_{bulk}/U_{cl} = K_u(X/D_e + C_u) \quad (4.1)$$

The mean streamwise centreline velocity decay rates and kinematic virtual origins are shown in Table 4.1.

**Table 4.1** Mean streamwise centreline velocity decay rates and kinematic virtual origins

Jet type	$K_u$	$C_u$	Fitted range
10° triangular	0.182	1.154	$13.98 \leq X/D_e \leq 59.92$
20° triangular	0.173	0.431	$14.08 \leq X/D_e \leq 59.84$
30° triangular	0.165	1.100	$13.70 \leq X/D_e \leq 57.08$
70° triangular	0.165	-0.094	$14.13 \leq X/D_e \leq 60.02$
160° triangular	0.180	2.625	$13.60 \leq X/D_e \leq 59.33$
Sharp-edged orifice round	0.157	-1.298	$13.75 \leq X/D_e \leq 60.00$
Contoured nozzle round	0.155	-1.979	$13.75 \leq X/D_e \leq 57.50$

According to Table 4.1, all the triangular jets have higher mean streamwise centreline velocity decay rates than the round jets and the 10° jet has the highest mean streamwise centreline velocity decay rate among all the test jets. The sharp-edged orifice round jet has a higher mean streamwise centreline velocity decay rate than the contoured nozzle round jet, although the difference is slight. The fact that the mean streamwise centreline velocity decay rate of the sharp-edged orifice round jet is higher than that of the contoured nozzle round jet is well known (Mi et al. 2001, Quinn 2006). Mi and Nathan (2010) reported the mean streamwise centreline velocity decay rates for their sharp-edged orifice round and contoured nozzle round jets as 0.156 and 0.158, respectively. These values are very close to the corresponding values of the present round jets. Quinn (2006) reported the mean streamwise centreline velocity decay rates as 0.167 and 0.164 for the sharp-edged orifice and contoured nozzle round jets, respectively. These values are higher than those of the present study. This difference is likely a result

of the fact that different instruments, and the concomitant measurement uncertainties, were used to measure  $U_{cl}$ , namely, Quinn (2006) used a pitot-static tube whereas hot-wire anemometry was used in the present experiments. Pitot-tube measurements in the present contoured nozzle round jet gave a mean streamwise centreline velocity decay rate of 0.165. There are few results in the literature for the mean streamwise centreline velocity decay in isosceles triangular jets. Quinn (2005a) reported a mean streamwise centreline velocity decay rate of 0.207 for his 30° triangular jet, a value which is higher than that of the present 30° jet. Quinn (2005a) used  $U_{max}$  to normalize the mean streamwise centreline velocity while  $U_{bulk}$  was used in the present study. Mi and Nathan (2010) have shown that the use of  $U_{max}$  instead of  $U_{bulk}$  to normalize the mean streamwise centreline velocity may lead to an overestimation of the mean streamwise centreline velocity decay rate by as high as 33% in the jets issuing from sharp-edged orifices.

Non-unity aspect ratio, sharp corners and long flat sides are important factors that govern mixing in jets (Miller et al 1995). The triangular orifice with the apex angle of 160° has the longest flat side, the sharpest base corners and the highest aspect ratio among all the orifices. Although this jet has the highest mean streamwise centreline velocity decay rate in the near field, the 10° jet has the highest mean streamwise centreline velocity decay rate in the far field. The reader is referred first to Figure 2.3(e) and then to Figures 4.1 and 4.2 in preparation for a discussion of the difference between the near-field and far-field decay rates of the mean streamwise centreline velocity in the 160° jet. It has already been stated that the base shear layer of this jet reaches the centreline earlier than the shear layers in any of the triangular jets and the jet consequently has the shortest potential core length and the highest near-field mean

streamwise centreline velocity decay rate. The side shear layers of the  $160^\circ$  jet, on the other hand, merge on the centreline later than the shear layers in any of the triangular jets tested and this leads to a longer flow development region and a lower mean streamwise centreline velocity decay rate in the far field of this jet.

The kinematic virtual origins are located upstream of the orifice exit plane in all the jets except in the  $70^\circ$  and in both round jets and it is at the farthest upstream location in the  $160^\circ$  jet. Note that the mean streamwise centreline velocity decay rates of the  $30^\circ$  and  $70^\circ$  jets are essentially the same (see Table 4.1), but the kinematic virtual origin of the  $30^\circ$  jet is located upstream of that of the  $70^\circ$  jet.

It is evident from Figure 3.7 that all the jets have three distinct mean streamwise centreline velocity decay regions. The first is the potential core region in which  $U_{cl}$  is constant. The potential core region is followed by a transition region, which is non-linear. Both round jets have a very short transition region, but this region is clearly present in all the other jets tested. In the third region, the velocity decays linearly with streamwise distance in all of the test jets.

## **4.2 Development of the jet half-velocity widths**

The development of the normalized half-velocity widths in the  $10^\circ$ ,  $20^\circ$ ,  $30^\circ$  and  $70^\circ$  jets was shown in Figure 3.8 and that for the  $160^\circ$  and round jets was shown in Figure 3.9. In all the triangular jets, the normalized half-velocity widths in the central  $X$ - $Y$  and  $X$ - $Z$  planes vary at different rates, which indicates that all the triangular jets continually change shape in the flow region investigated.

The horizontal ( $Y$ ) axis through the centroid of the cross-sectional area of the orifice and the vertical ( $Z$ ) axis, also through the centroid, are defined, in what follows, as the minor and major axis, respectively in the  $10^\circ$ ,  $20^\circ$ ,  $30^\circ$  and  $70^\circ$  jets. This nomenclature is reversed, for convenience, in the  $160^\circ$  jet.

Initially, triggered by the large-scale structures generated at the flat sides, all the triangular jets spread faster along the minor axis and shrink along the major axis, except for the  $70^\circ$  jet. These results are in agreement with those of the isosceles triangular jet of Quinn (2005a), the square jet of Grinstein et al (1995), the elliptic jets of Ho and Gutmark (1987) and Quinn (2007).

The contribution of Abramovich (1982) on the spreading of rectangular jets can be used to understand the difference in the spreading behaviour of all the other triangular jets of the present study on the one hand and the  $70^\circ$  and  $160^\circ$  triangular jets on the other hand. Abramovich (1982) proposed that rectangular vortex rings shed at the orifice will have a non-uniform pressure distribution in the shear layers due to the large-scale structures. This non-uniform pressure distribution consists of higher pressure on the shorter sides of the vortex rings, which are wider spaced, and lower pressure on the longer sides of the vortex rings, which are closer spaced. The resulting pressure imbalance induces flow from the shorter to the longer sides of the vortex rings and thus leads to growth (i.e., spreading) along the minor axes and shrinkage, for mass conservation reasons, along the major axes of the vortex rings. This model of the spreading behaviour of rectangular jets is supported by many experimental results in the extant literature, starting with the pioneering work of Sforza et al. (1966).

Figure 2.3 shows that each of the inclined sides of all the triangular orifices, except the  $70^\circ$  and  $160^\circ$  orifices, is closer to the centroid of the cross-sectional area, than the base side. Following Abramovich (1982) then, the pressure on the base sides of the triangular vortex rings shed from the orifices will be higher than that on the inclined sides and this difference in pressure will lead to spreading in the direction of the minor axes and to shrinkage in the direction of the major axes of the vortex rings, just as in the rectangular jets, described previously. In the  $70^\circ$  and  $160^\circ$  orifices, however, each inclined side is further away from the centroid of orifice area than the base side and reverse spreading behaviour is observed, namely, spreading in the direction of the major axis and shrinkage in the direction of the minor axis of the shed vortex rings in the case of the  $70^\circ$  jet. The reader is reminded that major and minor axes are defined differently in the  $160^\circ$  jet. This then means spreading in the direction of the minor axis and shrinkage in the direction of the major axis of a vortex ring shed from the  $160^\circ$  orifice. The experimental results presented in Figures 3.12 to 3.21 support the model of spreading behaviour in triangular jets described here. In addition, in the study of Quinn (1990) it was found that spreading on the base side of a  $60^\circ$  jet is more than that on the inclined side. It bears mentioning that, like the  $70^\circ$  orifice, the inclined sides in a  $60^\circ$  triangular orifice are further away from the centroid of the cross-sectional area of the orifice, than the base side.

The development of  $Z_{1/2}/D_e$  and  $Y_{1/2}/D_e$  in the  $30^\circ$  jet is especially similar to that of Quinn (2005a). The location of the first cross-over in the half-velocity widths of the present  $30^\circ$  jet is exactly the same as it was in the  $30^\circ$  jet of Quinn (2005a), namely, at  $X/D_e = 3.0$ . However, while the second cross-over in the half-velocity widths takes

place at  $X/D_e = 24.0$  in the present jet, it was at  $X/D_e = 30.0$  in the jet of Quinn (2005a).

### 4.3 Geometric mean of the jet half-velocity widths

The development of  $B_{1/2}/D_e$  in the streamwise direction for all the jets was shown in Figure 3.10 for ease of comparison of the spreading rates of the jets. The far field jet spread data have been fitted (see appendix E) by linear regression to:

$$B_{1/2}/D_e = K_s(X/D_e + C_s) \quad (4.2)$$

The results are shown in Table 4.2.

**Table 4.2** Spreading rates and geometric virtual origins

Jet type	$K_s$	$C_s$	Fitted range
10° triangular	0.112	-1.349	$10 \leq X/D_e \leq 25$
20° triangular	0.103	-0.912	$10 \leq X/D_e \leq 25$
30° triangular	0.097	0.527	$10 \leq X/D_e \leq 25$
70° triangular	0.092	1.542	$10 \leq X/D_e \leq 25$
160° triangular	0.090	1.829	$10 \leq X/D_e \leq 25$
Sharp-edged orifice round	0.092	-1.050	$10 \leq X/D_e \leq 25$
Contoured nozzle round	0.090	-0.631	$10 \leq X/D_e \leq 25$

This table shows that the 10° jet has the highest spreading rate and that the 160° jet, which originates from the orifice with the longest perimeter, has the lowest spreading rate among all the triangular jets. In addition, the results shown in Table 4.2 lead the

conclusion that the spreading rate of the jets decreases as the orifice perimeter decreases, except for the  $160^\circ$  jet. It should be recalled that the mean streamwise centreline velocity decay rates of the jets, shown in table 4.1, also decrease as the perimeter of the orifice decreases, except again for the  $160^\circ$  jet. The  $160^\circ$  jet has a higher mean streamwise centreline velocity decay rate than the other jets, except for the  $10^\circ$  jet, as was mentioned earlier. In spite of having a higher mean streamwise centreline velocity decay rate, this jet has a lower spreading rate than the other triangular jets. The inconsistency between the mean streamwise centreline velocity decay rate and the spreading rate in the far field of the  $160^\circ$  jet requires an explanation, which has, in part, been presented previously in the discussion of the difference between the near-field and far-field mean streamwise centreline velocity decay rates of the  $160^\circ$  jet. The fact that this jet has the lowest spreading rate among the triangular jets tested is more than likely due to the longest flow development region found in the jet compared to the others. The long flow development region of the  $160^\circ$  jet may also cause the far-field mean streamwise centreline velocity decay rate of this jet to be lower than that of the  $10^\circ$  jet.

There is a paucity of spreading rate data in the extant literature for isosceles triangular jets. Quinn (2005a) presented spreading data for a  $30^\circ$  isosceles triangular jet. These data and the spreading rate data for the  $30^\circ$  jet of the present study are shown in Figure 4.3 to facilitate comparison.

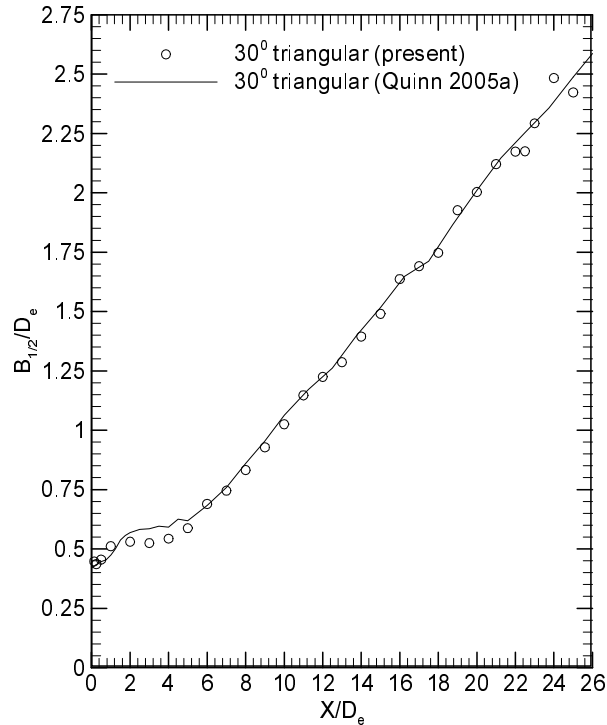


**Figure 4.3** Spreading of the 30° jets of the present study and of Quinn (2005a)

There is clearly good agreement between the two sets of data. It should be noted that, in the region  $10 \leq X/D_e \leq 25$ , the spreading rate of the jet of Quinn (2005a) is 0.096 and that of the present 30° jet is 0.097.

Compared to the triangular jets, there are more spreading rate results for round jets in the literature. The spreading rate data for a contoured nozzle round jet vary from 0.086 to 0.096 (Wyganski and Fiedler 1969, Panchapakesan and Lumley 1993, Quinn 2006) and those for a sharp-edged orifice round jet vary from 0.088 to 0.098 (Obot et al. 1984, Quinn and Militzer 1988, Quinn 2006, Quinn 2007). The spreading rates of the present round jets fall within the corresponding ranges.

The locations of the geometric virtual origins do not vary in any clearly defined manner. The geometric virtual origins of the 10° and 20° jets are located downstream of

the orifice exit plane while those for the other triangular jets are located upstream of the orifice exit plane. In both round jets, the geometric virtual origin is located downstream of the orifice or nozzle exit plane.

In the near field, the  $160^\circ$  jet spreads faster than any of the other jets. This faster spreading of the  $160^\circ$  jet and the fact that this jet has the highest near-field mean streamwise centreline velocity decay rate compared to the other jets, indicate that the  $160^\circ$  jet has the highest near-field mixing rate among the test jets. In the region  $5 \leq X/D_e \leq 10$ , the  $70^\circ$  jet has higher values of  $B_{1/2}/D_e$  than the other jets, except for the  $160^\circ$  jet, as has been mentioned in chapter 3. This result is consistent with the mean streamwise centreline velocity decay results, which were discussed in section 4.1.

#### 4.4 Mean streamwise velocity contour maps

It is evident from Figures 3.12-3.25 that the  $U/U_{cl}$  contours in all the jets have the shape of the corresponding orifice or nozzle, with a very large high velocity area close to the exit plane, at  $X/D_e = 0.14$  (at  $X/D_e = 0.07$  for the  $160^\circ$  jet), indicating that almost no mixing has taken place in the jets. Further downstream, the  $U/U_{cl}$  contours change shape (except for the sharp-edged orifice round jet) and the space between contour levels increases, indicating increased mixing in the jets. The  $U/U_{cl}$  contours of the sharp-edged orifice and contoured nozzle round jets at all the locations are comparable to those of Quinn (2006). At  $X/D_e = 1$ , the  $U/U_{cl}$  contours of the contoured nozzle round jet have a square shape, unlike those of the sharp-edged orifice round jet. It should be recalled that the contraction used in these experiments had a round shape at the upstream end and a square shape at the downstream end. Since there is flow separation both upstream and downstream of the exit plane in the orifice jets, the effect of the square end of the

contraction is not seen in those jets. On the other hand, there is no upstream separation in the flow of the contoured nozzle round jet. At the exit of the contoured nozzle, the  $U/U_{cl}$  contours are round. These contours become square after the exit and become round again further downstream. Only a few results of  $U/U_{cl}$  contours in triangular jets are available (Gutmark et al. 1989, Quinn 2005a). The  $U/U_{cl}$  contours of the present  $30^\circ$  jet agree very well with those of Quinn (2005a) at the corresponding locations. In the present study, the  $U/U_{cl}$  contours of the  $10^\circ$ ,  $20^\circ$  and  $30^\circ$  jets become oval at  $X/D_e = 1.0$ . The  $U/U_{cl}$  contours of the  $70^\circ$  jet at  $X/D_e = 1.0$  are very similar to those of the equilateral triangular jet of Quinn (2005c) at the same location. At  $X/D_e = 3.0$ , the shapes of the  $U/U_{cl}$  contours in the  $30^\circ$  and  $70^\circ$  jets are still triangular but inverted, a phenomenon that has been referred to as axis-switching in the literature on noncircular jets. At the same location, a triangular shape of the  $U/U_{cl}$  contours in the other jets cannot be identified, which indicates higher mixing in those jets compared to the  $30^\circ$  and  $70^\circ$  jets. As was the case at locations upstream, the  $U/U_{cl}$  contours are still triangular in shape at  $X/D_e = 5.0$  in the  $30^\circ$  and  $70^\circ$  jets. Memory of the initial geometry of the orifice persists for the longest distance (up to  $X/D_e = 10.0$ ) in the  $70^\circ$  jet. The  $U/U_{cl}$  contours become elliptic in all the other triangular jets at  $X/D_e = 10.0$  except in the  $160^\circ$  jet. The model of the spreading behaviour of the triangular jets, presented earlier, is perhaps the best framework to use to gain insight into the changing shapes of the  $U/U_{cl}$  contours in these jets.

#### 4.5 Mass entrainment into the jets

The mass entrainment ratios  $((Q - Q_0)/Q_0)$  for all the jets were presented in Figure 3.26. The  $160^\circ$  jet has the highest mass entrainment ratios in the near field ( $X/D_e \leq 10$ ); a result which is consistent with the fact that the near-field spreading rate and mean streamwise centreline velocity decay rate have their highest values in this jet. All the triangular jets have higher mass entrainment ratios than the round jets and the sharp-edged orifice round jet has lower mass entrainment ratios than the contoured nozzle round jet in the near field; these findings are also consistent with the near-field spreading rates and mean streamwise centreline velocity decay rates of these jets. In the region  $2 \leq X/D_e \leq 9$ , the  $70^\circ$  jet has higher mass entrainment ratios than the  $20^\circ$  and  $30^\circ$  jets; a result which is in agreement with the spreading rate and mean streamwise centreline velocity decay rate data. In the far field ( $10 \leq X/D_e \leq 25$ ), the mass entrainment ratio data of all the jets have been fitted (see appendix F) by linear regression to:

$$(Q - Q_0)/Q_0 = K_e(X/D_e + C_e) \quad (4.3)$$

The results are shown in Table 4.3.

**Table 4.3** Rates of mass entrainment of the jets and values of  $C_e$ 

Jet type	$K_e$	$C_e$	Fitted range
10° triangular	0.436	-3.368	$10 \leq X/D_e \leq 25$
20° triangular	0.417	-4.202	$10 \leq X/D_e \leq 25$
30° triangular	0.414	-3.759	$10 \leq X/D_e \leq 25$
70° triangular	0.370	-3.652	$10 \leq X/D_e \leq 25$
160° triangular	0.360	-3.299	$10 \leq X/D_e \leq 25$
Sharp-edged orifice round	0.393	-5.278	$10 \leq X/D_e \leq 25$
Contoured nozzle round	0.315	-4.381	$10 \leq X/D_e \leq 25$

The 10° jet has the highest and the contoured nozzle round jet has the lowest rate of mass entrainment (the spatial derivative of the mass entrainment ratios with respect to the streamwise direction) in the far field. As the perimeter of the triangular orifice decreases, the rate of mass entrainment also decreases, except for the 160° jet, which has the longest perimeter but its rate of mass entrainment is lower than that of any of the other triangular jets in the far field. In this context, it is important to note that up to  $X/D_e = 10$ , the 160° jet has higher mass entrainment ratios  $((Q - Q_0)/Q_0)$  than any of the other jets. The fact that this jet has a higher value of  $Q_0$  than the other jets should be considered in interpreting the results. Both the round jets in the present study have rates of mass entrainment lower than those of the triangular jets, except for the 70° and 160° jets. Based upon the rate of mass entrainment results and those presented previously for

the spreading rate and mean streamwise centreline velocity decay rate, the  $10^\circ$  jet has the highest far-field mixing rate among all the test jets.

There are no rate of mass entrainment data in the extant literature (to the best knowledge of the author) for any of the test jets, except for the contoured nozzle round jet. The rate of mass entrainment of the contoured nozzle round jet of the present study is 0.315, which agrees with the result (0.32) of Ricou and Spalding (1961), who measured the mass flow rates directly using a flow meter. The mass flow rates in the present study were calculated from the  $U$  data obtained on  $Y$ - $Z$  planes in the jet at different  $X/D_e$  locations. Hill (1972) also obtained a rate of mass entrainment of 0.32 in a contoured nozzle round jet using the same flow facility in the study of Ricou and Spalding (1961). Crow and Champagne (1971) reported a rate of mass entrainment of 0.29 for their contoured nozzle round jet; this value is slightly lower than that of the present jet. The difference in the two rates of mass entrainment may be due to the method used to obtain the flow rates. Crow and Champagne (1971) integrated the mean streamwise velocity profiles across the jet to calculate the mass flow rates, while the  $U$  values on entire  $Y$ - $Z$  planes at different streamwise locations were integrated to calculate the mass flow rates in the present study, as was mentioned previously. Panchapakesan and Lumley (1993) reported a rate of mass entrainment of 0.32 for their contoured nozzle round jet, which was obtained by integration of radial profiles of the mean streamwise velocity (the same method used by Crow and Champagne 1971). Although no rate of mass entrainment result is available for a sharp-edged orifice round jet, Mi et al. (2007) presented mass entrainment ratios for that jet. Their results show that the sharp-edged orifice round jet has higher mass entrainment ratios in the far field than the contoured nozzle round jet of

Zaman (1999). It should, however, be mentioned that in the experiment of Mi et al. (2007), the jet was delivered through a 0.99 m long tube with a diameter of 25.4 mm, which was capped with an orifice of 12 mm diameter. The exit mean streamwise velocity profile of the jet was, therefore, similar to that of a pipe jet rather than that of an orifice jet. The sharp-edged orifice round jet in the present study has higher mass entrainment ratios as well as a higher rate of mass entrainment in the far field than the contoured nozzle round jet. These results are consistent with the higher spreading rate and the higher mean streamwise centreline velocity decay rate of the sharp-edged orifice round jet compared to the contoured nozzle round jet.

#### 4.6 Streamwise turbulence intensities on the jet centreline

The profiles of  $\sqrt{u'^2}/U_{cl}$  along the jet centreline were presented in Figures 3.27 and 3.28 for all the test jets.  $\sqrt{u'^2}/U_{cl}$  increases rapidly in the near field and becomes nearly constant in the far field, with an asymptotic value of around 22% to 24% in all the test jets. These values are close to the asymptotic values of  $\sqrt{u'^2}/U_{cl}$  for the contoured nozzle round jets of Panchapakesan and Lumley (1993) and Xu and Antonia (2002), the elliptic jet of Hussain and Husain (1989) and the square jet of Quinn and Militzer (1988).

A close look at Figure 3.28 shows that in the near field ( $X/D_e \leq 10$ ), the growth of  $\sqrt{u'^2}/U_{cl}$  in the 160° jet is faster than in any of the other jets. This is not surprising since, as has already been mentioned, the 160° jet has the shortest potential core length. The potential core length in a jet is a measure of when turbulent mixing, i.e., the production of turbulence from mean flow shear, is initiated in the jet. In this region, the

growth rate of  $\sqrt{u'^2}/U_{cl}$  decreases as the perimeter of the orifice decreases, except for the region  $2 \leq X/D_e \leq 7$  in which the  $70^\circ$  jet has a higher growth rate of  $\sqrt{u'^2}/U_{cl}$  than the  $20^\circ$  and  $30^\circ$  jets. The higher growth rate of  $\sqrt{u'^2}/U_{cl}$  in the  $70^\circ$  jet in this region is, as has been mentioned already, due to the shorter flow development region of the jet compared to the  $20^\circ$  and  $30^\circ$  jets. This result is consistent with the other results, namely, the  $70^\circ$  jet has a higher rate of mass entrainment and a higher mean streamwise centreline velocity decay rate in comparison to the  $20^\circ$  and  $30^\circ$  jets in the aforementioned region.

There are dips in the  $\sqrt{u'^2}/U_{cl}$  profiles on the jet centreline of the triangular jets, as was observed in jets issuing from other noncircular orifices (elliptic, rectangular, and triangular jets of Mi et al. 2000). These dips in the jet centreline profiles of  $\sqrt{u'^2}/U_{cl}$  are known to be influenced by the merging of shear layers in jets with multiple shear layers (William et al. 1976). The deepest dip is observed in the  $160^\circ$  jet and those in the  $20^\circ$  and  $30^\circ$  jets are hardly noticeable. There is a region of slower growth in the jet centreline profile of  $\sqrt{u'^2}/U_{cl}$  in the  $10^\circ$ ,  $70^\circ$  and  $160^\circ$  jets after the dips. In this region, the  $\sqrt{u'^2}$  increases at a slower rate than at locations upstream but the decay in the mean streamwise centreline velocity in the region, shown in Figure 3.7, leads to increase in  $\sqrt{u'^2}/U_{cl}$ .

The axis-switching phenomenon was observed in elliptic, rectangular and triangular jets in the numerical investigation of Miller et al (1995). Mi et al (2000) used their own results and those of Miller et al (1995), to postulate that the dip in the jet centreline profile of  $\sqrt{u'^2}/U_{cl}$  is associated with the axis-switching phenomenon. This suggestion is supported by the results of the present investigation, since both the dips in

the jet centreline profile of  $\sqrt{u'^2}/U_{cl}$  and axis-switching are observed in all the triangular jets. However, a dip was observed in the jet centreline profile of  $\sqrt{u'^2}/U_{cl}$  in a rectangular jet of aspect ratio 5 but not in a rectangular jet of aspect ratio 2 in the experiments of Tsuchiya and Horikoshi (1986). Axis-switching was, however, observed in both jets.

The higher growth rate of  $\sqrt{u'^2}/U_{cl}$  in the near field of the  $160^\circ$  jet, together with the higher mean streamwise centreline velocity decay rate, higher spreading rate and higher rate of mass entrainment, indicates that the near field mixing rate in the  $160^\circ$  jet is higher than in the other jets.

#### 4.7 Spanwise turbulence intensities on the jet centreline

$\sqrt{v'^2}/U_{cl}$  also increases rapidly on the jet centreline in the near field of all the jets and becomes almost constant in the far field. The asymptotic centreline value of  $\sqrt{v'^2}/U_{cl}$  is about 18% in the  $10^\circ$ ,  $160^\circ$  and contoured nozzle round jets and about 15% in the other jets. The asymptotic centreline value of  $\sqrt{v'^2}/U_{cl}$  in the contoured nozzle round jet of Panchapakesan and Lumley (1993) and Xu and Antonia (2002) was 18.3% and 15%, respectively. In the square jet of Quinn and Militzer (1988), the asymptotic value was 20%. These values are close to those found in the present jets.

The profiles of  $\sqrt{v'^2}/U_{cl}$  on the jet centreline are very similar to those of  $\sqrt{u'^2}/U_{cl}$  but the values of  $\sqrt{v'^2}/U_{cl}$  are lower than those of  $\sqrt{u'^2}/U_{cl}$ . These lower

values of  $\sqrt{v'^2}/U_{cl}$  are expected because  $\sqrt{v'^2}$  is not produced directly, but is rather generated from  $\sqrt{u'^2}$  via the pressure fluctuations in the flow.

#### **4.8 One-dimensional energy spectra of the streamwise fluctuating velocity on the jet centreline**

The one-dimensional energy spectra of the streamwise fluctuating velocities at several streamwise locations on the jet centreline were shown in Figures 3.31-3.40 for the 10°, 20°, 30°, 70° and 160° jets and in Figures 3.41 and 3.42 for the sharp-edged orifice round jet.

As the jets evolve downstream, the peak frequency increases initially and then decreases in all the test jets. Liepmann and Gharib (1992) have shown, by using Laser Induced Fluorescence (LIF) imaging, that in a round jet the Kelvin-Helmholtz instability creates small disturbances which subsequently roll up into vortices. These vortices increase in size downstream through a pairing process. The vortices travel from the shear layers to the jet centreline and with increasing downstream distance more vortices cross the centreline, which is reflected in the increased frequency of the peaks in the one-dimensional energy spectra. When the vortices merge and become larger in size, the frequency starts to decrease and finally the large-scale vortical structures break up into smaller ones. This process occurs quickest in the 160° jet and the evidence shows that the large-scale vortical structures are present at the farthest downstream distance from the orifice exit plane in the sharp-edged orifice round jet.

The preferred mode frequency,  $f$ , defined as the “passage frequency of the most energetic disturbance occurring near the end of the potential core” (Petersen and Samet 1988), is used to calculate the values of the preferred mode Strouhal numbers from:

$$St_{D_e} = fD_e/U \quad (4.4)$$

The preferred mode Strouhal numbers are: 0.60, 0.42, 0.44, 0.41 and 0.83 in the 10°, 20°, 30°, 70° and 160° jets, respectively. The frequencies corresponding to the aforementioned Strouhal numbers are: 900 Hz, 650 Hz, 650 Hz, 650 Hz and 1225 Hz. The preferred mode Strouhal number of the sharp-edged orifice round jet is 0.44 and the corresponding frequency is 650 Hz. The aforementioned preferred mode Strouhal numbers of the present jets, except for the 10° and 160° jets, are close to or equal to the value of 0.44 in the unexcited round jet of Crow and Champagne (1971). Many other researchers have studied the preferred mode and have found that the preferred mode Strouhal number varies from 0.24 to 0.64 (Gutmark and Ho 1983). The preferred mode Strouhal numbers of the present jets fall within this range, except for the 160° jet. This jet has a much higher value of the preferred mode Strouhal number than the other jets, which indicates a higher mixing rate in the near field of the jet compared to the other test jets. The discrete spectral peaks are still present at  $X/D_e = 1.25$ ,  $X/D_e = 3.52$ ,  $X/D_e = 3.43$ ,  $X/D_e = 3.53$  and  $X/D_e = 0.99$  in the 10°, 20°, 30°, 70° and 160° jet, respectively. In the sharp-edged orifice round jet, the discrete peak in the one-dimensional energy spectra is found as far downstream as  $X/D_e = 4.50$ . It should be recalled that the potential core lengths were  $1.14 D_e$ ,  $3.15 D_e$ ,  $3.11 D_e$ ,  $3.13 D_e$ ,  $0.59 D_e$  and  $4.14 D_e$  for the 10°, 20°, 30°, 70°, 160° and sharp-edged orifice round jets, respectively. The peaks in the one-dimensional energy spectra disappear shortly after the potential core in all the jets and the one-dimensional

energy spectra become broadband thereafter. It is clearly evident that the longer orifice perimeter, the more rapid the transition to a fully-developed turbulent flow of the jet issuing from the orifice. This transition to fully-developed turbulent flow occurs most rapidly in the  $160^\circ$  jet, which issues from the orifice with the longest perimeter. The inertial subrange in the one-dimensional energy spectra, which separates the energy-containing structures from the energy-dissipating ones, appears first in the  $160^\circ$  jet. In the inertial subrange, the large-scale structures lose energy to the small-scale structures at the same rate as the large-scale structures receive the energy from the mean flow and, therefore, the slope of the energy spectrum remains unchanged. This slope in the one-dimensional energy spectra for the present jets is  $-5/3$ , which is in agreement with the  $-5/3$  law of Kolmogorov.

#### **4.9 Distribution of autocorrelation coefficients of the streamwise fluctuating velocity on the jet centreline**

The distribution of the autocorrelation coefficients of the streamwise fluctuating velocity on the centreline of all the jets was shown in Figures 3.43–3.54. In the near field, the distribution of the autocorrelation coefficients is periodic in all the jets. Periodicity was also found in the distribution of the cross-correlation coefficients of the streamwise fluctuating velocity in the flat sections of the triangular jets of Schadow et al. (1988) and in the distribution of the autocorrelation coefficients of the streamwise fluctuating velocity on the centreline of the round jet of Quinn (2006). The periodicity in the distribution of the autocorrelation coefficients indicates the presence of large-scale structures. The large-scale structures travel a longer streamwise distance in the sharp-edged orifice round jet than in any of the other jets. They subsequently break up into

small-scale structures. On the other hand, the large-scale structures travel the shortest streamwise distance in the  $160^\circ$  jet. The peak in the one-dimensional energy spectra consequently disappeared most rapidly in the  $160^\circ$  jet. The streamwise turbulence intensity peaked closest to, and farthest away from, the orifice exit plane in the  $160^\circ$  and sharp-edged orifice round jets, respectively.

# CHAPTER 5

## Conclusions and recommendations for future work

### 5.1 Conclusions

Isothermal, incompressible jets of air issuing from sharp-edged isosceles triangular orifices with apex angles of  $10^\circ$ ,  $20^\circ$ ,  $30^\circ$ ,  $70^\circ$  and  $160^\circ$  were used to study the effects of apex angle variation on mixing in jets issuing from the orifices. Two round jets, one issuing from a sharp-edged orifice and the other from a contoured nozzle, were used for comparison. The exit area of all the orifices and the nozzle was the same and all the jets issued into still air surroundings. A pitot-static tube and an x-array hot-wire probe were used to measure the mean velocities and turbulence quantities. The mean streamwise centreline velocity decay rate, jet spreading rate, rate of mass entrainment, streamwise and spanwise turbulence intensities, one-dimensional energy spectra and autocorrelation coefficients were calculated from the measured data. The Reynolds number, based on the equivalent diameter of the triangular orifices (the same as the diameter of the round orifice or nozzle), was the same (about  $1.93 \times 10^5$ ) in all the jets.

5.1.1 The mean streamwise centreline velocity decay, mass entrainment and jet spreading results show that the jet issuing from the triangular orifice with the apex angle of  $160^\circ$ , which has the longest perimeter, has the highest mixing rate in the near field ( $X/D_e \leq 10$ ). The near field high mixing rate of the  $160^\circ$  jet is supported by the streamwise turbulence intensity distribution along

the jet centreline. The streamwise turbulence intensity on the jet centreline grows most rapidly in the near field of this jet. In this near field region, the mixing rate decreases as the perimeter of the orifice, from which the jets originate, decreases, except for the region  $3 \leq X/D_e \leq 9$ . The  $70^\circ$  jet has a higher mixing rate in this region than the  $20^\circ$  and  $30^\circ$  jets (the orifices with the apex angles of  $20^\circ$  and  $30^\circ$  have longer perimeters than the orifice with the apex angle of  $70^\circ$ ).

- 5.1.2 In the far field ( $X/D_e > 10$ ), the jet issuing from the triangular orifice with the apex angle of  $10^\circ$  has the highest mixing rate, as deduced from the mean streamwise centreline velocity decay rate, rate of mass entrainment and jet spreading rate. The mixing rate in this far field region also decreases as the perimeter of the triangular orifice decreases, as was observed for the near field.
- 5.1.3 Both of the round jets have lower mixing rates than the triangular jets, regardless of the apex angle of the triangular orifice. In the near field, the contoured nozzle round jet has a higher mixing rate than the sharp-edged orifice round jet, because the sharp-edged orifice round jet shrinks initially, instead of spreading, due to the vena contracta effect. In the far field, the sharp-edged orifice round jet has a higher mixing rate than the contoured nozzle round jet.
- 5.1.4 The one-dimensional energy spectra of streamwise fluctuating velocities along the jet centreline show that the jet issuing from the triangular orifice with the apex angle of  $160^\circ$  develops faster than all the other test jets. The distributions

of the autocorrelation coefficients of streamwise fluctuating velocities along the jet centreline in the  $10^\circ$  and  $160^\circ$  jets, which have uniform or close to uniform exit velocity profiles, exhibit long tails, whereas in the other jets with less uniform initial velocity profiles, the distributions are more periodic.

5.1.5 The development of the jet half-velocity widths in the streamwise direction shows that all the triangular jets spread at different rates in the central  $X$ - $Y$  and  $X$ - $Z$  planes over the measurement range. Cross-overs in the development of the half-velocity widths are observed in the triangular jets. These observations imply that all the triangular jets continually change shape, a phenomenon which is evident in the  $U/U_{cl}$  contour maps of the jets. Unlike the triangular jets, the round jets do not exhibit any cross-over in the development of the half-velocity widths.

5.1.6 Among the jets tested, the  $160^\circ$  triangular jet is the best candidate for applications in which near field mixing is important, such as in combustion systems.

## 5.2 Recommendations for future work

Research on mixing in turbulent free triangular jets will benefit from the following:

5.2.1 The  $U/U_{cl}$  contours of the  $10^\circ$  jet at  $X/D_e = 0.14$  and  $X/D_e = 1.0$  (Figure 3.12) appear to be “flaring” at the apex. This “flaring” behaviour is barely noticeable in the  $20^\circ$  jet (Figure 3.14) and is absent in the  $30^\circ$  and  $70^\circ$  jets (Figures 3.16 & 3.18). It is conjectured that the “flaring” behaviour may be due to strong flow separation as a result of the very sharp corner at the apex of

the  $10^\circ$  triangular orifice. It is suggested that the in-plane velocities (i.e.,  $V$  and  $W$ ) be measured over entire Y-Z planes at  $X/D_e = 0.14$  and  $X/D_e = 1.0$  in the  $10^\circ$  and  $20^\circ$  jets. The results obtained can then be used to obtain secondary flow velocity vector plots and the mean streamwise vorticity and thus confirm or deny that the observed “flaring” in the  $U/U_{cl}$  contour maps is due to flow separation at the exit planes of the  $10^\circ$  and  $20^\circ$  triangular orifices.

5.2.2 Scaling should be used to collapse the far field results for the mean streamwise centreline velocity decay, jet spreading, mass entrainment and turbulence quantities and thus obtain universal expressions for the corresponding metrics in triangular jets. It may be necessary, hereby, to reduce the exit area of the orifices to extend the measurement range. The equivalent diameter ( $D_e$ ) is clearly not the appropriate length scale for triangular jets unlike elliptic jets.

5.2.3 The perimeter and aspect ratio of the triangular orifices of the present study were determined from the exit area and the apex angle. This procedure resulted in aspect ratios for the triangular orifices which cannot be compared to those of other non-circular orifices for which experimental results are available in the literature. It will be useful to test triangular jets issuing from orifices with the same exit area and aspect ratios of 0.25, 0.5, 1.0, 2.0 and 5.0. This will lead to results that can directly be compared to those of other non-circular jets which are in the archival literature.

## References

- Abramovich G.N., (1982), On the deformation of the rectangular turbulent jet cross-section, *Int. J. Heat Mass Transfer*, 25, 1885-1894
- Bradshaw P., 1975, *An Introduction to Turbulence and its Measurement*, Oxford, Pergamon Press
- Brunn H. H., 1995, *Hot wire anemometry: principles and signal analysis*, New York, Oxford University Press
- Crow S.C., Champagne F.H., (1971), Orderly structure in jet turbulence, *J. Fluid Mech.*, 89, 547–591
- Deo R.C., Mi J., Nathan G.J., (2007), The influence of nozzle aspect ratio on plane jets, *Exp. Thermal Fluid Sci.*, 31, 825–838
- Faghani E., Maddahian R., Faghani P., Farhanieh B, (2010), Numerical investigation of turbulent free jet flows issuing from rectangular nozzles: the influence of small aspect ratio, *Arch. Appl. Mech.*, 80, 727-745
- Grinstein F. F., Gutmark E., Parr T., (1995), Near field dynamics of subsonic free square jets. A computational and experimental study, *Phys. Fluids*, 7, 1483-97
- Gutmark E., Ho C. M., (1983), Preferred modes and the spreading rates of jets, *Phys. Fluids*, 26, 2932-2938
- Gutmark E., Schadow K.C., Parr T., Hanson-Parr D. M., Wilson K. J., (1989), Noncircular jets in combustion systems, *Exp. Fluids*, 7, 248-258
- Hill B. J., (1972), Measurement of local entrainment rate in the initial region of axisymmetric turbulent air jets, *J. Fluid Mech.*, 51, 773-779
- Ho C.M., Gutmark E., (1987), Vortex induction and mass entrainment in a small-aspect-ratio elliptic jet, *J. Fluid Mech.*, 179, 383–405

Hussain F., Husain H. S., (1989), Elliptic jets. Part 1. Characteristics of unexcited and excited jets, *J. Fluid Mech.*, 208, 257–320

Husain H.S., Hussain F., (1991), Elliptic jets. Part 2. Dynamics of coherent structures: pairing, *J. Fluid Mech.*, 233, 439–482

Iyogun C. O., Birouk M., (2009), Effect of Sudden Expansion on Entrainment and Spreading Rates of a Jet Issuing from Asymmetric Nozzles, *Flow Turbulence Combust*, 82, 287–315

Liepmann D., Gharib M., (1992), The role of streamwise vorticity in the near-field entrainment of round jets, *J. Fluid Mech.*, 245, 643-668

Mi J., Nathan G. J., (2010), Statistical Properties of Turbulent Free Jets Issuing from Nine Differently-Shaped Nozzles, *Flow Turbulence Combust*, 84, 583-606

Mi J., Nathan G. J., Luxton R. E., (2000), Centreline mixing characteristics of jets from nine differently shaped nozzles, *Exp. Fluids*, 28, 93-94

Mi J., Nathan G. J., Nobes D. S., (2001), Mixing Characteristics of Axisymmetric Free Jets From a Contoured Nozzle, an Orifice Plate and a Pipe, *J. Fluids Engrg*, 123, 878-883

Mi J., Kalt P., Nathan G.J., Wong C.Y., (2007), PIV measurements of a turbulent jet issuing from round sharp-edged plate, *Exp Fluids*, 42, 625–637

Miller R. S., Madina C. K., Givi P., (1995), Numerical simulation of non-circular jets, *Computers & Fluids*, 24, 1-25

Obot N.T., Graska M.L., Trabold T.A., (1984), The near field behaviour of round jets at moderate Reynolds numbers, *Canad. J. Chem. Engrg.* 62, 587–593

Panchapakesan N. R., Lumley J. L., (1993), Turbulence measurements in axisymmetric jets of air and helium. Part 1: Air Jet, *J. Fluid Mech.*, 246, 197–223

Petersen R. A., Samet M. M., (1988), On the preferred mode of jet instability, *J. Fluid Mech.*, 194, 153-173

- Quinn W.R., (1989), On mixing in an elliptic turbulent free jet, *Phys. Fluids*, 10, 1716-1722
- Quinn W. R., (1990), Mean flow and turbulence measurements in a triangular turbulent free jet, *Int. J. Heat and Fluid Flow*, 11, 220-224
- Quinn W. R., (1992), Turbulent free jet flows issuing from sharp-edged rectangular slots: the influence of slot aspect ratio, *Exp. Therm. Fluid Sci.*, 5, 203-215
- Quinn W. R., (2005a), Measurements in the near flow field of an isosceles triangular turbulent free jet, *Exp. Fluids*, 39, 111–126
- Quinn W. R., (2005b), Phase-averaged measurements in an isosceles triangular turbulent free jet, *Exp. Fluids*, 39, 941–943
- Quinn W. R., (2005c), Near-field measurements in an equilateral triangular turbulent free jet, *AIAA J.*, 43, 2574–2585
- Quinn W. R., (2006), Upstream nozzle shaping effects on near field flow in round turbulent free jets, *Eur. J. Mech. B/Fluids*, 25, 279–301
- Quinn W. R., (2007), Experimental study of the near field and transition region of a free jet issuing from a sharp-edged elliptic orifice plate, *Eur. J. Mech. B/Fluids*, 26, 583-614
- Quinn W. R., Militzer J., (1988), Experimental and numerical study of a turbulent free square jet, *Phys. Fluids*, 31, 1017-1025
- Ricou F. P., Spalding D. B., (1961), Measurements of entrainment by axisymmetrical turbulent jets, *J. Fluid Mech*, 11, 21-32
- Schadow K. C., Gutmark E., Parr D. M., Wilson K. J., (1988), Selective control of flow coherence in triangular jets, *Exp. Fluids*, 6, 129-135
- Schlichting H., 1968, *Boundary-Layer Theory*, New York, McGraw-Hill
- Seif A., Zedan M., Shibl A., (1994), Effect of Nozzle Exit Geometry on the Development of Turbulent jets, *J. King Saud Univ.*, 6, 217-240

Sforza P. M., Steiger M.H., Trentacoste N., (1966), Studies on three-dimensional viscous jets, *AIAA J.*, 4, 800-806

Tavoularis S., 2005, *Measurement in fluid mechanics*, Cambridge, Cambridge university press

Tsuchiya Y., Horikoshi C., Sato T., (1986), On the spread of rectangular jets, *Exp. Fluids*, 4, 197-204

Vandsburger U., Ding C., (1995), The spatial modulation of a forced triangular jet, *Exp. Fluids*, 18, 239-248

William G. H. J., Richard C. J., Barry L. G., (1976), Effects of the initial boundary-layer state on turbulent jet mixing, *AIAA J.*, 14, 1513-1514

Wynanski I., Fiedler H., (1969), Some measurements in the self-preserving jet, *J. Fluid Mech.* 38, 577–612

Xu G., Antonia R. A., (2002), Effect of different initial conditions on a turbulent round free jet, *Exp. Fluids*, 33, 677–683

Yoon J.H., Lee S.J., (2003), Investigation of the near-field structure of an elliptic jet using stereoscopic particle image velocimetry, *Meas. Sci. Technol.* 14, 2034–2046

Zaman, K.B.M.Q., (1999), Spreading characteristics of compressible jets from nozzles of various geometries, *J. Fluid Mech.*, 383, 197-228

## APPENDIX A

### Hot wire calibration curves

#### A.1 Velocity calibration curve

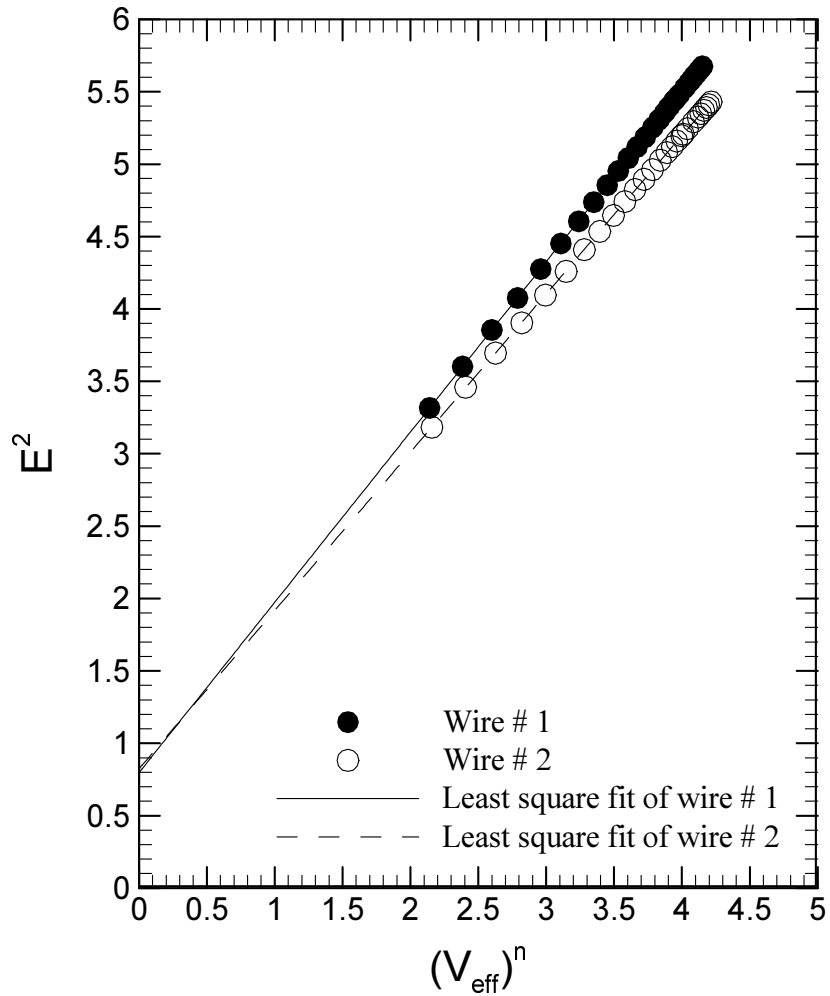


**Figure A.1** Typical linear least squares fit for the velocity calibration of the x-array probe used.

For wire # 1 the linear equation is  $E_1^2 = 0.7971201 + 1.176366V_{eff1}^{0.372}$

For wire # 2 the linear equation is  $E_2^2 = 0.8236765 + 1.093488V_{eff2}^{0.376}$

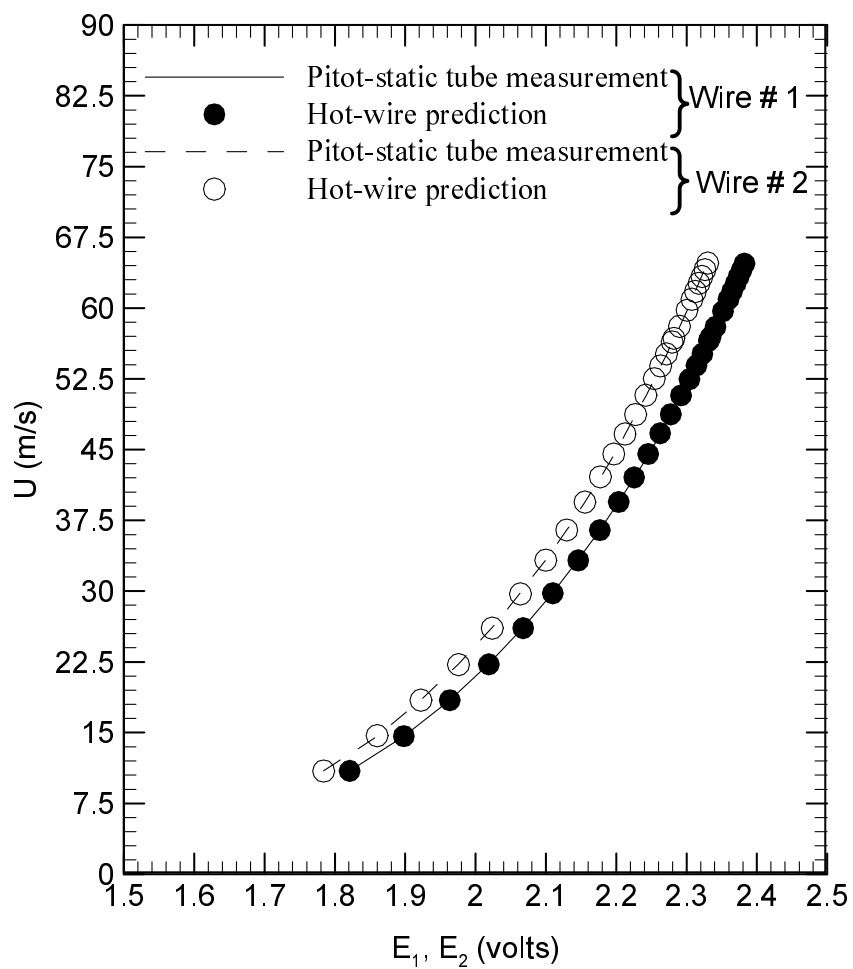


**Figure A.2** Typical velocity calibration curve for the x-array probe used.

## A.2 Yaw calibration curve

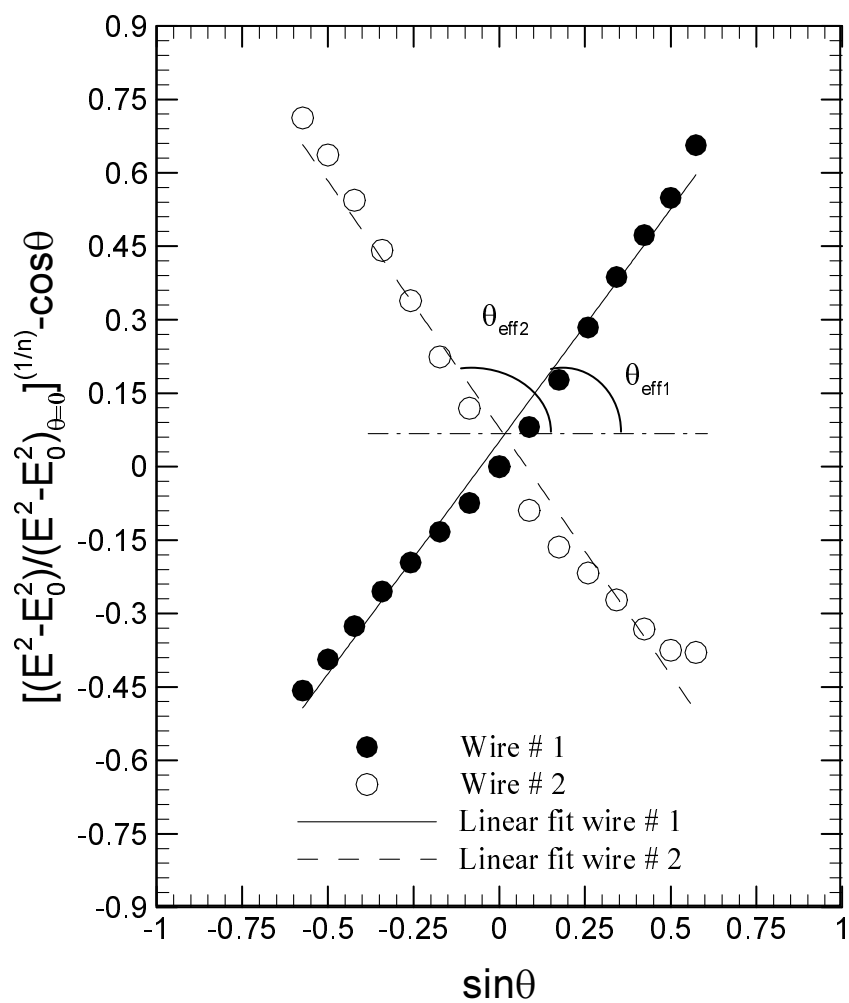
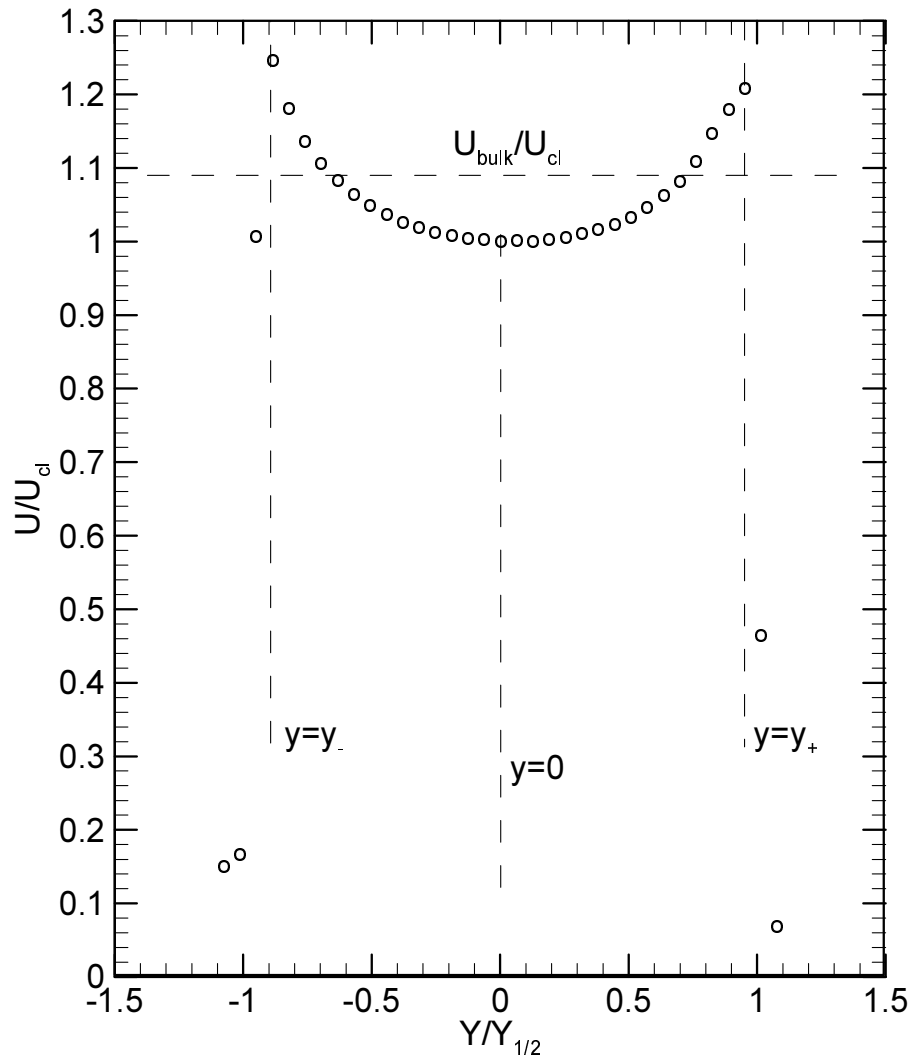


Figure A.3 Typical Yaw calibration curve of the x-array probe used.

## APPENDIX B

### Calculation of bulk velocity



**Figure B.1** A typical velocity profile close to the exit of an orifice jet.

A typical mean streamwise velocity profile close to the exit (at  $X/D_e = 0.035$ ) of a jet issuing from a sharp-edged orifice is shown in Figure B.1. It should be recalled that  $U$ ,  $U_{cl}$  and  $Y_{1/2}$  are the mean streamwise velocity, its value on the jet centreline and the half-velocity width in the  $Y$  direction, respectively. The mean streamwise velocity profile

has pronounced off-centre peaks. As the jet evolves downstream its mean streamwise velocity on the centreline is accelerated up to a certain distance and reaches a maximum value,  $U_{max}$ . This  $U_{max}$  has been used as the normalizing mean streamwise velocity to calculate the mean streamwise centreline velocity decay rate (for instance, see Quinn 1989, Quinn 2005a, Mi et al. 2007). The use of  $U_{max}$  to normalize the mean streamwise centreline velocity may lead, as mentioned in chapter 4, to an overestimation of the mean streamwise centreline velocity decay rate by as high as 33% (Mi and Nathan 2010). The mean streamwise velocity at the centre of the orifice exit plane,  $U_{exit}$ , (at  $y=0$  in Figure B.1) has also been widely used to normalize the mean streamwise centreline velocity (for instance, see Obot et al. 1984, Quinn and Militzer 1988, Xu and Antonia 2002, Yoon and Lee 2003, Deo et al. 2007) and this may lead to an underestimation of the mean streamwise centreline velocity decay rate. Since both  $U_{max}$  and  $U_{exit}$  have their limitations as normalizing velocities, the area-average of the Y-profile of the initial mean streamwise velocity, which is known as bulk velocity,  $U_{bulk}$ , is used as normalizing velocity (see Quinn 2006, Quinn 2007, Mi and Nathan 2010) to circumvent these limitations.

The bulk velocity is calculated using the formula:

$$AU_{bulk} = \int U dA \quad (B.1)$$

where  $A$  is the area of the orifice and  $dA$  is an elemental area. The axial symmetry of the round jet enables calculation of the bulk velocity using the formula:

$$\pi y^2 U_{bulk} = \frac{1}{2} \left[ \int_{y_-}^0 2\pi y U dy + \int_0^{y_+} 2\pi y U dy \right] \quad (B.2)$$

$$\Rightarrow U_{bulk} = \frac{1}{y^2} \left[ \int_{y_-}^0 y U dy + \int_0^{y_+} y U dy \right] \quad (\text{B.3})$$

(for integration limits, see Figure B.1) while in the triangular jet, due to the asymmetric geometry, the width of the area is taken as unity. Therefore, the bulk velocity in triangular jet is calculated using the formula:

$$(y_+ - y_-) U_{bulk} = \int_{y_-}^{y_+} U dy \quad (\text{B.4})$$

$$\Rightarrow U_{bulk} = \frac{1}{y_+ - y_-} \int_{y_-}^{y_+} U dy \quad (\text{B.5})$$

## APPENDIX C

### Mean streamwise centreline velocity decay and potential core length data

The potential core length of a jet is the distance from the orifice exit to the point on the jet centreline up to which the mean streamwise velocity remains constant. However, in orifice jets, due to the vena contracta effect, the flow first accelerates to a maximum mean streamwise velocity value and remains almost constant before starting to decay. The end of the potential core has been considered in the literature to be the location where  $U_{cl}/U_{max}$  or  $U_{cl}/U_{exit} = 0.98$  to  $1.0$  (Mi et al. 2007, Faghani et al. 2010, Mi and Nathan 2010). In present study, the end of the potential core was taken to be the location where  $U_{cl}/U_{max} = 0.99$ .

The location of  $U_{cl}/U_{max} = 0.99$  was calculated by linear interpolation as shown below

$$\frac{x_{pc}}{D_e} = \frac{x_l}{D_e} + \frac{(U_{cl}/U_{max})_l - 0.99}{(U_{cl}/U_{max})_l - (U_{cl}/U_{max})_h} \times \left( \frac{x_h}{D_e} - \frac{x_l}{D_e} \right)$$

where  $x_{pc}$  is length of the potential core.  $x_h$  and  $x_l$  are the shortest and longest distance, respectively, in the streamwise direction such that  $x_l < x_{pc} < x_h$ .  $(U_{cl}/U_{max})_h$  and  $(U_{cl}/U_{max})_l$  are the normalized mean streamwise velocity at  $x_h$  and  $x_l$ , respectively.  $D_e$  is the equivalent diameter of the orifices.

### C.1 Mean streamwise centreline velocity decay and potential core length data for the 10° jet

$X/D_e$	$U_{cl}/U_{max}$	$U_{bulk}/U_{cl}$
0	0.895077036	1.040214631
0.250952915	0.998576834	0.932399187
0.50190583	1	0.931072228
0.746244395	0.998786512	0.932203446
0.997141256	0.996016127	0.934796338
1.24809417	0.985289553	0.944973206
1.499047085	0.965155558	0.96468618
1.75	0.938254096	0.992345498
1.994338565	0.908379176	1.024981916
2.99809417	0.791476526	1.176373774
3.995235426	0.706986389	1.316959198
4.992376682	0.664184107	1.401828527
5.989517937	0.640469083	1.453734852
6.993273543	0.614772855	1.51449795
7.990470852	0.570917232	1.630835743
9.984753363	0.480577587	1.937402519
10.98189462	0.436248126	2.134272155
11.98565022	0.403411305	2.307997364
13.97998879	0.342972996	2.714710017
15.9742713	0.303061622	3.07222083
17.97522422	0.266087384	3.499122029
19.96950673	0.239715895	3.884065457
23.96474215	0.203783441	4.568929758
27.95997758	0.17597888	5.290818002
31.955213	0.154525733	6.025353918
35.95044843	0.137464256	6.773195133
39.9456278	0.123642049	7.53038497
44.93800448	0.109233736	8.523669176
49.93043722	0.100400864	9.273547984
54.9228139	0.091414448	10.18517582
59.91519058	0.083750487	11.11721568

$$x_{pc}/D_e = 0.9971 + \frac{0.9960 - 0.99}{0.9960 - 0.9853} \times (1.2481 - 0.9971)$$

$$\Rightarrow x_{pc} = 1.1378 D_e$$

## C.2 Mean streamwise centreline velocity decay and potential core length data for the 20° jet

$X/D_e$	$U_{cl}/U_{max}$	$U_{bulk}/U_{cl}$
0	0.789084423	1.098922648
0.178307175	0.951147926	0.911680213
0.35	0.990944621	0.875066805
0.528307175	0.999135756	0.867892815
0.70661435	1	0.867142743
0.878307175	0.999042116	0.867974162
1.05661435	0.999258561	0.867786154
1.234865471	0.998455719	0.868483926
1.40661435	0.997959892	0.868915425
2.113172646	0.998939266	0.868063527
2.813172646	0.999341455	0.867714172
3.519786996	0.979842993	0.884981318
4.226345291	0.926376497	0.93605866
4.926345291	0.86181298	1.006184362
5.632959641	0.789214904	1.098740963
7.039517937	0.670603098	1.293078939
7.746132287	0.609904887	1.421767167
8.446132287	0.564333258	1.536579196
9.859304933	0.48054145	1.804511855
11.26586323	0.420741255	2.060988157
12.67247758	0.373438066	2.322052361
14.07903587	0.345310975	2.511193698
16.89882287	0.286576118	3.02587232
19.71199552	0.25120503	3.451932243
22.53178251	0.220667878	3.929628316
25.3448991	0.195825837	4.428132447
28.1646861	0.175678041	4.935976862
31.68447309	0.15403048	5.629682782
35.20420404	0.139496436	6.216235846
38.72399103	0.127770034	6.786745801
42.24372197	0.11937013	7.264319333
45.76350897	0.109749845	7.901083992
49.28323991	0.099934606	8.677101734
52.80302691	0.092242369	9.400698952
56.32275785	0.089921343	9.643347332
59.84254484	0.084629956	10.24628612

$$x_{pc}/D_e = 2.8132 + \frac{0.9993 - 0.99}{0.9993 - 0.9798} \times (3.5198 - 2.8132)$$

$$\Rightarrow x_{pc} = 3.1502 D_e$$

### C.3 Mean streamwise centreline velocity decay and potential core length data for the 30° jet

$X/D_e$	$U_{cl}/U_{max}$	$U_{bulk}/U_{cl}$
0	0.763576537	1.106279718
0.14529148	0.904863859	0.933542905
0.28396861	0.962802267	0.877365233
0.42926009	0.983808081	0.858632137
0.56793722	0.990062622	0.853207885
0.7132287	0.993733198	0.85005637
0.858464126	0.993268821	0.850453792
0.997141256	0.992019752	0.851524613
1.142432735	0.992910192	0.850760967
1.710369955	0.994395282	0.84949039
2.284865471	0.998675834	0.845849281
2.852802691	1	0.844729236
3.427298206	0.977469249	0.864200318
3.995235426	0.937934301	0.900627299
4.563172646	0.887033592	0.952308056
5.705605381	0.780634374	1.082106123
6.280100897	0.723719743	1.167204908
6.848038117	0.671557704	1.257865453
7.990470852	0.579872978	1.456748749
9.132903587	0.510466125	1.654819378
10.27533632	0.453338463	1.863352231
11.41776906	0.405726713	2.082015329
13.69602018	0.351639729	2.402257671
15.98088565	0.301937513	2.797695548
18.26580717	0.264396477	3.194933774
20.5440583	0.239082524	3.533211964
22.82892377	0.220171774	3.8366827
25.68172646	0.193616415	4.362900928
28.53452915	0.173162336	4.878250403
31.39389013	0.157241688	5.372170997
34.24669283	0.138464274	6.100701747
37.09949552	0.134847338	6.264337508
39.95224215	0.126264778	6.690141529
42.80504484	0.113535003	7.44025378
45.65784753	0.107865916	7.831289695
48.51065022	0.101536278	8.31948197
51.36345291	0.100112493	8.437800435
54.2228139	0.093894735	8.996555945
57.07561659	0.088306876	9.565837658

$$x_{pc}/D_e = 2.8528 + \frac{1 - 0.99}{1 - 0.9775} \times (3.4273 - 2.8528)$$

$$\Rightarrow x_{pc} = 3.1081 D_e$$

#### C.4 Mean streamwise centreline velocity decay and potential core length data for the 70° jet

$X/D_e$	$U_{cl}/U_{max}$	$U_{bulk}/U_{cl}$
0	0.750312961	1.093276142
0.085874439	0.845132764	0.970615853
0.178307175	0.911629078	0.899816908
0.264125561	0.949008313	0.864375208
0.35	0.970706904	0.845053492
0.442432735	0.983025027	0.834464268
0.528307175	0.988868472	0.829533231
0.62073991	0.991640732	0.827214163
0.70661435	0.994209663	0.825076731
1.05661435	0.994684604	0.824682774
1.413172646	0.996672377	0.823038019
1.763172646	0.998441646	0.82157957
2.119786996	1	0.820299258
2.469786996	0.999283794	0.820887182
2.826401345	0.999056188	0.821074199
3.532959641	0.978184572	0.838593536
3.882959641	0.948152509	0.865155395
4.239573991	0.89897258	0.912485294
4.946132287	0.800524711	1.024701982
5.646132287	0.70848779	1.157817071
6.352746637	0.636773192	1.288212614
7.059360987	0.587351998	1.396605887
8.472533632	0.508044411	1.614621165
9.885706278	0.451618973	1.816352518
11.29887892	0.406212777	2.019383204
12.71210762	0.367385957	2.232799709
14.12528027	0.341071485	2.405065487
15.88845291	0.308215572	2.661446513
17.65162556	0.279831388	2.931405456
19.42141256	0.255459168	3.211077782
21.1845852	0.236135284	3.473852975
22.94775785	0.216503371	3.788852133
24.71754484	0.204283878	4.015487005
26.48077354	0.192384554	4.263851972
28.24394619	0.17877969	4.588324662
30.01373318	0.166690692	4.921086169
31.77690583	0.15710386	5.221381935
33.54007848	0.148172539	5.536108551
35.30986547	0.140705492	5.829902188
38.83621076	0.128269014	6.395147457
42.3691704	0.115747562	7.086967921

45.9021861	0.11051107	7.422779075
49.42853139	0.102122972	8.032465603
52.96149103	0.095056515	8.629595339
56.49445067	0.086378596	9.496556934
60.02085202	0.085964351	9.54231903

$$x_{pc}/D_e = 2.8264 + \frac{0.9991 - 0.99}{0.9991 - 0.9782} \times (3.5330 - 2.8264)$$

$$\Rightarrow x_{pc} = 3.1341 D_e$$

### C.5 Mean streamwise centreline velocity decay and potential core length data for the 160° jet

$X/D_e$	$U_{cl}/U_{max}$	$U_{bulk}/U_{cl}$
0	0.939110152	1.030149112
0.033015695	0.962091606	1.005541971
0.05941704	0.97451933	0.992718625
0.092432735	0.983460823	0.983692962
0.12544843	0.991386957	0.975828341
0.15190583	0.995648462	0.971651668
0.184921525	0.997834235	0.969523249
0.21793722	0.998661194	0.968720419
0.244338565	1	0.96742349
0.369786996	0.997785884	0.96957023
0.49529148	0.994104584	0.973160677
0.62073991	0.988792707	0.978388577
0.739630045	0.981721875	0.985435401
0.865078475	0.974054166	0.993192703
0.990526906	0.965054319	1.002454961
1.234865471	0.949275411	1.019117823
1.360369955	0.938890074	1.030390581
1.485818386	0.928498069	1.041922995
1.730156951	0.903816015	1.070376574
1.974495516	0.879564113	1.099889679
2.22544843	0.850450493	1.137542394
2.469786996	0.823455954	1.174833316
2.965078475	0.771530941	1.253901092
3.460313901	0.724544339	1.335216408
3.955605381	0.679726837	1.423253338
4.450896861	0.636976732	1.518773672
4.946132287	0.606234203	1.595791668
5.560313901	0.568557557	1.701540113
6.181053812	0.541666389	1.786013512
6.795179372	0.519186779	1.863343845
7.415919283	0.500798616	1.93176151
8.036659193	0.483325775	2.001597141
8.650840807	0.466228067	2.075000536
9.271580717	0.450564199	2.147137946
9.885706278	0.434181744	2.228153308
10.50644619	0.417055693	2.319650603
11.12057175	0.402425524	2.403981439
11.74136771	0.38585967	2.507189955
12.36210762	0.372741702	2.595425959
13.59697309	0.344204952	2.810603052
14.83183857	0.319531234	3.027633563

16.06676009	0.297320053	3.253811775
17.30162556	0.27529227	3.514168741
18.53654709	0.258616378	3.740766528
19.77802691	0.24109352	4.012648249
21.01289238	0.229649476	4.212609172
22.2478139	0.217210081	4.453860915
23.48267937	0.206999807	4.673547795
24.7176009	0.195494075	4.948607735
25.95246637	0.187022748	5.172758393
27.19394619	0.180145318	5.370239428
28.42886771	0.174081509	5.557301843
29.66373318	0.165130013	5.858556385
30.89859865	0.158706076	6.095692825
32.13352018	0.154796361	6.249652647
33.36838565	0.148437448	6.517381586
34.60986547	0.142230255	6.801812257
35.844787	0.137553602	7.033065464
37.07965247	0.133803944	7.230156752
38.31457399	0.129817536	7.452178827
39.54943946	0.127353332	7.596373634
40.78436099	0.122741702	7.881783235
42.02584081	0.120117441	8.053980151
43.26070628	0.118176756	8.186241729
44.4956278	0.11342341	8.529310598
45.73049327	0.112458069	8.602526278
46.96535874	0.110250622	8.774766737
48.20028027	0.105233849	9.193082797
51.91154709	0.097952943	9.876410614
54.38133408	0.094550074	10.23186387
56.85767937	0.093448018	10.35253082
59.32746637	0.08681234	11.14384759

$$x_{pc}/D_e = 0.4953 + \frac{0.9941 - 0.99}{0.9941 - 0.9888} \times (0.6207 - 0.4953)$$

$$\Rightarrow x_{pc} = 0.5923 D_e$$

### C.6 Mean streamwise centreline velocity decay and potential core length data for the sharp-edged orifice round jet

$X/D_e$	$U_{cl}/U_{max}$	$U_{bulk}/U_{cl}$
0	0.733883221	1.115373894
0.05941704	0.795639417	1.028800446
0.12544843	0.848246257	0.964995931
0.184921525	0.887610815	0.922199429
0.250952915	0.921305239	0.888472302
0.310369955	0.94125455	0.869641678
0.376401345	0.958249332	0.854218373
0.435874439	0.969655185	0.84417038
0.50190583	0.978375103	0.836646582
0.752802691	0.993550633	0.82386761
0.997141256	0.996156927	0.821712086
1.24809417	0.996016385	0.821828034
1.499047085	0.99799648	0.820197468
1.75	0.997445239	0.820650753
2.000896861	0.997810651	0.820350219
2.502802691	0.997606083	0.82051844
2.747141256	0.998396247	0.819869054
2.99809417	1	0.818554186
3.499943946	0.999242629	0.819174606
4.001849776	0.994560983	0.823030665
4.497085202	0.978083086	0.836896372
4.998991031	0.953258491	0.858690684
6.002746637	0.876804613	0.933565101
6.999887892	0.786978839	1.040122232
7.997029148	0.704314517	1.162199794
9.000840807	0.626600434	1.306341556
9.997982063	0.570024033	1.43599943
11.25269058	0.506117528	1.617320366
12.50078475	0.455448621	1.797248137
13.74887892	0.419839687	1.949682727
14.99697309	0.374092911	2.188103974
16.25168161	0.343624731	2.382116629
17.49977578	0.325019949	2.518473676
18.74786996	0.301453996	2.715353574
20.00252242	0.281287625	2.910025593
21.25061659	0.264559874	3.094022442
22.49871076	0.243687663	3.359030061
23.74680493	0.236407531	3.462470853
25.00151345	0.223783639	3.65779282
27.49770179	0.19768791	4.140638577
30.00050448	0.180035698	4.546621563

32.49669283	0.166356171	4.92049188
34.99949552	0.154022734	5.314502393
37.50229821	0.145068577	5.64253267
39.99848655	0.133965673	6.11017858
42.50128924	0.125283233	6.533629157
44.99747758	0.119344507	6.858750409
47.50028027	0.112486004	7.276942512
50.00308296	0.107490478	7.615132057
52.4992713	0.102399695	7.993717022
55.00201794	0.09738543	8.405304427
57.49826233	0.092825588	8.818195582
60.00100897	0.088874765	9.210198022

$$x_{pc}/D_e = 4.0018 + \frac{0.9946 - 0.99}{0.9946 - 0.9781} \times (4.4971 - 4.0018)$$

$$\Rightarrow x_{pc} = 4.1399 D_e$$

### C.7 Mean streamwise centreline velocity decay and potential core length data for the contoured nozzle round jet

$X/D_e$	$U_{cl}/U_{max}$	$U_{bulk}/U_{cl}$
0	0.994906405	1.003809948
0.05941704	0.995752682	1.002956823
0.12544843	0.994384121	1.004337182
0.184921525	0.994777162	1.003940364
0.250952915	0.994598346	1.00412086
0.310369955	0.993475879	1.005255354
0.376401345	0.993112936	1.005622735
0.435874439	0.992677404	1.006063946
0.50190583	0.992539308	1.006203923
0.752802691	0.994047735	1.00467705
0.997141256	0.995832352	1.002876583
1.24809417	0.996460863	1.002244025
1.499047085	0.997434613	1.00126558
1.75	0.997898472	1.000800156
2.000896861	0.999892003	0.998804815
2.502802691	0.999442307	0.999254223
2.747141256	1	0.998696946
2.99809417	0.999049267	0.999647344
3.499943946	0.99816581	1.000532112
4.001849776	0.996620204	1.002083785
4.497085202	0.99141507	1.007344931
4.998991031	0.979386609	1.019716767
6.002746637	0.937352499	1.065444374
6.999887892	0.877746637	1.137796379
7.997029148	0.809780694	1.233293105
9.000840807	0.7470429	1.336866927
9.997982063	0.689025135	1.449434709
11.25269058	0.624199976	1.599963127
12.50078475	0.569546073	1.753496324
13.74887892	0.520377036	1.919179513
14.99697309	0.48276906	2.068684653
16.25168161	0.445897593	2.239745091
17.49977578	0.4120058	2.42398759
18.74786996	0.383659067	2.603084434
20.00252242	0.359961546	2.774454544
21.25061659	0.335267259	2.978808458
22.49871076	0.314349349	3.177028831
23.74680493	0.292578081	3.413437334
25.00151345	0.274372507	3.639930827
27.49770179	0.252829627	3.950078779
30.00050448	0.233174052	4.283053537

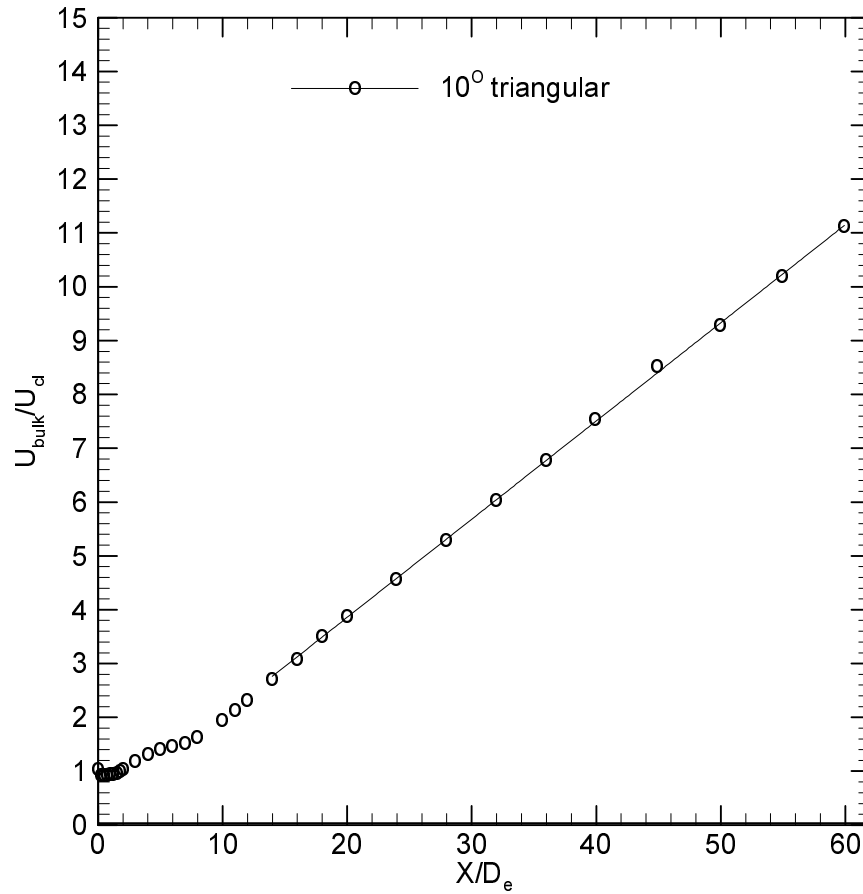
32.49669283	0.210299791	4.7489203
34.99949552	0.196800082	5.074677486
37.50229821	0.181719358	5.495820343
39.99848655	0.170839921	5.845805482
42.50128924	0.160049006	6.23994469
44.99747758	0.152377631	6.55409158
47.50028027	0.14265784	7.000645345
50.00308296	0.134621751	7.41854073
52.4992713	0.125896956	7.932653635
55.00201794	0.120704216	8.273919357
57.49826233	0.11459438	8.715060408

$$x_{pc}/D_e = 4.4971 + \frac{0.9914 - 0.99}{0.9914 - 0.9794} \times (4.9990 - 4.4971)$$

$$\Rightarrow x_{pc} = 4.5557 D_e$$

## APPENDIX D

### Curve fitting of the mean streamwise centreline velocity decay data

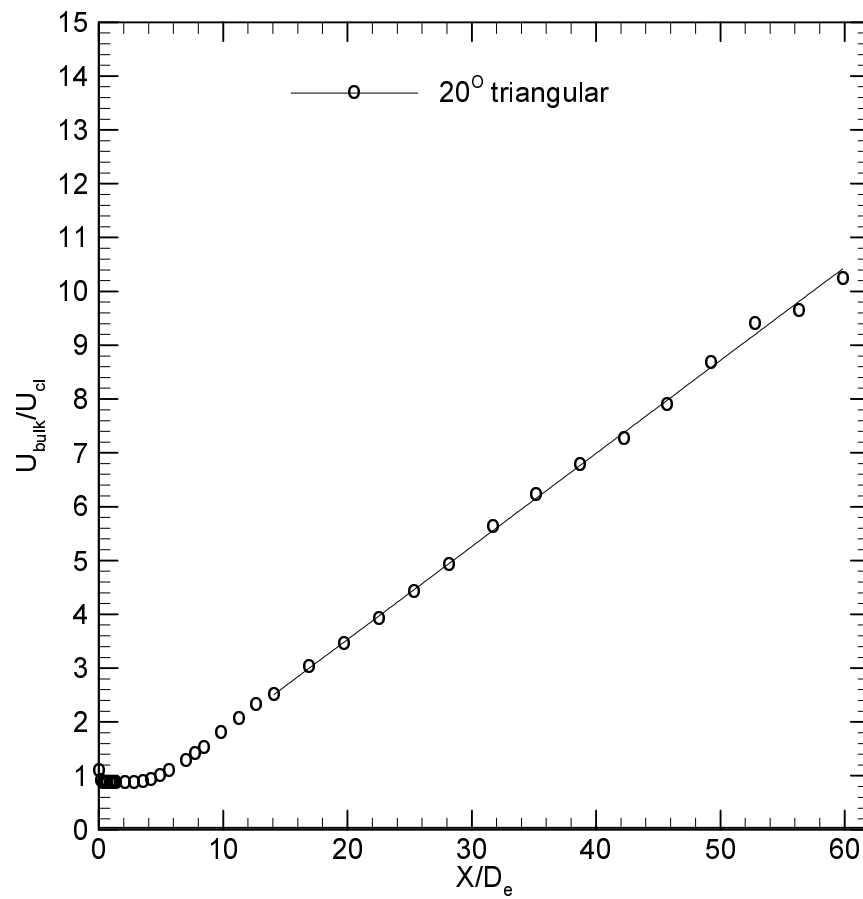


Fitted range:  $13.98 \leq X/D_e \leq 59.92$

$K_U = 0.182$

$C_U = 1.154$

**Figure D.1** Curve fitting of the mean streamwise centreline velocity decay data for the 10° jet.

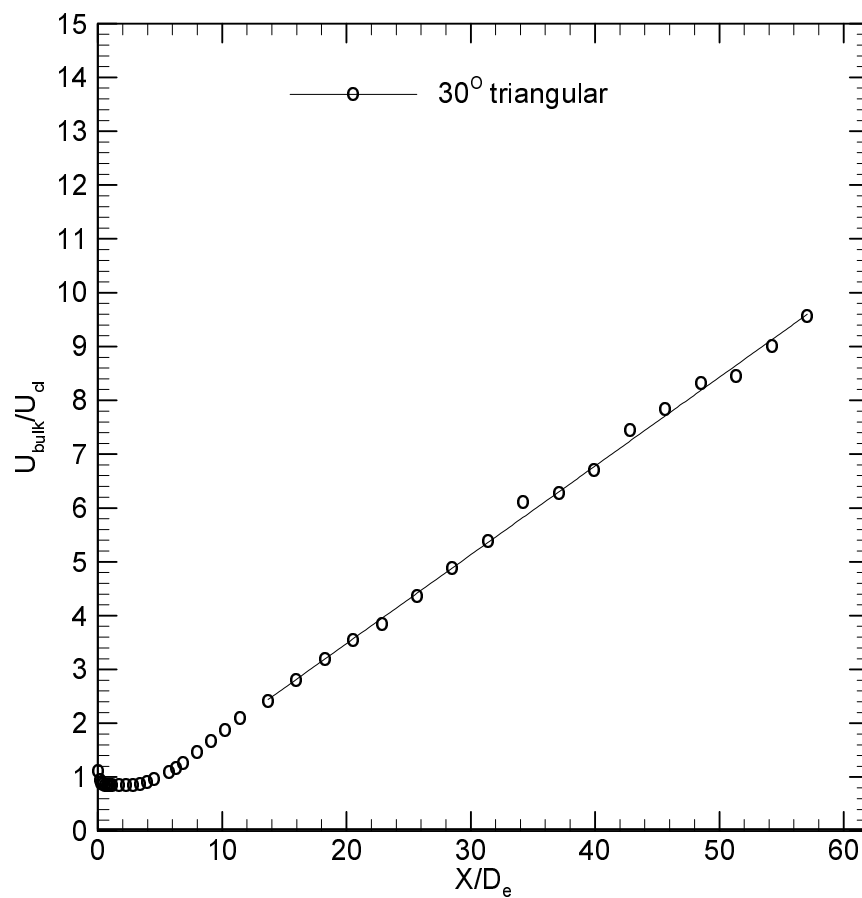


Fitted range:  $14.08 \leq X/D_e \leq 59.84$

$K_U = 0.173$

$C_U = 0.431$

**Figure D.2** Curve fitting of the mean streamwise centreline velocity decay data for the 20° jet.

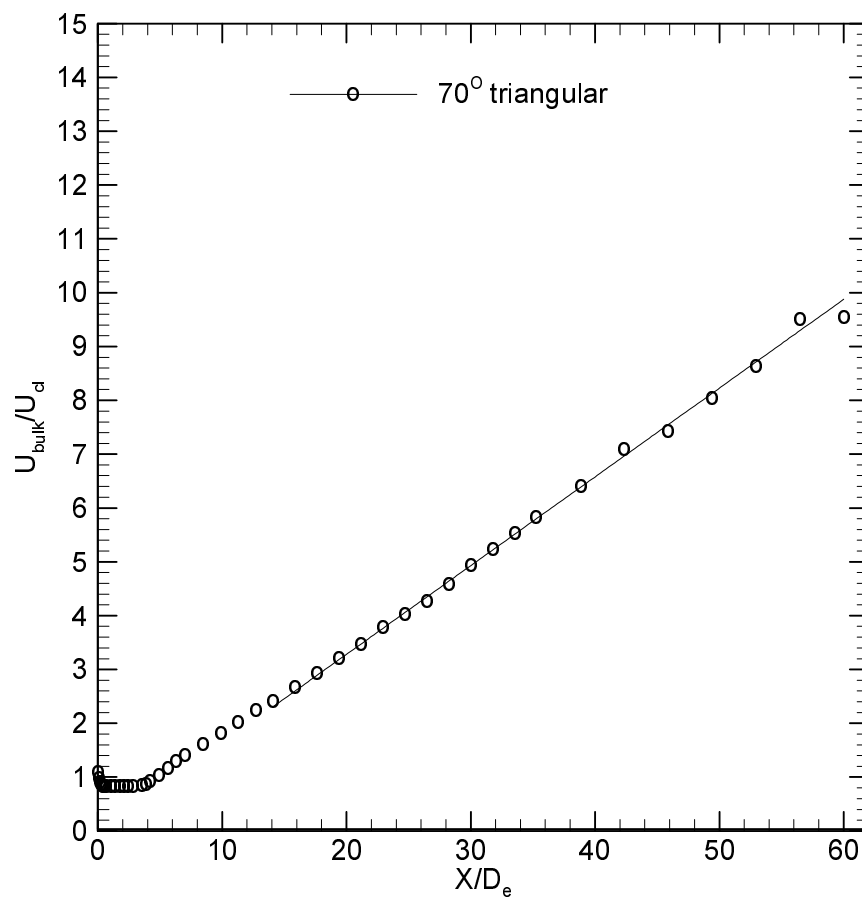


Fitted range:  $13.70 \leq X/D_e \leq 57.08$

$K_U = 0.165$

$C_U = 1.100$

**Figure D.3** Curve fitting of the mean streamwise centreline velocity decay data for the 30° jet.

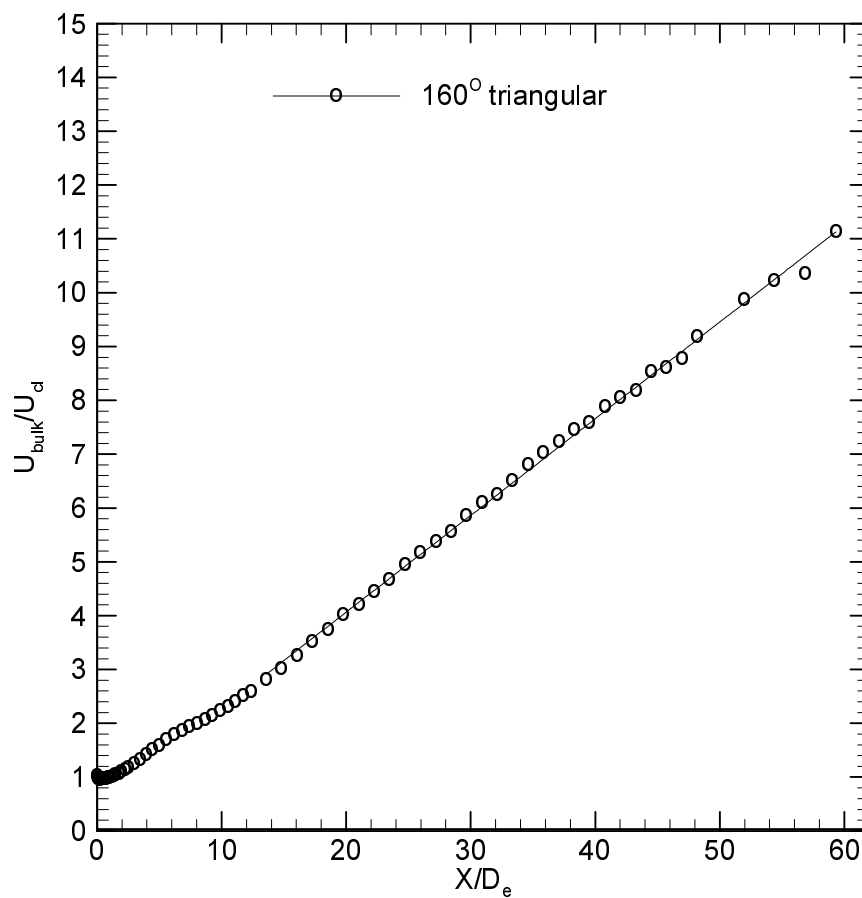


Fitted range:  $14.13 \leq X/D_e \leq 60.02$

$K_U = 0.165$

$C_U = -0.094$

**Figure D.4** Curve fitting of the mean streamwise centreline velocity decay data for the 70° jet.

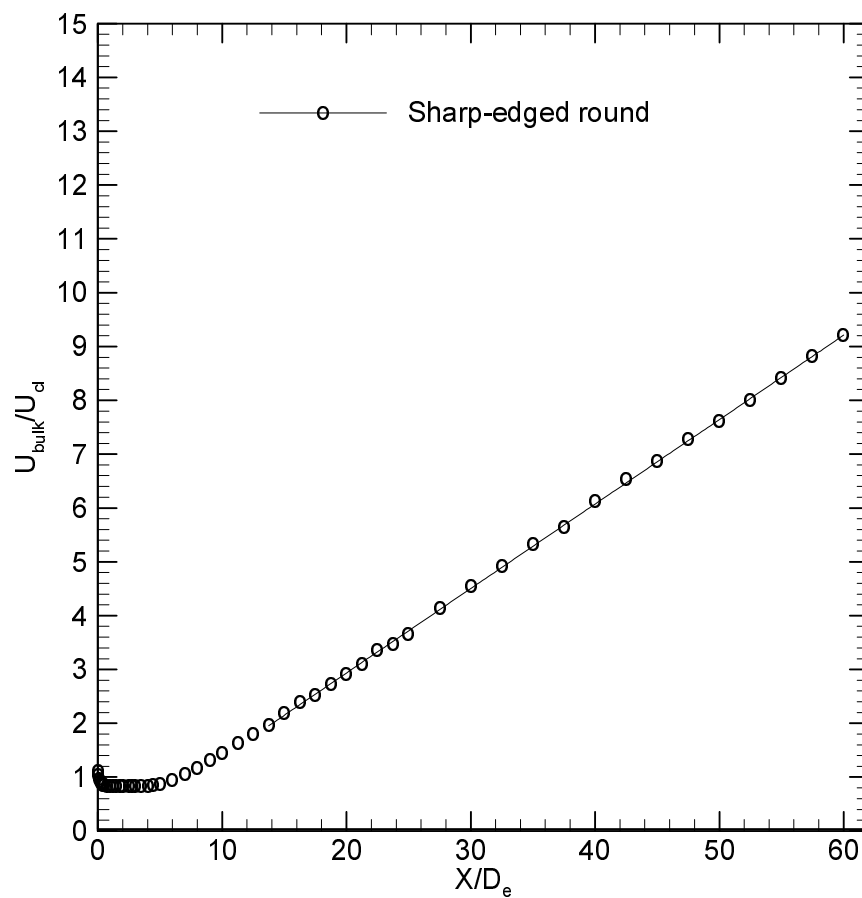


Fitted range:  $13.60 \leq X/D_e \leq 59.33$

$K_U = 0.180$

$C_U = 2.625$

**Figure D.5** Curve fitting of the mean streamwise centreline velocity decay data for the 160° jet.

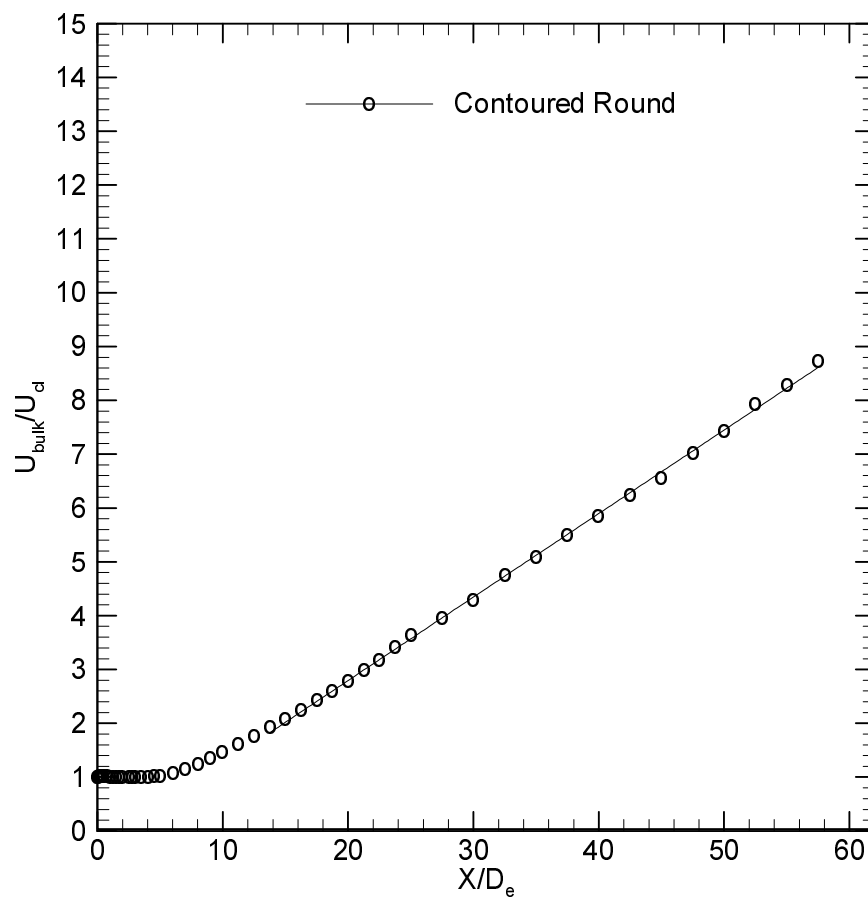


Fitted range:  $13.75 \leq X/D_e \leq 60.0$

$K_U = 0.157$

$C_U = -1.298$

**Figure D.6** Curve fitting of the mean streamwise centreline velocity decay data for the sharp-edged orifice round jet.



Fitted range:  $13.75 \leq X/D_e \leq 57.50$

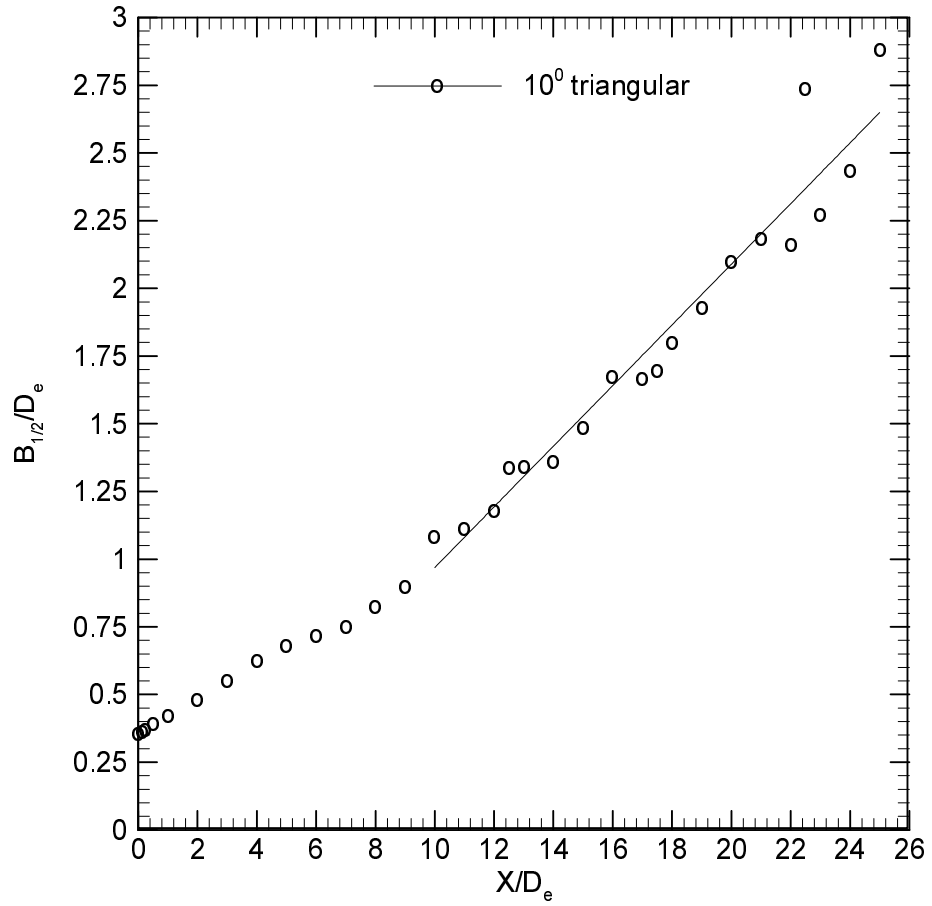
$K_U = 0.155$

$C_U = -1.979$

**Figure D.7** Curve fitting of the mean streamwise centreline velocity decay data for the contoured nozzle round jet.

## APPENDIX E

### Curve fitting of the geometric mean of the half-velocity widths

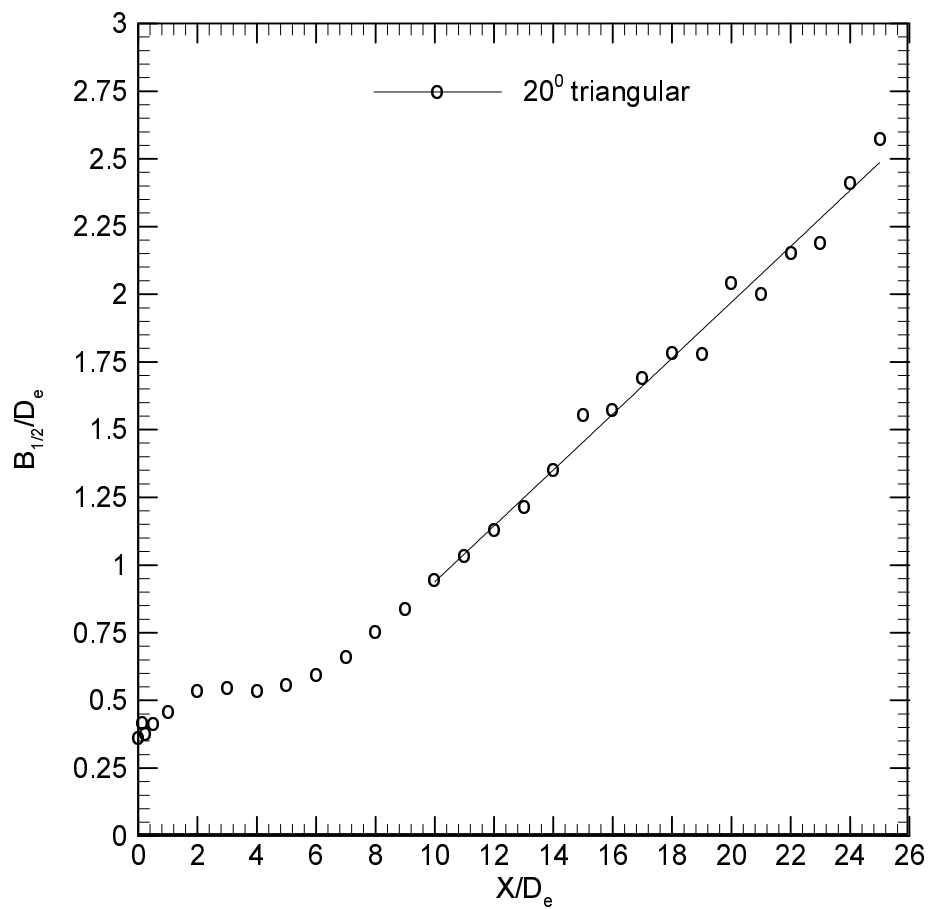


Fitted range:  $10 \leq X/D_e \leq 25$

$K_s = 0.112$

$C_s = -1.349$

**Figure E.1** Curve fitting of the geometric mean of half-velocity width data for the  $10^\circ$  jet.

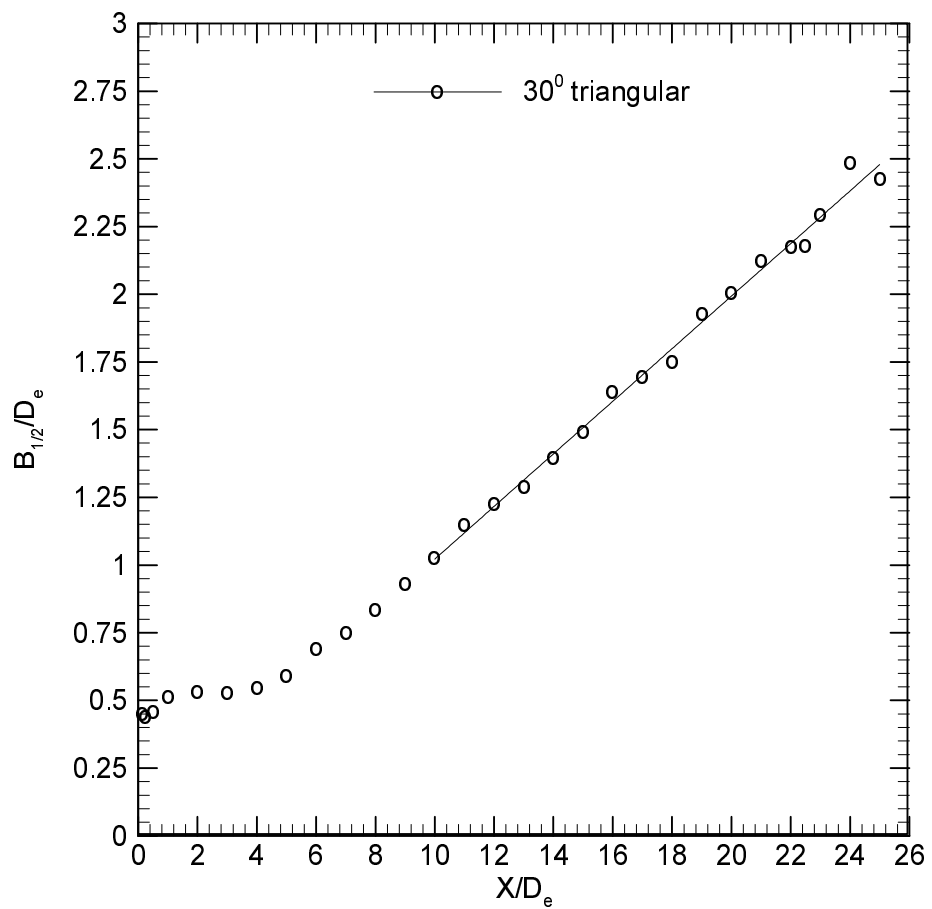


Fitted range:  $10 \leq X/D_e \leq 25$

$K_s = 0.103$

$C_s = -0.912$

**Figure E.2** Curve fitting of the geometric mean of half-velocity width data for the 20° jet.

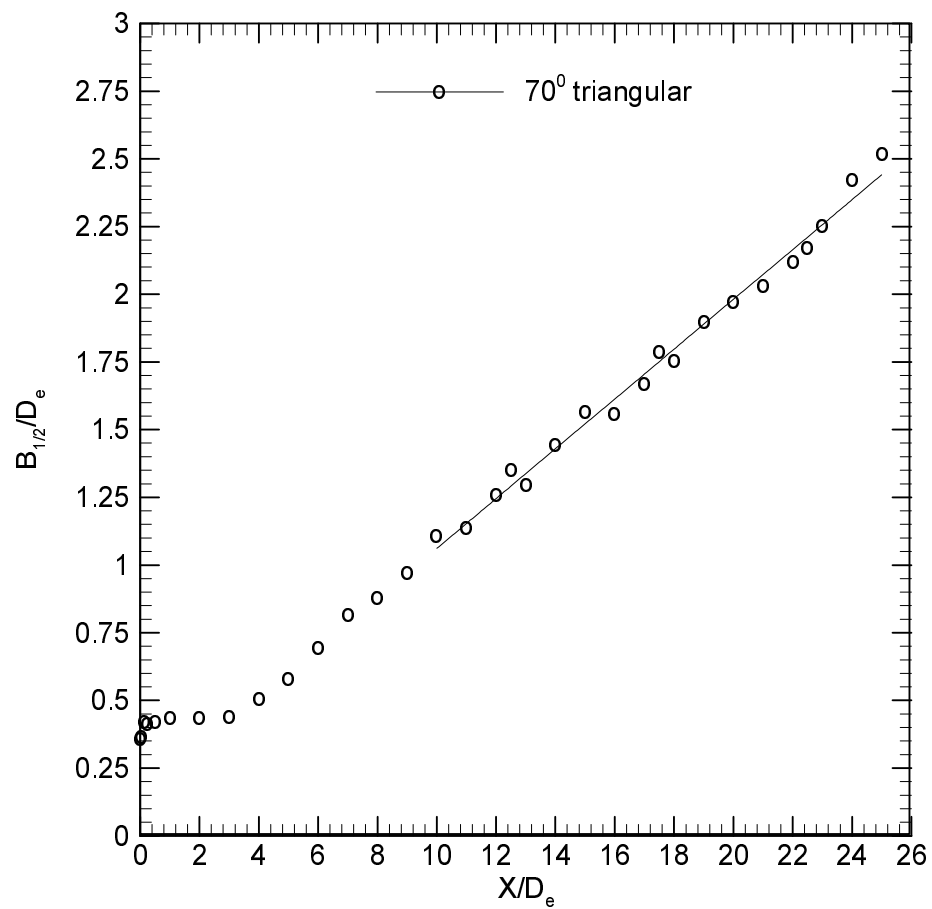


Fitted range:  $10 \leq X/D_e \leq 25$

$K_s = 0.097$

$C_s = 0.527$

**Figure E.3** Curve fitting of the geometric mean of half-velocity width data for the 30° jet.

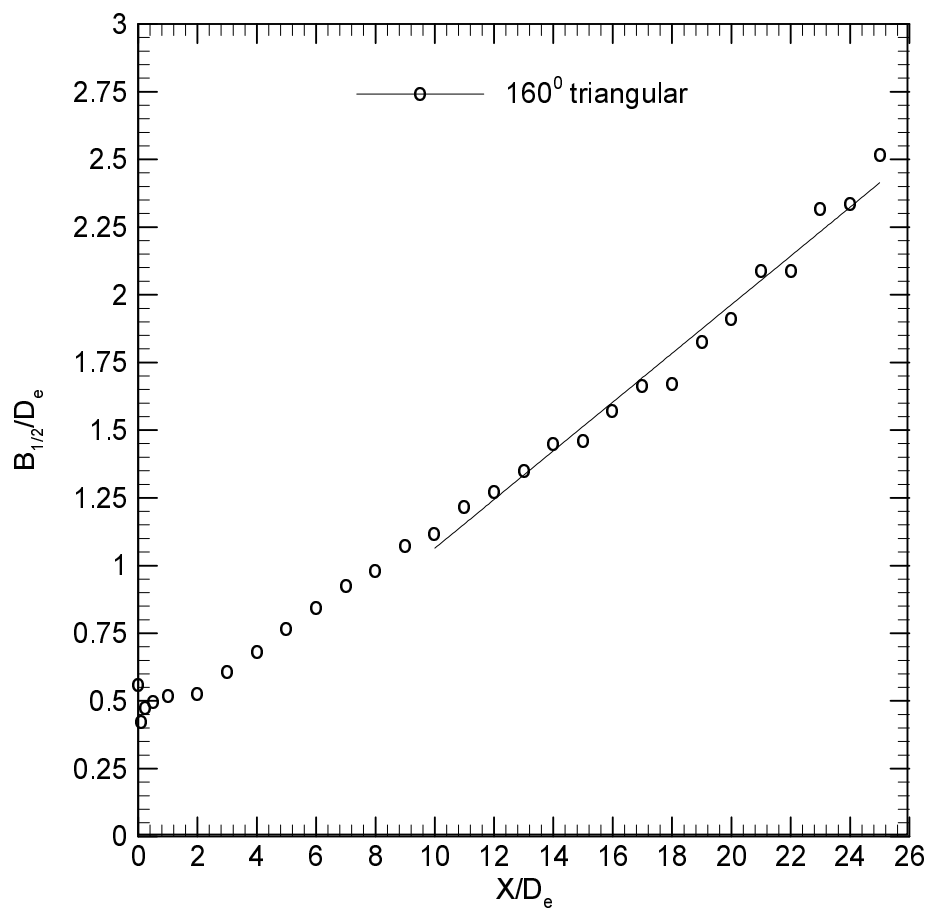


Fitted range:  $10 \leq X/D_e \leq 25$

$K_s = 0.092$

$C_s = 1.542$

**Figure E.4** Curve fitting of the geometric mean of half-velocity width data for the 70° jet.

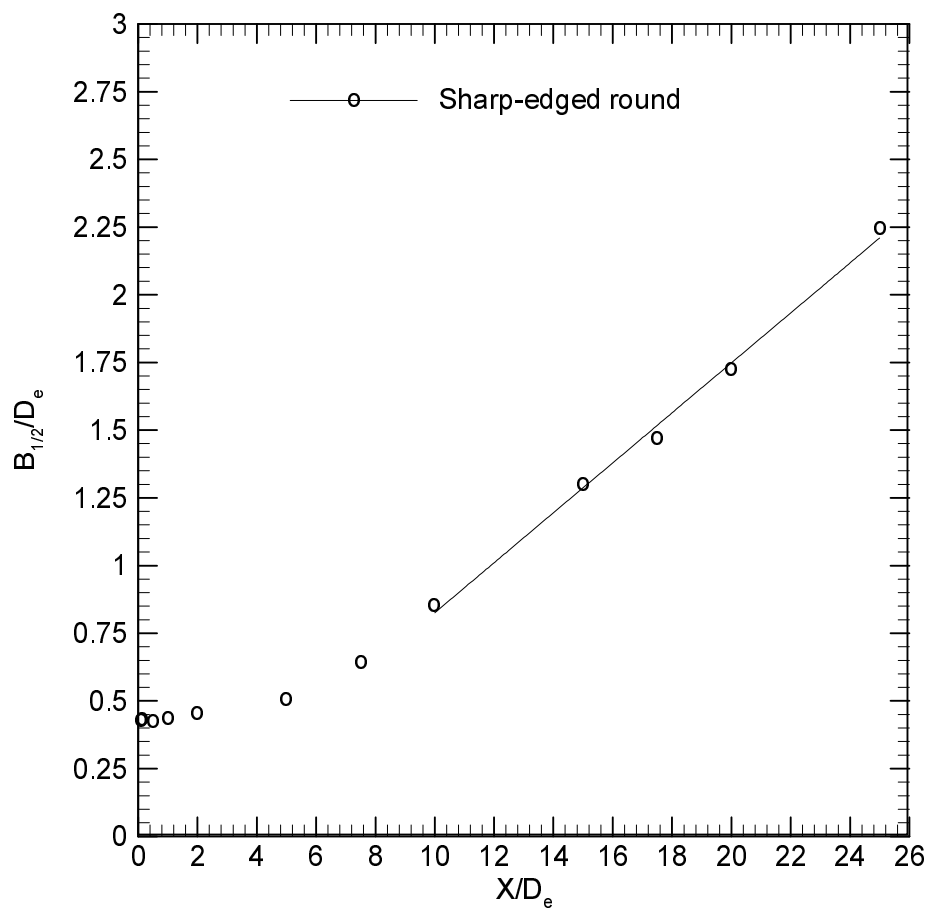


Fitted range:  $10 \leq X/D_e \leq 25$

$K_s = 0.090$

$C_s = 1.829$

**Figure E.5** Curve fitting of the geometric mean of half-velocity width data for the 160° jet.

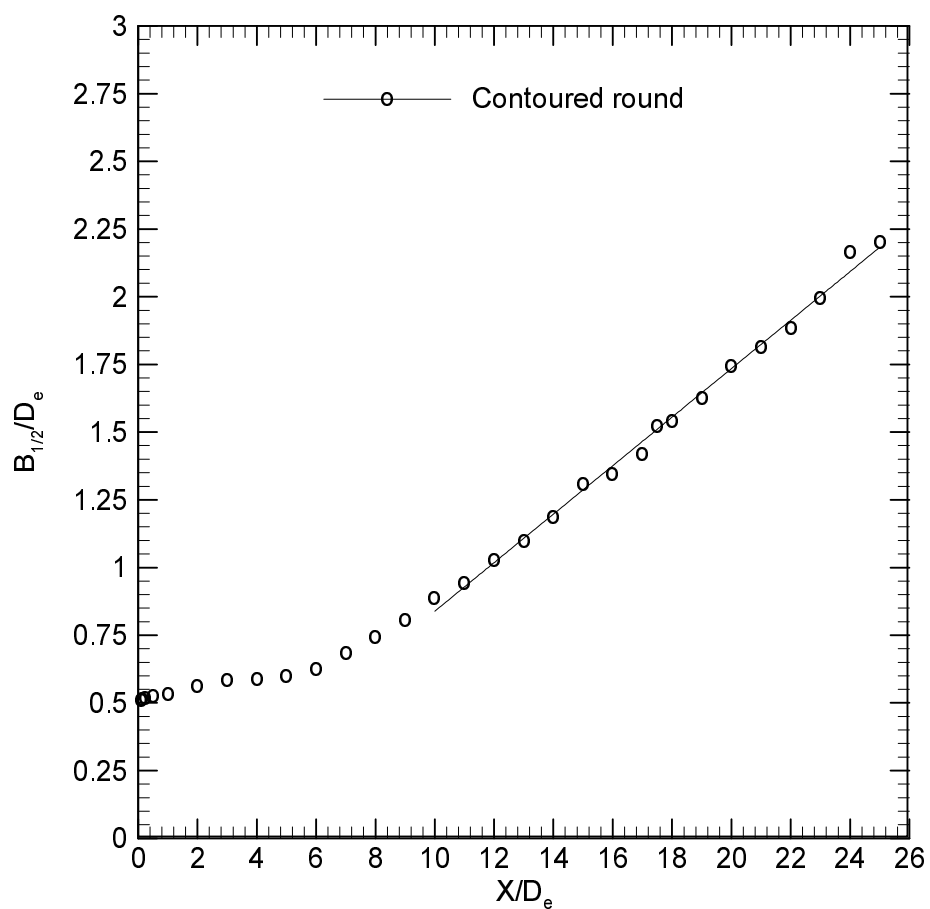


Fitted range:  $10 \leq X/D_e \leq 25$

$K_s = 0.092$

$C_s = -1.050$

**Figure E.6** Curve fitting of the geometric mean of half-velocity width data for the sharp-edged orifice round jet.



Fitted range:  $10 \leq X/D_e \leq 25$

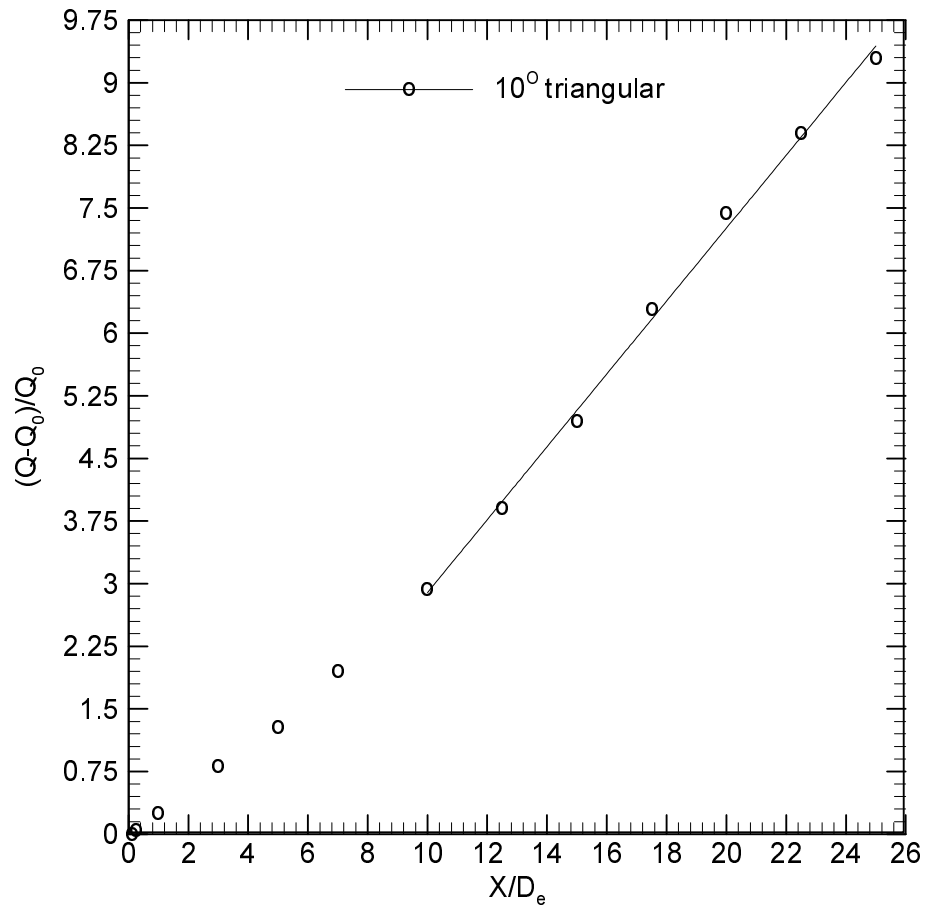
$K_s = 0.090$

$C_s = -0.631$

**Figure E.7** Curve fitting of the geometric mean of half-velocity width data for the contoured nozzle round jet.

## APPENDIX F

### Curve fitting of the mass entrainment ratio data



Fitted range:  $10 \leq X/D_e \leq 25$

$K_e = 0.436$

$C_e = -3.368$

**Figure F.1** Curve fitting of the mass entrainment ratio data for the  $10^\circ$  jet.

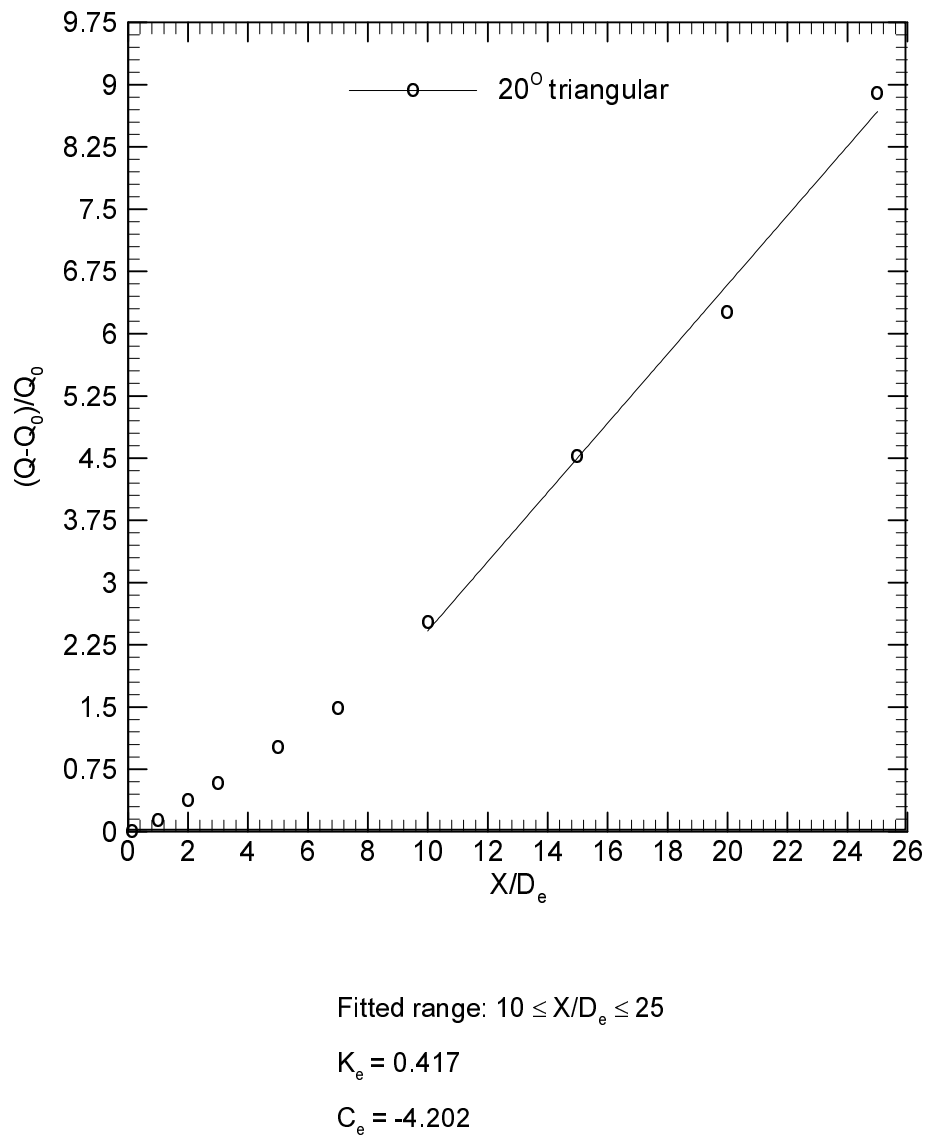
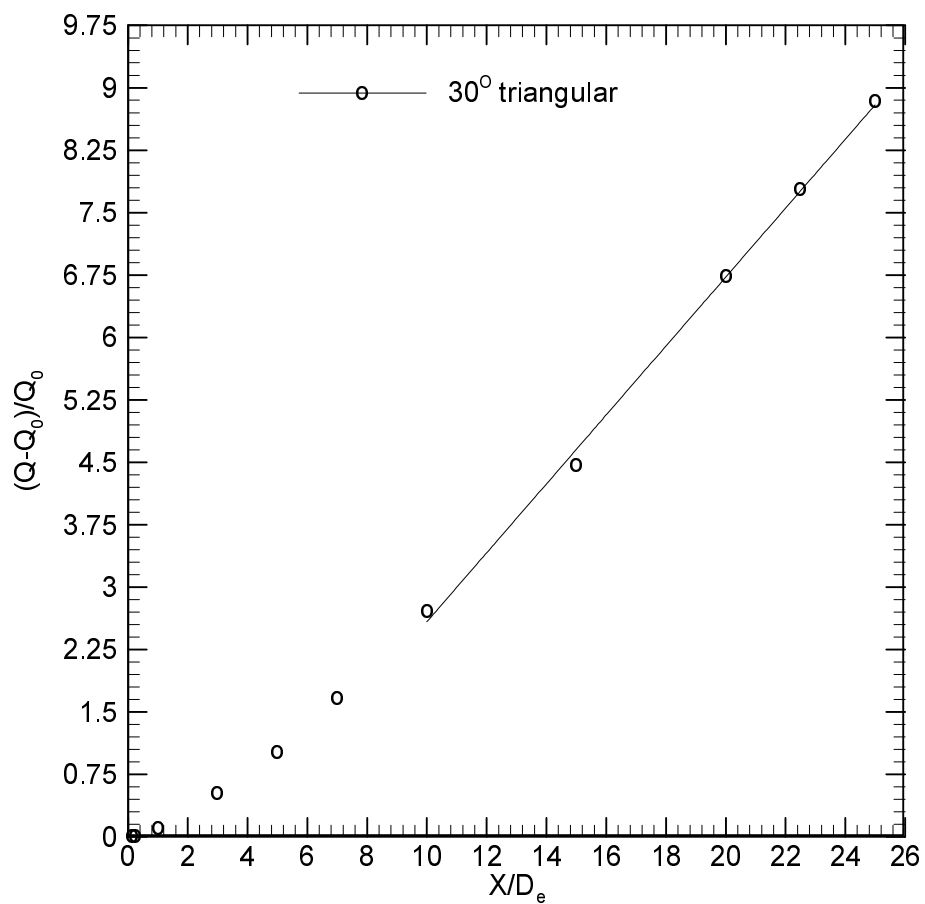


**Figure F.2** Curve fitting of the mass entrainment ratio data for the 20° jet.

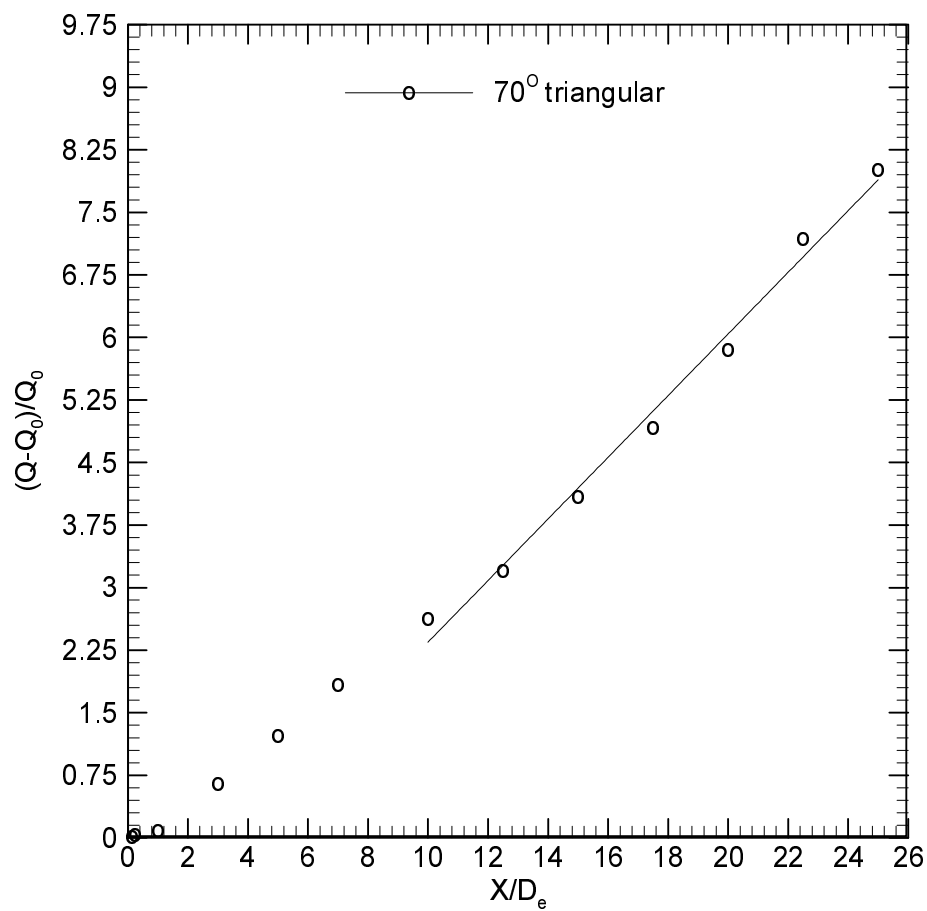


Fitted range:  $10 \leq X/D_e \leq 25$

$K_e = 0.414$

$C_e = -3.759$

**Figure F.3** Curve fitting of the mass entrainment ratio data for the 30° jet.



Fitted range:  $10 \leq X/D_0 \leq 25$

$K_e = 0.370$

$C_e = -3.652$

**Figure F.4** Curve fitting of the mass entrainment ratio data for the 70° jet.

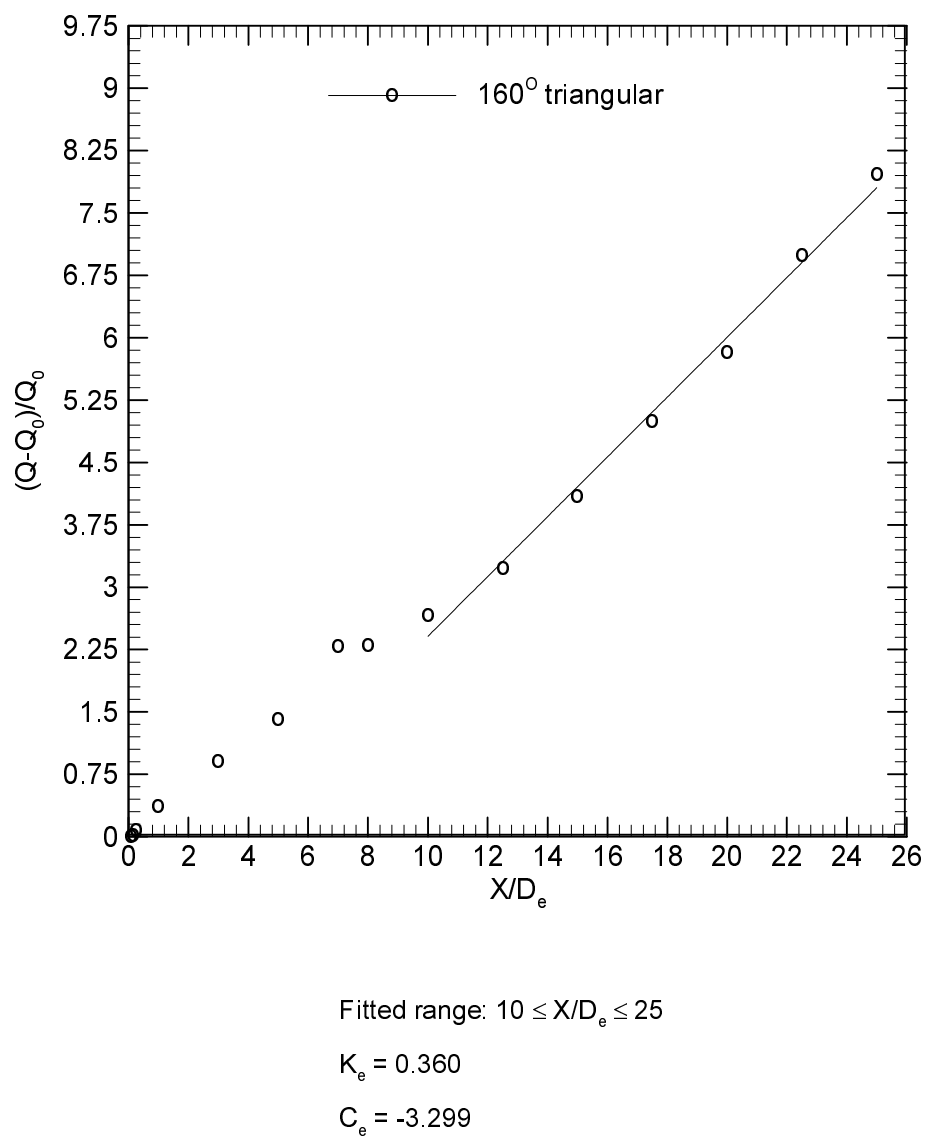


**Figure F.5** Curve fitting of the mass entrainment ratio data for the 160° jet.

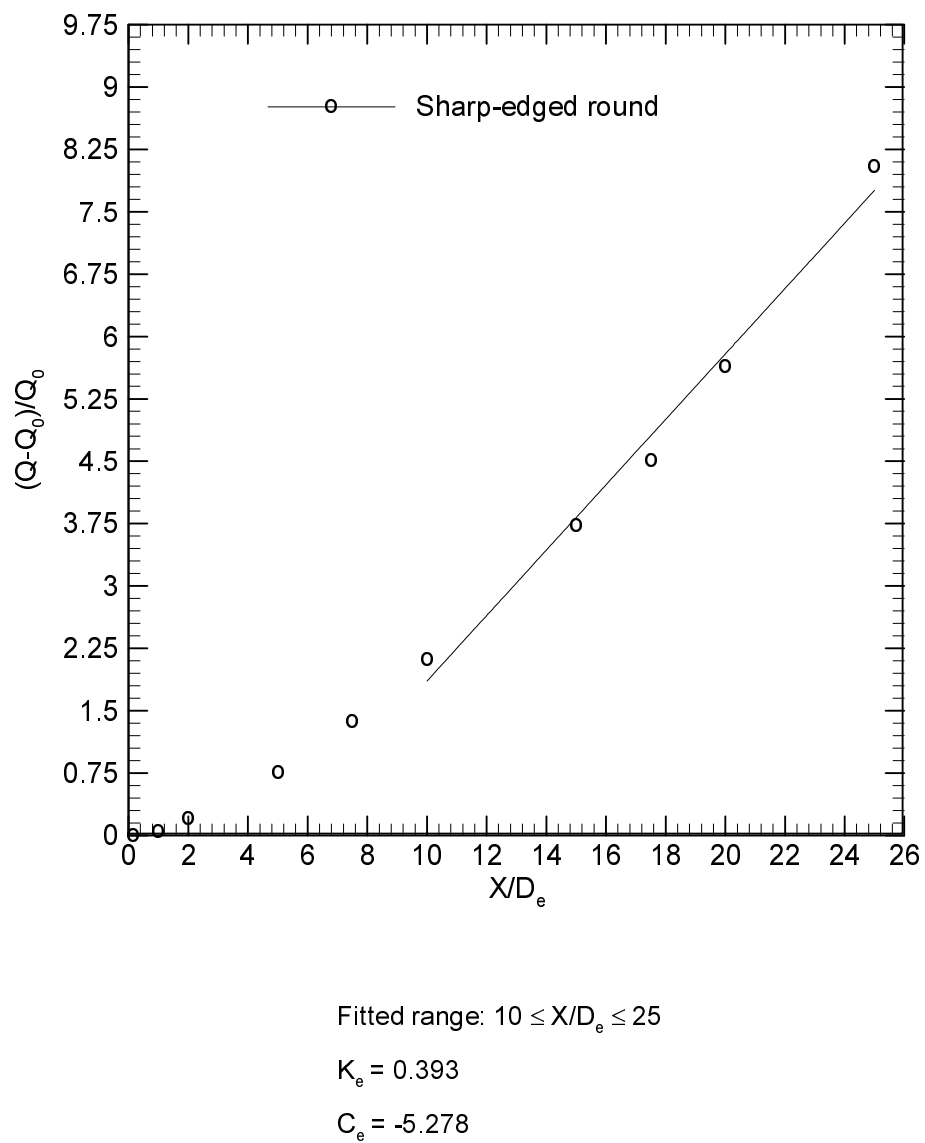
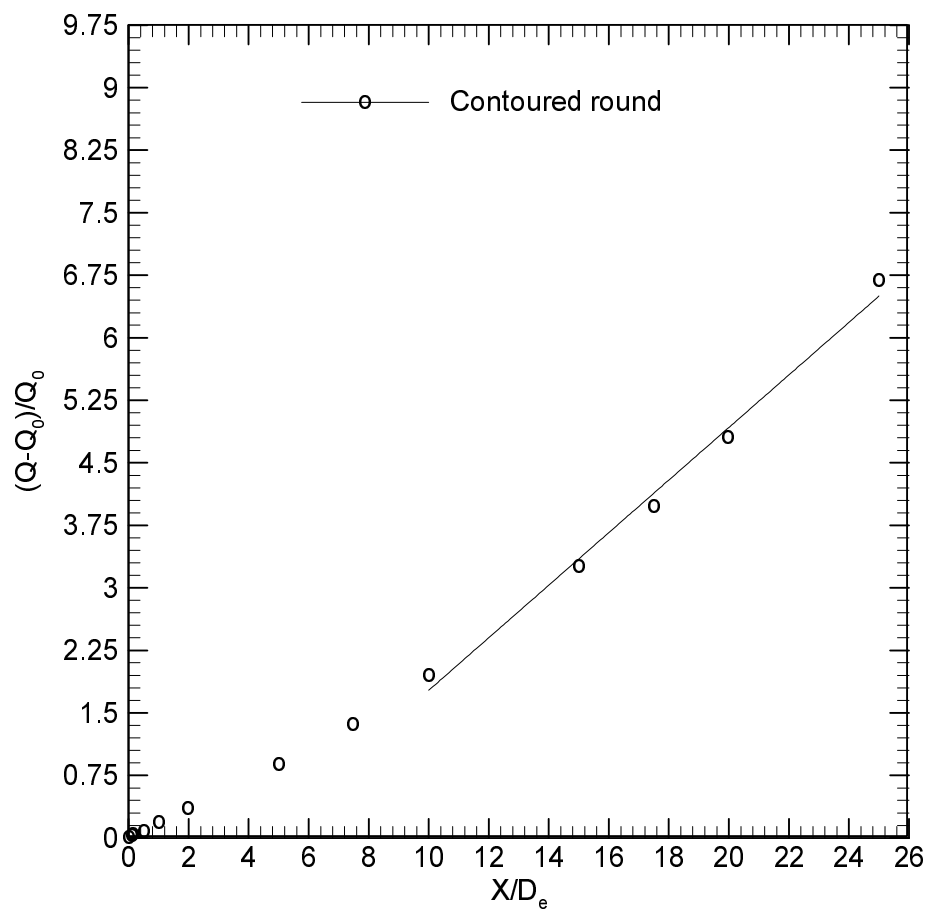


**Figure F.6** Curve fitting of the mass entrainment ratio data for the sharp-edged orifice round jet.



Fitted range:  $10 \leq X/D_e \leq 25$

$K_e = 0.315$

$C_e = -4.381$

**Figure F.7** Curve fitting of the mass entrainment ratio data for the contoured nozzle round jet.

## APPENDIX G

### Derivation of the decay law of the mean streamwise centreline velocity in the developed flow region

The Navier-Stokes equations for incompressible steady flow can be written as:

$$\frac{\partial u^2}{\partial x} + \frac{\partial uv}{\partial y} + \frac{\partial uw}{\partial z} = -\frac{1}{\rho} \frac{\partial p}{\partial x} + \nu \left[ \frac{\partial^2 u}{\partial x^2} + \frac{\partial^2 u}{\partial y^2} + \frac{\partial^2 u}{\partial z^2} \right] \quad (\text{G.1})$$

$$\frac{\partial vu}{\partial x} + \frac{\partial v^2}{\partial y} + \frac{\partial vw}{\partial z} = -\frac{1}{\rho} \frac{\partial p}{\partial y} + \nu \left[ \frac{\partial^2 v}{\partial x^2} + \frac{\partial^2 v}{\partial y^2} + \frac{\partial^2 v}{\partial z^2} \right] \quad (\text{G.2})$$

$$\frac{\partial wu}{\partial x} + \frac{\partial wv}{\partial y} + \frac{\partial w^2}{\partial z} = -\frac{1}{\rho} \frac{\partial p}{\partial z} + \nu \left[ \frac{\partial^2 w}{\partial x^2} + \frac{\partial^2 w}{\partial y^2} + \frac{\partial^2 w}{\partial z^2} \right] \quad (\text{G.3})$$

and the continuity equation as:

$$\frac{\partial u}{\partial x} + \frac{\partial v}{\partial y} + \frac{\partial w}{\partial z} = 0 \quad (\text{G.4})$$

(see Schlichting 1968).

Decomposing the instantaneous velocity and pressure into mean and fluctuating parts, the so called double decomposition, and Reynolds averaging subsequently, the continuity equation becomes:

$$\frac{\partial \bar{u}}{\partial x} + \frac{\partial \bar{v}}{\partial y} + \frac{\partial \bar{w}}{\partial z} = 0 \quad (\text{G.5})$$

$$\frac{\partial u'}{\partial x} + \frac{\partial v'}{\partial y} + \frac{\partial w'}{\partial z} = 0 \quad (\text{G.6})$$

So, both of time-averaged and fluctuating velocity components satisfy the incompressible flow form of the continuity equation.

Applying double decomposition and Reynolds averaging also to the Navier-Stokes equations results in:

$$\bar{u} \frac{\partial \bar{u}}{\partial x} + \bar{v} \frac{\partial \bar{u}}{\partial y} + \bar{w} \frac{\partial \bar{u}}{\partial z} = -\frac{1}{\rho} \frac{\partial \bar{p}}{\partial x} + \nu \left[ \frac{\partial^2 \bar{u}}{\partial x^2} + \frac{\partial^2 \bar{u}}{\partial y^2} + \frac{\partial^2 \bar{u}}{\partial z^2} \right] - \left[ \frac{\partial}{\partial x} (\overline{u'^2}) + \frac{\partial}{\partial y} (\overline{u'v'}) + \frac{\partial}{\partial z} (\overline{u'w'}) \right] \quad (\text{G.7})$$

$$\bar{u} \frac{\partial \bar{v}}{\partial x} + \bar{v} \frac{\partial \bar{v}}{\partial y} + \bar{w} \frac{\partial \bar{v}}{\partial z} = -\frac{1}{\rho} \frac{\partial \bar{p}}{\partial y} + \nu \left[ \frac{\partial^2 \bar{v}}{\partial x^2} + \frac{\partial^2 \bar{v}}{\partial y^2} + \frac{\partial^2 \bar{v}}{\partial z^2} \right] - \left[ \frac{\partial}{\partial x} (\overline{u'v'}) + \frac{\partial}{\partial y} (\overline{v'^2}) + \frac{\partial}{\partial z} (\overline{v'w'}) \right] \quad (\text{G.8})$$

$$\bar{u} \frac{\partial \bar{w}}{\partial x} + \bar{v} \frac{\partial \bar{w}}{\partial y} + \bar{w} \frac{\partial \bar{w}}{\partial z} = -\frac{1}{\rho} \frac{\partial \bar{p}}{\partial z} + \nu \left[ \frac{\partial^2 \bar{w}}{\partial x^2} + \frac{\partial^2 \bar{w}}{\partial y^2} + \frac{\partial^2 \bar{w}}{\partial z^2} \right] - \left[ \frac{\partial}{\partial x} (\overline{u'w'}) + \frac{\partial}{\partial y} (\overline{v'w'}) + \frac{\partial}{\partial z} (\overline{w'^2}) \right] \quad (\text{G.9})$$

Where,  $\bar{u}$ ,  $\bar{v}$ ,  $\bar{w}$  and  $u'$ ,  $v'$ ,  $w'$  are respectively mean and fluctuating parts of the velocities,  $\bar{p}$  is the mean pressure,  $\rho$  is the density and  $\nu$  is kinematic viscosity.

(G.5), (G.7), (G.8) and (G.9) are the governing equations of three dimensional turbulent jets.

The thin shear-layer approximation, namely,  $\partial/\partial x \ll \partial/\partial y$  and  $\partial/\partial x \ll \partial/\partial z$  will make  $\partial^2 \bar{u}/\partial x^2$  in (G.7) negligible and (G.7) can then be written as:

$$\bar{u} \frac{\partial \bar{u}}{\partial x} + \bar{v} \frac{\partial \bar{u}}{\partial y} + \bar{w} \frac{\partial \bar{u}}{\partial z} = -\frac{1}{\rho} \frac{\partial \bar{p}}{\partial x} + \nu \left[ \frac{\partial^2 \bar{u}}{\partial y^2} + \frac{\partial^2 \bar{u}}{\partial z^2} \right] - \left[ \frac{\partial}{\partial x} (\overline{u'^2}) + \frac{\partial}{\partial y} (\overline{u'v'}) + \frac{\partial}{\partial z} (\overline{u'w'}) \right] \quad (\text{G.10})$$

Application of the thin shear-layer approximation to (G.8) and (G.9) results in (G.11) and (G.12), respectively.

$$0 = -\frac{1}{\rho} \frac{\partial \bar{p}}{\partial y} - \frac{\partial}{\partial y} (\overline{v'^2}) \quad (\text{G.11})$$

$$0 = -\frac{1}{\rho} \frac{\partial \bar{p}}{\partial z} - \frac{\partial}{\partial z} (\overline{w'^2}) \quad (\text{G.12})$$

Integration of (G.11) with respect to  $y$  from  $y = y$  to  $y = \infty$  gives:

$$\begin{aligned} \int_y^\infty \frac{1}{\rho} \frac{\partial \bar{p}}{\partial y} dy &= - \int_y^\infty \frac{\partial}{\partial y} (\overline{v'^2}) dy \\ \Rightarrow \int_y^\infty d\bar{p} &= -\rho \int_y^\infty \overline{v'^2} \\ \Rightarrow \bar{p}_\infty - \bar{p} &= \rho \overline{v'^2} \\ \Rightarrow \bar{p} &= \bar{p}_\infty - \rho \overline{v'^2} \end{aligned} \quad (\text{G.13})$$

Differentiation of (G.13) with respect to  $x$  gives:

$$\frac{\partial \bar{p}}{\partial x} = \frac{\partial \bar{p}_x}{\partial x} - \frac{\partial}{\partial x} (\rho \overline{v'^2}) \quad (\text{G.14})$$

Similarly, integration of (G.12) with respect to  $z$  from  $z = z$  to  $z = \infty$  and differentiation with respect to  $x$ , afterwards, give:

$$\frac{\partial \bar{p}}{\partial x} = \frac{\partial \bar{p}_x}{\partial x} - \frac{\partial}{\partial x} (\rho \overline{w'^2}) \quad (\text{G.15})$$

Addition of (G.14) and (G.15) yields:

$$\begin{aligned} 2 \frac{\partial \bar{p}}{\partial x} &= 2 \frac{\partial \bar{p}_x}{\partial x} - \frac{\partial}{\partial x} (\rho \overline{v'^2} + \rho \overline{w'^2}) \\ \Rightarrow \frac{\partial \bar{p}}{\partial x} &= \frac{\partial \bar{p}_x}{\partial x} - \frac{\partial}{\partial x} \left[ \rho \left( \frac{\overline{v'^2} + \overline{w'^2}}{2} \right) \right] \end{aligned} \quad (\text{G.16})$$

Inserting (G.16) into (G.10) results in:

$$\begin{aligned} \bar{u} \frac{\partial \bar{u}}{\partial x} + \bar{v} \frac{\partial \bar{u}}{\partial y} + \bar{w} \frac{\partial \bar{u}}{\partial z} &= -\frac{1}{\rho} \frac{\partial \bar{p}_x}{\partial x} + \frac{\partial}{\partial x} \left( \frac{\overline{v'^2 + w'^2}}{2} \right) + \nu \left[ \frac{\partial^2 \bar{u}}{\partial y^2} + \frac{\partial^2 \bar{u}}{\partial z^2} \right] - \left[ \frac{\partial}{\partial x} (\overline{u'^2}) + \frac{\partial}{\partial y} (\overline{u' \cdot v'}) + \right. \\ &\quad \left. \frac{\partial}{\partial z} (\overline{u' \cdot w'}) \right] \\ \Rightarrow \bar{u} \frac{\partial \bar{u}}{\partial x} + \bar{v} \frac{\partial \bar{u}}{\partial y} + \bar{w} \frac{\partial \bar{u}}{\partial z} &= -\frac{1}{\rho} \frac{\partial \bar{p}_x}{\partial x} + \nu \left[ \frac{\partial^2 \bar{u}}{\partial y^2} + \frac{\partial^2 \bar{u}}{\partial z^2} \right] - \frac{\partial}{\partial x} \left( \overline{u'^2} - \frac{\overline{v'^2 + w'^2}}{2} \right) - \frac{\partial}{\partial y} (\overline{u' \cdot v'}) - \\ &\quad \frac{\partial}{\partial z} (\overline{u' \cdot w'}) \end{aligned} \quad (\text{G.17})$$

and since  $\overline{v'^2} \simeq \overline{w'^2}$

$$\begin{aligned} \Rightarrow \bar{u} \frac{\partial \bar{u}}{\partial x} + \bar{v} \frac{\partial \bar{u}}{\partial y} + \bar{w} \frac{\partial \bar{u}}{\partial z} &= -\frac{1}{\rho} \frac{\partial \bar{p}_x}{\partial x} + \nu \left[ \frac{\partial^2 \bar{u}}{\partial y^2} + \frac{\partial^2 \bar{u}}{\partial z^2} \right] - \frac{\partial}{\partial x} (\overline{u'^2} - \overline{v'^2}) - \frac{\partial}{\partial y} (\overline{u' \cdot v'}) - \\ &\quad \frac{\partial}{\partial z} (\overline{u' \cdot w'}) \end{aligned} \quad (\text{G.18})$$

From the thin shear-layer approximation,  $\frac{\partial}{\partial x} (\overline{u'^2} - \overline{v'^2})$  is much smaller than other terms in (G.18). So, ignoring this term gives:

$$\begin{aligned} \Rightarrow \bar{u} \frac{\partial \bar{u}}{\partial x} + \bar{v} \frac{\partial \bar{u}}{\partial y} + \bar{w} \frac{\partial \bar{u}}{\partial z} &= -\frac{1}{\rho} \frac{\partial \bar{p}_x}{\partial x} + \nu \left[ \frac{\partial^2 \bar{u}}{\partial y^2} + \frac{\partial^2 \bar{u}}{\partial z^2} \right] - \frac{\partial}{\partial y} (\overline{u' \cdot v'}) - \frac{\partial}{\partial z} (\overline{u' \cdot w'}) \\ \Rightarrow \bar{u} \frac{\partial \bar{u}}{\partial x} + \bar{v} \frac{\partial \bar{u}}{\partial y} + \bar{w} \frac{\partial \bar{u}}{\partial z} &= -\frac{1}{\rho} \frac{\partial \bar{p}_x}{\partial x} + \nu \frac{\partial^2 \bar{u}}{\partial y^2} - \frac{\partial}{\partial y} (\overline{u' \cdot v'}) + \nu \frac{\partial^2 \bar{u}}{\partial z^2} - \frac{\partial}{\partial z} (\overline{u' \cdot w'}) \\ \Rightarrow \bar{u} \frac{\partial \bar{u}}{\partial x} + \bar{v} \frac{\partial \bar{u}}{\partial y} + \bar{w} \frac{\partial \bar{u}}{\partial z} &= -\frac{1}{\rho} \frac{\partial \bar{p}_x}{\partial x} + \nu \frac{\partial^2 \bar{u}}{\partial y^2} - \frac{\partial}{\partial y} (\overline{u' \cdot v'}) + \nu \frac{\partial^2 \bar{u}}{\partial z^2} - \frac{\partial}{\partial z} (\overline{u' \cdot w'}) \\ \Rightarrow \bar{u} \frac{\partial \bar{u}}{\partial x} + \bar{v} \frac{\partial \bar{u}}{\partial y} + \bar{w} \frac{\partial \bar{u}}{\partial z} &= -\frac{1}{\rho} \frac{\partial \bar{p}_x}{\partial x} + \frac{1}{\rho} \frac{\partial}{\partial y} \left( \mu \cdot \frac{\partial \bar{u}}{\partial y} \right) + \frac{1}{\rho} \frac{\partial}{\partial y} (-\rho \overline{u' \cdot v'}) + \frac{1}{\rho} \frac{\partial}{\partial z} \left( \mu \cdot \frac{\partial \bar{u}}{\partial z} \right) + \\ &\quad \frac{1}{\rho} \frac{\partial}{\partial z} (-\rho \overline{u' \cdot w'}) \end{aligned}$$

$$\Rightarrow \bar{u} \frac{\partial \bar{u}}{\partial x} + \bar{v} \frac{\partial \bar{u}}{\partial y} + \bar{w} \frac{\partial \bar{u}}{\partial z} = -\frac{1}{\rho} \frac{\partial \bar{p}_x}{\partial x} + \frac{1}{\rho} \frac{\partial}{\partial y} (\tau_l + \tau_t)_y + \frac{1}{\rho} \frac{\partial}{\partial z} (\tau_l + \tau_t)_z \quad (\text{G.19})$$

In free turbulent flows, such as the free jet flows studied here,  $\tau_t$  is much larger than  $\tau_l$ .

As the pressure gradient in the axial direction is negligibly small, (G.19) can be written

as:

$$\bar{u} \frac{\partial \bar{u}}{\partial x} + \bar{v} \frac{\partial \bar{u}}{\partial y} + \bar{w} \frac{\partial \bar{u}}{\partial z} = \frac{1}{\rho} \frac{\partial \tau_t}{\partial y} + \frac{1}{\rho} \frac{\partial \tau_t}{\partial z} \quad (\text{G.20})$$

Multiplication of (G.20) by  $\rho$  and double integration from  $y = 0$  to  $y = \infty$  and  $z = 0$  to

$z = \infty$  give:

$$\begin{aligned} \rho \int_0^\infty \int_0^\infty \bar{u} \frac{\partial \bar{u}}{\partial x} dydz + \rho \int_0^\infty \int_0^\infty \bar{v} \frac{\partial \bar{u}}{\partial y} dydz + \rho \int_0^\infty \int_0^\infty \bar{w} \frac{\partial \bar{u}}{\partial z} dydz &= \int_0^\infty \int_0^\infty \frac{\partial \tau_t}{\partial y} dydz + \\ &\int_0^\infty \int_0^\infty \frac{\partial \tau_t}{\partial z} dydz \end{aligned} \quad (\text{G.21})$$

The first term in (G.21) is:

$$\begin{aligned} \rho \int_0^\infty \int_0^\infty \bar{u} \frac{\partial \bar{u}}{\partial x} dydz &= \frac{1}{2} \int_0^\infty \int_0^\infty \frac{\partial}{\partial x} (\rho \bar{u}^2) dydz \\ &= \frac{1}{2} \frac{d}{dx} \int_0^\infty \int_0^\infty (\rho \bar{u}^2) dydz; \end{aligned} \quad (\text{G.22})$$

the second term is:

$$\begin{aligned} \rho \int_0^\infty \int_0^\infty \bar{v} \frac{\partial \bar{u}}{\partial y} dydz &= \rho \int_0^\infty \left( |\bar{u}\bar{v}|_0^\infty - \int_0^\infty \frac{\partial \bar{v}}{\partial y} \bar{u} dy \right) dz \\ &= -\rho \int_0^\infty \int_0^\infty \frac{\partial \bar{v}}{\partial y} \bar{u} dy dz \\ &= -\rho \int_0^\infty \int_0^\infty \bar{u} \left( -\frac{\partial \bar{u}}{\partial x} - \frac{\partial \bar{w}}{\partial z} \right) dy dz \end{aligned}$$

$$\begin{aligned}
&= \rho \int_0^\infty \int_0^\infty \bar{u} \frac{\partial \bar{u}}{\partial x} dydz + \rho \int_0^\infty \int_0^\infty \bar{u} \frac{\partial \bar{w}}{\partial z} dydz \\
&= \frac{1}{2} \frac{d}{dx} \int_0^\infty \int_0^\infty (\rho \bar{u}^2) dydz + \rho \int_0^\infty \int_0^\infty \bar{u} \frac{\partial \bar{w}}{\partial z} dydz
\end{aligned} \tag{G.23}$$

Similarly, the third term is:

$$\rho \int_0^\infty \int_0^\infty \bar{w} \frac{\partial \bar{u}}{\partial x} dydz = \frac{1}{2} \frac{d}{dx} \int_0^\infty \int_0^\infty (\rho \bar{u}^2) dydz + \rho \int_0^\infty \int_0^\infty \bar{u} \frac{\partial \bar{v}}{\partial y} dydz \tag{G.24}$$

Inserting (G.22), (G.23) and (G.24) into (G.21) gives:

$$\begin{aligned}
&\frac{3}{2} \frac{d}{dx} \int_0^\infty \int_0^\infty (\rho \bar{u}^2) dydz + \rho \int_0^\infty \int_0^\infty \bar{u} \frac{\partial \bar{w}}{\partial z} dydz + \rho \int_0^\infty \int_0^\infty \bar{u} \frac{\partial \bar{v}}{\partial y} dydz = \int_0^\infty \int_0^\infty \frac{\partial \tau_t}{\partial y} dydz + \\
&\quad \int_0^\infty \int_0^\infty \frac{\partial \tau_t}{\partial z} dydz \\
&\Rightarrow \frac{3}{2} \frac{d}{dx} \int_0^\infty \int_0^\infty (\rho \bar{u}^2) dydz + \rho \int_0^\infty \int_0^\infty \bar{u} \left( -\frac{\partial \bar{u}}{\partial x} - \frac{\partial \bar{v}}{\partial y} \right) dydz + \rho \int_0^\infty \int_0^\infty \bar{u} \frac{\partial \bar{v}}{\partial y} dydz = \\
&\quad \int_0^\infty (|\tau_t|_0^\infty) dz + \int_0^\infty (|\tau_t|_0^\infty) dy \\
&\Rightarrow \frac{3}{2} \frac{d}{dx} \int_0^\infty \int_0^\infty (\rho \bar{u}^2) dydz - \frac{1}{2} \frac{d}{dx} \int_0^\infty \int_0^\infty (\rho \bar{u}^2) dydz = 0 \\
&\Rightarrow \frac{d}{dx} \int_0^\infty \int_0^\infty (\rho \bar{u}^2) dydz = 0
\end{aligned} \tag{G.25}$$

From (G.25), the linear momentum of the jet ( $\rho \bar{u}^2$ ) is constant in the streamwise direction.

Let the streamwise centreline velocity of the jet be  $U_{cl}$  and half-velocity widths in the central X-Y and X-Z planes be  $y_{1/2}$  and  $z_{1/2}$ , respectively. Normalization of (G.25) by the streamwise centreline velocity and half-velocity widths gives:

$$\frac{d}{dx} \int_0^\infty \int_0^\infty \left( \rho \left( \frac{\bar{u}}{U_{cl}} \right)^2 U_{cl}^2 y_{1/2} z_{1/2} \right) d\left(\frac{y}{y_{1/2}}\right) d\left(\frac{z}{z_{1/2}}\right) = 0 \quad (\text{G.26})$$

Assuming that  $U_{cl}$ ,  $y_{1/2}$ ,  $z_{1/2}$  vary with  $x$  as follows:

$$U_{cl} = C_1 x^p \quad (\text{G.27})$$

$$y_{1/2} = C_2 x^q \quad (\text{G.28})$$

$$z_{1/2} = C_3 x^r \quad (\text{G.29})$$

where  $C_1$ ,  $C_2$  and  $C_3$  are proportionality constants;  $p$  is the order of velocity decay rate along the streamwise direction and  $q$  and  $r$  are the orders of spreading rate along the streamwise direction in the central X-Y and X-Z planes, respectively.

(G.26) can now be written as:

$$\begin{aligned} & \frac{d}{dx} \int_0^\infty \int_0^\infty \left( \rho \left( \frac{\bar{u}}{U_{cl}} \right)^2 C_1^2 x^{2p} C_2 x^q C_3 x^r \right) d\left(\frac{y}{y_{1/2}}\right) d\left(\frac{z}{z_{1/2}}\right) = 0 \\ & \Rightarrow C_1^2 \cdot C_2 \cdot C_3 \frac{d}{dx} \int_0^\infty \int_0^\infty \left( \rho \left( \frac{\bar{u}}{U_{cl}} \right)^2 x^{2p+q+r} \right) d\left(\frac{y}{y_{1/2}}\right) d\left(\frac{z}{z_{1/2}}\right) = 0 \\ & \Rightarrow \frac{d}{dx} (x^{2p+q+r}) \int_0^\infty \int_0^\infty \rho \left( \frac{\bar{u}}{U_{cl}} \right)^2 d\left(\frac{y}{y_{1/2}}\right) d\left(\frac{z}{z_{1/2}}\right) = 0 \end{aligned}$$

Since  $\int_0^\infty \int_0^\infty \rho \left( \frac{\bar{u}}{U_{cl}} \right)^2 d\left(\frac{y}{y_{1/2}}\right) d\left(\frac{z}{z_{1/2}}\right)$  is constant,

$$\frac{d}{dx} (x^{2p+q+r}) = 0$$

So,

$$2p + q + r = 0 \quad (\text{G.30})$$

In the developed flow region, jets spread linearly with  $x$  both in the central X-Y and X-Z planes. So,  $q = 1$  and  $r = 1$ .

From (G.30),

$$p = -1$$

So, in the developed flow region, the velocity decays as  $1/x^1$ . This result is strictly for an axisymmetric jet. For a plane jet, the spreading in one of the central planes (X-Y or X-Z) is negligible. Therefore,  $p = -1/2$ , by similar reasoning.